

Microscopic Spatio-Temporal Dynamics of Semiconductor Quantum Well Lasers and Amplifiers

Von der Fakultät Mathematik und Physik der Universität Stuttgart
zur Erlangung der Würde eines
Doktors der Naturwissenschaften (Dr. rer. nat.)
genehmigte Abhandlung

Vorgelegt von
Klaus Böhringer
aus Waiblingen

Hauptberichter: Prof. Dr. O. Hess
Mitberichter: Prof. Dr. G. Mahler

Tag der mündlichen Prüfung: 4. April 2007

Institut für Technische Physik
Deutsches Zentrum für Luft- und Raumfahrt (DLR)
Pfaffenwaldring 38-40
D-70569 Stuttgart

2007

Summary

This work discusses light-matter interaction and optical nonlinearities in semiconductor nanostructures and presents a detailed numerical analysis of the spatio-temporal dynamics in novel high-power diode lasers. We derive a microscopic, spatially resolved model that combines a density matrix approach to the optoelectronic properties of quantum well gain media with the macroscopic Maxwell equations for the electromagnetic field dynamics. We present Maxwell semiconductor Bloch equations in full time-domain that cover many-particle interactions, a diversity of time scales and gain saturation mechanisms, and include the fast-oscillating carrier wave and a sub-wavelength spatial resolution. Microscopically calculated scattering rates are incorporated into our spatially resolved model.

Our work focuses on ultrafast carrier effects, a quantitative understanding of optical nonlinearities, the engineering of the mode structure in microcavities, and their impact on the laser emission characteristics. Optical dephasing and carrier and energy redistribution due to the screened Coulomb interaction and scattering with phonons are explored in detail.

We study the technologically important structure of a broad area edge-emitting laser within the framework of the paraxial wave approximation. The excitation of multiple transverse modes and the occurrence of unstable optical filaments are quantitatively analysed. We show how transverse instabilities originate from spatial hole burning, gain- and index-guiding and from self-focussing. We investigate the dependence of emission dynamics on characteristics of the gain material (e.g. the amplitude-phase coupling factor), the stripe width, pumping and carrier diffusion. Depending on the width of the laser, several dynamic emission regimes can be distinguished. We also project the spatio-temporal dynamics onto the laser modes.

We analyse VCSEL devices with a periodically structured defect as an example of a photonic band edge band gap laser. In particular, we explore the utilisation of photonic crystal structures: gain enhancement for band edge modes due to the more efficient interaction of photons with the gain medium and increased localisation over the active layers, and the reduction of optical losses. We numerically confirm that photonic crystal effects can be obtained for finite crystal structures, and demonstrate that they lead to a significant improvement in laser performance, e.g. reduced lasing thresholds.

Optically pumped VECSEL are a device concept designed to increase the power output of surface-emitters in combination with near-diffraction-limited beam quality. We explore the complex interplay between the intracavity optical fields and the quantum well gain material in VECSEL structures. Our simulations reveal the dynamical balance between carrier generation due to pumping into high energy states, momentum relaxation of carriers, and stimulated recombination from states near the band edge. We

show that the longitudinal multi-mode behaviour is composed of several external cavity modes.

We also consider the interaction of high-intensity femtosecond and picosecond pulses with semiconductor structures. We identify the microscopic origin of the fast nonlinearities, and consider the physical effects behind the various saturation mechanisms. We also obtain the nonlinear gain coefficients and recovery rates. It is demonstrated that group velocity dispersion, dynamical gain saturation and fast self-phase modulation are the main causes for changes and asymmetries in the amplified pulse shape and spectrum. We show that the time constants of the intraband scattering processes are critical to gain recovery. Our results are essential for the interpretation and the quantitative understanding of nonlinear pulse reshaping in semiconductor optical amplifiers and absorbers.

The accurate and spectrally broad modelling of semiconductor gain and complex structured laser cavities that is presented in this work extends the scientific discussion of semiconductor laser systems. Built upon efficient numerical algorithms and the increased availability of inexpensive high-performance computing resources, our microscopic time-domain approach is also well suitable for the engineering and design optimisation of modern nanostructured high-power diode lasers.

Contents

Summary	iii
Contents	v
1 Introduction, Overview and Outlook	1
2 Microscopic Description of the Gain Dynamics	11
2.1 Introduction	11
2.2 Parabolic Band Structure Approximation and Confinement Functions . . .	13
2.3 Density Matrix Formalism	18
2.4 Coherent Coupling to the Optical Field	20
2.5 Coupling to a Full Time-Domain Scheme	23
2.6 Phenomenological Terms and Additional Many-Body Hamiltonians . . .	26
2.7 Many-Body Interactions—Hartree-Fock Terms	30
2.8 Many-Body Interactions—Correlation Terms	32
2.9 Quantum Dot Lasers and Multi-Level Bloch Equations	40
2.10 Fitting the Dielectric Function	42
2.11 Spectral Summation and Coupling to the Maxwell Equations	44
2.12 Conclusion	52
3 Light Field Dynamics in Laser Cavities	55
3.1 Introduction—Macroscopic Maxwell Equations	55
3.2 Paraxial Approximation—Transverse Wave Equation	58
3.3 Full Time-Domain Maxwell Equations	64
3.4 Conclusion	67
4 Semiconductor Laser Fundamentals	69
4.1 Calculation of Scattering Rates	69
4.1.1 Microscopic Scattering Rates in Semiconductor Quantum Wells . .	69
4.1.2 Extension to the Multi-Subband Case	74
4.2 Calculations of Quantum Well Laser Gain	78
4.3 Relaxation Oscillations	89
4.4 Quantisation of Light	94
4.5 Thermodynamics of Semiconductor Lasers	97
4.6 Conclusion	99

5	Transverse Multi-Mode Laser Dynamics	101
5.1	Introduction—Effects of Spatial Degrees of Freedom	101
5.2	Transverse Instabilities in Broad Area Lasers	103
5.3	Simulations—Different Dynamic Emission Regimes	105
5.4	Conclusion	116
6	Longitudinal Multi-Mode Laser Dynamics	117
6.1	VCSEL with Resonant Periodic Gain and Refractive Index Structures	117
6.2	Optically Pumped VECSEL	124
6.3	Small Signal Gain Calculations	129
6.4	Nonlinear Pulse Propagation	132
6.5	Ultrafast Gain Dynamics	142
6.6	Chirped Pulse Amplification	147
6.7	Ultrashort Coherent Optical Pulse Interactions	150
6.8	Conclusion	156
A	Discretisation Schemes and Numerical Implementations	159
A.1	Discretisation Scheme of the Transverse Wave Equation Model	160
A.2	Discretisation Scheme of the Longitudinal Full Time-Domain Model	162
A.3	Numerical Analysis of the Scattering Integrals	167
A.4	Conclusion	170
B	Dynamical Treatment of the Scattering Contributions	173
C	Zusammenfassung	177
C.1	Kurzzusammenfassung	177
C.2	Einleitung und Motivation	178
C.3	Überblick	182
C.4	Ausblick	188
	Bibliography	189

1 Introduction, Overview and Outlook

Introduction and Motivation

The concept of light amplification by the process of stimulated emission of radiation (i.e. LASER operation [1]) in semiconductor gain materials was first demonstrated in the year 1962. Following a theoretical suggestion by Basov, three laboratories independently reported lasing in direct band gap compound semiconductor structures, with pulsed operation at cryogenic temperatures [2–4]. Stimulated emission of radiation was realised in these semiconductor diode lasers by the radiative recombination of electron-hole pairs injected across a pn-junction. The population inversion necessary for lasing was created in the depletion region of a GaAs(P) homojunction. The introduction of heterostructures in 1970 was a pioneering contribution to the development of efficient optoelectronic devices and a breakthrough towards industrial applications. Heterostructures are composed of multiple layers of compound semiconductors with different compositions. In particular, double heterostructures consisting of an intrinsic active GaAs layer, a thin film for light generation and amplification, sandwiched between two doped AlGaAs cladding layers enabled continuous wave operation at room temperature [3]. The improved performance characteristics (e.g. high efficiency, low heat dissipation) and reduced lasing thresholds in these structures were achieved by enhanced carrier and optical confinement [2–4].

Sophisticated crystal growth techniques (e.g. molecular beam epitaxy, metal-organic chemical vapor deposition, liquid-phase epitaxy, self-organised growth methods) [5], and processing and etching technologies, allow the manufacture of high quality, complex semiconductor nanostructures (such as graded index layers, superlattices, quantum wells and quantum dots, or photonic crystals). These technologies permit better control over the electronic properties of the gain material by employing the concepts of size quantisation and reduced dimensionality, and engineering of the optical mode structure and the density of states in functional photonic materials. At the same time, theory and simulation of semiconductor laser dynamics and structures has developed into a topic of more than only an academic interest. Due to its predictive character, computational modelling constitutes an invaluable tool for the engineering of novel active structures and improved device designs. Driven by the increasing demands for higher power output, different operating wavelengths, and high-speed modulation performance, the development of novel laser and amplifier structures and the introduction of new gain material systems and lasing concepts have been pushed forward. This is accompanied with the successive miniaturisation of coherent light sources and amplifiers (with the aim of on-chip realisation). This intense research in the world of semiconductor lasers stimulated the transition from a research structure to a mass product with applications in our everyday

life. Semiconductor diode lasers feature some key advantages compared to other coherent light sources: compact size, reliability, very high conversion efficiency of pump energy into coherent light, tunability and tailoring of the optoelectronic properties, direct signal modulation up to tens of GHz, and inexpensive production costs. This has created a huge market for diode lasers, with worldwide sales revenue for semiconductor lasers estimated at \$3.2 billion in 2005. The main industrial applications of diode lasers include optical storage (CD- and DVD-based technologies), optical fibre communications, high-power applications (such as solid-state laser pumping) and medical therapeutics. Besides their technological relevance, the complexity of physical interactions in diode lasers, the nonlinear coupling of various subsystems, and the diversity of time and length scales also make semiconductor lasers ideal laboratories for investigating nonlinear [6, 7] and quantum optical phenomena [8], as well as ultrafast interaction processes in semiconductors, and concepts of nonlinear dynamics and synergetics [9, 10].

New and exciting developments are aimed to control and manipulate light-matter interaction, light emission and propagation, and to engineer the optoelectronic properties of semiconductor gain media. In the following we give an overview on recent research activities that are related to this work.

Laser and amplifier structures: Vertical cavity surface-emitting lasers (VCSEL) [11, 12] are designed as highly reflective Bragg mirrors with an enclosed defect cavity and additional transverse confinement (using oxide apertures). In particular, VCSEL show strong coupling between active gain material and the light field. Microcavities [13, 14] promise high quality factors, small mode volumes and low lasing thresholds. They are fundamental tools to study and tailor the emission characteristics of a light source, and allow the modification of light-matter interactions, e.g. spontaneous emission, as the local optical density of states is defined by the dielectric structure. Semiconductor optical amplifiers (SOA) are attractive as repeaters and functional devices in all-optical networks. Resonant periodic gain structures [11, 15] offer an enhancement of the effective modal gain. Vertical external cavity surface-emitters (VECSEL) [16, 17] are a design scheme for increasing laser output powers with high quality output beams, and give easy access to nonlinear optical effects, such as dynamical gain saturation and pulse shaping or frequency conversion. Photonic crystals and photonic band gap materials facilitate light propagation with very low group velocities [18, 19]. They can function as frequency-selective mirrors or optical microcavities, and offer a guiding mechanism based on multiple Bragg interference and not on total internal reflection [20]. This guiding in the low index core (air) is used in photonic crystal fibres.

Semiconductor gain material systems: New semiconductor compound materials (binary, ternary and quaternary alloys) can be designed for a wide range of optical emission wavelengths spanning from the infrared to the ultraviolet. Most recent research focuses on II-VI compounds, wide band gap group-III nitride-based semiconductors [21–23], and dilute nitrides, e.g. GaInNAs [24], for advanced telecommunications device applications. Quantum confined active nanostructures [25] with reduced dimensionality, such as quantum wells [26], nanowires or quantum dashes [27, 28], and quantum dots [29], fundamentally change the electronic band structure and optoelectronic properties by

applying the concept of size quantisation, resulting in more efficient carrier inversions. The application of tensile or compressive strain allows further band and gain engineering. In addition, organic semiconductor lasers [30] may become viable candidates for visible solid-state semiconductor lasers and provide green light in display and illumination technologies. The scope for simple fabrication and shaping of these conjugated polymer films is attractive [31]. Most lasers of this type utilise a corrugated structure which acts as a resonator based on the concept of distributed feedback.

Laser and gain concepts: Optical pumping schemes provide an alternative to electrical pumping, and offer the possibility of defining the spatial distribution of the population inversion over large areas. The generation of ultrashort optical pulses by passive mode-locking using saturable absorber elements [32,33] is based upon the systematic utilisation of nonlinear effects and the complex dynamic interplay between gain and light field. The proposed gain material concept and structure of quantum cascade lasers depends on intersubband transitions (i.e. intraband polarisations). This intersubband nature (involving only a single type of carriers) gives rise to several key advantages compared to devices based on stimulated electron-hole recombinations [34]. For example, tunability on basis of the size quantisation concept in multiple quantum well heterostructures (i.e. no restriction given by the energy band gaps), and higher efficiency. Achieving optical gain for recombination processes in indirect band gap semiconductor materials is challenging, which motivates the investigation of other physical interactions and gain mechanisms. Recently, light amplification and lasing in silicon has been demonstrated [35], where amplification is achieved by stimulated Raman scattering.

The numerical simulation of laser dynamics plays an important role in the development of novel structures, concepts, and improved designs of active semiconductor laser devices. It is also valuable in analysing the underlying physical limitations and optical and electronic properties of the various subsystems. Because of the complex nature of the problem and the nonlinear character of the governing coupled equations, an analytical treatment is difficult. With only little restriction on the geometrical and physical setup, time-domain methods offer a flexible and expandable tool appropriate to tackle the coupled dynamics of intracavity optical fields and active gain material. The only restriction in the implementation of such methods is set by the required computing resources. The basis for semiconductor laser models are the fundamental laser equations, derived by Haken and Lamb, Jr. [36]: The basic set of dynamical variables is given by the optical field, the induced polarisation of the active material, and the carrier inversion. An overview of commonly applied time-domain models to simulate semiconductor lasers within the semiclassical framework (i.e. the combination of classical electromagnetic fields with the quantum electronic properties of the active material) is presented in [3, 37]. We summarise the various approaches to modelling semiconductor gain dynamics in FIGURE 1.1, and the dynamics of the optical fields in FIGURE 1.2. Therein, we also define the scope and merits of our novel models compared to other methods.

In distinction to other laser structures, semiconductor diode lasers are characterised by some unique features that have to be reflected in realistic computer models [2,4,37]: Due to the high carrier density, many-body interactions are important, particularly in gain

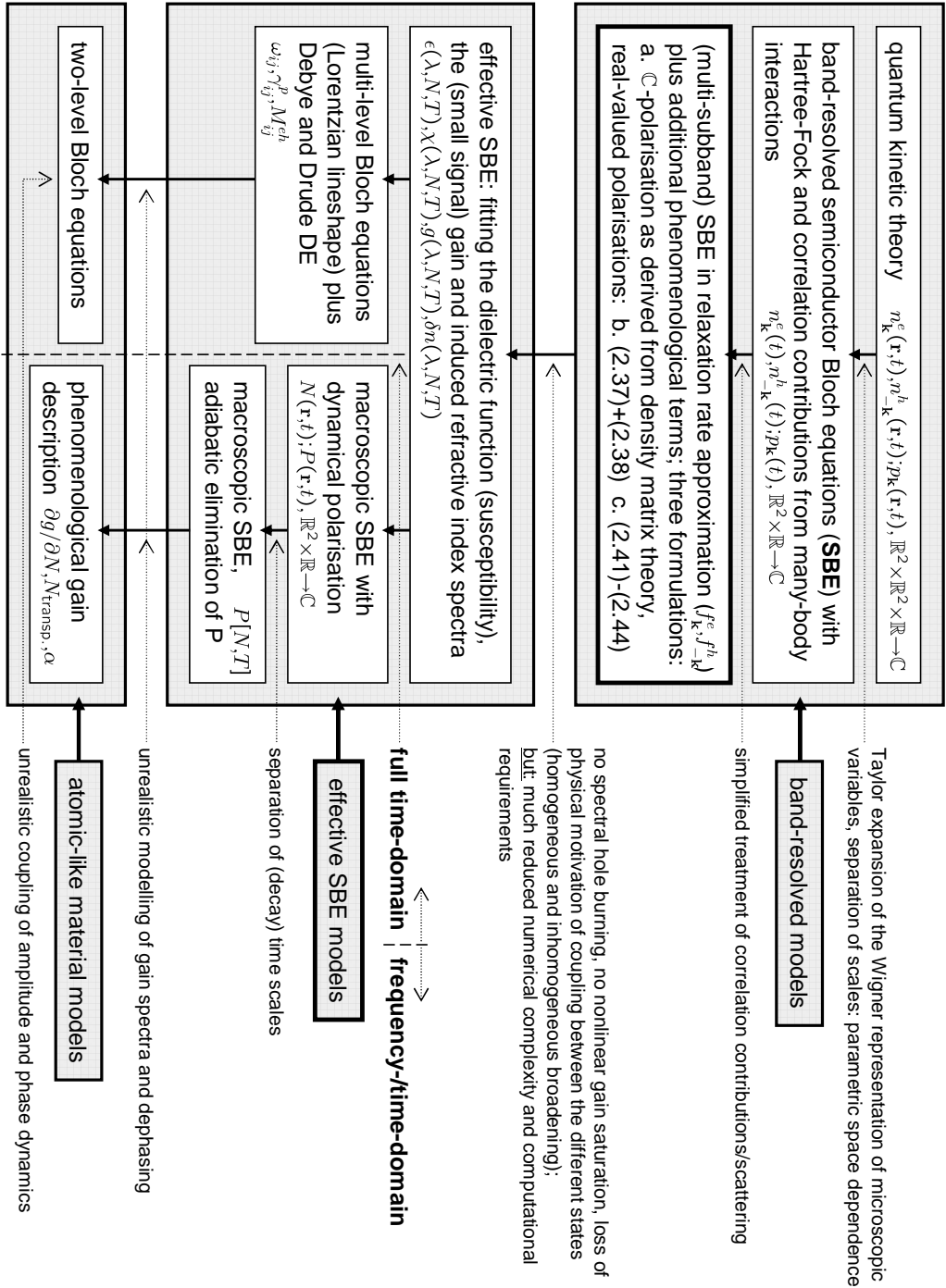


FIGURE 1.1: Overview on commonly applied approaches for describing the semiconductor quantum well gain dynamics as the source term of an optical wave equation. Symbols and applied approximations are discussed in CHAPTER 2. Our simulations employ the band-resolved semiconductor Bloch equations in relaxation rate approximation and effective SBE models (as highlighted in the drawing).

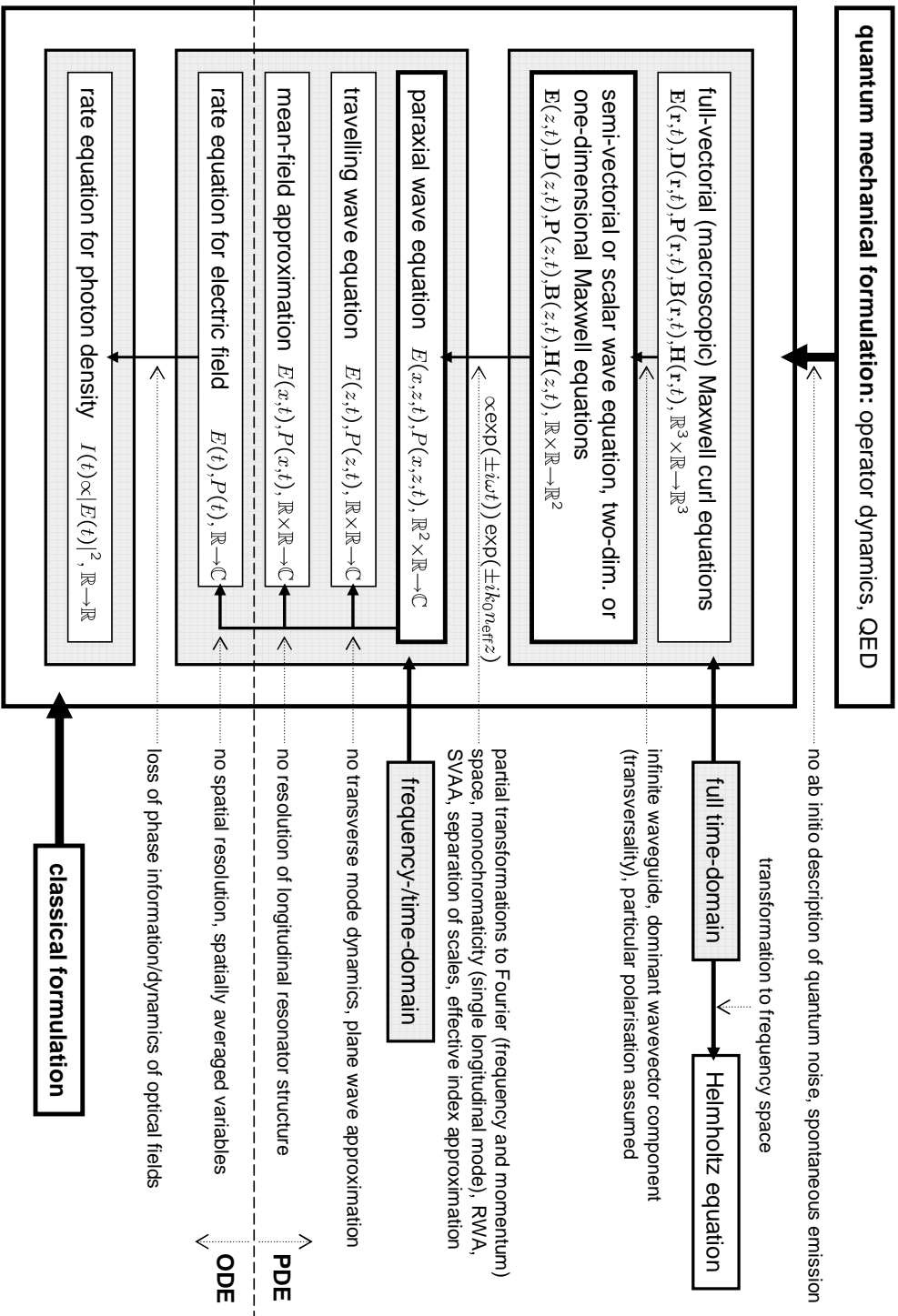


FIGURE 1.2: Overview on mathematical descriptions of the optical field dynamics in diode laser models. The laser fields are coupled to the semiconductor material response by the induced polarisation. Symbols and assumptions are described in CHAPTER 3. The optical models implemented in this work, namely the scalar one-dimensional Maxwell curl equations and the paraxial transverse wave equation, are highlighted.

structures with quantum confinement, and there is a strong dephasing of the induced polarisation. Semiconductor gain materials are characterised by broad gain spectra, and a strong coupling of the amplitude and phase dynamics (qualified by a high α factor). Diode lasers include a multitude of relevant time scales ranging from a few femtoseconds (for intraband Coulomb scattering) to several nanoseconds (for macroscopic transport processes such as carrier diffusion). Furthermore, strong spatial and spectral hole burning, nonlinearities and saturation effects are all important. Modern semiconductor diode lasers are composed of complex structured cavities. The lasing modes may strongly differ from cold-cavity modes because the lasing action and carrier dynamics (e.g. hole burning and thermal effects) change the refractive index structure. The output performance and characteristics of a diode laser are limited by the nonlinear properties of the gain material, important aspects comprise the quantum well carrier dynamics (e.g. spectral hole burning and scattering processes), spatial effects (e.g. spatial hole burning, self-focussing) and thermally induced changes of the gain medium. In conclusion, the theory of semiconductor lasers has to be continuously revised and successively adapted to the novel structures, concepts, and gain materials, which have been described in the previous sections.

The main objective of this work is developing a theoretical description of the spatio-temporal dynamics in novel high-power semiconductor lasing structures. We also aim to obtain a quantitative understanding of the nonlinear interplay between the semiconductor gain dynamics and the intracavity light field dynamics. To this end, we revise and extend existing theoretical approaches to semiconductor laser dynamics to account for the challenging requirements imposed by the improved gain and cavity designs discussed above. Special attention is paid with regard to quantum confined gain structures, complex dielectric microcavities, and photonic structures. Taking into account the above specified requirements for a realistic model of semiconductor laser dynamics, our time-domain approach within the semiclassical framework combines the spatially resolved Maxwell equations, or an approximated paraxial wave equation, with an energy-resolved description of the material response, as given by the semiconductor Bloch equations. Two classes of models are developed: 1) a transverse model for the analysis of transverse multimode dynamics in broad area lasers, and 2) a longitudinal model to target ultrashort pulse propagation in semiconductor optical amplifiers. We also employ the latter model to study complex structured active laser devices, e.g. vertical cavity surface-emitting lasers with a periodically structured defect, and optically pumped vertical external cavity surface-emitters. To solve the model equations for the optical field dynamics (partial differential equations) simultaneously with the polarisation and carrier dynamics of the active semiconductor structures, we convert them to finite-difference equations which are numerically integrated on a uniform grid.

Overview of Thesis

This work aims to improve the quantitative understanding of lasing systems with technological or fundamental relevance. On basis of a full microscopic gain model with

many-body interactions we focus on the investigation of femtosecond and picosecond phenomena and analyse spatial optical near-field patterns. We analyse the microscopic origin of optical nonlinearities and the impact of the carrier dynamics on the output characteristics of diode lasers. We concentrate on high-power structures such as broad area lasers and semiconductor optical amplifiers. We numerically validate novel concepts to increase the output powers of surface-emitting lasers, e.g. by the engineering of the optical mode structure. More specifically, we investigate photonic band edge band gap lasers and optically pumped VECSEL. The thesis is organised in the following way:

In CHAPTER 2 we derive the multi-subband semiconductor Bloch equations, which consist of a quantum mechanical description of the ultrafast gain dynamics in quantum wells based on the density matrix formalism. Our approach, formulated in momentum space, covers the relevant interactions in semiconductor-based optically active gain materials, and a diversity of time scales. Light interaction with semiconductor gain media is modelled, within the semiclassical framework, using the electric dipole approximation. Many-body interactions, namely the screened Coulomb interaction and the scattering with phonons, effect the renormalisation of transition energies, the Coulomb enhancement of the Rabi frequency, and relaxation and dephasing processes. We perform full microscopic many-body calculations. The equations are also derived in full time-domain. To the best of our knowledge, this formulation of the full time-domain semiconductor Bloch equations has not been reported before. Our approach does not imply the usual rotating wave approximation, and thus it represents an accurate and spectrally broad modelling of the gain medium. Our model allows the simulation of ultrafast nonlinear pulse interactions in semiconductor lasers and amplifiers. The response of the amplifier medium is qualified by the induced macroscopic polarisation $\mathbf{P}(\mathbf{r}, t)$, the carrier density, and the material dispersion $n_{\text{background}}(\mathbf{r}; \omega)$. In addition, we propose the fitting and parametrisation of the complex dielectric susceptibility using only a few oscillators as an effective way to reproduce the optoelectronic properties of a complex semiconductor gain medium.

In CHAPTER 3 we consider the description of the light field dynamics in laser cavities. The propagation, diffraction, reflection and guiding of electromagnetic fields in refractive index structures and optical cavities of laser resonators is modelled using the macroscopic Maxwell curl equations, or a derived approximated wave equations. The spectrally resolved induced macroscopic polarisation, that we calculate in CHAPTER 2, acts as a source term for the optical laser fields. We develop two different models to account for the passive problem: 1) The full time-domain Maxwell equations are targeted towards problems that involve a very broad range of relevant frequencies or spatially strong localised cavity modes. This approach, however, is limited to micrometer-sized active devices. We investigate microcavity lasers and nonlinear pulse interactions in semiconductor amplifiers. We combine the Maxwell curl equations with a band-resolved description of the semiconductor gain dynamics, within the finite-difference time-domain framework. Our numerically challenging approach is generic and has not been implemented before. 2) Depending on the resonator characteristics the paraxial, slowly varying amplitude and rotating wave approximations are applied to simplify the model equations.

A transverse scalar wave equation model is developed for the analysis of high-power large edge-emitting semiconductor lasers and amplifier structures, and for the study of transverse multi-mode laser dynamics.

In CHAPTER 4 we consider the local properties of the active laser gain medium using models which are not spatially resolved. Instead, the resonator structure is accounted for through effective parameters. Microscopic scattering and dephasing rates for the Coulomb and Fröhlich interaction in GaAs quantum well systems are calculated for various carrier sheet densities and temperatures. We employ these microscopic parameters in our simulations of the spatio-temporal laser dynamics, which is demonstrated to improve the model quantitatively. We show that the relaxation rates are a crucial factor for the accurate modelling of the gain properties, nonlinear pulse propagation, and the dynamical saturation behaviour of gain and absorber elements. A dynamical treatment of scattering is presented in APPENDIX B. The important optical gain properties of semiconductor amplifier media, the spontaneous emission spectra and the radiative recombination rates are calculated using a microscopic approach, derived from first principles. Basic concepts of semiconductor lasers, such as density pinning and gain clamping, gain saturation, and thermal rollover, are discussed within the framework of our models. The transient dynamic response when a laser is switched-on or perturbed during operation, i.e. laser relaxation oscillations, is investigated. We obtain a realistic set of input parameters for the analysis of spatio-temporal laser dynamics, which improve our approach quantitatively. The close agreement between numerical results and experimental findings, as well as theoretical predictions from more simple models, verifies our approach.

In CHAPTER 5 we study broad area lasers by applying the paraxial optical model introduced in CHAPTER 3. We show that on increasing the width of the active zone or the pump power, more transverse modes are excited, spatial and temporal fluctuations in the near-field occur, and unstable optical filaments are formed. We link the transverse multi-mode and filamentation behaviour with the carrier and gain dynamics, and to the selective depletion of the carrier density by the various transverse laser modes. We show that the coexistence of multiple modes is supported by the interaction of the various modes with different domains of the gain material, spatially due to the transverse degree of freedom and spectrally as a result of inhomogeneous broadening. The impact of optical nonlinearities due to spatial hole burning and of the physical effects of carrier diffusion, gain- and index-guiding, self-focussing and diffraction, are quantitatively analysed. We present a linear stability analysis of the transverse instability. This allows us to identify the main control parameters: the stripe width, and the linewidth enhancement factor. We numerically show that, depending on the width of the structure, different degrees of spatio-temporal complexity and dynamic emission regimes can be distinguished. We employ a complex mode analysis of the numerically calculated optical field amplitudes to find out the lasing frequencies, and project the spatio-temporal near-fields onto the laser modes (in the quasi-periodic regime).

In CHAPTER 6 we apply the full time-domain model, i.e. the Maxwell equations coupled to the semiconductor Bloch equations, to investigate the longitudinal multi-mode dynamics of novel laser structures and the interaction of femtosecond and picosecond

pulses with an optically active medium. VCSEL with embedded periodic gain and refractive index structures are considered. The calculation of the laser modes, lasing frequencies and thresholds, numerically shows that photonic crystal effects can be obtained for finite crystal structures, and lead to a significant improvement of the laser performance. We show how photonic band edge lasers capitalise on the special properties of the singularities in the optical band structure diagrams, e.g. the flat dispersion at band edges. Our results demonstrate gain enhancement by an increased localisation of the modes over the active quantum confined structures and by the more efficient interaction of photons with the gain medium. The latter is due to the reduced group velocity. We analyse the suppression of optical losses of the inner finite photonic structure by introducing a surrounding photonic band gap region. Realistic optically pumped external cavity surface-emitting laser structures are studied. We show that the longitudinal multi-mode behaviour in such structures is composed of several external cavity modes. A microscopic analysis reveals the dynamical balance between carrier generation from pumping into high energy states, relaxation of carriers towards the Fermi-Dirac distribution, and lasing from states near the band edge. We also consider the propagation of femtosecond and picosecond pulses in active semiconductor structures. We identify the microscopic origin of the fast nonlinearities, and discuss the physical effects behind the various saturation mechanisms, e.g. the depletion of available resonant carriers for stimulated emission. We also calculate the nonlinear gain coefficients and the different recovery rates. Group velocity dispersion, the dynamical saturation and fast self-phase modulation, are the main causes of the asymmetries observed in pulse shape and spectrum. The most critical parameters of gain recovery are given by the time constants of intraband scattering processes. We also investigate nonlinear coherent pulse propagation phenomena in active gain media, in particular the pulse area theorem and self-induced transparency. Our numerical full time-domain simulations are employed with realistic parameters for the dephasing processes and the homogeneous broadenings. The results show that coherent ultrafast nonlinear propagation effects become less distinctive in semiconductor quantum well gain materials at room temperature.

APPENDIX A provides details about the numerical implementation of the theoretical time-domain models, such as the applied discretisations of the fields and differential operators on regular grids, and the integration schemes used. We also discuss the numerical complexity, accuracy and the stability of our algorithms. For the paraxial transverse wave equation model we propose the Hopscotch method as an efficient, stable and reasonable accurate solver. We employ a numerical algorithm which involves the partitioning of the grid into two groups of grid points, and an integration scheme with alternating explicit and implicit discretisations. The merit of this method is that it does not require solving a matrix-valued problem. We discuss the finite-difference time-domain (FDTD) method which solves the first order Maxwell curl equations by arranging the electric and magnetic field quantities on staggered grids in time and space according to the Yee scheme. A fully explicit numerical implementation of our full time-domain model of the active nonlinear material response and the passive refractive index structure is developed.

Outlook

In summary, in this work we develop and present time-domain methods, which are demonstrated to be valuable tools in the analysis of the coupled intracavity optical field dynamics and band-resolved semiconductor material response. Our novel approaches are successfully applied to the investigation of one-dimensional photonic band edge band gap lasers and optically pumped VECSEL. We also consider high-power structures, such as broad area lasers and semiconductor optical amplifiers, where optical nonlinearities and ultrafast processes are significant. The theoretical framework presented in this work is rather general, and thus can be easily extended to more complex gain systems and laser structures. Their implementation, however, is limited by the available supercomputing resources.

Possible extensions of the model and topics for further research include microcavity and photonic crystal lasers, which would require to consider the three-dimensional full-vectorial Maxwell equations [14, 38]. The study of σ -type electric dipole transitions, i.e. circular polarisation, can be implemented with complex-valued electromagnetic and polarisation fields [39]. Femtosecond nonlinear pulse interactions in semiconductors can be analysed. To this end, a microscopic dynamical treatment of the carrier scattering and energy redistribution [40], and the consideration of gain and material dispersion [41], are very important. We note that with the miniaturisation of laser structures (e.g. microcavities), the study of spontaneous emission becomes a significant topic as the radiative lifetimes can be controlled by the dielectric structure and cavity design, and thresholdless lasing is possible [20, 42–44]. We thus suggest our model could be extended by including a description of quantum noise and spontaneous emission, as well as cavity quantum electrodynamics, into the time-domain approach [45–47].

2 Microscopic Description of the Gain Dynamics

2.1 Introduction

The static and dynamical performance characteristics of a diode laser or semiconductor optical amplifier device are determined by both, the electronic and optoelectronic properties of the active gain medium and the refractive index structure and geometry of the optical resonator, modelled by the use of the macroscopic Maxwell equations or some derived approximated wave equations (CHAPTER 3) [2]. In this chapter, the response of the semiconductor material to applied electromagnetic fields is calculated. The response of the material system includes the nonlinear and noninstantaneous induced electric polarisation $\mathbf{P}(\mathbf{r}, t)$ of the active gain medium and the dispersion of the background material $n_{\text{background}}(\mathbf{r}; \omega)$, which is accounting for far off-resonant excitations or resonances of the host medium.

There are a couple of different model equations to qualify the physics of gain media and to describe the coherent processes of stimulated emission and absorption [3, 10]. In solid-state or gas lasers one can regard the active medium effectively as an ensemble of absorption or amplification centres (like e.g. atoms, molecules) with only two electronic energy levels which couple to the resonant optical field mode [1]. Other electronic states are used to excite or pump the system. Depending on the occupations, amplification or absorption of the light fields takes place. The optical Bloch equations [2, 10], which are a set of equations for the population inversion and the induced electric polarisation, form the very basis of the semiclassical two-level model. The two-level system with homogeneous broadening describes a driven damped harmonic oscillator with a symmetric Lorentzian gain profile. This, however, does not constitute a sufficiently precise model for the gain profile of a semiconductor-based active medium [3, 24, 48–51]. The big advantages of this approach are low complexity of the description and the fact that it requires only marginal numerical efforts. Besides its shortcomings, such a simple model enables the possibility to perform extensive parameter scans, for instance in a bifurcation analysis of nonlinear laser dynamics [9, 10, 52]. In other situations, e.g. when concentrating on the optical properties of the cavity structure of novel nanostructured devices or microcavity lasers [13], a three-dimensional modelling is necessary. As the numerical effort may already be high, a two-level gain model can come into consideration [14]. In reality, the gain spectrum of a semiconductor medium is highly asymmetric and shows a typical profile in frequency, i.e. a sharp structure at the direct band edge and absorption for high frequencies [4, 51]. As starting point, one could interpret a semiconductor

medium as the sum of two-level systems with different transition frequencies as determined by the electronic band structure and with separated carrier inversions, and then make a superposition of the contributions of the various transitions. This would result in an inhomogeneously broadened system. However, due to the high carrier densities in a semiconductor laser and operation at room temperature, the diverse emission centres are strongly coupled and many-body effects like the carrier-carrier Coulomb interaction or the interaction of the carrier subsystem with quantised excitations of the lattice (phonons) are prominent features [4,48,53]. Besides that, the coupling between the phase and amplitude dynamics in semiconductor-based active structures is typically large [2]. Other effects, such as the renormalisation of the transition energies, the Coulomb enhancement of the Rabi frequency, various scattering and dephasing processes, spectral hole burning and multi-mode operation, the diversity of optical nonlinearities, poor beam quality or enhanced laser linewidths are covered by the semiconductor Bloch model. As a result, the semiconductor laser is both, an inhomogeneously and homogeneously broadened system. The most important laser properties, such as the transparency density, threshold current, differential gain factor, nonlinear saturation behaviour or the density dependent linewidth enhancement factor [4] are calculated in a straightforward and appropriate way. To summarise, we could say that, the more detailed the description of the active semiconductor material, the less need for phenomenological factors, which are typical for more generic laser models [54].

In this chapter we will introduce a detailed quantum mechanical description based on the density matrix formalism. The gain dynamics includes many-body effects. Multi-subband semiconductor Bloch equations are derived in both, a time-domain formulation with a split-off frequency and in a full time-domain formulation. All the active material properties and microscopic interactions determine the induced macroscopic polarisation $\mathbf{P}[\mathbf{E}, n_{\mathbf{k}}^{\circ}, N, T_{\text{pl}}, T_{\text{lat}}]$, which is a dynamical material response functional. This source term of the optical wave equation is connected with the microscopic gain dynamics by a spectral summation, and in low-dimensional nanostructures by an additional necessary transformation to a volume-based density quantity. An adiabatic elimination of the polarisation is an approximation which is motivated by the separation of decay time scales of the different macroscopic variables. This enables us to derive an effective microscopic model from the microscopic set of equations [36,55]. A further simplification is to neglect the phase dynamics of the optical fields. This leads to standard rate equation models [9, 52]. For complicated active gain media, e.g. polymer or organic materials [30,31], carbon nanotubes [56], or other nanostructures [27,57], it is considered impractical to microscopically calculate the optoelectronic material response properties. An approach to model the interaction of the active material with electromagnetic fields is to fit the susceptibility coefficients with as few as possible excitations of Lorentzian, Debye or Drude type [58,59] (a multi-level system). FIGURE 1.1 gives an overview on commonly applied models which can be used to simulate for the semiconductor gain dynamics or generic optically active gain media. The various levels of description are developed and discussed in more detail in the following sections.

2.2 Parabolic Band Structure Approximation and Confinement Functions

In this section we review the basic concepts, terminology and properties of semiconductor crystals [5]. The simulations in this work are done for the Indium Gallium Arsenide/Aluminium Gallium Arsenide $\text{In}_x\text{Ga}_{1-x}\text{As}/\text{Al}_y\text{Ga}_{1-y}\text{As}$ material system, which is a typical representative of the III-V semiconductors [60]. III-V semiconductors are composed of atoms of the group of metals (In,Ga,Al) and atoms of the nitrogen group (group-V of the periodic table of elements). They often crystallise with a cubic crystal symmetry, the zincblende structure. The chemical bonding in these materials is mediated through the exchange interaction between the eight outer electrons (per unit cell), and sp^3 hybrid orbitals are formed. To describe the formation of a crystal from first principles one would have to solve the many-body Schrödinger equation for a macroscopic system with about 10^{23} atoms, which is apparently not possible. However, in order to understand the optoelectronic properties of bulk semiconductor crystals around the band edge, a single particle approximation can be applied, where the time-independent Schrödinger equation for a representative electron is solved. The interaction with the nuclei and the inner strongly bound electrons and other free electrons is summarised by an effective periodic potential V_{eff} . The spin degree of freedom and the resulting spin-orbit coupling are accounted for by an additional term $H_{\text{spin-orbit}}$. The single particle Hamiltonian can thus be written as

$$H_0 = \frac{p^2}{2m_0} + V_{\text{eff}}(\mathbf{x}) + H_{\text{spin-orbit}}, \quad V_{\text{eff}}(\mathbf{x}) = V_{\text{eff}}(\mathbf{x} - \mathbf{X}). \quad (2.1)$$

Due to the translation symmetry of the lattice, the eigensolutions obey the Bloch theorem and can be labelled with a wavevector \mathbf{k} . Equation (2.1) is the starting point for band structure calculations using various numerical methods, such as tight-binding theory (or linear combination of atomic orbitals, abbr. LCAO), pseudo-potential methods or semi-empirical, perturbatively $\mathbf{k} \cdot \mathbf{p}$ theory [5, 61]. The eigenstates are delocalised over the crystal and form rather complicated energy band structure diagrams with several conduction and valence bands. The for lasing crucial process of coherent interaction between light fields and the two-component carrier plasma involves only a small portion of the band structure. Transitions are designed to occur with energies around the band gap and around the high-symmetry Γ point (i.e. $\mathbf{k}_0 = 0$) of the direct band gap gain material. Photon momentum transfer is negligible, and optical transitions primarily take place at the band edge. A simplification of the energy level structure for a bulk semiconductor laser is the effective mass approximation which introduced a parabolic dispersion of the conduction band (cb) and the heavy-hole valence band (vb). Then, by replacing the free electron mass with (in the general case tensor-valued) effective masses, we can write

$$E_{\mathbf{k}}^e = \frac{\hbar^2 k^2}{2m_e}, \quad E_{-\mathbf{k}}^h = \frac{\hbar^2 k^2}{2m_h} \quad (2.2)$$

for the energies of free electrons and holes. For $\mathbf{k}_0 = 0$ some similarities to atomic physics may be drawn, and the different energy bands can be characterised by atomic quantum numbers for the total and projected orbital and spin angular momenta $|l s; m_l m_s\rangle$ or, if we assume the spin-orbit coupling in the Russell-Saunders scheme, by total angular momentum numbers $|l s; j m_j\rangle$. The conduction band states are s-like and show a two-fold degeneracy due to the spin degree of freedom $|0 1/2; 1/2 \pm 1/2\rangle$, whereas the valence band states are p-like and six-fold degenerated. The consideration of the spin-orbit coupling partially lifts this energetic degeneracy and separates the split-off band $|1 1/2; 1/2 \pm 1/2\rangle$ from the heavy-hole, light-hole energy band states $|1 1/2; 3/2 \pm 3/2\rangle$ and $|1 1/2; 3/2 \pm 1/2\rangle$ [4].

Sophisticated crystal growth techniques, namely molecular beam epitaxy (MBE), liquid-phase epitaxy (LPE), metal-organic chemical vapor deposition (MOCVD) [5], and modern self-organised growth methods [29] are used to manufacture high quality semiconductor structures (e.g. layers, superlattices or quantum dots). The precision of some of these techniques allows to create or grow quantum confined structures, and to engineer the band gap and energy levels. In a quantum well heterostructure the carriers are quantum confined in one direction, namely in the growth direction of the structure. The motion in the two perpendicular directions is free. We choose the z -direction, in the transverse wave equation model it would be the lateral y -direction. Quantum confinement occurs if one dimension of the structure is comparable to the characteristic length scale of elementary excitations. In summary, we have a quasi two-dimensional system with a wavevector $\mathbf{k} = (k_x, k_y)$. As the result of the lower symmetries and dimensions properties are modified. The envelope function approach incorporates the quantum well confinement into the $\mathbf{k} \cdot \mathbf{p}$ method. The wave functions are approximated in plane wave mode expansions [62]

$$\psi_{i,\mathbf{k}}^{\text{cb}}(z, \mathbf{r}) = \frac{1}{\sqrt{A}} e^{i\mathbf{k}\cdot\mathbf{r}} \sum_{n(\text{bands})} u_{n,\mathbf{k}_0}^{\text{cb}}(z, \mathbf{r}) \phi_{n,i,\mathbf{k}}(z), \quad (2.3)$$

$$\psi_{j,\mathbf{k}}^{\text{vb}}(z, \mathbf{r}) = \frac{1}{\sqrt{A}} e^{i\mathbf{k}\cdot\mathbf{r}} \sum_{n(\text{bands})} u_{n,\mathbf{k}_0}^{\text{vb}}(z, \mathbf{r}) \phi_{n,j,\mathbf{k}}(z), \quad (2.4)$$

in which $u_{n,\mathbf{k}_0}^{\text{cb}}(z, \mathbf{r}), u_{n,\mathbf{k}_0}^{\text{vb}}(z, \mathbf{r})$ denote the lattice-periodic Bloch functions at the band minima, and A is a normalisation area. $\phi_i(z), \phi_j(z)$ are the electronic confinement or envelope functions for the electrons and holes, respectively. The Bloch functions vary on the atomic length scale in contrast to the envelope (confinement) functions which vary on the nanoscale. With the above given ansatz we solve the matrix-valued eigenvalue problem

$$\sum_m H_{nm} \left(\frac{p^2}{2m_0}, V_{\text{eff}}(\mathbf{x}), H_{\text{spin-orbit}}, V_{\text{conf}}(z), \mathbf{E}, e, \dots \right) \phi_{m,i,\mathbf{k}} = E_{i,\mathbf{k}} \phi_{n,i,\mathbf{k}}, \quad (2.5)$$

where i represents a combination of quantum numbers. The diagonalisation of this matrix equation returns the energy eigenvalues and the envelope functions. The Hamilton operator covers the effective crystal symmetry and the relativistic spin-orbit coupling,

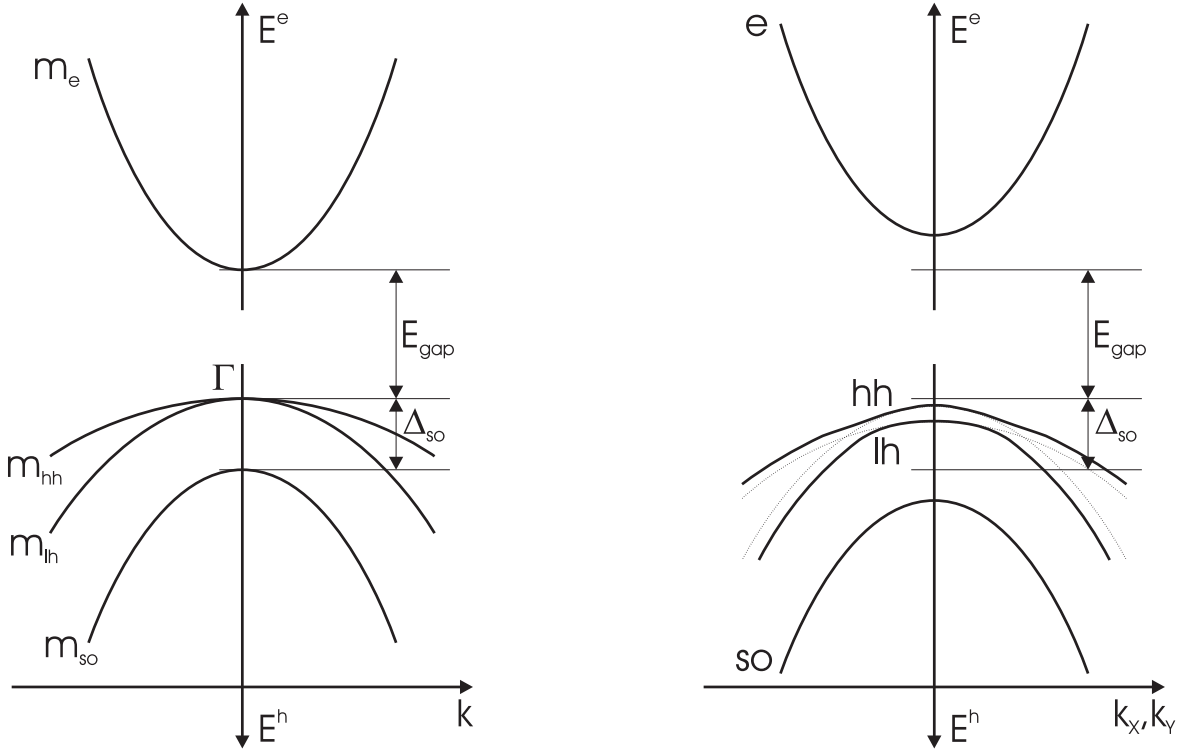


FIGURE 2.1: For direct optical transitions relevant section of the energy band structure diagram around the high-symmetry point Γ . Eigensolutions of the one-electron Schrödinger equation for the (In)GaAs gain material system in the case of bulk (left) and quantum well (right graph) structures [4,5]: The energy bands are classified by the total and projected angular momentum numbers. The split-off energy Δ_{so} is often comparably large (not for phosphide and nitride compounds). The energy level structure is modified as a result of lowered dimension and symmetries (for a quantum well, right diagram). Because of the effects of mass reversal and level-anticrossing the energy dispersion relations are more complicated, the hole energy bands become nonparabolic. In our microscopic time-domain simulations the energy structures of active gain elements are approximated by effective masses $m_e/m_0(\text{GaAs}) = 0.067$, $m_h/m_0(\text{GaAs}) = 0.33$ and $m_e/m_0(\text{InGaAs}) = 0.06$, $m_h/m_0(\text{InGaAs}) = 0.35$ (proportional to the inverse curvatures of the energy dispersions), and by the band gap and quantum confinement energy. Completely filled (inner) bands and resonances of lattice and strong bound electrons do not contribute directly to the dynamical material response $\mathbf{P}(t)$, that means to resonant optical transitions and excitations. However, they are included into the linear, static response specified by the background refractive index $n_{\text{background}}(\lambda)$.

usually quantified by the experimentally determined Kohn-Luttinger parameters [60], the carrier quantum confinement potential $V_{\text{conf}}(z)$ which is formed by the band edge discontinuities, and the impact of tensile or compressive elastic strain e (in not perfectly lattice matched heterostructures). In compounds of group-III nitrides, which are important for wide band gap materials emitting in the green to ultraviolet [21, 22], the calculations are even more complicated. These compounds crystallise in the (asymmetric) hexagonal wurtzite structure, and strain induced piezoelectric fields have to be taken into account by solving the Poisson equation together with the Schrödinger equation. We would like to give a brief sketch of the different levels of that problem [62] and then introduce the set of single particle energy eigenstates used in the rest of this work. The simplest representative of $\mathbf{k} \cdot \mathbf{p}$ models applies a 4×4 matrix Hamiltonian, which already features effects like mass reversal, heavy-hole and light-hole band mixing as typical for quantum confined structures [5]. In active laser compounds based on phosphides or nitrides with comparatively small split-off energies the additional coupling of the split-off band enlarges the problem to a 6×6 matrix eigenvalue problem [4]. More complicated Hamiltonians exist to model the mixture of conduction and valence bands and leading to nonparabolic conduction subbands [61, 62].

Based on the fact that we concentrate on (In)GaAs quantum wells, the basic optoelectronic properties can be well approximated by restricting the description to the conduction and the heavy-hole band. We apply the effective mass approximation, and assume an isotropic (averaging over all possible directions of k) and parabolic band structure. As first step we solve the following one-dimensional problems: The quantum confinement of the carriers as imposed by the grown layer heterostructure¹ and possible external potentials give rise to the following Schrödinger-like energy eigenvalue problems²

$$\left[-\partial_z \left(\frac{\hbar^2}{2m_{e,z}(z)} \partial_z \right) + \frac{\hbar^2 k^2}{2m_{e,\perp}} + V_{\text{conf}}(z) \right] \phi_i(z) = \left(E_i^e + \frac{\hbar^2 k^2}{2m_{e,\perp}} \right) \phi_i(z), \quad (2.6)$$

$$\left[-\partial_z \left(\frac{\hbar^2}{2m_{h,z}(z)} \partial_z \right) + \frac{\hbar^2 k^2}{2m_{h,\perp}} + V_{\text{conf}}(z) \right] \phi_j(z) = \left(E_j^h + \frac{\hbar^2 k^2}{2m_{h,\perp}} \right) \phi_j(z). \quad (2.7)$$

In addition to this electronic confinement of the eigensolutions $\phi_i(z), \phi_j(z)$, the grown heterostructure also represents a refractive index waveguiding structure $n(z)$ which focuses the optical field profiles over the active quantum wells. Due to the very different length scales, configurations which separate these two confinements have been proposed³.

¹The band edge discontinuities in heterostructures form a potential $V_{\text{conf}}(z)$. For an infinitely deep potential well the wave functions have to vanish at the layer interfaces, and we can calculate the confinement energies analytically as $E_n = \hbar^2 / (2m_z) \pi^2 / d_{\text{QW}}^2 \cdot n^2$.

²The demand of continuity of the quantum mechanical wave function and of the probability current at band gap discontinuities (at positions z_{int}) give rise to the so-called Bastard boundary conditions [5, 26] $1/m_z(z_{\text{int}}^-) \partial_z \phi_n(z_{\text{int}}^-) = 1/m_z(z_{\text{int}}^+) \partial_z \phi_n(z_{\text{int}}^+)$.

³The basic objective of these structures is to enhance the modal gain $G_{\text{mod},m}$, the effective amplification of the spatial field profile or mode m . The dynamics is given by the multi-mode rate equation $1/v_{\text{gr}} \partial_t |\tilde{E}_m|^2 = (G_{\text{mod},m} - 2\gamma_{\text{resonator},m}) |\tilde{E}_m|^2$ [63]. The modal gain can be enhanced by increasing the semiconductor material gain $g(\omega = \omega_m)$ (e.g. by an electronic quantum confinement) and/or by optimising the optical confinement Γ_m , this is because of the relation $G_{\text{mod},m} = 2\tilde{\kappa} \Gamma_m g(\omega_m)$.

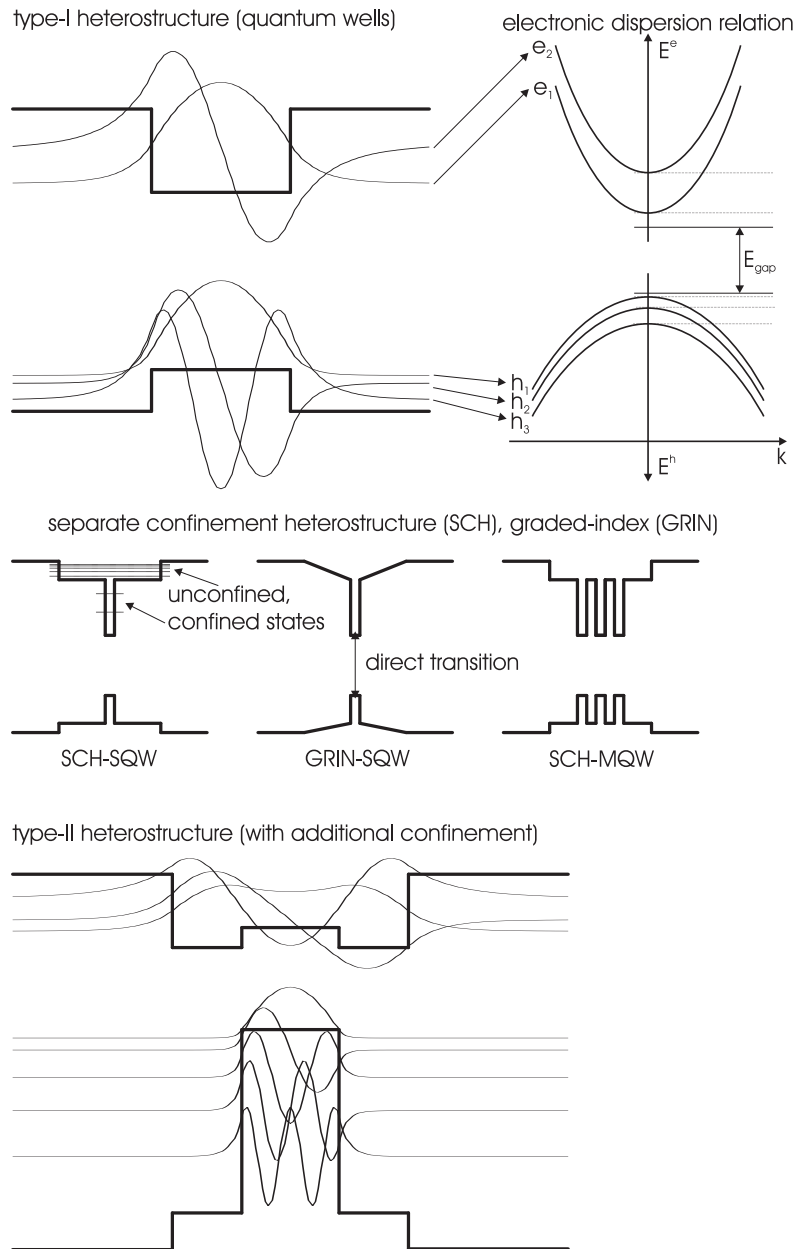


FIGURE 2.2: Overview on epitaxially grown heterostructures with electronic and additional optical confinement: (Top) The lowest confined eigenstates in a type-I heterostructure (e.g. GaAs/AlGaAs quantum wells with a one-dimensional quantum confinement potential $V_{\text{conf}}(z)$, and an inverted profile $n(z)$ for the refractive index) are displayed. This gives rise to the existence of subbands. The energy dispersion relations are composed by the energy eigenvalue plus by a free motion in-plane. (Middle) Layer structures which separate the optical from the electronic confinement. (Bottom) Calculated electronic confinement in a type-II heterostructure (e.g. GaAsSb/InGaAs quantum wells with a spatially indirect band gap). The radiative transition rates are mainly determined by the overlap integrals of the envelope functions $\int dz \phi_i^*(z) \phi_j(z)$.

The above eigenvalues E_i^e, E_j^h of bound states have to be added to the dispersion relation (2.2) of a free electron, hole

$$E_{i,\mathbf{k}}^e = E_i^e + \frac{\hbar^2 k^2}{2m_e}, \quad E_{j,-\mathbf{k}}^h = E_j^h + \frac{\hbar^2 k^2}{2m_h}. \quad (2.8)$$

As a result, a finite number of subbands are formed. We neglect the unconfined states of the quantum well. The energy eigenstates are fully determined by the two-dimensional wavevector \mathbf{k} and the number of the subband i, j . To account for recombination and loss processes, to be flexible concerning the number of electrons and holes, and for symmetries associated with fermionic particles, the description of the semiconductor gain medium by the wave function of the system is extended to second quantisation. The following plane wave mode expansion is made [64]

$$\psi(z, \mathbf{r}) = \frac{1}{\sqrt{A}} \sum_i \sum_{\mathbf{k}} \phi_i(z) c_{i,\mathbf{k}} e^{i\mathbf{k}\cdot\mathbf{r}} + \frac{1}{\sqrt{A}} \sum_j \sum_{\mathbf{k}} \phi_j(z) d_{j,-\mathbf{k}}^\dagger e^{i\mathbf{k}\cdot\mathbf{r}}. \quad (2.9)$$

The creation, annihilation operators for electrons in the states of the conduction subband i and with wavevector \mathbf{k} are introduced as $c_{i,\mathbf{k}}^\dagger, c_{i,\mathbf{k}}$. $d_{j,-\mathbf{k}}^\dagger, d_{j,-\mathbf{k}}$ are the corresponding quantities for the holes.

2.3 Density Matrix Formalism

A quantum theoretical treatment of a macroscopic system of many identical, indistinguishable and interacting particles (e.g. 10^{23}) by calculating the many-body wave function from Schrödinger equation is far too complicated. This is due to interaction processes such as recombination, collision, energy and momentum relaxation, the interaction with classical radiation fields, and the Coulomb interaction. In addition, open systems such as a laser are characterised by a coupling to its external environment. Therefore, a statistical description and the concepts of ensembles and baths are applied. The quantum mechanical equivalent to the classical phase space distribution is the statistical or density operator ρ , a Hermitian, positive semidefinite and basis-independent operator [65]. Expectation or average values of quantum mechanical operators O (observables) can be derived from a trace operation over their product with the statistical operator

$$\langle O \rangle = \text{tr}[O\rho] = \text{tr}[\rho O] = \sum_{n,n'} \rho_{n,n'} O_{n',n}, \quad (2.10)$$

and include both the quantum theoretical uncertainty $O_{n',n}$ and an incoherent summation, which expresses statistical ensemble averaging. The dynamical evolution of an expectation value could be either computed by calculating the dynamics of the density operator using the non-dissipative Liouville-von Neumann equation together with coupling terms to reservoirs and baths or by calculating the dynamics of O in the Heisenberg picture. In the latter case, we use $\partial_t O = i/\hbar [H, O]$ and a static statistical operator $\rho(t_0)$.

The statistical operator can be represented in the basis of a complete set of orthonormal vectors as a sum of projection operators (of ket and bra vectors)

$$\rho = \sum_{n,n'} \rho_{n,n'} |n\rangle \langle n'|, \quad \text{tr}[\rho] = \sum_n \rho_{n,(n)} = 1. \quad (2.11)$$

$\rho_{n,n'}$ is called the density matrix. The diagonal elements represent probabilities of finding the system in the states $|n\rangle$, whereas nondiagonal elements give information about relative phases, about coherences between the different states $|n\rangle$ and $|n'\rangle$ [64]. We will work in the basis of the energy eigenfunctions of the single particle Hamiltonian $H = \sum_{\mathbf{k}} H_{\mathbf{k}} = \sum_{\mathbf{k}} E_{\mathbf{k}} N_{\mathbf{k}}$, which is the basis of eigenfunctions of the number operators $N_{\mathbf{k}}$ at the same time. The collision or interaction processes and the coupling to reservoirs drive the diagonal part of the expectation value of the statistical operator to a thermal equilibrium function $f_{\mathbf{k}} = \text{tr}[\rho N_{\mathbf{k}}] = (1 + \exp(\beta(E_{\mathbf{k}} - \mu)))^{-1}$, $\beta = 1/(k_B T)$. This is the Fermi-Dirac function which can be calculated for a (quantum) grand canonical equilibrium ensemble represented by the density operator $\rho = 1/Z \prod_{\mathbf{k}} \rho_{\mathbf{k}} = 1/Z \exp(-\beta \sum_{\mathbf{k}} (H_{\mathbf{k}} - \mu N_{\mathbf{k}}))$, and a partition function $Z = \text{tr}[\prod_{\mathbf{k}} \exp(-\beta(H_{\mathbf{k}} - \mu N_{\mathbf{k}}))]$. Coherences described by nondiagonal elements are frequently lost in statistical averaging operations.

In the following we concentrate on single particle density operators. The electronic density operator $\rho \rightarrow n(\mathbf{r}, \mathbf{r}')$ as an example of a matrix in real space representation can be written as

$$\langle n(\mathbf{r}, \mathbf{r}') \rangle = \langle \psi^\dagger(\mathbf{r}) \psi(\mathbf{r}') \rangle. \quad (2.12)$$

By inserting the mode expansion ansatz $\psi(\mathbf{r}) = 1/\sqrt{V} \sum_{\mathbf{k}} c_{\mathbf{k}} \phi_{\mathbf{k}}(\mathbf{r})$ with plane wave expansion functions $\phi_{\mathbf{k}}$, a representation in momentum space $n_{\mathbf{k},\mathbf{k}'} = \langle c_{\mathbf{k}}^\dagger c_{\mathbf{k}'} \rangle$ can be created. The mathematical concept of the Wigner distribution function [66], a fractional Fourier transformation with respect to a relative coordinate, gives a representation in mixed real and momentum space

$$\langle n_{\mathbf{k}}(\mathbf{r}) \rangle = \int d^3 \mathbf{r}' \left\langle n \left(\mathbf{r} - \frac{\mathbf{r}'}{2}, \mathbf{r} + \frac{\mathbf{r}'}{2} \right) \right\rangle e^{-i\mathbf{k}\mathbf{r}'} = \sum_{\mathbf{k}'} n_{\mathbf{k}-\mathbf{k}'/2, \mathbf{k}+\mathbf{k}'/2} e^{i\mathbf{k}'\mathbf{r}}. \quad (2.13)$$

This allows for the modelling of spatially inhomogeneous structures [67] and is one basis of quantum kinetic transport theory. A systematic Taylor expansion of (2.13) in real and momentum space [36] would lead in lowest order to terms in which the position has only parametric character. This means, that locally one has the same dynamics as in the homogeneous case [66] which can be explained by the fact that the density matrix elements vary in space and momentum with very different scales⁴.

⁴In the following we will limit our calculations therefore on measures diagonal in Fourier space and account for spatial dependencies and carrier or energy transport not on the microscopic but on the macroscopic level. This means that the basic dynamical variables are reduced to the expectation values $n_{\mathbf{k}} = \langle c_{\mathbf{k}}^\dagger c_{\mathbf{k}} \rangle$. As the macroscopic fields define the equilibrium microscopic functions $f_{\mathbf{k}}(\mathbf{r})$ spatial inhomogeneities enter the microscopic description.

2.4 Coherent Coupling to the Optical Field

In this section we motivate the equations which describe the coherent interaction of the electronic subsystem with an externally applied classical (electromagnetic) radiation field. The basic single particle carrier energy and interaction Hamiltonian $H = H_{\text{carrier}} + H_{\text{carrier-light}}$ is given by

$$H = \frac{1}{2m_{\circ}}(\mathbf{p} - e\mathbf{A})^2 + V_{\text{eff}} = \left(-\frac{\hbar^2}{2m_{\circ}}\Delta + V_{\text{eff}} \right) - \frac{e}{m_{\circ}}\mathbf{A} \cdot \mathbf{p} + \frac{e^2}{2m_{\circ}}\mathbf{A}^2, \quad \circ = e, h. \quad (2.14)$$

The electromagnetic vector potential $\mathbf{A}(\mathbf{r}, t)$ ⁵ specifies the terms of the minimal coupling and the canonical momenta⁶. The effective potential V_{eff} seen by a representative carrier, and additional terms accounting for spin-orbit coupling, strain, piezoelectric fields, quantum confinement potentials etc., define the single particle energies $E_{i,\mathbf{k}}^e, E_{j,-\mathbf{k}}^h$ [62]. Based on the fact that the wavelength of the electromagnetic field is far larger than a typical atomic dimension $R_{\text{atomic}}/\lambda \ll 1$, we may neglect the spatial variation of the vector potential on the atomic length scale (long-wavelength approximation [26]). A unitary time-dependent transformation $T(t)$ is introduced to transform the interaction Hamiltonian in minimal coupling $\propto \mathbf{A} \cdot \mathbf{p}$ to the direct coupling $e\mathbf{r} \cdot \mathbf{E} \rightarrow \mathbf{M}^{eh} \cdot \mathbf{E}$ [68]. For this, an electric dipole moment of the charge distribution with respect to the origin $\mathbf{M}^{eh} = e/V_{\text{(unit cell)}} \int d^3\mathbf{R} u_{\mathbf{k}_0}^{\text{cb}}(\mathbf{R}) \mathbf{R} u_{\mathbf{k}_0}^{\text{vb}}(\mathbf{R})$ and the unitary translation operator $T(t) = \exp[-i/\hbar \mathbf{M}^{eh} \cdot \mathbf{A}(\mathbf{R} = \mathbf{0}, \mathbf{r}, t)]$ are defined [68]. In the new representation, the electric dipole approximation, the Hamiltonian is given by

$$H'(t) = TH(t)T^\dagger + i\hbar(\partial_t T)T^\dagger = H_{\text{carrier}} + H_{\text{carrier-light}} = H_{\text{carrier}} - \mathbf{M}^{eh} \cdot \mathbf{E}(\mathbf{r}, t). \quad (2.15)$$

The light-carrier interaction couples the dipole moment to the external electric field. A more intuitive motivation could be given by calculating the energy of a dipole moment (volume) density in an external field $-V\mathbf{P}(\mathbf{r}) \cdot \mathbf{E}(\mathbf{r})$ [69, 70].

In second quantisation the single particle Hamiltonian (2.15) of the electron-hole plasma interacting with a classical external light field is defined by

$$H_{\text{carrier}} + H_{\text{carrier-light}} = \int d^3\mathbf{r} \psi^\dagger(\mathbf{r}) (H_{\text{carrier}} - \mathbf{M}^{eh} \cdot \mathbf{E}) \psi(\mathbf{r}). \quad (2.16)$$

We utilise the orthonormality relation of the expansion basis and analyse the above expression after inserting the mode expansion ansatz (2.9). The dipole interaction term couples only bilinear terms (two states) which are diagonal in \mathbf{k} . These terms describe

⁵The subsequent derivation is done in the Coulomb gauge. The scalar electromagnetic potential is assumed to vanish, and we demand the transversality condition $\text{div}\mathbf{A} = 0$.

⁶The quadratic term in the vector potential in equation (2.14) may be neglected compared to the linear terms due to its smallness as two-photon processes (products of annihilation and creation operators) are much less probable than the one-photon processes described by the linear terms, except in the case of extremely high intensities.

transitions between different subbands ($c_{i_1, \mathbf{k}}^\dagger c_{i_2, \mathbf{k}}$ or $d_{j_1, -\mathbf{k}}^\dagger d_{j_2, -\mathbf{k}}$) and interband transitions (polarisations) with one electron and one hole operator. When modelling laser devices or the pulse propagation in active semiconductor materials, we assume that the optical frequencies are in the order of magnitude of the band edge. Therefore, intersubband transitions which are far off-resonant may be neglected⁷. The strength of the coupling between a transition and the optical field can be approximated as the product of \mathbf{M}^{eh} with an overlap integral of the envelope functions

$$\mathbf{M}_{ij}^{eh} = \mathbf{M}^{eh} \int dz \phi_i^*(z) \phi_j(z). \quad (2.17)$$

With these assumptions the multi-subband Bloch Hamiltonian can be written as

$$\begin{aligned} H_{\text{carrier}} + H_{\text{carrier-light}} = & \sum_{\mathbf{k}} H_{\mathbf{k}} = \sum_i \sum_{\mathbf{k}} E_{i, \mathbf{k}}^e c_{i, \mathbf{k}}^\dagger c_{i, \mathbf{k}} + \sum_j \sum_{\mathbf{k}} E_{j, -\mathbf{k}}^h d_{j, -\mathbf{k}}^\dagger d_{j, -\mathbf{k}} \\ & - \sum_{i, j} \sum_{\mathbf{k}} \left[\mathbf{M}_{ij}^{eh} c_{i, \mathbf{k}}^\dagger d_{j, -\mathbf{k}}^\dagger + \mathbf{M}_{ij}^{eh*} d_{j, -\mathbf{k}} c_{i, \mathbf{k}} \right] \cdot \mathbf{E}. \end{aligned} \quad (2.18)$$

The basic dynamical variables in the microscopic equations of motion are defined using a single particle density matrix

$$n_{i_1 i_2, \mathbf{k}}^e = \langle c_{i_1, \mathbf{k}}^\dagger c_{i_2, \mathbf{k}} \rangle, \quad n_{j_1 j_2, -\mathbf{k}}^h = \langle d_{j_1, -\mathbf{k}}^\dagger d_{j_2, -\mathbf{k}} \rangle. \quad (2.19)$$

The diagonal elements of these two intraband expectation values are distribution functions while the nondiagonal parts describe coherences between different subband states (intersubband transitions), namely the intraband polarisations. In addition we define the interband polarisations, the material response to the applied electric field, as

$$p_{ji, \mathbf{k}} = \langle d_{j, -\mathbf{k}} c_{i, \mathbf{k}} \rangle, \quad p_{ji, \mathbf{k}}^* = \langle c_{i, \mathbf{k}}^\dagger d_{j, -\mathbf{k}}^\dagger \rangle. \quad (2.20)$$

We can link the nonlinear induced macroscopic polarisation⁸, as the source term in the later derived wave equations (3.37) and (3.46), to the microscopic dynamical variables by

$$\mathbf{P} = \sum_{i, j} \frac{1}{A} \sum_{\mathbf{k}} (\mathbf{M}_{ij}^{eh} p_{ji, \mathbf{k}}^* + \mathbf{M}_{ij}^{eh*} p_{ji, \mathbf{k}}). \quad (2.21)$$

⁷The proposed novel gain material concept and structure of quantum cascade lasers is based on intersubband transitions and thus on intraband polarisations. This intersubband nature (only a single type of carriers, e.g. electrons needed) gives rise to several key advantages compared to devices based on stimulated electron-hole recombinations [34]. Tunability by using the concept of size quantisation in multi quantum well heterostructures (i.e. no restriction given by the energy band gaps) and efficiency are two key features.

⁸The dipole matrix elements, which in the general case are complex-valued vectors, represent the connection between the optical excitation \mathbf{E} and the material response functional \mathbf{P} . After an adiabatic elimination of the microscopic polarisations, one can write $\mathbf{P} = \sum_{i, j} 1/A \sum_{\mathbf{k}} C_{\mathbf{k}} (\mathbf{M}_{ij}^{eh} \otimes \mathbf{M}_{ij}^{eh}) \mathbf{E}$. If we assume that the light field is linearly polarised and the dipole vectors are randomly oriented the ensemble average is given by $(M_{ij}^{eh})^2 = 1/3(|M_{ij, x}^{eh}|^2 + |M_{ij, y}^{eh}|^2 + |M_{ij, z}^{eh}|^2)$. In the following simulations we use the material parameters $M^{eh}(\text{GaAs}) = 0.3 \text{ enm} = 4.8 \cdot 10^{-29} \text{ Cm}$, $M^{eh}(\text{InGaAs}) = 8 \cdot 10^{-29} \text{ Cm}$.

The derivation of equations of motion in the Heisenberg picture for both, the particle number and polarisation operators involves the computation of commutator operations with the bilinear operators of the basic Hamiltonian (2.18). The result is a closed set of equations⁹, the multi-subband semiconductor (optical) Bloch equations¹⁰ [64]

$$\partial_t n_{i_1 i_2, \mathbf{k}}^e = -\frac{i}{\hbar} (E_{i_2, \mathbf{k}}^e - E_{i_1, \mathbf{k}}^e) n_{i_1 i_2, \mathbf{k}}^e + \frac{i}{\hbar} \sum_j (\mathbf{M}_{i_2 j}^{eh} p_{j i_1, \mathbf{k}}^* - \mathbf{M}_{i_1 j}^{eh*} p_{j i_2, \mathbf{k}}) \cdot \mathbf{E}, \quad (2.22)$$

$$\partial_t n_{j_1 j_2, -\mathbf{k}}^h = -\frac{i}{\hbar} (E_{j_2, -\mathbf{k}}^h - E_{j_1, -\mathbf{k}}^h) n_{j_1 j_2, -\mathbf{k}}^h + \frac{i}{\hbar} \sum_i (\mathbf{M}_{i j_2}^{eh} p_{j_1 i, \mathbf{k}}^* - \mathbf{M}_{i j_1}^{eh*} p_{j_2 i, \mathbf{k}}) \cdot \mathbf{E}, \quad (2.23)$$

$$\begin{aligned} \partial_t p_{j_1 i_1, \mathbf{k}} &= -\frac{i}{\hbar} (E_{i_1, \mathbf{k}}^e + E_{j_1, -\mathbf{k}}^h + E_{\text{gap}}) p_{j_1 i_1, \mathbf{k}} \\ &\quad - \frac{i}{\hbar} \left(\sum_i \mathbf{M}_{i j_1}^{eh} n_{i i_1, \mathbf{k}}^e + \sum_j \mathbf{M}_{i_1 j}^{eh} n_{j j_1, -\mathbf{k}}^h - \mathbf{M}_{i_1 j_1}^{eh} \right) \cdot \mathbf{E} \end{aligned} \quad (2.24)$$

for the basic dynamical variables. In order to gain a formulation in frequency-/time-domain, we decompose the electric field and the induced (microscopic and macroscopic) polarisation terms into a slowly varying amplitude and in a fast, with a frequency ω oscillating phase factor. In other words, we transform the equations into a frame which rotates with the frequency ω [37]. We note that we will apply the same approach in the derivation of the paraxial optical wave equation (in CHAPTER 3). In the rotating wave approximation we now only take into account slowly varying terms and neglect terms that are $\approx \omega$ out of phase. Applied to the Bloch equations, this results in

$$\partial_t n_{\mathbf{k}}^e = \partial_t n_{-\mathbf{k}}^h = -\tilde{g}_{\mathbf{k}} = \frac{i}{2\hbar} \left(\mathbf{M}^{eh} \tilde{p}_{\mathbf{k}}^* \cdot \tilde{\mathbf{E}} - \mathbf{M}^{eh*} \tilde{p}_{\mathbf{k}} \cdot \tilde{\mathbf{E}}^* \right), \quad (2.25)$$

$$\partial_t \tilde{p}_{\mathbf{k}} = -\frac{i}{\hbar} (E_{\mathbf{k}}^e + E_{-\mathbf{k}}^h + E_{\text{gap}} - \hbar\omega) \tilde{p}_{\mathbf{k}} - \frac{i}{2\hbar} \mathbf{M}^{eh} \cdot \tilde{\mathbf{E}} (n_{\mathbf{k}}^e + n_{-\mathbf{k}}^h - 1), \quad (2.26)$$

where we consider the special case of only one electron and one hole subband. The above set of equations describe a system equivalent to an ensemble of uncoupled harmonic oscillators with different resonance frequencies which are driven by the product of an electric field with the carrier inversion $(n_{\mathbf{k}}^e + n_{-\mathbf{k}}^h - 1)$. This corresponds to a purely inhomogeneously broadened system. The factor $\tilde{g}_{\mathbf{k}}$ is called the spectrally resolved carrier generation rate and qualifies the impact of the laser field on the gain medium. Both, the spatial and spectral hole burning and the gain saturation are related to $\tilde{g}_{\mathbf{k}}$. The effect of hole burning is considered to be a limiting factor in high-speed applications and of great importance in laser amplifier structures and pulse propagation [2, 73].

⁹The following decomposition (to anti-commutators) may be helpful to evaluate the commutators in the Heisenberg picture and shows that the resulting term is a sum of bilinear operators $[AB, CD] = A[B, C]_+ D - C[A, D]_+ B - [A, C]_+ B D + C A[B, D]_+$.

¹⁰The optical Bloch equations do conserve the quantities $d_{\mathbf{k}}^2 = (n_{\mathbf{k}}^e + n_{-\mathbf{k}}^h - 1)^2 + 4|p_{\mathbf{k}}|^2$, $\partial_t d_{\mathbf{k}} = 0$. The time evolution of N-level quantum systems may be characterised by the evolution of a number of independent coherence vectors. For each of these vectors and for the generalised pseudo-spin vector a nonlinear constant of motion (associated with the length of the vector) can be derived [71, 72].

2.5 Coupling to a Full Time-Domain Scheme

The (semiclassical) semiconductor Bloch equations describe the coherent interaction between electromagnetic fields and the carrier subsystem. As they were derived by applying the quantum mechanical density matrix formalism, they are formulated in complex space. In order to incorporate the dynamics of active semiconductor gain media into a full time-domain description of the optical fields as specified by the macroscopic Maxwell equations¹¹ it is advantageous to transform the Bloch equations to real space [14, 74]. This is in the following done for a two-band gain model

$$\partial_t p_{\mathbf{k}} = - (i\Omega_{\mathbf{k}} + \gamma_{\mathbf{k}}^p) p_{\mathbf{k}} - i \frac{M^{eh} E}{\hbar} (n_{\mathbf{k}}^e + n_{-\mathbf{k}}^h - 1), \quad \hbar\Omega_{\mathbf{k}} = E_{\text{gap}} + E_{\mathbf{k}}^e + E_{-\mathbf{k}}^h, \quad (2.27)$$

$$\partial_t p_{\mathbf{k}}^* = (\partial_t p_{\mathbf{k}})^* = - (-i\Omega_{\mathbf{k}} + \gamma_{\mathbf{k}}^p) p_{\mathbf{k}}^* + i \frac{M^{eh} E}{\hbar} (n_{\mathbf{k}}^e + n_{-\mathbf{k}}^h - 1), \quad (2.28)$$

$$\partial_t n_{\mathbf{k}} = i \frac{M^{eh} E}{\hbar} (p_{\mathbf{k}}^* - p_{\mathbf{k}}) = \frac{2M^{eh} E}{\hbar} \text{Im}(p_{\mathbf{k}}). \quad (2.29)$$

Note that here, the dipole matrix element M^{eh} (in general a rank-one tensor) and the electric field E are defined as scalar measures and are assumed to be real-valued¹². In addition, we have added a dephasing term $\gamma_{\mathbf{k}}^p$ for the nonlinear induced polarisation. Equations (2.27)+(2.28) for the dynamical polarisation $p_{\mathbf{k}}(t), \mathbb{R} \rightarrow \mathbb{C}$, and the conjugate complex variable are first order in time. It is well known that this oscillator equations are equivalent to an equation second order in time for a real quantity $\mathbf{p}_{\mathbf{k}}(t)$

$$\partial_t^2 \mathbf{p}_{\mathbf{k}} + 2\gamma_{\mathbf{k}}^p \partial_t \mathbf{p}_{\mathbf{k}} + \omega_{\mathbf{k}}^2 \mathbf{p}_{\mathbf{k}} = -\mathbf{C}_{\mathbf{k}} \frac{M^{eh} E}{\hbar} (n_{\mathbf{k}}^e + n_{-\mathbf{k}}^h - 1), \quad \omega_{\mathbf{k}} = \sqrt{\Omega_{\mathbf{k}}^2 + (\gamma_{\mathbf{k}}^p)^2} \quad (2.30)$$

$$\rightarrow \partial_t \mathbf{P}_{\mathbf{k}} = \mathcal{A}_{\mathbf{k}} \mathbf{P}_{\mathbf{k}} + \mathbf{F}_{\mathbf{k}}. \quad (2.31)$$

The vectors $\mathbf{P}_{\mathbf{k}}(t), \mathbb{R} \rightarrow \mathbb{R}^2$, and $\mathbf{F}_{\mathbf{k}}$ and the real-valued quadratic matrix $\mathcal{A}_{\mathbf{k}}$ are given by

$$\mathbf{P}_{\mathbf{k}} = \begin{pmatrix} p_{\mathbf{k}} \\ \partial_t p_{\mathbf{k}} \end{pmatrix}, \quad \mathbf{F}_{\mathbf{k}} = \begin{pmatrix} 0 \\ -\mathbf{C}_{\mathbf{k}} M^{eh} E / \hbar (n_{\mathbf{k}}^e + n_{-\mathbf{k}}^h - 1) \end{pmatrix}, \quad \mathcal{A}_{\mathbf{k}} = \begin{pmatrix} 0 & 1 \\ -\omega_{\mathbf{k}}^2 & -2\gamma_{\mathbf{k}}^p \end{pmatrix}. \quad (2.32)$$

With the objective to derive a real space equation from the complex counterpart we apply the mathematical techniques of diagonalisation and principal axis transformation.

¹¹The Maxwell equations are formulated for real quantities as the computational costs of operating on complex variables would be doubled and all physical, measurable quantities have to be real-valued.

¹²This assumption is not a restriction in the case of linear polarised light, as via the multiplication with an appropriate phase factor (and with it a rotation in complex space) M^{eh} may be chosen to be real. For systems with elliptically polarised light a more general ansatz for the (dipole) carrier-light interaction given by the substitution $\mathbf{M}^{eh} \cdot \mathbf{E}(z, t) \rightarrow \sum_{i=x,y} (\text{Re}(M_i^{eh}) \text{Re}(E_i) + \text{Im}(M_i^{eh}) \text{Im}(E_i)) = \sum_{i=x,y} 1/2 (M_i^{eh*} E_i + M_i^{eh} E_i^*)$ is advantageous [39]. This term represents the energy of a dipole (vector) in an external electromagnetic field, a measurable quantity that must be real-valued.

Therefore, one determines the eigenvalues of $\mathcal{A}_{\mathbf{k}}$ as $\lambda_{\pm, \mathbf{k}} = -(\gamma_{\mathbf{k}}^p \pm i\Omega_{\mathbf{k}})$ and $\lambda_{-, \mathbf{k}} = \lambda_{+, \mathbf{k}}^*$, and constructs a transformation matrix $\mathcal{U}_{\mathbf{k}}$ from the two linearly independent eigenvectors $\mathcal{U}_{\mathbf{k}} = (\mathbf{U}_{+, \mathbf{k}} \ \mathbf{U}_{+, \mathbf{k}}^*)$ with $\mathbf{U}_{+, \mathbf{k}}^T = (1 \ \lambda_{+, \mathbf{k}})$. With the help of the inverse matrix $\mathcal{U}_{\mathbf{k}}^{-1}$, the quadratic matrix $\mathcal{A}_{\mathbf{k}}$ can be diagonalised

$$\begin{aligned} \partial_t (\mathcal{U}_{\mathbf{k}}^{-1} \mathbf{P}_{\mathbf{k}}) &= (\mathcal{U}_{\mathbf{k}}^{-1} \mathcal{A}_{\mathbf{k}} \mathcal{U}_{\mathbf{k}}) (\mathcal{U}_{\mathbf{k}}^{-1} \mathbf{P}_{\mathbf{k}}) + (\mathcal{U}_{\mathbf{k}}^{-1} \mathbf{F}_{\mathbf{k}}) = \mathcal{D}_{\mathbf{k}} (\mathcal{U}_{\mathbf{k}}^{-1} \mathbf{P}_{\mathbf{k}}) + (\mathcal{U}_{\mathbf{k}}^{-1} \mathbf{F}_{\mathbf{k}}), \quad (2.33) \\ \mathcal{U}_{\mathbf{k}} &= \begin{pmatrix} 1 & 1 \\ \lambda_{+, \mathbf{k}} & \lambda_{+, \mathbf{k}}^* \end{pmatrix}, \quad \mathcal{U}_{\mathbf{k}}^{-1} = \frac{1}{i2\Omega_{\mathbf{k}}} \begin{pmatrix} \lambda_{+, \mathbf{k}}^* & -1 \\ -\lambda_{+, \mathbf{k}} & 1 \end{pmatrix}, \quad \mathcal{D}_{\mathbf{k}} = \begin{pmatrix} \lambda_{+, \mathbf{k}} & 0 \\ 0 & \lambda_{+, \mathbf{k}}^* \end{pmatrix}. \end{aligned} \quad (2.34)$$

The transformation to the new vector $\tilde{\mathbf{P}}_{\mathbf{k}} = \mathcal{U}_{\mathbf{k}}^{-1} \mathbf{P}_{\mathbf{k}}$ results in a set of two conjugate complex equations similar to (2.27)+(2.28)

$$\begin{aligned} \partial_t \left(\mathbf{p}_{\mathbf{k}} + i \left(\frac{\gamma_{\mathbf{k}}^p}{\Omega_{\mathbf{k}}} \mathbf{p}_{\mathbf{k}} + \frac{1}{\Omega_{\mathbf{k}}} \partial_t \mathbf{p}_{\mathbf{k}} \right) \right) &= \lambda_{+, \mathbf{k}} \left(\mathbf{p}_{\mathbf{k}} + i \left(\frac{\gamma_{\mathbf{k}}^p}{\Omega_{\mathbf{k}}} \mathbf{p}_{\mathbf{k}} + \frac{1}{\Omega_{\mathbf{k}}} \partial_t \mathbf{p}_{\mathbf{k}} \right) \right) \\ &\quad - i \frac{\mathbf{C}_{\mathbf{k}} M^{eh} E}{\Omega_{\mathbf{k}} \hbar} (n_{\mathbf{k}}^e + n_{-\mathbf{k}}^h - 1). \end{aligned} \quad (2.35)$$

To create a mapping of the equations and to connect the two formulations $p_{\mathbf{k}} \in \mathbb{C} \leftrightarrow \mathbf{p}_{\mathbf{k}}, \partial_t \mathbf{p}_{\mathbf{k}} \in \mathbb{R}$, we identify

$$\text{Re}(p_{\mathbf{k}}) = \mathbf{p}_{\mathbf{k}} \rightarrow P = \frac{2}{A} \sum_{\mathbf{k}} M^{eh} \mathbf{p}_{\mathbf{k}}, \quad \text{Im}(p_{\mathbf{k}}) = \frac{1}{\Omega_{\mathbf{k}}} \partial_t \mathbf{p}_{\mathbf{k}} + \frac{\gamma_{\mathbf{k}}^p}{\Omega_{\mathbf{k}}} \mathbf{p}_{\mathbf{k}}, \quad \mathbf{C}_{\mathbf{k}} = \Omega_{\mathbf{k}}. \quad (2.36)$$

Thus, the equivalent microscopic dynamical equations of the active semiconductor material response in \mathbb{R} for our simulations within full time-domain are defined as

$$\partial_t^2 \mathbf{p}_{\mathbf{k}} + 2\gamma_{\mathbf{k}}^p \partial_t \mathbf{p}_{\mathbf{k}} + \omega_{\mathbf{k}}^2 \mathbf{p}_{\mathbf{k}} = -\Omega_{\mathbf{k}} \frac{M^{eh} E}{\hbar} (n_{\mathbf{k}}^e + n_{-\mathbf{k}}^h - 1), \quad (2.37)$$

$$\partial_t n_{\mathbf{k}} = 2 \frac{M^{eh} E}{\hbar} \frac{1}{\Omega_{\mathbf{k}}} (\partial_t \mathbf{p}_{\mathbf{k}} + \gamma_{\mathbf{k}}^p \mathbf{p}_{\mathbf{k}}). \quad (2.38)$$

A more intuitive derivation of the coherent carrier generation term $1/\Omega_{\mathbf{k}} \partial_t \mathbf{p}_{\mathbf{k}}$ can be given from Poynting's energy density theorem (in the case of $\partial_t \mathbf{p}_{\mathbf{k}} \gg \gamma_{\mathbf{k}}^p \mathbf{p}_{\mathbf{k}} \rightarrow \omega_{\mathbf{k}} \approx \Omega_{\mathbf{k}}$). In the next sections we will discuss the strong many-body interactions in semiconductors which distinguish these materials from other laser gain media. As a result changes of transition energies $\hbar\Omega_{\mathbf{k}}$ and Rabi frequencies $M^{eh}E/\hbar$ have to be incorporated, which would make the equivalence transformation more complicated¹³. An extension to the multi-subband semiconductor Bloch equations, however, is straightforward as each independent (interband or intraband) polarisation term is linked with an harmonic damped oscillator equation (2.37) and describes a homogeneously broadened Lorentz medium [58], driven

¹³As a consequence the quadratic matrix $\mathcal{A}_{\mathbf{k}}$ is now implicitly time-dependent, and the same is true for the basis of the diagonalisation transformation $\lambda_{\pm, \mathbf{k}}, \mathbf{U}_{\pm, \mathbf{k}}, \mathcal{U}_{\mathbf{k}}, \mathcal{U}_{\mathbf{k}}^{-1}(t)$. The transformation to a new vector (2.33) may be written as $\partial_t \tilde{\mathbf{P}}_{\mathbf{k}} = (\mathcal{D}_{\mathbf{k}} - \mathcal{U}_{\mathbf{k}}^{-1}(\partial_t \mathcal{U}_{\mathbf{k}})) \tilde{\mathbf{P}}_{\mathbf{k}} + \tilde{\mathbf{F}}_{\mathbf{k}}$.

by the electric field times the respective carrier inversion. Lasing action in a four-level atomic model system, implemented in a similar way, is reported in [38, 75].

A fairly different approach to incorporate the Bloch equations for a simple two-level system into the full time-domain method was suggested in [76]. In close analogy to atomic or nuclear spin systems (interacting with a static and an oscillating magnetic field) the carrier state is represented by a pseudo-spin vector. We generalise this approach to a more realistic band-resolved description by introducing the following vectors with three components for each transition identified by the wavevector \mathbf{k}

$$\rho_{1,\mathbf{k}} = 2\text{Re}(p_{\mathbf{k}}), \quad \rho_{2,\mathbf{k}} = 2\text{Im}(p_{\mathbf{k}}), \quad (2.39)$$

$$\rho_{3,\mathbf{k}} = n_{\mathbf{k}}^e + n_{-\mathbf{k}}^h - 1. \quad (2.40)$$

The dynamics of the pseudo-vector, which completely quantifies the occupation probabilities and coherences of the carrier system, is determined by

$$\partial_t \rho_{1,\mathbf{k}} = -\gamma_{\mathbf{k}}^p \rho_{1,\mathbf{k}} + \Omega_{\mathbf{k}} \rho_{2,\mathbf{k}}, \quad (2.41)$$

$$\partial_t \rho_{2,\mathbf{k}} = -\Omega_{\mathbf{k}} \rho_{1,\mathbf{k}} - \gamma_{\mathbf{k}}^p \rho_{2,\mathbf{k}} - 2 \frac{M^{eh} E}{\hbar} \rho_{3,\mathbf{k}}, \quad (2.42)$$

$$\partial_t \rho_{3,\mathbf{k}} = 2 \frac{M^{eh} E}{\hbar} \rho_{2,\mathbf{k}}, \quad (2.43)$$

or written in a matrix form for the vectors $\boldsymbol{\rho}_{\mathbf{k}}(t), \mathbb{R} \rightarrow \mathbb{R}^3$,

$$\partial_t \boldsymbol{\rho}_{\mathbf{k}} = \mathcal{R}_{\mathbf{k}} \boldsymbol{\rho}_{\mathbf{k}} - \mathcal{T}_{\mathbf{k}} (\boldsymbol{\rho}_{\mathbf{k}} - \boldsymbol{\rho}_{\mathbf{k}}^{\text{eq}}) = \mathbf{R}_{\mathbf{k}} \times \boldsymbol{\rho}_{\mathbf{k}} - \mathcal{T}_{\mathbf{k}} (\boldsymbol{\rho}_{\mathbf{k}} - \boldsymbol{\rho}_{\mathbf{k}}^{\text{eq}}), \quad (2.44)$$

$$\mathcal{R}_{\mathbf{k}} = \begin{pmatrix} 0 & \Omega_{\mathbf{k}} & 0 \\ -\Omega_{\mathbf{k}} & 0 & -2\Omega_{\text{Rabi}} \\ 0 & 2\Omega_{\text{Rabi}} & 0 \end{pmatrix}, \quad \mathbf{R}_{\mathbf{k}} = \begin{pmatrix} 2\Omega_{\text{Rabi}} \\ 0 \\ -\Omega_{\mathbf{k}} \end{pmatrix}, \quad \Omega_{\text{Rabi}} = \frac{M^{eh} E}{\hbar}, \quad (2.45)$$

$$\mathcal{T}_{\mathbf{k}} = \begin{pmatrix} -\gamma_{\mathbf{k}}^p & 0 & 0 \\ 0 & -\gamma_{\mathbf{k}}^p & 0 \\ 0 & 0 & -\gamma_{\mathbf{k}} \end{pmatrix}, \quad \boldsymbol{\rho}_{\mathbf{k}}^{\text{eq}} = \begin{pmatrix} 0 \\ 0 \\ \rho_{3,\mathbf{k}}^{\text{therm}} \end{pmatrix}. \quad (2.46)$$

We have added a relaxation term $-\gamma_{\mathbf{k}}(\rho_{3,\mathbf{k}} - \rho_{3,\mathbf{k}}^{\text{therm}})$ towards the quasi-equilibrium state to equation (2.43). $\rho_{3,\mathbf{k}}^{\text{therm}} = f_{\mathbf{k}}^e + f_{-\mathbf{k}}^h - 1$ represents the thermal occupation (or inversion) for each \mathbf{k} . We conclude this section, and note that there are three homomorphic formulations of the semiconductor Bloch equations, which are coupled to the full time-domain Maxwell curl equations model:

The formulation (2.27)–(2.29) as derived from quantum mechanical density matrix theory operates on complex-valued microscopic quantities what doubles the numerical effort and memory requirements. This set of equations provides a straightforward starting point for dynamical models in frequency-/time-domain wherein a mode expansion ansatz (for E and $p_{\mathbf{k}}$) and a partial transformation to Fourier space are carried out. To our knowledge this full time-domain formulation has only been implemented once [77], namely for the simulation of the dynamics of a two-level atom in a photonic crystal cavity, and the investigation of normal-mode coupling or Rabi splitting in the transmission

spectra. This is a nonclassical phenomenon with the coherent exchange of energy in (excitonic) polariton systems [78, 79], in which the strong coupling exceeds the cavity decay rate and the decoherence linewidth. (2.27)–(2.29) are a preferred choice for simulating active systems with circularly or elliptically polarised light as the electromagnetic fields are then in general complex-valued anyway.

The pseudo-spin approach (2.41)–(2.43) is strongly adapted to resonant atomic-like systems, i.e. systems with only two relevant electronic energy states. It helps to obtain a deeper insight into nonlinear coherent resonant optical phenomena, such as photon echos, π or 2π pulses, pulse area theorem [80], self-induced transparency or transmission [81, 82], soliton solutions [76], or carrier wave Rabi flopping [83] (see SECTION 6.7). All these effects are easy to visualise using the $\partial_t \boldsymbol{\rho} = \mathbf{R} \times \boldsymbol{\rho}$ equation with the pseudo-spin Bloch vector $\boldsymbol{\rho}$ and the torque vector \mathbf{R} . They are based on the oscillation of the electronic inversion (in systems in which the Rabi frequency fulfils certain restrictive conditions) and on the resonance of the transition frequency with the frequency of the optical wave. However, we note that in active semiconductor structures at room temperature and for high carrier densities (even in novel rather atomic-like quantum dots) these coherent resonant occurrences are highly unlikely [82, 84, 85], due to strong dephasing mechanisms, renormalisation, the presence of homogeneous and inhomogeneous broadenings, and a statistical spread of material parameters (e.g. dipole matrix elements) in ensembles of active structures.

For our full time-domain simulations we have opted for the approach (2.37)–(2.38) as we consider its numerical implementation to be more efficient compared to the two other formulations. With an appropriate discretisation and iteration scheme it is possible to time-step the material gain dynamics in synchronism with Maxwell curl equations and to avoid computationally costly Runge-Kutta or predictor-corrector integration schemes (see SECTION A.2). This is significant as we are not focussed on simple two-level systems but rather on band-resolved gain models. It enables us to simulate semiconductor laser and amplifier structures (typical multi-scale systems) on time scales of up to a few nanoseconds which is necessary due to the rather slow macroscopic carrier dynamics and recombination or relaxation processes.

2.6 Phenomenological Terms and Additional Many-Body Hamiltonians

The Bloch equations derived in the previous sections describe only the coherent interaction between the two-component carrier plasma and an external electric field. To gain a more realistic description of a semiconductor laser or amplifier device other important, mostly incoherent processes have to be incorporated into the laser model. For example diverse recombination processes in semiconductor quantum wells are known to drastically reduce the efficiency of light-emitting structures [86]. The main recombination processes and carrier loss channels discussed in literature [2, 53] are nonradiative recombination, spontaneous emission, Auger recombination, carrier leakage and thermionic

emission out of the optically active states. In imperfect semiconductors impurities, crystal defects and surfaces are responsible for states with energies deep within the band gap. These traps allow for nonradiative recombination. The most common mechanism is called Shockley-Read-Hall recombination. The process of spontaneous emission also removes carriers which are then no longer available for coherent stimulated emission into the laser mode. The radiative recombination rate in direct band gap semiconductors is proportional to the product of $\gamma_{ij,\mathbf{k}}^{\text{sp}}$ with $n_{ii,\mathbf{k}}^e n_{jj,-\mathbf{k}}^h$, and as two particles are involved it is often referred to as bimolecular recombination. However, for high densities this process is not proportional to N^2 because of the degenerate character of the distribution functions (for more details see SECTION 4.4). For high densities and longer wavelength material systems the mechanism of Auger recombination becomes more and more important. One distinguishes between direct and phonon-assisted processes and classifies the interactions wherein four carrier states are involved [87] by the incorporated bands of the initial and final states [2]. In our simulations we include the different carrier loss channels by

$$\partial_t n_{ii,\mathbf{k}}^e \Big|_{\text{loss}} = -\gamma^{\text{nr}} n_{ii,\mathbf{k}}^e - \sum_j \gamma_{ij,\mathbf{k}}^{\text{sp}} n_{ii,\mathbf{k}}^e n_{jj,-\mathbf{k}}^h - \gamma_{ii,\mathbf{k}}^{e,\text{Auger}}, \quad (2.47)$$

$$\gamma_{ij,\mathbf{k}}^{\text{sp}} = \frac{2n}{3\epsilon_0 \hbar \pi} |\mathbf{M}_{ij}^{eh}|^2 \frac{1}{c^3 \hbar^3} (E_{i,\mathbf{k}}^e + E_{j,-\mathbf{k}}^h + E_{\text{gap}})^3. \quad (2.48)$$

$\gamma_{ij,\mathbf{k}}^{\text{sp}}$ is evaluated using the Weißkopf-Wigner theory. The Auger recombination is normally implemented on the macroscopic level

$$\partial_t N = -\Gamma_N^{\text{Auger}} = -\Gamma^{\text{Auger}} N^3. \quad (2.49)$$

The different recombination processes (and loss channels) and the total carrier lifetime, which is typically assumed as $\tau = (A + BN + CN^2)^{-1}$, $\partial_t N = -1/\tau N$, strongly depend on the actual used semiconductor material system, the grown heterostructure, and the applied operating conditions, such as temperature or carrier density (pumping). High pressure techniques are a powerful diagnostic tool as they allow for a change of the band gap and the laser frequency [88]. This technique can be used to investigate and optimise semiconductor-based laser devices.

To compensate for the various loss channels and to build up inversion and reach the threshold density, carriers and energy have to be injected into the active regions. This is essential for lasing, i.e. for the establishment of coherent stimulated emission. An applied electric contact (over d_{act}) results in the macroscopic carrier pump rate

$$\Lambda = \frac{\eta J}{e}, \quad (2.50)$$

where d_{act} describes the thickness of the active area and η the efficiency of the carrier injection. One assumes that the carriers reach the quantum wells in a thermalised state, but because of the Pauli exclusion principle for fermionic particles there has to be an unoccupied final state available. The effective carrier pump includes this pump blocking

and is described by

$$\partial_t n_{ii,\mathbf{k}}^e \Big|_{\text{pump}} = \Lambda_{ii,\mathbf{k}}^e = \Lambda \frac{f_{ii,\mathbf{k}}^e (1 - n_{ii,\mathbf{k}}^e)}{\sum_i 1/A \sum_{\mathbf{k}} f_{ii,\mathbf{k}}^e (1 - n_{ii,\mathbf{k}}^e)}. \quad (2.51)$$

Besides the electrical pumping over current contacts, in novel laser structures like vertical extended (external) cavity surface-emitters [16, 17] optical pumping schemes are discussed. The central frequency of the pumping light has to be chosen carefully: The pumping wavelength has to be smaller than the lasing wavelength. The coupling to the active medium is stronger for states higher in the energy band as the electronic density of states is larger. However, this also results in increasing thermal energy flows. The optical pumping term may be written as¹⁴

$$\partial_t n_{ii,\mathbf{k}}^e \Big|_{\text{pump}} = - \sum_j \frac{|\mathbf{M}_{ij}^{eh} \cdot \tilde{\mathbf{E}}_{\text{pump}}|^2}{2\hbar^2} \frac{\gamma_{ij,\mathbf{k}}^p}{(\gamma_{ij,\mathbf{k}}^p)^2 + (\Omega_{ij,\mathbf{k}} - \omega_{\text{pump}})^2} (n_{ii,\mathbf{k}}^e + n_{jj,-\mathbf{k}}^h - 1). \quad (2.52)$$

The last phenomenological terms we want to introduce are relaxation rates for the distribution functions and (interband) polarisations which are measures how fast the system relaxes towards the quasi-equilibrium state. We will see that these processes are due to scattering interactions and will discuss these correlation contributions in more detail in a later section. At this point we introduce the relaxation time approximation by imposing simple scattering rates

$$\partial_t n_{ii,\mathbf{k}}^e \Big|_{\text{relax}} = -\gamma^e (n_{ii,\mathbf{k}}^e - f_{ii,\mathbf{k}}^e), \quad (2.53)$$

$$\partial_t p_{ji,\mathbf{k}} \Big|_{\text{relax}} = -\gamma^p p_{ji,\mathbf{k}}, \quad (2.54)$$

which account for relaxation to quasi-equilibrium.

One of the most characteristic and distinguishing properties of semiconductor gain media is the importance of many-body interactions [3, 48]. A general two-particle Hamiltonian in second quantisation is given by [89]

$$H = \frac{1}{2} \int d^3\mathbf{x} d^3\mathbf{x}' \psi^\dagger(\mathbf{x}) \psi^\dagger(\mathbf{x}') W(\mathbf{x}, \mathbf{x}') \psi(\mathbf{x}') \psi(\mathbf{x}), \quad (2.55)$$

wherein $W(\mathbf{x}, \mathbf{x}')$ is the matrix element in real space representation. An important case is the Coulomb interaction between charged particles

$$V(\mathbf{r} - \mathbf{r}', z - z') = \frac{e^2}{4\pi\epsilon_0\epsilon} \frac{1}{\sqrt{(\mathbf{r} - \mathbf{r}')^2 + (z - z')^2}}. \quad (2.56)$$

¹⁴From a physical point of view the optical pumping as stimulated absorption process should be modelled exactly in the same way the coherent process of stimulated emission is treated, i.e. by the optical Bloch equations with an associated dynamical polarisation response at the pumping frequency. This is not possible in commonly applied frequency-/time-domain models, but with our band-resolved full time-domain approach.

Using the mode expansion (2.9) we can transform the above interaction Hamiltonian to momentum space. The orthonormality of the plane waves (the expansion functions) secures the total momentum conservation of the interaction, and the integrations over the envelope functions modifies the interaction strength of the quasi two-dimensional system. The expansion would give rise to 16 different combinations but terms with an odd number of electron and hole operators (describing processes like Auger recombination or impact ionisation), terms changing the number of particles in the conduction and hole bands, and interband exchange interaction terms (arising from mixed charge densities) are neglected. One ends up with a carrier-carrier Hamiltonian which has the form

$$\begin{aligned}
H_{\text{carrier-carrier}} &= \frac{1}{2} \sum_{\mathbf{k}, \mathbf{k}', \mathbf{q}} \sum_{i_1, i_2, i_3, i_4} V_{i_1 i_2 i_3 i_4}(\mathbf{q}) c_{i_1, \mathbf{k}+\mathbf{q}}^\dagger c_{i_2, \mathbf{k}'-\mathbf{q}}^\dagger c_{i_3, \mathbf{k}'} c_{i_4, \mathbf{k}} \\
&+ \frac{1}{2} \sum_{\mathbf{k}, \mathbf{k}', \mathbf{q}} \sum_{j_1, j_2, j_3, j_4} V_{j_4 j_3 j_2 j_1}(\mathbf{q}) d_{j_1, \mathbf{k}+\mathbf{q}}^\dagger d_{j_2, \mathbf{k}'-\mathbf{q}}^\dagger d_{j_3, \mathbf{k}'} d_{j_4, \mathbf{k}} \\
&- \sum_{\mathbf{k}, \mathbf{k}', \mathbf{q}} \sum_{i_1, j_1, j_2, i_2} V_{i_1 j_2 j_1 i_2}(\mathbf{q}) c_{i_1, \mathbf{k}+\mathbf{q}}^\dagger d_{j_1, \mathbf{k}'-\mathbf{q}}^\dagger d_{j_2, \mathbf{k}'} c_{i_2, \mathbf{k}}.
\end{aligned} \tag{2.57}$$

The Coulomb matrix elements in momentum space are given by [64]

$$V_{n_1 n_2 n_3 n_4}(\mathbf{q}) = \frac{e^2}{2\epsilon_0 \epsilon} \frac{1}{A} \frac{1}{q} F_{n_1 n_2 n_3 n_4}(q). \tag{2.58}$$

The above introduced form factors are defined as [90]

$$F_{n_1 n_2 n_3 n_4}(q) = \int_{-\infty}^{\infty} dz dz' \phi_{n_1}^*(z) \phi_{n_2}^*(z') e^{-q|z-z'|} \phi_{n_3}(z') \phi_{n_4}(z). \tag{2.59}$$

In this work we also consider the energy exchange mechanism between carriers and the crystalline lattice (carrier cooling) as the interactions of the quantised lattice oscillation modes of the polar semiconductor medium with the electronic subsystem¹⁵. The most important scattering processes are related to longitudinal optical phonons due to the polar Fröhlich interaction. The interaction Hamiltonian is given by

$$\begin{aligned}
H_{\text{carrier-phonon}} &= \sum_{\mathbf{k}, \mathbf{q}, q_z} \sum_{i_1, i_2} \left[\gamma_{i_1 i_2}(\mathbf{q}, q_z) c_{i_1, \mathbf{k}+\mathbf{q}}^\dagger b_{\mathbf{q}, q_z} c_{i_2, \mathbf{k}} + \gamma_{i_1 i_2}^*(\mathbf{q}, q_z) c_{i_2, \mathbf{k}}^\dagger b_{\mathbf{q}, q_z}^\dagger c_{i_1, \mathbf{k}+\mathbf{q}} \right] \\
&+ \sum_{\mathbf{k}, \mathbf{q}, q_z} \sum_{j_1, j_2} \left[\gamma_{j_1 j_2}(\mathbf{q}, q_z) d_{j_1, \mathbf{k}+\mathbf{q}}^\dagger b_{\mathbf{q}, q_z} d_{j_2, \mathbf{k}} + \gamma_{j_1 j_2}^*(\mathbf{q}, q_z) d_{j_2, \mathbf{k}}^\dagger b_{\mathbf{q}, q_z}^\dagger d_{j_1, \mathbf{k}+\mathbf{q}} \right],
\end{aligned} \tag{2.60}$$

¹⁵Details of the lattice unit cell define the vibrational properties of a semiconductor, the dynamics can be composed of different (independent) normal modes, leading to distinctive phonon dispersion branches ($b_{\mathbf{q}, q_z}^\dagger, b_{\mathbf{q}, q_z}$). These branches are classified into acoustic and optical, longitudinal and transverse phonons, the possible interaction processes can be divided into polar and that over deformation potentials [5, 66]. In this work the effect of the confinement structure on the phonons is neglected [64]. As only longitudinal phonons couple effectively to electrons and holes and since in the long-wavelength limit around the Γ point the acoustic branches (with $\omega_{\mathbf{q}, q_z} \approx c_{l-a} q$) are vanishing, we do only consider longitudinal optical phonons.

where we are assuming bulk phonons with a constant dispersion relation $\omega_{\mathbf{q},q_z} = \omega_{1-o}$. An interaction process of the carriers with phonons is possible under absorption and under emission of a longitudinal optical phonon. The strength of the interaction is given by the matrix elements

$$\gamma_{i_1 i_2}(\mathbf{q}, q_z) = -\frac{i}{\epsilon_0} \sqrt{\frac{e^2 \hbar}{2\gamma\omega_{1-o}AL_{\text{ref}}}} \frac{1}{\sqrt{q^2 + q_z^2}} \int_{-\infty}^{\infty} dz \phi_{i_1}^*(z) \phi_{i_2}(z) e^{iq_z z}, \quad (2.61)$$

$$\gamma = \frac{1}{\omega_{1-o}^2 \epsilon_0} \left(\frac{1}{\epsilon_\infty} - \frac{1}{\epsilon_s} \right)^{-1}, \quad (2.62)$$

$$\gamma_{j_1 j_2}(\mathbf{q}, q_z) = \frac{i}{\epsilon_0} \sqrt{\frac{e^2 \hbar}{2\gamma\omega_{1-o}AL_{\text{ref}}}} \frac{1}{\sqrt{q^2 + q_z^2}} \int_{-\infty}^{\infty} dz \phi_{j_1}(z) \phi_{j_2}^*(z) e^{iq_z z}. \quad (2.63)$$

2.7 Many-Body Interactions—Hartree-Fock Terms

In this section we will show the consequences that arise when one takes the step from a free non-interacting electron-hole plasma, whose dynamics is described by a number of uncoupled Bloch equations, to a more realistic model for the dynamics of the gain medium. The many-body interactions strongly affect the optical and electronic properties of the active medium. The name comes from the fact that more than one particle or coupled electron-hole quasi-particle is involved. The Coulomb interaction appears as interband attraction between electrons and holes and as intraband repulsion, whereas the interaction with phonons couples the subsystem carriers with the lattice. In the derivation of the equations of motion for the single particle expectation values, namely distribution functions and polarisations, the Hamiltonian for the Coulomb interaction couples the dynamics of these variables with higher order correlations, with products of four fermionic operators. The differential equations for these new variables would be governed by products of six operators, and so on. An infinite hierarchy of coupled differential equations is the result. There are different levels of approximation to close the set of equations and to truncate the hierarchy [4]. We will start with the lowest contributions of the Coulomb interactions, the so-called mean-field approximation or Hartree-Fock terms. As starting point we evaluate the Heisenberg equation, calculate the commutators of the one particle operators with the carrier-carrier Hamiltonian and compute the expectation values

$$\begin{aligned} \partial_t n_{i_1 i_2, \mathbf{k}}^e \Big|_{\text{carrier-carrier}} = & -\frac{i}{\hbar} \sum_{\mathbf{k}', \mathbf{q}} \sum_{i_5, i_6, i_7, i_8} V_{i_5 i_6 i_7 i_8}(\mathbf{q}) \left[\delta_{i_2, i_5} \left\langle c_{i_1, \mathbf{k}}^\dagger c_{i_6, \mathbf{k}'} c_{i_7, \mathbf{k}'+\mathbf{q}} c_{i_8, \mathbf{k}-\mathbf{q}} \right\rangle \right. \\ & \left. - \delta_{i_1, i_8} \left\langle c_{i_5, \mathbf{k}-\mathbf{q}}^\dagger c_{i_6, \mathbf{k}'+\mathbf{q}}^\dagger c_{i_7, \mathbf{k}'} c_{i_2, \mathbf{k}} \right\rangle \right] \\ & + \frac{i}{\hbar} \sum_{\mathbf{k}', \mathbf{q}} \sum_{i_5, j_6, j_7, i_8} V_{i_5 j_6 j_7 i_8}(\mathbf{q}) \left[\delta_{i_2, i_5} \left\langle c_{i_1, \mathbf{k}}^\dagger d_{j_6, -\mathbf{k}'-\mathbf{q}}^\dagger d_{j_7, -\mathbf{k}'} c_{i_8, \mathbf{k}-\mathbf{q}} \right\rangle \right. \\ & \left. - \delta_{i_1, i_8} \left\langle c_{i_5, \mathbf{k}-\mathbf{q}}^\dagger d_{j_6, -\mathbf{k}'}^\dagger d_{j_7, -\mathbf{k}'-\mathbf{q}} c_{i_2, \mathbf{k}} \right\rangle \right]. \quad (2.64) \end{aligned}$$

We realise that on the right-hand side of the equation new quantities, namely expectation values of products of four operators emerge. If one does not want to introduce new variables one may truncate the hierarchy by factorising these new measures in all possible combinations of the expectation values of products of two operators (the basic dynamical variables). As an example we could factorise the expression¹⁶

$$\left\langle c_{i_1, \mathbf{k}}^\dagger c_{i_6, \mathbf{k}'}^\dagger c_{i_7, \mathbf{k}'+\mathbf{q}} c_{i_8, \mathbf{k}-\mathbf{q}} \right\rangle \approx \delta_{\mathbf{q}, \mathbf{0}} n_{i_1 i_8, \mathbf{k}}^e n_{i_6 i_7, \mathbf{k}'}^e - \delta_{\mathbf{k}', \mathbf{k}-\mathbf{q}} n_{i_1 i_7, \mathbf{k}}^e n_{i_6 i_8, \mathbf{k}-\mathbf{q}}^e. \quad (2.65)$$

This level of truncation is called Hartree-Fock approximation¹⁷. The additional terms to the optical Bloch equations can be written down in a very concise way by introducing the self-energy matrices arising from electron-electron or hole-hole interaction terms, and internal fields resulting from the electron-hole Coulomb interaction [49, 50]

$$\delta E_{i_1 i_2, \mathbf{k}}^e = - \sum_{\mathbf{k}'} \sum_{i_3, i_4} V_{i_1 i_3 i_2 i_4}(\mathbf{k} - \mathbf{k}') n_{i_3 i_4, \mathbf{k}'}^e, \quad (2.66)$$

$$\delta E_{j_1 j_2, -\mathbf{k}}^h = - \sum_{\mathbf{k}'} \sum_{j_3, j_4} V_{j_4 j_2 j_3 j_1}(\mathbf{k} - \mathbf{k}') n_{j_3 j_4, -\mathbf{k}'}^h, \quad (2.67)$$

$$\Delta_{i_1 j_1, \mathbf{k}} = - \sum_{\mathbf{k}'} \sum_{i_2, j_2} V_{i_1 j_2 j_1 i_2}(\mathbf{k} - \mathbf{k}') p_{j_2 i_2, \mathbf{k}'}. \quad (2.68)$$

One result is that different \mathbf{k} states are now strongly coupled and the equations become nonlinear. Thereby, single particle energies are renormalised

$$E_{i_1 i_2, \mathbf{k}}^e = E_{i_1, \mathbf{k}}^e \delta_{i_1, i_2} + \delta E_{i_1 i_2, \mathbf{k}}^e, \quad (2.69)$$

$$E_{j_1 j_2, -\mathbf{k}}^h = E_{j_1, -\mathbf{k}}^h \delta_{j_1, j_2} + \delta E_{j_1 j_2, -\mathbf{k}}^h. \quad (2.70)$$

This means that with increasing carrier density the repulsive interaction leads to lower energies and reduced transition frequencies. Furthermore, the optical Rabi frequency is shifted due to the field renormalisation

$$\Omega_{i_1 j_1, \mathbf{k}}^{\text{Rabi}} = \frac{U_{i_1 j_1, \mathbf{k}}}{\hbar} = \frac{1}{\hbar} (\mathbf{M}_{i_1 j_1}^{eh} \cdot \mathbf{E} - \Delta_{i_1 j_1, \mathbf{k}}). \quad (2.71)$$

The attractive electrostatic interaction between electrons and holes effects in a higher Rabi frequency, the so-called the Coulomb enhancement. At low temperature and low density conditions this term should not be neglected as the resulting excitonic resonances are then dominant effects. In summary, the dynamics of an interacting electron-hole plasma in an optical field (without higher correlations) can be described by the multi-

¹⁶Below direct Hartree terms with $\delta_{\mathbf{q}, \mathbf{0}}$ will be neglected.

¹⁷For an expectation value of a product of four operators (on the right-hand side) we can specify the general approach $\partial_t \langle AB \rangle = \langle CDEF \rangle_{\text{H-F}} + (\langle CDEF \rangle - \langle CDEF \rangle_{\text{H-F}}) = \langle CDEF \rangle_{\text{H-F}} + \delta \langle CDEF \rangle$. The contributions beyond Hartree-Fock are called higher correlations, the Heisenberg equation would link the dynamical evolution of $\langle CDEF \rangle$ with expectation values of products of six operators.

subband semiconductor optical Bloch equations¹⁸

$$\begin{aligned} \partial_t n_{i_1 i_2, \mathbf{k}}^e &= -\frac{i}{\hbar} \sum_{i_3, i_4} (E_{i_2 i_4, \mathbf{k}}^e \delta_{i_1, i_3} - E_{i_3 i_1, \mathbf{k}}^e \delta_{i_2, i_4}) n_{i_3 i_4, \mathbf{k}}^e \\ &\quad + \frac{i}{\hbar} \sum_j (U_{i_2 j, \mathbf{k}} p_{j i_1, \mathbf{k}}^* - U_{i_1 j, \mathbf{k}}^* p_{j i_2, \mathbf{k}}), \end{aligned} \quad (2.72)$$

$$\begin{aligned} \partial_t n_{j_1 j_2, -\mathbf{k}}^h &= -\frac{i}{\hbar} \sum_{j_3, j_4} (E_{j_2 j_4, -\mathbf{k}}^h \delta_{j_1, j_3} - E_{j_3 j_1, -\mathbf{k}}^h \delta_{j_2, j_4}) n_{j_3 j_4, -\mathbf{k}}^h \\ &\quad + \frac{i}{\hbar} \sum_i (U_{i j_2, \mathbf{k}} p_{j_1 i, \mathbf{k}}^* - U_{i j_1, \mathbf{k}}^* p_{j_2 i, \mathbf{k}}), \end{aligned} \quad (2.73)$$

$$\begin{aligned} \partial_t p_{j_1 i_1, \mathbf{k}} &= -\frac{i}{\hbar} \sum_{i_2, j_2} (E_{i_1 i_2, \mathbf{k}}^e \delta_{j_1, j_2} + E_{j_1 j_2, -\mathbf{k}}^h \delta_{i_1, i_2} + E_{\text{gap}} \delta_{i_1, i_2} \delta_{j_1, j_2}) p_{j_2 i_2, \mathbf{k}} \\ &\quad - \frac{i}{\hbar} \left(\sum_i U_{i j_1, \mathbf{k}} n_{i i_1, \mathbf{k}}^e + \sum_j U_{i_1 j, \mathbf{k}} n_{j j_1, -\mathbf{k}}^h - U_{i_1 j_1, \mathbf{k}} \right), \end{aligned} \quad (2.74)$$

which describe an ensemble of driven and coupled oscillators.

2.8 Many-Body Interactions—Correlation Terms

Apart from the discussed modifications of the optical Bloch equations by adding the coherent processes of energy and field renormalisation other important consequences of the Coulomb interaction arise. Carrier-carrier scattering drives (on a sub-picosecond time scale) the dynamical distribution functions of electron and hole states towards the quasi-equilibrium Fermi-Dirac distributions. These processes also dominantly contribute to the fast optical dephasing or loss of coherence due to a decay of the various polarisations. Another effect of the Coulomb interaction is the plasma screening, this means that due to the presence of all other charged carriers an individual carrier experiences a weakened interaction. The spectra of the optical gain and induced refractive index change are altered by diagonal and nondiagonal terms arising from the many-body interactions. Finally, the carrier-phonon interaction couples the hot carrier system with the colder crystalline lattice which in turn is coupled to the bath. Similar to the Coulomb interaction, these scattering processes redistribute the carriers and destroy coherence within the carrier system. The specified processes can be reproduced by the many-body approach, but we will outline an approximative ansatz where some of these correlations are only treated in a phenomenological way. This approach is necessary because of the complexity of the investigated systems, namely by reason that in the simulations the energy-resolved dynamics has to be calculated on a huge spatial grid for a long time

¹⁸When we disregard intraband (intersubband) polarisations the renormalised equations have a more simple structure $\delta E_{ii, \mathbf{k}}^e = -\sum_{\mathbf{k}'} \sum_{i_3} V_{ii_3 i_3}(\mathbf{k} - \mathbf{k}') n_{i_3 i_3, \mathbf{k}'}^e$, $\partial_t n_{ii, \mathbf{k}}^e = i/\hbar \sum_j (U_{ij, \mathbf{k}} p_{j i, \mathbf{k}}^* - U_{ij, \mathbf{k}}^* p_{j i, \mathbf{k}})$, $\partial_t p_{j i, \mathbf{k}} = -i/\hbar (E_{ii, \mathbf{k}}^e + E_{jj, -\mathbf{k}}^h + E_{\text{gap}}) p_{j i, \mathbf{k}} - i/\hbar U_{ij, \mathbf{k}} (n_{ii, \mathbf{k}}^e + n_{jj, -\mathbf{k}}^h - 1)$.

window. To give a rough idea about these higher correlation contributions and the used assumptions, we calculate the dynamical equations for the product of four operators in (2.65). In doing so we only evaluate the commutators with the single particle energy Hamiltonian and the repulsive part of the Coulomb interaction

$$\begin{aligned}
& \partial_t \left\langle c_{i_1, \mathbf{k}}^\dagger c_{i_2, \mathbf{k}'}^\dagger c_{i_3, \mathbf{k}'+\mathbf{q}} c_{i_4, \mathbf{k}-\mathbf{q}} \right\rangle \\
&= -\frac{i}{\hbar} \left(-E_{i_1, \mathbf{k}}^e - E_{i_2, \mathbf{k}'}^e + E_{i_3, \mathbf{k}'+\mathbf{q}}^e + E_{i_4, \mathbf{k}-\mathbf{q}}^e \right) \left\langle c_{i_1, \mathbf{k}}^\dagger c_{i_2, \mathbf{k}'}^\dagger c_{i_3, \mathbf{k}'+\mathbf{q}} c_{i_4, \mathbf{k}-\mathbf{q}} \right\rangle \\
&- \frac{i}{\hbar} \sum_{\mathbf{k}'', \mathbf{q}'} \sum_{i_5, i_6, i_7, i_8} \left\{ V_{i_5 i_6 i_7 i_8}(\mathbf{q}') \left[\delta_{i_4, i_5} \left(\delta_{i_3, i_6} \delta_{\mathbf{k}'+\mathbf{q}, \mathbf{k}''-\mathbf{q}'} \left\langle c_{i_1, \mathbf{k}}^\dagger c_{i_2, \mathbf{k}'}^\dagger c_{i_7, \mathbf{k}'+\mathbf{q}+\mathbf{q}'} c_{i_8, \mathbf{k}-\mathbf{q}-\mathbf{q}'} \right\rangle \right. \right. \right. \\
&- \left. \left. \left\langle c_{i_1, \mathbf{k}}^\dagger c_{i_2, \mathbf{k}'}^\dagger c_{i_6, \mathbf{k}''}^\dagger c_{i_3, \mathbf{k}'+\mathbf{q}} c_{i_7, \mathbf{k}''+\mathbf{q}'} c_{i_8, \mathbf{k}-\mathbf{q}-\mathbf{q}'} \right\rangle \right) \right. \\
&+ \left. \delta_{i_3, i_5} \left\langle c_{i_1, \mathbf{k}}^\dagger c_{i_2, \mathbf{k}'}^\dagger c_{i_6, \mathbf{k}''}^\dagger c_{i_4, \mathbf{k}-\mathbf{q}} c_{i_7, \mathbf{k}''+\mathbf{q}'} c_{i_8, \mathbf{k}'+\mathbf{q}-\mathbf{q}'} \right\rangle \right] \\
&+ V_{i_8 i_7 i_6 i_5}(\mathbf{q}') \left[\delta_{i_1, i_5} \left(-\delta_{i_2, i_6} \delta_{\mathbf{k}', \mathbf{k}''} \left\langle c_{i_8, \mathbf{k}-\mathbf{q}'}^\dagger c_{i_7, \mathbf{k}'+\mathbf{q}'}^\dagger c_{i_3, \mathbf{k}'+\mathbf{q}} c_{i_4, \mathbf{k}-\mathbf{q}} \right\rangle \right. \right. \\
&+ \left. \left. \left\langle c_{i_8, \mathbf{k}-\mathbf{q}'}^\dagger c_{i_7, \mathbf{k}''+\mathbf{q}'}^\dagger c_{i_2, \mathbf{k}'}^\dagger c_{i_6, \mathbf{k}''}^\dagger c_{i_3, \mathbf{k}'+\mathbf{q}} c_{i_4, \mathbf{k}-\mathbf{q}} \right\rangle \right) \right. \\
&- \left. \left. \delta_{i_2, i_5} \left\langle c_{i_8, \mathbf{k}-\mathbf{q}'}^\dagger c_{i_7, \mathbf{k}''+\mathbf{q}'}^\dagger c_{i_1, \mathbf{k}}^\dagger c_{i_6, \mathbf{k}''}^\dagger c_{i_3, \mathbf{k}'+\mathbf{q}} c_{i_4, \mathbf{k}-\mathbf{q}} \right\rangle \right] \right\}. \tag{2.75}
\end{aligned}$$

Other terms arising from $-\sum_{\mathbf{k}, \mathbf{k}', \mathbf{q}} \sum_{i_5, j_6, j_7, i_8} V_{i_5 j_7 j_6 i_8}(\mathbf{q}) c_{i_5, \mathbf{k}+\mathbf{q}}^\dagger d_{j_6, \mathbf{k}'-\mathbf{q}}^\dagger d_{j_7, \mathbf{k}'} c_{i_8, \mathbf{k}}$ have a similar structure. We abbreviate the deviations of the full correlation terms from the factorised Hartree-Fock approximation terms with $\delta \langle \rangle (t)$. An example of this deviation and its time derivative $\partial_t \delta \langle \rangle (t)$ is

$$\begin{aligned}
\delta \left\langle c_{i_1, \mathbf{k}}^\dagger c_{i_2, \mathbf{k}'}^\dagger c_{i_3, \mathbf{k}'+\mathbf{q}} c_{i_4, \mathbf{k}-\mathbf{q}} \right\rangle &= \left\langle c_{i_1, \mathbf{k}}^\dagger c_{i_2, \mathbf{k}'}^\dagger c_{i_3, \mathbf{k}'+\mathbf{q}} c_{i_4, \mathbf{k}-\mathbf{q}} \right\rangle + \delta_{\mathbf{k}', \mathbf{k}-\mathbf{q}} n_{i_1 i_3, \mathbf{k}}^e n_{i_2 i_4, \mathbf{k}-\mathbf{q}}^e, \\
\partial_t \delta \left\langle c_{i_1, \mathbf{k}}^\dagger c_{i_2, \mathbf{k}'}^\dagger c_{i_3, \mathbf{k}'+\mathbf{q}} c_{i_4, \mathbf{k}-\mathbf{q}} \right\rangle &= \partial_t \left\langle c_{i_1, \mathbf{k}}^\dagger c_{i_2, \mathbf{k}'}^\dagger c_{i_3, \mathbf{k}'+\mathbf{q}} c_{i_4, \mathbf{k}-\mathbf{q}} \right\rangle \\
&+ \delta_{\mathbf{k}', \mathbf{k}-\mathbf{q}} \left(\partial_t \left(n_{i_1 i_3, \mathbf{k}}^e \right) n_{i_2 i_4, \mathbf{k}-\mathbf{q}}^e + n_{i_1 i_3, \mathbf{k}}^e \partial_t \left(n_{i_2 i_4, \mathbf{k}-\mathbf{q}}^e \right) \right). \tag{2.76}
\end{aligned}$$

This can be written in the general form

$$\partial_t \delta \langle \rangle_4 = -i\Omega \delta \langle \rangle_4 - \frac{i}{\hbar} I[\langle \rangle_2], \quad \Omega = \Omega_{i_1 i_2 i_3 i_4, \mathbf{k} \mathbf{k}' \mathbf{q}}^e, \tag{2.77}$$

where the subscript indicates the number of operators. Equation (2.77) has to be solved along with the equation of motion of the basic dynamical variables, that is

$$\partial_t \langle \rangle_2 = \langle \rangle_{2, \text{optical Bloch terms}} + \langle \rangle_{4, \text{H-F}} + \delta \langle \rangle_4. \tag{2.78}$$

To truncate the hierarchy of coupled differential equations involving expectation values, the inhomogeneity $I(t)$ is factorised into products of distribution functions, intraband polarisations and interband polarisations. Self-energies for correlation contributions and a self-consistent treatment of plasma screening are disregarded. Indeed, the mechanism of screening is included in the above Coulomb interaction terms, but for computational

efficiency we model this mechanism merely by replacing the bar potential by an effective screened potential. Furthermore, we neglect terms with $\mathbf{q} = \mathbf{0}, \mathbf{q}' = \mathbf{0}, \mathbf{k} = \mathbf{k}'$ in the factorisation and disregard exchange terms with $V(\mathbf{k} - \mathbf{k}' - \mathbf{q})$ [64]. We see from equation (2.77) that quantum mechanical scattering processes are not instantaneous as assumed in the usual Boltzmann ansatz. Energy-time uncertainty, transitions not allowed by classical selection rules and Coulombic memory effects play a role. The formal integration of (2.77) reads

$$\delta \langle \rangle (t) = \delta \langle \rangle (t_0) e^{-i\Omega(t-t_0)} - \frac{i}{\hbar} \int_{t_0}^t dt' e^{-i\Omega(t-t')} I(t'). \quad (2.79)$$

It is therefore possible to transform the microscopic equations of motion into non-Markovian integro-differential equations with memory effects for the single particle density matrices. In active laser systems which require rather high carrier densities neglecting Coulombic memory effects and applying the Markov approximation is considered a reasonable approach until we deal with extremely short time scales. We assume an adiabatic activation of the interaction by introducing a phenomenological decay constant, $\Omega \rightarrow \Omega - i\gamma, \gamma \rightarrow 0$. As a result we obtain

$$\delta \langle \rangle (t) = \lim_{\gamma \rightarrow 0} \left(-\frac{i}{\hbar} \frac{1}{i\Omega + \gamma} I(t) \right) = -i \left(\pi \delta(\hbar\Omega) - i \frac{\mathcal{P}}{\hbar\Omega} \right) I(t), \quad (2.80)$$

wherein \mathcal{P} describes the Cauchy integral principal value, and $\delta(\hbar\Omega)$ secures the strict energy conservation of the Coulomb interaction on long time scales (the generalised δ or Heitler-Zeta function). The correlation contributions can be expressed by scattering matrices Γ and internal fields Δ [64]. In summary, the scattering terms for the electron expectation values (and similar for the hole matrices) and the interband polarisations can be written as

$$\begin{aligned} \partial_t n_{i_1 i_2, \mathbf{k}}^e \Big|_{\text{relax}} &= \sum_{i_5} \left[-\Gamma_{i_2 i_5, \mathbf{k}}^{ee, \text{out}} n_{i_1 i_5, \mathbf{k}}^e - \Gamma_{i_1 i_5, \mathbf{k}}^{ee, \text{out}*} n_{i_2 i_5, \mathbf{k}}^{e*} \right. \\ &\quad \left. + \Gamma_{i_2 i_5, \mathbf{k}}^{ee, \text{in}} (\delta_{i_1, i_5} - n_{i_1 i_5, \mathbf{k}}^e) + \Gamma_{i_1 i_5, \mathbf{k}}^{ee, \text{in}*} (\delta_{i_2, i_5} - n_{i_2 i_5, \mathbf{k}}^{e*}) \right] \\ &\quad - \frac{i}{\hbar} \sum_{j_5} \left[\Delta_{i_2 j_5, \mathbf{k}}^{eh} p_{j_5 i_1, \mathbf{k}}^* - \Delta_{i_1 j_5, \mathbf{k}}^{eh*} p_{j_5 i_2, \mathbf{k}} \right], \end{aligned} \quad (2.81)$$

$$\begin{aligned} \partial_t p_{j_1 i_1, \mathbf{k}} \Big|_{\text{relax}} &= - \sum_{i_5} \left(\Gamma_{i_1 i_5, \mathbf{k}}^{ee, \text{out}} + \Gamma_{i_1 i_5, \mathbf{k}}^{ee, \text{in}} \right) p_{j_1 i_5, \mathbf{k}} - \sum_{j_5} \left(\Gamma_{j_1 j_5, \mathbf{k}}^{hh, \text{out}} + \Gamma_{j_1 j_5, \mathbf{k}}^{hh, \text{in}} \right) p_{j_5 i_1, \mathbf{k}} \\ &\quad + \sum_{i_5} \left[\Gamma_{j_1 i_5, \mathbf{k}}^{he, \text{out}} n_{i_5 i_1, \mathbf{k}}^e + \Gamma_{j_1 i_5, \mathbf{k}}^{he, \text{in}} (\delta_{i_5, i_1} - n_{i_5 i_1, \mathbf{k}}^e) \right] \\ &\quad + \sum_{j_5} \left[\Gamma_{i_1 j_5, \mathbf{k}}^{eh, \text{out}} n_{j_5 j_1, -\mathbf{k}}^h + \Gamma_{i_1 j_5, \mathbf{k}}^{eh, \text{in}} (\delta_{j_5, j_1} - n_{j_5 j_1, -\mathbf{k}}^h) \right]. \end{aligned} \quad (2.82)$$

A numerical simulation of the above equations is still complicated. However, in semiconductor laser systems operated at optical frequencies, it is reasonable to disregard

scattering processes comprising intraband polarisations, and to neglect nonlinear terms in the interband polarisations. On that level the scattering is described by the quantum Boltzmann collision terms in second Born approximation

$$\begin{aligned}\partial_t n_{ii,\mathbf{k}}^e \Big|_{\text{relax}} &= -2\Gamma_{ii,\mathbf{k}}^{ee,\text{out}} n_{ii,\mathbf{k}}^e + 2\Gamma_{ii,\mathbf{k}}^{ee,\text{in}} (1 - n_{ii,\mathbf{k}}^e) \\ &= -2 \left(\Gamma_{ii,\mathbf{k}}^{ee,\text{out}} + \Gamma_{ii,\mathbf{k}}^{ee,\text{in}} \right) n_{ii,\mathbf{k}}^e + 2\Gamma_{ii,\mathbf{k}}^{ee,\text{in}}.\end{aligned}\quad (2.83)$$

The scattering matrices for the out-scattering of an electron in a state characterised by the momentum \mathbf{k} and the subband index i_1 are given by

$$\begin{aligned}\mathbf{k} \rightarrow \mathbf{k} - \mathbf{q}, \mathbf{k}' \rightarrow \mathbf{k}' + \mathbf{q} : \\ \Gamma_{i_1 i_1, \mathbf{k}}^{ee,\text{out}} &= \frac{\pi}{\hbar} \sum_{\mathbf{k}', \mathbf{q}} \sum_{i_2, i_3, i_4} \delta(-E_{i_1, \mathbf{k}}^e - E_{i_2, \mathbf{k}'}^e + E_{i_3, \mathbf{k}'+\mathbf{q}}^e + E_{i_4, \mathbf{k}-\mathbf{q}}^e) |V_{i_1 i_2 i_3 i_4}(\mathbf{q})|^2 \\ &\quad \times n_{i_2 i_2, \mathbf{k}'}^e (1 - n_{i_3 i_3, \mathbf{k}'+\mathbf{q}}^e) (1 - n_{i_4 i_4, \mathbf{k}-\mathbf{q}}^e) \\ &\quad + \frac{\pi}{\hbar} \sum_{\mathbf{k}', \mathbf{q}} \sum_{j_2, j_3, i_4} \delta(-E_{i_1, \mathbf{k}}^e - E_{j_2, -\mathbf{k}'}^h + E_{j_3, -\mathbf{k}'-\mathbf{q}}^h + E_{i_4, \mathbf{k}-\mathbf{q}}^e) |V_{i_1 j_2 j_3 i_4}(\mathbf{q})|^2 \\ &\quad \times n_{j_2 j_2, -\mathbf{k}'}^h (1 - n_{j_3 j_3, -\mathbf{k}'-\mathbf{q}}^h) (1 - n_{i_4 i_4, \mathbf{k}-\mathbf{q}}^e).\end{aligned}\quad (2.84)$$

In a similar way we can determine the matrices of in-scattering contributions

$$\begin{aligned}\mathbf{k} - \mathbf{q} \rightarrow \mathbf{k}, \mathbf{k}' + \mathbf{q} \rightarrow \mathbf{k}' : \\ \Gamma_{i_1 i_1, \mathbf{k}}^{ee,\text{in}} &= \frac{\pi}{\hbar} \sum_{\mathbf{k}', \mathbf{q}} \sum_{i_2, i_3, i_4} \delta(-E_{i_1, \mathbf{k}}^e - E_{i_2, \mathbf{k}'}^e + E_{i_3, \mathbf{k}'+\mathbf{q}}^e + E_{i_4, \mathbf{k}-\mathbf{q}}^e) |V_{i_1 i_2 i_3 i_4}(\mathbf{q})|^2 \\ &\quad \times (1 - n_{i_2 i_2, \mathbf{k}'}^e) n_{i_3 i_3, \mathbf{k}'+\mathbf{q}}^e n_{i_4 i_4, \mathbf{k}-\mathbf{q}}^e \\ &\quad + \frac{\pi}{\hbar} \sum_{\mathbf{k}', \mathbf{q}} \sum_{j_2, j_3, i_4} \delta(-E_{i_1, \mathbf{k}}^e - E_{j_2, -\mathbf{k}'}^h + E_{j_3, -\mathbf{k}'-\mathbf{q}}^h + E_{i_4, \mathbf{k}-\mathbf{q}}^e) |V_{i_1 j_2 j_3 i_4}(\mathbf{q})|^2 \\ &\quad \times (1 - n_{j_2 j_2, -\mathbf{k}'}^h) n_{j_3 j_3, -\mathbf{k}'-\mathbf{q}}^h n_{i_4 i_4, \mathbf{k}-\mathbf{q}}^e.\end{aligned}\quad (2.85)$$

Scattering processes and associated matrices mediated through the Coulomb interaction have a typical Boltzmann structure (see FIGURE 2.3): The δ function in the product guarantees for the strict energy conservation (on long time scales), the strength of the interaction is quantified by $|V(\mathbf{q})|^2$. The single scattering process is proportional to the occupation of the initial states and the available unoccupied final states (Pauli principle), and finally we have to sum over all possibilities. The collision terms in the equation for the interband polarisation [51] are given by

$$\partial_t p_{ji,\mathbf{k}} \Big|_{\text{relax}} = - \sum_{\mathbf{k}'} \Lambda_{ij,\mathbf{k}\mathbf{k}'} p_{ji,\mathbf{k}'} - \sum_{\mathbf{k}'} \sum_{i_5 \neq i, j_5 \neq j} \tilde{\Lambda}_{ij i_5 j_5, \mathbf{k}\mathbf{k}'} p_{j_5 i_5, \mathbf{k}'}. \quad (2.86)$$

The diagonal relaxation elements are determined by the above given matrices (2.84)–(2.85) as $\Lambda_{ij,\mathbf{k}\mathbf{k}} = \Gamma_{ii,\mathbf{k}}^{ee,\text{out}} + \Gamma_{ii,\mathbf{k}}^{ee,\text{in}} + \Gamma_{jj,\mathbf{k}}^{hh,\text{out}} + \Gamma_{jj,\mathbf{k}}^{hh,\text{in}}$. The off-diagonal elements $\Lambda_{ji,\mathbf{k}\mathbf{k}'}^{19}$

¹⁹These nondiagonal elements determine in parts the shape of the gain spectra [4]: Calculating the gain spectra with solely diagonal relaxation terms leads to noticeable amplification or gain below

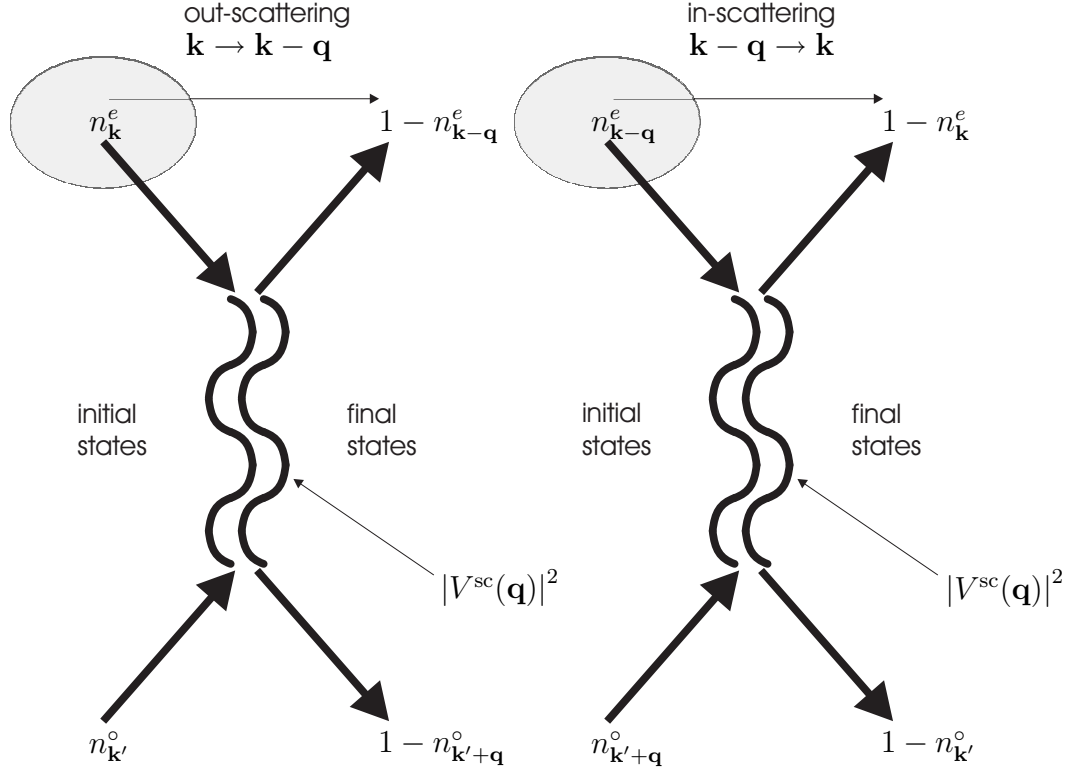


FIGURE 2.3: In order to visualise and describe the correlation contributions from quantum theoretical many-body interactions the schematic Feynman diagrams for out-scattering and in-scattering processes, respectively, are given. This illustrates the characteristic structure of the scattering matrices: The initial states (before the interaction) are plotted on the left, the final states (on the right) have to be available (as per Pauli exclusion principle for fermionic particles). The strength of the interaction is given by $|V^{sc}(\mathbf{q})|^2$, and we do sum over all possible scattering partners $\circ = e, h$ and $\sum_{\mathbf{k}', \mathbf{q}}$ (and in the case of quantum confined structures over all thinkable combinations of the discrete subband quantum numbers).

have a similar structure and partially compensate the impacts of the diagonal terms [4]. Apart from the conservation of the total momentum, the carrier-carrier scattering does neither change the particle numbers (the carrier density) nor the total kinetic energy. If a hot carrier non-equilibrium distribution is generated, for example by high-power pulse excitation or pumping at high energy states, the kinetic energy density (as the second moment of the distribution) is characterised by an effective plasma temperature which may be well above the lattice temperature (by some ten Kelvin) [91].

The process of thermal relaxation is characterised by the coupling of the carrier to the lattice subsystem and is mediated by the Fröhlich interaction. There is no coherent

the band edge. That is clear from the structure of the polarisation differential equation as a sum of (independent) damped harmonic oscillators which can also be driven (because of the finite decoherence time) at frequencies unequal the respective resonance frequency. The more general ansatz for the decoherence terms removes this problem.

(Hartree-Fock) contribution of this interaction. Using similar approximations as above the scattering matrices in (2.81) and (2.82) can be written as

$$\begin{aligned} \mathbf{k} \rightarrow \mathbf{k} - \mathbf{q} : \Gamma_{i_1 i_1, \mathbf{k}}^{ee, \text{out}} &= \frac{\pi}{\hbar} \sum_{\mathbf{q}, q_z} \sum_{i_2} \sum_{\pm} \delta(-E_{i_1, \mathbf{k}}^e + E_{i_2, \mathbf{k} - \mathbf{q}}^e \pm \hbar\omega_{l-o}) |\gamma_{i_1 i_2}(\mathbf{q}, q_z)|^2 \\ &\times \left(1 - n_{i_2 i_2, \mathbf{k} - \mathbf{q}}^e\right) \left(n_{\text{ph}, \mathbf{q}, q_z} + \frac{1}{2} \pm \frac{1}{2}\right), \end{aligned} \quad (2.87)$$

$$\begin{aligned} \mathbf{k} - \mathbf{q} \rightarrow \mathbf{k} : \Gamma_{i_1 i_1, \mathbf{k}}^{ee, \text{in}} &= \frac{\pi}{\hbar} \sum_{\mathbf{q}, q_z} \sum_{i_2} \sum_{\pm} \delta(-E_{i_1, \mathbf{k}}^e + E_{i_2, \mathbf{k} - \mathbf{q}}^e \mp \hbar\omega_{l-o}) |\gamma_{i_1 i_2}(\mathbf{q}, q_z)|^2 \\ &\times n_{i_2 i_2, \mathbf{k} - \mathbf{q}}^e \left(n_{\text{ph}, \mathbf{q}, q_z} + \frac{1}{2} \pm \frac{1}{2}\right). \end{aligned} \quad (2.88)$$

The Boltzmann collision integrals contain factors guaranteeing for the energy conservation, describing the strength of the phonon-carrier interaction, and the probability factors for initial and final states. A scattering is possible under emission (upper sign) and under absorption (lower sign) of a longitudinal optical phonon. The transfer of kinetic energy to the phonon bath results in a cooling of the hot carrier system. To simplify the problem, we assume the phonons to be in an equilibrium state qualified by the Bose-Einstein distribution

$$n_{\text{ph}, \mathbf{q}, q_z} = \frac{1}{\exp(\beta\hbar\omega_{l-o}) - 1}, \quad \beta = \frac{1}{k_B T_{l-o}}. \quad (2.89)$$

In typical semiconductor lasers with high carrier densities, equation (2.83) may be further approximated [37]. One usually can assume that carrier-carrier scattering drives the distribution on a very fast sub-picosecond time scale towards the quasi-equilibrium distribution. For these distributions the correlation contributions vanish

$$2\Gamma_{ii, \mathbf{k}}^{ee, \text{out}} \{f_{\mathbf{k}}^o\} f_{ii, \mathbf{k}}^e = 2\Gamma_{ii, \mathbf{k}}^{ee, \text{in}} \{f_{\mathbf{k}}^o\} (1 - f_{ii, \mathbf{k}}^e). \quad (2.90)$$

The above relation describes the principle of detailed balance, for which the scattering into a state is exactly balanced by the out-scattering term. If the deviations of the distribution from the quasi-equilibrium function are relatively small (and if we look at time scales of some times the characteristic momentum scattering time), one can linearise the Boltzmann equation in this deviation and introduce relaxation rates

$$\gamma_{ii, \mathbf{k}}^e = 2 \left(\Gamma_{ii, \mathbf{k}}^{ee, \text{out}} \{f_{\mathbf{k}}^o\} + \Gamma_{ii, \mathbf{k}}^{ee, \text{in}} \{f_{\mathbf{k}}^o\} \right), \quad (2.91)$$

$$\partial_t n_{ii, \mathbf{k}}^e \Big|_{\text{relax}} = -\gamma_{ii, \mathbf{k}}^e (n_{ii, \mathbf{k}}^e - f_{ii, \mathbf{k}}^e). \quad (2.92)$$

This ansatz with \mathbf{k} -dependent scattering times (rates) fails to preserve the carrier density, and there is another criticism on this widely used approach [4]. Relaxation times descriptions are a good approximation in the case of analysing a system interacting with an infinitely big bath. However, in a semiconductor laser there is no distinction between a system and a bath, and the reservoir carriers are part of the system [4]. Recent

numerical investigations [92] (and APPENDIX B) show through a comparison with a dynamical treatment of the scattering interactions that the relaxation rate approximation is a surprisingly well-justified approach. We conclude that (2.92) is a reasonable accurate description except for the cases of the propagation of few femtosecond or very strong optical pulses.

In a last step, we would like to include the screening effect into our model equations. We will do this using a phenomenological approach by replacing the bare Coulomb potential by the screened potential

$$V^{\text{sc}}(\mathbf{q}, \omega) = \frac{V(\mathbf{q})}{\epsilon(\mathbf{q}, \omega)}. \quad (2.93)$$

For simplicity, we neglect for a moment the dependence on four subband quantum numbers. The spatial and spectral dispersion in the density dependent (longitudinal) dielectric function of the two-component plasma are given by the Lindhard formula, which is derived within the random phase approximation (RPA), with $\omega \rightarrow \omega + i\delta$ [25]

$$\epsilon(\mathbf{q}, \omega) = 1 - V(\mathbf{q}) \sum_{\mathbf{k}} \left[\sum_i \frac{n_{ii, \mathbf{k}+\mathbf{q}}^e - n_{ii, \mathbf{k}}^e}{E_{i, \mathbf{k}+\mathbf{q}}^e - E_{i, \mathbf{k}}^e - \hbar\omega} + \sum_j \frac{n_{jj, -\mathbf{k}-\mathbf{q}}^h - n_{jj, -\mathbf{k}}^h}{E_{j, -\mathbf{k}-\mathbf{q}}^h - E_{j, -\mathbf{k}}^h - \hbar\omega} \right]. \quad (2.94)$$

In this work the long-wavelength ($|\mathbf{q}| \rightarrow 0$) and the static ($\omega \rightarrow 0$) limits of the Lindhard formula are calculated. Two approximations are discussed for the screened Coulomb potential [36]. The (total) inverse screening length is calculated by

$$\kappa = \frac{e^2}{2\epsilon_0\epsilon\pi\hbar^2} \left[m_e \sum_i f_{ii, \mathbf{k}=\mathbf{0}}^e + m_h \sum_j f_{jj, -\mathbf{k}=\mathbf{0}}^h \right]. \quad (2.95)$$

We can write the free-carrier dispersion as

$$\epsilon(\mathbf{q} \rightarrow \mathbf{0}, \omega \rightarrow 0) = 1 + \frac{\kappa}{q}, \quad (2.96)$$

which would result in the simple Yukawa potential. In the single effective plasmon pole approximation one replaces the continuum of resonances, the multiple poles in the Lindhard formula, by an effective plasmon frequency and get an expression similar to the classical Drude dielectric function with a numerical constant C which is usually taken between 1 and 4 [4, 48]

$$V^{\text{sc}}(\mathbf{q}) = V(\mathbf{q}) \left(1 - \frac{\omega_{\text{pl}}^2}{\omega_{\mathbf{q}}^2} \right), \quad (2.97)$$

$$\omega_{\text{pl}}^2 = \frac{e^2 N}{2\epsilon_0\epsilon m_r} q, \quad \omega_{\mathbf{q}}^2 = \omega_{\text{pl}}^2 \left(1 + \frac{q}{\kappa} \right) + \frac{C}{4} \left(\frac{\hbar q^2}{2m_r} \right)^2. \quad (2.98)$$

This phenomenologically defined screened potential modifies all our above calculations, for example the band gap renormalisation (shrinkage), which in the screened Hartree-Fock approximation is given by $\delta E_{ij, \mathbf{k}}^{\text{SX}} = \delta E_{ii, \mathbf{k}}^{e, \text{SX}} + \delta E_{jj, -\mathbf{k}}^{h, \text{SX}}$, or the renormalisation of

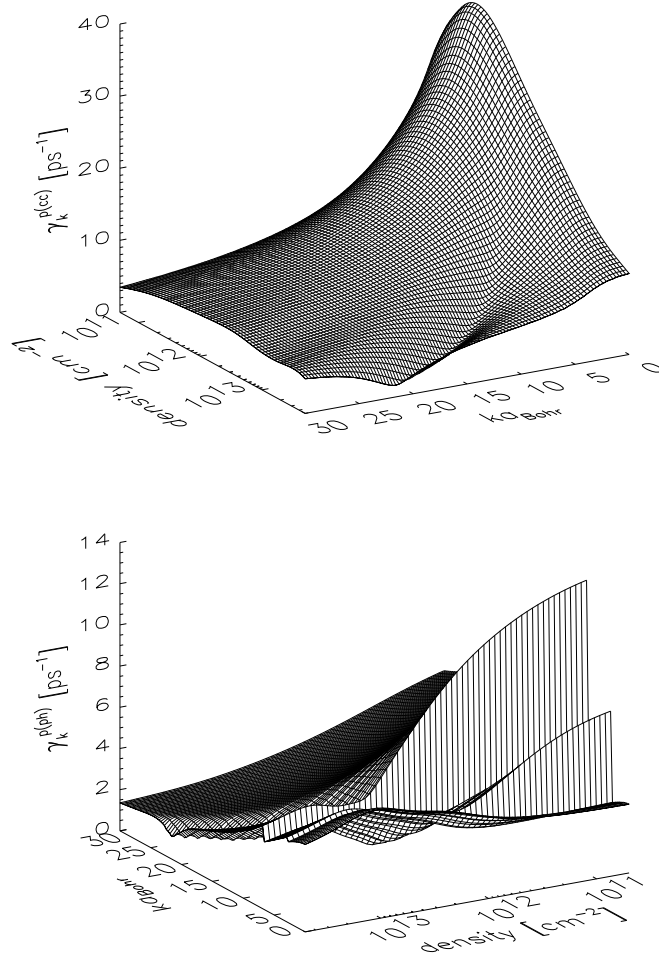


FIGURE 2.4: Microscopic dephasing rates (as integrals over all possible individual scattering processes) of the interband polarisation $\gamma_{11,\mathbf{k}}^p$ versus the carrier density and the momentum due to carrier-carrier scattering (upper graph) and due to the interaction of carriers with longitudinal optical phonons (below). These momentum relaxation rates $\gamma_{\mathbf{k}}(N, T)$ are incorporated into the spatially resolved time-domain simulations using lookup tables. The sharp structures in $\gamma_{\mathbf{k}}^{p(\text{ph})}$ are caused by the restrictive threshold condition for out-scattering processes which involve the emission of an optical phonon (and for in-scattering processes with the absorption of a phonon). For realistic laser operating conditions (that imply states near the band edge and a density of the active GaAs quantum well structure of around the threshold carrier sheet density $\approx 2 \cdot 10^{12} \text{ cm}^{-2}$) typical dephasing times for the screened Coulomb interaction are 50 fs, and for the Fröhlich interaction 350 fs. For more details see SECTION 4.1. In the calculations of the scattering matrices and rates due to the carrier-carrier interaction we have neglected exchange contributions. At high densities these terms may weaken the overall interaction strengths and reduce the relaxation rates.

the Rabi frequency. In addition to the exchange shift of the single particle energies, a further term arises due to the presence of the two-component plasma: The Debye shift²⁰ or Coulomb hole self-energy

$$\delta E^{\text{CH}} = \sum_{\mathbf{q} \neq \mathbf{0}} [V^{\text{sc}}(\mathbf{q}) - V(\mathbf{q})] \quad (2.99)$$

contributes to a change in transition energies $\hbar\Omega_{ij,\mathbf{k}}(N) = E_{i,\mathbf{k}}^e + E_{j,-\mathbf{k}}^h + \delta E_{ij,\mathbf{k}}^{\text{SX}} + \delta E^{\text{CH}} + E_{\text{gap}}$.

2.9 Quantum Dot Lasers and Multi-Level Bloch Equations

In recent years the application of the size quantisation concept has been extended to two dimensions (quantum wires [28, 57]) and to three dimensions, namely to quantum dot systems [29]. This process has been motivated by the success of optically active semiconductor multi-layer heterostructures, such as quantum well-based lasers and amplifiers. The electronic and optoelectronic properties of quantum dots (fabricated by self-organised growth of islands on the nanometer scale) are rather comparable to that of single atoms than to the characteristics known from solid state semiconductor systems. Accompanied with the electronic quantum confinement is a strong modification of the electronic density of states, states at high energies are relatively suppressed, and states around the band edge (where the lasing process takes place) are pronounced [25]. For this reason quantum dot lasers should outperform semiconductor bulk or quantum well laser structures with respect to parameters like the transparency or threshold current, the material gain, the linewidth enhancement factor or the beam quality [29, 93]. Due to the discrete energy level structure one would expect only very few (intradot) relaxation and decoherence channels as the scattering processes are not allowed by reason of strict energy conservation (in Markov approximation). Recent experimental investigations [94], however, show ultrafast carrier relaxation and recovery of the gain dynamics and fast dephasing times, both of which makes quantum dot structures promising materials for high-speed applications such as amplifiers or saturable absorbers.

Starting from a paraxial semiconductor quantum dot Maxwell Bloch model [95] we will specify equations of the dynamics of the carriers within a quantum dot interacting with a classical electromagnetic field. The atomic-like gain system may be modelled by multi-level Bloch equations, including additional phenomenological terms. The individual two-level systems (i.e. dipole transitions) are characterised by the energy levels i, j for electrons and holes, respectively, with energetic degeneracies d_i^e, d_j^h , which account for

²⁰For quantum well structures with a quasi two-dimensional (two-component) plasma this shift is approximately given by $\delta E^{\text{CH}} = -e^2\kappa/(4\pi\epsilon_0\epsilon) \ln(1 + \sqrt{8e^2Nm_r/(C\epsilon_0\epsilon\hbar^2\kappa^3)})$ [48], but the exchange contributions to the shifts of the transition energies and the field renormalisation (the Coulomb enhancement) have to be calculated numerically applying for the screened potential with (2.98) $V^{\text{sc}}(\mathbf{q}) = e^2/(2\epsilon_0\epsilon Aq)F(q) (q/\kappa + q^3C\epsilon_0\epsilon\hbar^2/(8e^2Nm_r)) (1 + q/\kappa + q^3C\epsilon_0\epsilon\hbar^2/(8e^2Nm_r))^{-1}$.

the maximum occupations $n_i^e \in [0, d_i^e]$, $n_j^h \in [0, d_j^h]$, by the transition frequencies Ω_{ij} , the homogeneous broadenings γ_{ij}^p , and the dipole matrix elements M_{ij}^{eh} (measures of the strength of the interaction). The dynamics is given by the differential equations of driven damped harmonic oscillators, which here are written in full time-domain

$$\begin{aligned} \partial_t^2 \mathbf{p}_{ji} + 2\gamma_{ij}^p \partial_t \mathbf{p}_{ji} + \omega_{ij}^2 \mathbf{p}_{ji} &= -\Omega_{ij} \frac{M_{ij}^{eh} E}{\hbar} (n_i^e n_j^h - (d_i^e - n_i^e)(d_j^h - n_j^h)) \\ &= -\Omega_{ij} \frac{M_{ij}^{eh} E}{\hbar} (d_j^h n_i^e + d_i^e n_j^h - d_i^e d_j^h). \end{aligned} \quad (2.100)$$

The electron or hole interlevel polarisations have been neglected on the basis of their typically strong energetic non-resonant nature with the optical fields. The carrier dynamics of the electron and hole populations is presented by

$$\begin{aligned} \partial_t n_i^e &= \sum_j 2 \frac{M_{ij}^{eh} E}{\hbar} \frac{1}{\Omega_{ij}} (\partial_t \mathbf{p}_{ji} + \gamma_{ij}^p \mathbf{p}_{ji}) \\ &+ \Lambda \frac{f_i^e (d_i^e - n_i^e)}{\sum_i f_i^e (d_i^e - n_i^e)} - \gamma_i^{\text{nr}} n_i^e - \sum_j \gamma_{ij}^{\text{sp}} n_i^e n_j^h - \gamma_i^{\text{Auger}} + \partial_t n_i^e|_{\text{relax}}, \end{aligned} \quad (2.101)$$

$$\partial_t n_j^h = \sum_i 2 \frac{M_{ij}^{eh} E}{\hbar} \frac{1}{\Omega_{ij}} (\partial_t \mathbf{p}_{ji} + \gamma_{ij}^p \mathbf{p}_{ji}) + \partial_t n_j^h|_{\text{ph}} + \partial_t n_j^h|_{\text{relax}}. \quad (2.102)$$

The electrical pumping term contains the Pauli blocking effect for fermionic particles, and quasi-equilibrium populations have been introduced. But the various (interlevel) scattering, thermalisation and relaxation processes, many-body interactions and renormalisation effects, the coupling to the wetting layer states by carrier capture (via the interaction processes phonons, Coulomb, Auger and impact ionisation) and thermionic emission have to be addressed in more detail [95]. Furthermore, a many-particle treatment would allow for a quantum statistical description of energy level occupations and a more precise definition of blocking factors. A spectral summation results in $N^e = 2 \sum_i n_i^e$, $N^h = 2 \sum_j n_j^h$, $P = 2 \cdot 2 \sum_{i,j} M_{ij}^{eh} \mathbf{p}_{ji}$. The inclusion of these active quantum dot measures into macroscopic field equations like the Maxwell wave equation requires to treat ensembles of quantum dots, or define macroscopic effective quantum dots, and a conversion into carrier and dipole polarisation volume densities $D = \epsilon_0 \epsilon E + \Gamma N_{\text{QD}} / V_{\text{ref}} P$. The transition from the electron and hole representation to a more general electronic multi-level picture can be done by the replacement $n_j^h \rightarrow d_j^e - n_j^e$, $d_j^e = d_j^h$, where the induced polarisation \mathbf{p}_{ji} is driven by the appropriate occupation inversion $d_j^e n_i^e - d_i^e n_j^e$.

A set of few uncoupled and independent two-level systems, each modelled by a homogeneously broadened harmonic oscillator in time-domain is equivalent to a sum of Lorentzians in frequency-domain. The superpositions of Lorentzians can be used to create an efficient realisation of the asymmetric semiconductor gain profile. The effective semiconductor Bloch equations [12, 55, 96] are an approximative fit to the dielectric dispersion and absorption (or amplification), given by the many-body calculations of the

semiconductor permittivity $\epsilon(\omega, N, T)$ or electric susceptibility $\chi(\omega, N, T)$. For more details see the section on spectral summation 2.11. By treating the macroscopic fields such as the carrier densities or occupations as dynamical variables, nonlinear behaviour and the effect of gain saturation are included.

2.10 Fitting the Dielectric Function

We now consider more complicated active gain media, and try to understand the nature of electromagnetic pulse interactions with these novel materials, which feature linear and nonlinear dispersion and nonlinearities, over a broad frequency range. Possible systems include optically active carbon nanotubes [56, 97], organic [30] or polymer [31] materials for lasers, metallic nanoparticles and one-dimensional nanostructures [27], or biological materials subject to impulsive excitation [98]. These dispersive media will be modelled within the finite-difference time-domain framework [99] by the Maxwell curl equations

$$\text{curl}\mathbf{E} + \partial_t\mathbf{B} = 0, \quad \frac{1}{\mu_0}\text{curl}\mathbf{B} - \epsilon_0\epsilon\partial_t\mathbf{E} = \mathbf{J} + \partial_t\mathbf{P}, \quad (2.103)$$

and constitutive relations between electromagnetic excitations and the dielectric response

$$\mathbf{D}(\mathbf{r}, t) = \epsilon_0\epsilon(\mathbf{r})\mathbf{E} + \mathbf{P}(\mathbf{r}, t), \quad \mathbf{P} = \epsilon_0\epsilon\chi\mathbf{E}, \quad (2.104)$$

$$\tilde{E}(\omega)e^{-i\omega t}, \tilde{P}(\omega)e^{-i\omega t}, \tilde{J}(\omega)e^{-i\omega t}, \partial_t \leftrightarrow -i\omega; \quad \chi(\omega) = \frac{\tilde{P}(\omega)}{\epsilon_0\epsilon\tilde{E}(\omega)}, \quad \epsilon(\omega) = \epsilon(1 + \chi(\omega)). \quad (2.105)$$

The complex-valued dielectric function $\epsilon(\omega)$ is crucial to understand the optical properties of metallic, dielectric systems. Its characteristics are associated with intraband free-electron excitations and an additive complex contribution from interband transitions. Theoretically this can be explained by the Drude model, and multiple-pole Debye and Lorentz dispersions. A positive imaginary part of ϵ is associated with absorption, a negative real part with reflection. The dispersion in frequency-domain is translated to a temporally nonlocal response in the time-domain. Convolution relations or differential equations connect the effective dielectric response with the excitation. The Kramers-Kronig relations connect the real and imaginary part of a any complex-valued response function of a linear and causal physical process. From Cauchy theorem for an analytic and bound function in the upper half plane (from causality principle and analyticity domain) we can give the reformulations for positive values of the frequency [69]

$$\text{Re}(\epsilon(\omega)) = \epsilon + \frac{2}{\pi}\mathcal{P} \int_0^\infty \frac{\omega' \text{Im}(\epsilon(\omega'))}{\omega'^2 - \omega^2} d\omega', \quad \text{Im}(\epsilon(\omega)) = -\frac{2\omega}{\pi}\mathcal{P} \int_0^\infty \frac{\text{Re}(\epsilon(\omega')) - \epsilon}{\omega'^2 - \omega^2} d\omega', \quad (2.106)$$

with $\epsilon = \epsilon_{\text{background}} = \epsilon_\infty$. The empirical knowledge of the imaginary part of $\epsilon(\omega)$ from absorption studies and measurements enables the calculation of the real part. It

turns out that $\text{Re}(\epsilon)$ is monotonically increasing between the absorption bands, but shows anomalous dispersion within resonances. A fit over a given frequency range is possible by a superposition of a finite number of Lorentz, Debye and Drude dispersions, which will inherently satisfy causality requirements. Two efficient, rather complementary approaches are known to model nonmagnetic, dispersive (and hence lossy, absorptive) dielectric materials [58, 59, 72], such as insulators, semiconductors or metals²¹. We will follow the auxiliary differential equations approach (ADE) which introduce polarisation and induced polarisation current terms $\mathbf{P}, \mathbf{J} \in \mathbb{R}$ into the Maxwell equations (Ampère's law) which are the time-domain equivalent of the complex-valued dielectric constant $\epsilon(\omega) \in \mathbb{C}$ in frequency-domain [58]. The ADE approach operates on real-valued fields. The basic model to describe the material response of bound charge carriers to an applied electromagnetic field is the Lorentz model. For a more general material response we assume that l labels a discrete resonance with frequency ω_l , with the damping factor γ_l , and $\Delta\epsilon_l$ as the relative permittivity increment or strength of the coupling. The time-domain description is given by a damped driven harmonic oscillator

$$(\partial_t^2 + 2\gamma_l\partial_t + \omega_l^2) P_l = \epsilon_0\Delta\epsilon_l\omega_l^2 E. \quad (2.107)$$

Transformed from the differential equations representation we attain the electric susceptibility in frequency-domain

$$\chi(\omega) = \frac{1}{\epsilon} \sum_l \Delta\epsilon_l\omega_l^2 \cdot \left(\frac{\omega_l^2 - \omega^2}{(\omega_l^2 - \omega^2)^2 + 4\gamma_l^2\omega^2} + i \frac{2\gamma_l\omega}{(\omega_l^2 - \omega^2)^2 + 4\gamma_l^2\omega^2} \right), \quad (2.108)$$

$$\chi(\omega) \approx \frac{1}{\epsilon} \sum_l \Delta\epsilon_l\omega_l^2 \cdot \left(\frac{1}{2\omega} \frac{\omega_l - \omega}{(\omega_l - \omega)^2 + \gamma_l^2} + i \frac{1}{2\omega} \frac{\gamma_l}{(\omega_l - \omega)^2 + \gamma_l^2} \right), \quad (2.109)$$

where the second line is an approximation near the resonance frequency $\omega_l^2 - \omega^2 \approx 2\omega(\omega_l - \omega)$. Other models discussed in literature can be derived from the Lorentz model. In the slow rise time signal regime limit [72], that is $\partial_t^2(\omega^2) \ll \omega_l^2$, $2\gamma_l/\omega_l^2 \rightarrow \tau_d$, one obtains the Debye rotational relaxation model with real-valued single-poles. This material model is widely applied as a result of the growing interest in electromagnetic pulse interactions with biological (i.e. water-based) substances and accounts for the excitations

²¹The piecewise-linear recursive convolution (PLRC) method [58, 59] is based on a systematic evaluation of $\epsilon_0\epsilon[\chi(t) * E(t)]$. It incorporates the discretised form of the convolution integral into the finite-difference time-domain paradigm $D^n = \epsilon_0\epsilon E^n + \epsilon_0\epsilon \int_{t_0}^t dt' \chi(t') E(t - t')$, $t = t_0 + n\Delta t$. For greater accuracy of second order, $E(t - t')$ is approximated by piecewise-linear line segments in the integration of the time-domain convolution integrals. An efficient on-the-fly approach is realised by the introduction of a new, additional time-dependent variable $\Psi^n \in \mathbb{C}$ [59], representing the recursive accumulator (which may be complex-valued). An updating of $E(t)$ is performed without explicitly evaluating the convolutional sum (thereby it is not required to store the complete time history). It can be reduced to a cumulative sum (to add the most recent contributions) that is updated at each time step by $\Psi^n(E^n, E^{n-1}, \Psi^{n-1})$, $E^{n+1}(E^n, H^{n+1/2}, \Psi^n)$.

of permanent dipole moments (as established in water)

$$(\tau_d \partial_t + 1) P_d = \epsilon_0 \Delta \epsilon_d E, \quad (2.110)$$

$$\chi(\omega) = \frac{1}{\epsilon} \sum_d \Delta \epsilon_d \cdot \left(\frac{1}{1 + \tau_d^2 \omega^2} + i \frac{\tau_d \omega}{1 + \tau_d^2 \omega^2} \right), \quad \epsilon(\omega) = \epsilon + \sum_d \frac{\Delta \epsilon_d}{1 - i \omega \tau_d}. \quad (2.111)$$

In the fast time response limit of the Lorentz model [72], $\partial_t^2(\omega^2) \gg \omega_l^2$, $\sum_l \Delta \epsilon_l \omega_l^2 \rightarrow \omega_{m,pl}^2$, $2\gamma_l \rightarrow 1/\tau_m$, the standard Drude model emerges as applicable for metals, plasmas of free charge carriers or intraband transitions

$$J \doteq \partial_t P \rightarrow \left(\partial_t + \frac{1}{\tau_m} \right) J_m = \epsilon_0 \omega_{m,pl}^2 E, \quad (2.112)$$

$$\chi_f(\omega) = \sum_m \left(-\frac{\omega_{m,pl}^2 \tau_m^2}{1 + \omega^2 \tau_m^2} + i \frac{\omega_{m,pl} \tau_m}{\omega(1 + \omega^2 \tau_m^2)} \right), \quad \epsilon_f(\omega) = 1 + \chi_f(\omega) \rightarrow \epsilon(\omega) + \epsilon_f(\omega). \quad (2.113)$$

$\omega_{m,pl}$ is the bulk plasmon frequency and τ_m a collision time. There is a considerable interest to study light interacting with metallic nanoparticles [100], in particular, to investigate surface plasmon polaritons as resonance interactions of light with the electronic charge density near the metal surface. Arrays of such particles could be used to confine and guide light at the sub-diffraction dimension, as coupled plasmons are generated [101]. The above approaches to incorporate dynamic material responses into the Maxwell equations can be extended to model nonlinear dispersive media ($D = \epsilon_0 \epsilon E + P^{\text{linear}} + P^{\text{nonlinear}}$) which are characterised by nonlinear susceptibility kernels $\chi^{(n)}(t - t_1, \dots, t - t_n)^{22}$ [6].

2.11 Spectral Summation and Coupling to the Maxwell Equations

In this section we establish the connection between our microscopic description of the active gain medium in momentum space and the macroscopic real space description

²²The third order nonlinear polarisations $\chi^{(3)}(t - t_1, t - t_2, t - t_3)$ (Kerr effect or inelastic Raman scattering by phonons) are of particular interest [7], specifically convolution integrals (as the constitutive relations) that depend on the product of electric field squared and $\tilde{\chi}^{(3)}$ [58, 102]. Using the Born Oppenheimer approximation [58] we may decompose the susceptibility function into a Kerr-type instantaneous nonlinearity plus a Raman-type dispersive nonlinearity $P^{\text{nonlinear},(3)} = P^{\text{Kerr}} + P^{\text{Raman}}$, more precisely $P^{\text{nonlinear},(3)} = \epsilon_0 \epsilon E(t) \sum_p \chi_{0,p}^{(3)} \int_{t_0}^t dt' [E(t')]^2 (\alpha_p \delta(t - t') + (1 - \alpha_p) \tilde{\chi}_p^{(3)}(t - t'))$ ($\chi_{0,p}^{(3)}$ is the strength of the third order nonlinearity, α_p determines the ratio of the two types). The ADE method allows for the modelling of arbitrary nonlinear dispersive media and is very efficient (because in contrast to the PLRC ansatz finding the roots of nonlinear polynomial equations for the updated field values at each time step is not necessary). In close analogy to the linear case, see for example (2.107), additional (polarisation) variables, the convolutions $R_p(t) = \epsilon_0 \chi_{0,p}^{(3)} (1 - \alpha_p) [\tilde{\chi}_p^{(3)}(t) * E^2(t)] \in \mathbb{R}$ are time stepped in synchronism with the Maxwell curl equations by $(\partial_t^2 + 2\gamma_p \partial_t + \omega_p^2) R_p = \epsilon_0 \chi_{0,p}^{(3)} (1 - \alpha_p) E^2(t)$. The Bloch equations models represent a different character of nonlinear material description, nonlinear behaviour arises from the implementation of additional variables, the carrier density and distributions, and the effects of hole burning.

including the dynamics of optical, thermal and carrier fields. Macroscopic quantities can be derived from microscopic variables by a spectral summation over the portion of interest of the band structure. The macroscopic fields, on the other hand, specify the quasi-equilibrium distribution functions with a parametric spatial dependency. The thermal quasi-equilibrium is understood as a local quasi-stationary state that a subsystem, e.g. electrons, tries to establish due to fast scattering processes. The various subsystems and variables and their coupling and connections are summarised in FIGURE 2.5. The carrier sheet density, for example, is connected with the microscopic carrier distribution functions by

$$N^e = \sum_i \frac{1}{A} \sum_{\mathbf{k}} n_{ii,\mathbf{k}}^e, \quad N^h = \sum_j \frac{1}{A} \sum_{\mathbf{k}} n_{jj,-\mathbf{k}}^h. \quad (2.114)$$

The summation over the momentum vector \mathbf{k} is frequently replaced by an continuous integral

$$\sum_{k_x} \rightarrow \int dk_x \frac{L_x}{2\pi}, \quad \sum_{k_y} \rightarrow \int dk_y \frac{L_y}{2\pi}, \quad (2.115)$$

where we assume periodic boundary conditions in the semiconductor. In semiconductor quantum well gain materials with an isotropic band structure diagram, i.e. $d^2\mathbf{k} = 2\pi k dk$, one can write

$$\sum_i \frac{1}{A} \sum_{\mathbf{k}} \rightarrow \sum_i \frac{1}{A} \frac{A}{(2\pi)^2} \cdot 2 \int d^2\mathbf{k} = \sum_i \frac{1}{\pi} \int_0^{k_{\text{cut-off}}} dk k, \quad \rho_k^{2D} = \frac{k}{\pi}. \quad (2.116)$$

The electronic density of states in momentum space ρ_k^{2D} includes a factor of two because of the summation over the two degenerated spin states. This translates to an energy-based density of states which is given by $\rho_E^{2D} = \sum_i m_i / (\pi \hbar^2) \Theta(E - E_i)$ (for a parabolic band structure)²³. In a similar way, the microscopic interband polarisation can be summed up to the induced macroscopic polarisation

$$\mathbf{P} = \sum_{i,j} \frac{1}{A} \sum_{\mathbf{k}} (\mathbf{M}_{ij}^{eh} p_{ji,\mathbf{k}}^* + \mathbf{M}_{ij}^{eh*} p_{ji,\mathbf{k}}), \quad (2.117)$$

which is a sheet density related measure. In order to couple this quantity to the Maxwell equation, the density of quantum wells has to be accounted for by applying the factor N_{QW}/L_{ref} . For more details see FIGURE 2.6. In the hydrodynamic approach [103] the

²³The equivalent calculations performed for a bulk medium give $\rho_k^{3D} = k^2/\pi^2$, $\rho_E^{3D} = m/(\pi^2 \hbar^3) \sqrt{2mE}$ [3], novel (quasi) one-dimensional quantum wire nanostructures [28, 57] are characterised by $\rho_k^{1D} = 2/\pi$, $\rho_E^{1D} = \sum_i d_i 2m_i / (\pi \hbar) / \sqrt{2m_i(E - E_i)} \Theta(E - E_i)$, and atomic-like quantum dots [29] by $\rho_E^{0D} = 2 \sum_i d_i \delta(E - E_i)$. In structures where more than one direction is quantum confined there may be besides the degeneracy of two because of the spin degree of freedom an additional energetic degeneracy (different combinations of quantum numbers leading to the same energy) d_i . These considerations show that states at high energies are relatively suppressed, states near the band edge (here the lasing takes place) are pronounced. The quantum confinement (the size quantisation concept) in novel systems with reduced dimensionality thus increases the efficiency of the inversion.

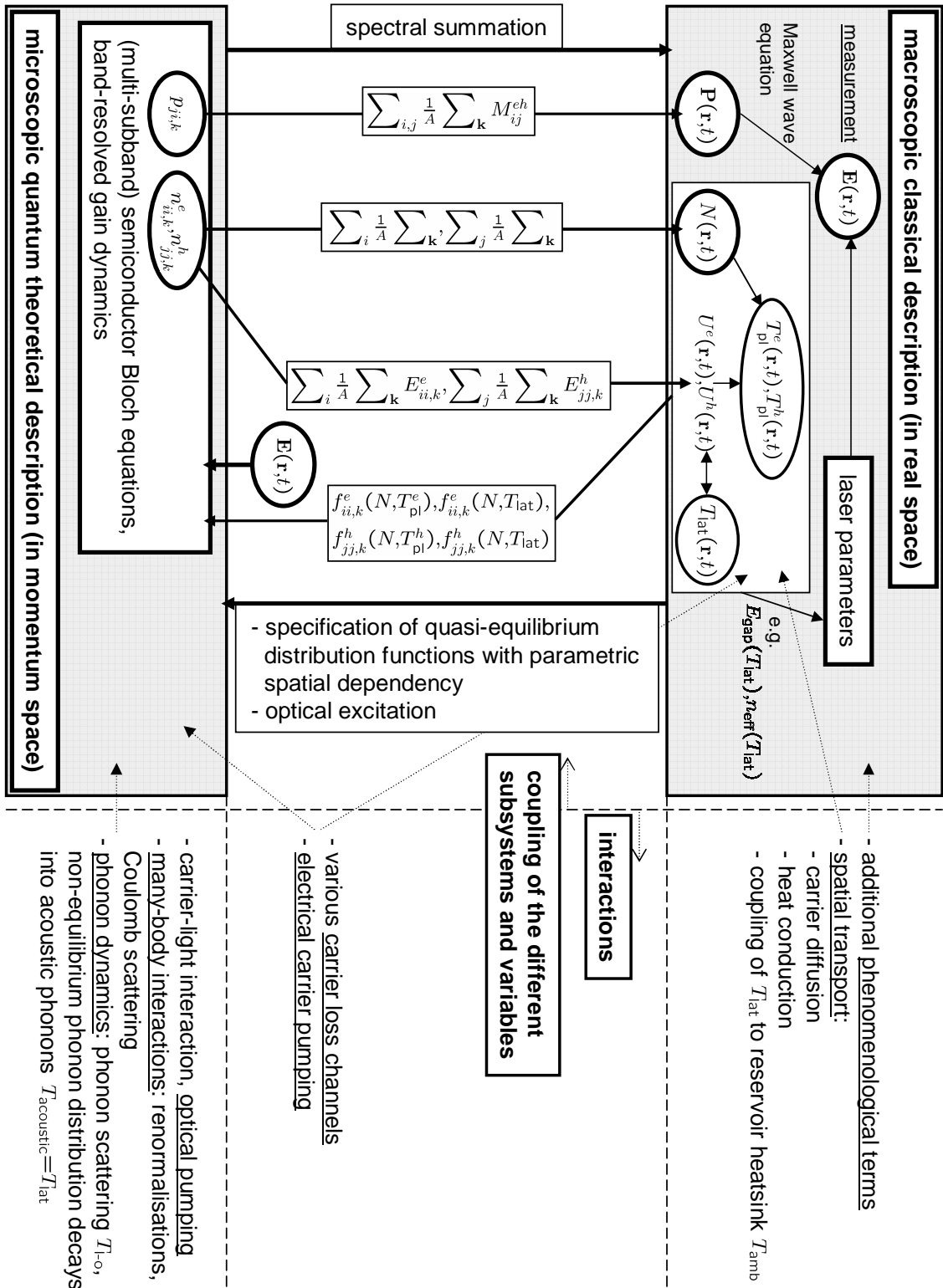


FIGURE 2.5: Coupling of the various subsystems (levels of description) and variables of a semiconductor laser structure, and overview on interactions and phenomenological terms.

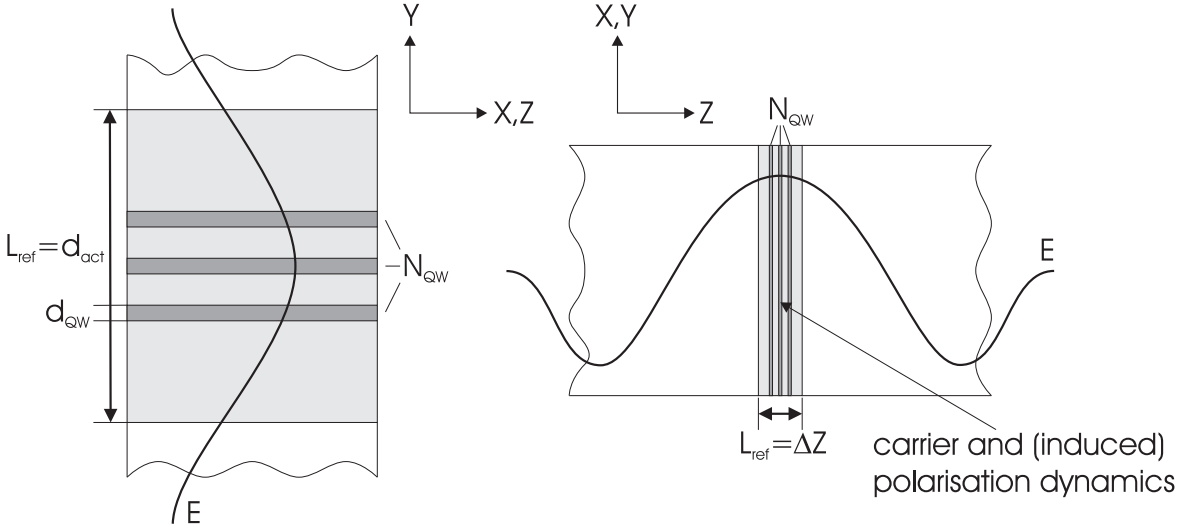


FIGURE 2.6: Coupling of the induced polarisation of the active gain medium with the electric field. The microscopic variables are dimensionless quantities. In the spectral summation the various spectral components are weighted by the respective electronic density of states. This leads to terms which are dependent on the dimension of the quantum confined structure, e.g. P [C/m] is a dipole sheet densities for quantum wells. The physical polarisation quantity which couples to the electric field has to be given by an electric dipole volume density, that may qualify for a volume conversion factor $E \leftarrow \mathcal{V}_{\text{conv}} \Gamma \cdot P / \epsilon_0$. (Left) In the case of an edge-emitting structure the coupling term in the paraxial wave equation is given by the product of a confinement factor of the slab optical waveguide $(\Gamma_y)_{d_{\text{act}}}$ with the density of quantum wells $(N_{\text{QW}} d_{\text{QW}} / d_{\text{act}}) \cdot 1 / d_{\text{QW}}$, that is $E(x, z, t) \leftarrow (\Gamma_y)_{d_{\text{act}}} N_{\text{QW}} / d_{\text{act}} \cdot P(x, z, t) / \epsilon_0$. The strength is thus independent of the width of the quantum wells but on the density of active sheets. (Right) If resolving the spatial direction of quantum confinement, the reference length is given by $L_{\text{ref}} = \Delta z$, and the correct coupling is expressed by $E(z, t) \leftarrow \Gamma_{x,y} N_{\text{QW}} / \Delta z \cdot P(z, t) / \epsilon_0$.

carrier state is characterised by the first moments of the distributions: density, momentum density and energy density. Non-equilibrium distribution functions can be calculated from the microscopic semiconductor Bloch equations including the discussed Boltzmann transport or scattering terms (SECTION 2.8). A quantity of particular interest is the second moment, the plasma energy density

$$U^e = \sum_i \frac{1}{A} \sum_{\mathbf{k}} \left(E_{i,\mathbf{k}}^e + \delta E_{ii,\mathbf{k}}^{e,\text{SX}} \right) n_{ii,\mathbf{k}}^e, \quad U^h = \sum_j \frac{1}{A} \sum_{\mathbf{k}} \left(E_{j,-\mathbf{k}}^h + \delta E_{jj,-\mathbf{k}}^{h,\text{SX}} \right) n_{jj,-\mathbf{k}}^h. \quad (2.118)$$

As discussed before, an important result of the Coulomb many-body interaction is the establishment of a quasi-equilibrium distribution function. The Fermi-Dirac distribution of the electron plasma is determined by the carrier density and energy density (2.118). By replacing the extensive variables N, U^e by the intensive measures temperature T_{p}^e and chemical potential μ_e , the Fermi-Dirac distribution for the electrons can be written

as

$$f_{ii,\mathbf{k}}^e(N^e, U^e; \mu_e, T_{\text{pl}}^e) = \frac{1}{1 + \exp\left(\beta \left(E_{ii,\mathbf{k}}^{e,\text{SX}} - \mu_e\right)\right)}, \quad (2.119)$$

$$\beta\mu_e = \ln \left[\exp\left(\frac{\beta\pi\hbar^2 N^e}{m_e}\right) - 1 \right], \quad \beta = \frac{1}{k_B T_{\text{pl}}^e}. \quad (2.120)$$

The chemical potential μ can be calculated analytically as in (2.120) in the case of one subband. For the multi-subband case this has to be done numerically.

In summary, the microscopic carrier dynamics in the active quantum well regions

$$\begin{aligned} \partial_t n_{ii,\mathbf{k}}^e = & - \sum_j \tilde{g}_{ij,\mathbf{k}} - \gamma^{\text{nr}} n_{ii,\mathbf{k}}^e - \sum_j \gamma_{ij,\mathbf{k}}^{\text{sp}} n_{ii,\mathbf{k}}^e n_{jj,-\mathbf{k}}^h - \gamma_{ii,\mathbf{k}}^{e,\text{Auger}} \\ & + \Lambda \frac{f_{ii,\mathbf{k}}^e(T_{\text{lat}}) (1 - n_{ii,\mathbf{k}}^e(T_{\text{pl}}^e))}{\sum_i 1/A \sum_{\mathbf{k}} f_{ii,\mathbf{k}}^e (1 - n_{ii,\mathbf{k}}^e)} - \gamma_{ii,\mathbf{k}}^{e(\text{ph})} (n_{ii,\mathbf{k}}^e(T_{\text{pl}}^e) - f_{ii,\mathbf{k}}^e(T_{\text{lat}})) \\ & - \gamma_{ii,\mathbf{k}}^{ee(\text{cc})} (n_{ii,\mathbf{k}}^e(T_{\text{pl}}^e) - f_{ii,\mathbf{k}}^e(T_{\text{pl}}^e)) - \gamma_{ii,\mathbf{k}}^{eh(\text{cc})} (n_{ii,\mathbf{k}}^e(T_{\text{pl}}^e) - f_{ii,\mathbf{k}}^h(T_{\text{pl}}^h)) \end{aligned} \quad (2.121)$$

comprises the processes of coherent coupling to an electromagnetic field, various carrier recombination and loss channels, and an electrical pumping term. Here, the scattering contributions due to many-body interactions are specified in the relaxation rate approximation. A macroscopic equation in real space for the sheet carrier density can be derived by applying a spectral summation over (2.121)

$$\sum_i \frac{1}{A} \sum_{\mathbf{k}} \cdot (2.121) \rightarrow \partial_t N = -\tilde{G}_N - \Gamma^{\text{nr}} N - \Gamma_N^{\text{sp}} - \Gamma_N^{\text{Auger}} + \Lambda + D_N \Delta_{\parallel} N. \quad (2.122)$$

On this level of description, a phenomenological ambipolar diffusion term [48, 53] that reduces density inhomogeneities has been added. A systematic derivation of this term from the hydrodynamic approach starting from the microscopic equations including Boltzmann transport terms is presented in [36, 103]. We try to motivate this balancing process in the following: A complete treatment of electron and hole carrier dynamics includes classical transport in bulk regions, the connectivity to quantum wells or more general nanostructures by quantum carrier capture and thermionic emission, self-heating or self-cooling effects (hot electrons and hot phonons). Besides a formulation in energy space by (2.121) electronic equations in real space [63] are necessary, e.g. to describe the dynamic impact of the electrostatic potential which is arising from the Poisson equation [63, 104]

$$\nabla \cdot \epsilon \nabla \Phi = -\frac{\rho}{\epsilon_0} = \frac{e}{\epsilon_0} (N^e - N^h + N_A^- - N_D^+). \quad (2.123)$$

Here, the divergence of the dielectric displacement is given by the space charge density due to a deviation from local charge neutrality. N_A^- , N_D^+ are ionised acceptor and donor concentrations, respectively. In addition, the real space electronic problem includes generalised continuity equations for electrons (and for holes) [63, 104]

$$\nabla \cdot j_{N_{3D}^e} + \partial_t N_{3D}^e + \Gamma_{N_{3D}^e}^{\text{net loss}} + C_{N_{3D}^e, N^e}^{\text{net cap}} = 0, \quad (2.124)$$

$$\nabla \cdot j_{N^e} + \partial_t N^e + \Gamma_{N^e}^{\text{net loss}} + \tilde{G}_N - C_{N_{3D}^e, N^e}^{\text{net cap}} = 0. \quad (2.125)$$

The above equations balance the divergence of the carrier fluxes by recombination and loss processes and by the macroscopic carrier generation rate in the active areas. Abrupt heterojunctions that define the quantum wells or embedded nanostructures (the quantum regime) are treated as scattering centres characterised by the net carrier capture rates from the wetting layers. Carrier capture represents a source term for bound electrons and a drain for continuum carriers. In bulk material or in the plane of the quantum well the Shockley drift-diffusion theory can be applied. It relates the carrier transport, which is a flow of charged electrons, to a drift component and a diffusive process

$$j_{N_{3D}^e} = \mu^e N_{3D}^e \nabla \Phi - D^e \nabla N_{3D}^e, \quad (2.126)$$

qualified by the particle mobility μ^e and the diffusion constant D^e . While the diffusion is caused by density gradients, the drift originates from the electrostatic force. In semiconductor diode lasers, the carrier densities are typically high, and the ultrafast interband coupling due to Coulomb electron-hole scattering dominates over the carrier-phonon interaction. This has two implications. Firstly, a common plasma temperature $T_{\text{pl}}^e = T_{\text{pl}}^h = T_{\text{pl}}$ can be assumed in good approximation. Secondly, the charge imbalances are usually very small, which justifies to set $N^e = N^h = N$. This local charge neutrality allows to use the so-called ambipolar diffusion approximation [103]

$$j_N = -D_N \nabla_{\parallel} N, \quad D_N = \frac{\mu^e D^h + \mu^h D^e}{\mu^e + \mu^h}. \quad (2.127)$$

In microlasers (such as VCSEL or microcavity lasers) the heat dissipation from the active quantum regime to the ambient is seriously hindered. In general, thermal effects are more problematic for smaller and more complicated structured lasers as they significantly contribute to the saturation of the gain and a reduction of output power [105–108]. The effects of carrier and lattice self-heating have been included in self-consistent electro-thermo-optical simulators [63, 109]. Whereas, the concept of temperatures as dynamical variables $T_{\text{pl}}, T_{\text{lat}}$ demands for formulations that balance the various sinks and sources of the electron-hole plasma energy density [12, 108]

$$\begin{aligned} \partial_t U &= \partial_t (U^e + U^h) = \sum_i \frac{1}{A} \sum_{\mathbf{k}} E_{ii,\mathbf{k}}^{e,\text{SX}} \cdot (2.121) + \sum_j \frac{1}{A} \sum_{\mathbf{k}} E_{jj,-\mathbf{k}}^{h,\text{SX}} (\partial_t n_{jj,-\mathbf{k}}^h) \rightarrow \\ \partial_t U &= -\tilde{G}_U - \Gamma^{\text{nr}} U - \Gamma_U^{\text{sp}} - \left(\Gamma_U^{e,\text{Auger}} + \Gamma_U^{h,\text{Auger}} \right) + \Lambda_U \\ &\quad - \sum_i \frac{1}{A} \sum_{\mathbf{k}} \gamma_{ii,\mathbf{k}}^{e(\text{ph})} E_{ii,\mathbf{k}}^{e,\text{SX}} (n_{ii,\mathbf{k}}^e(T_{\text{pl}}) - f_{ii,\mathbf{k}}^e(T_{\text{lat}})) \\ &\quad - \sum_j \frac{1}{A} \sum_{\mathbf{k}} \gamma_{jj,-\mathbf{k}}^{h(\text{ph})} E_{jj,-\mathbf{k}}^{h,\text{SX}} (n_{jj,-\mathbf{k}}^h(T_{\text{pl}}) - f_{jj,-\mathbf{k}}^h(T_{\text{lat}})) + D_U \Delta_{\parallel} U. \end{aligned} \quad (2.128)$$

A phenomenological balance process to equalise existing inhomogeneities has been added. Of particular importance is the pumping with Pauli blocking. For numerical efficiency, it is of advantage to calculate the total differential of the plasma temperature by the

changes of the related extensive measures N and U

$$\partial_t T_{\text{pl}} = J_N[N, T_{\text{pl}}] \partial_t N - J_U[N, T_{\text{pl}}] \partial_t U, \quad (2.129)$$

where the coefficients J_N and J_U are nonlinear functionals of the carrier density and the plasma temperature [91, 106]. The dynamics of the phonon system is not treated on a microscopic level, but by a macroscopic phenomenological equation for the lattice temperature

$$\begin{aligned} \partial_t T_{\text{lat}} = & \Gamma^{\text{nr}} (U + N E_{\text{gap}}) \frac{N_{\text{QW}}}{L_{\text{ref}}} \frac{1}{c_{q,V}} + (\delta U^{e(\text{ph})} + \delta U^{h(\text{ph})}) \frac{N_{\text{QW}}}{L_{\text{ref}}} \frac{1}{c_{q,V}} \\ & - \sigma_{\text{th}} \frac{T_{\text{lat}} - T_{\text{amb}}}{d_{\text{amb}} d_{\text{act}}} \frac{1}{c_{q,V}} + \rho J^2 \frac{1}{c_{q,V}}. \end{aligned} \quad (2.130)$$

The hot carrier system is coupled to the lattice subsystem by means of carrier-phonon scattering, by the terms $\delta U^{e(\text{ph})}, \delta U^{h(\text{ph})}$. In addition, the active region is coupled to the reservoir heatsink by thermal conduction (cooling due to phonon diffusion). This relaxation to the ambient temperature is strongly dependent on the device design. σ_{th} [J/(Ksm)] represents the heat conductivity, $c_{q,V}$ [J/(Km³)] is the specific heat per volume. An important process is the Joule heating determined by the specific resistivity ρ [Vsm/C] and the injection current density. One should keep in mind, that the approach is based on the assumption that the electron and phonon subsystems are in different quasi-equilibrium states with individual temperatures, although they are coupled. Thus, the dynamics is described only correct if the coupling is weak, and when looking at comparatively long time scales of a few characteristic energy relaxation or thermalisation time constants (that is some ten picoseconds or longer). Then, a quasi-stationary situation can be established within the subsystems.

In the following we establish an effective semiconductor Bloch equations model [36, 55], based on self-consistency and the spectral summation over microscopic (quasi-equilibrium) variables: The full microscopic model is known to give the correct nonlinear dependence of the gain and refractive index on the carrier density and temperature, and realistic dispersions of the susceptibility. The basic idea now is to reproduce this complex behaviour by an effective and numerically less demanding model on the basis of a macroscopic, effectively two-level [36] or a multi-level [12, 41, 55] system; for each macroscopic state the parameterised susceptibility spectrum is approximated as the superposition of few Lorentzians. Because of the very different decay time scales of the various dynamical variables, more specifically $\gamma_{\text{micr}}, \gamma_{\text{polarisation}}, \gamma_{\text{energy relaxation}} \gg \gamma_{\text{electric field}} \gg \gamma_{\text{density}}$, one can assume that the polarisation follows the variations of \mathbf{E} , N and $T_{\text{pl}}, T_{\text{lat}}$ quasi-instantaneously. For an overview see FIGURE 2.7. In this case, the polarisation can be adiabatically eliminated [10]. The idea behind the effective microscopic model is: We first calculate the Fermi-Dirac distributions and the renormalised individual transition energies for a given carrier density and given temperatures. The band gap shrinkage due to the lattice temperature is thereby modelled by a phenomenological fit with the

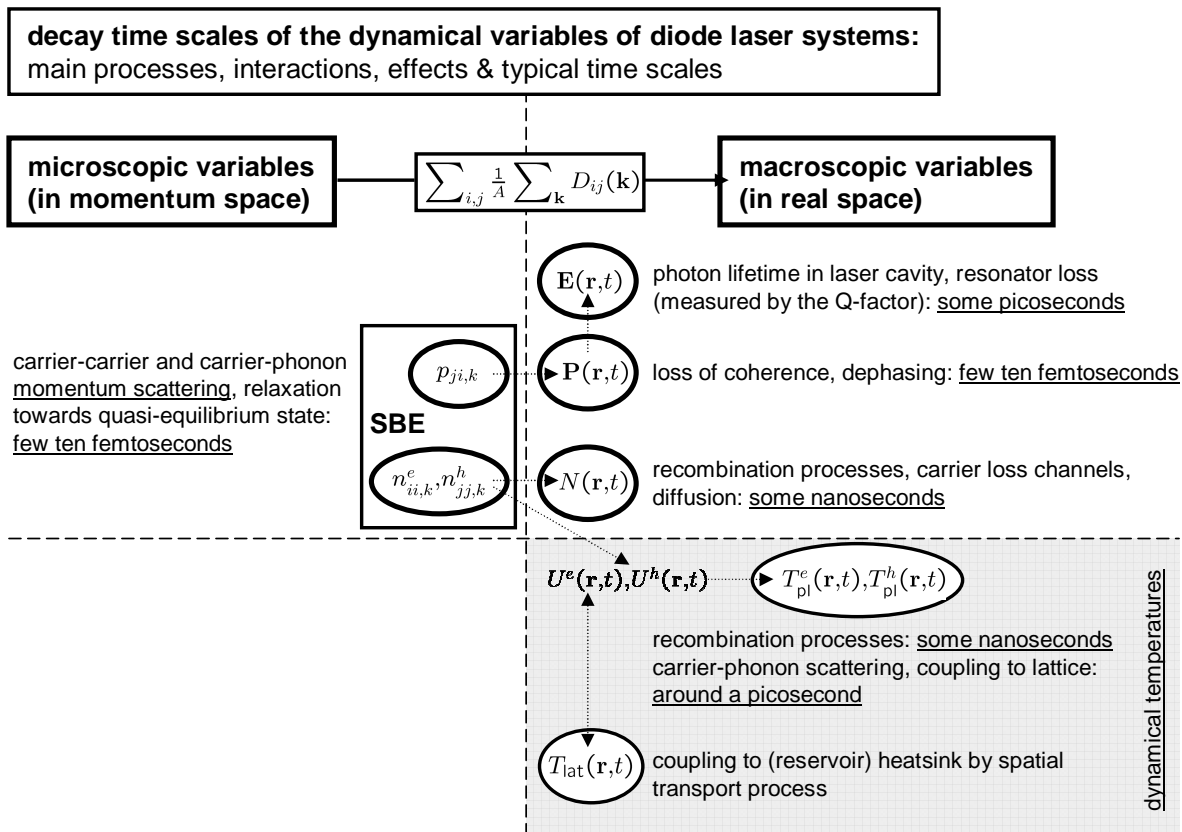


FIGURE 2.7: Overview on the various dynamical variables and belonging decay time scales. By treating the plasma and the lattice temperatures as parameters we are left with three macroscopic variables, namely the electric field $\mathbf{E}(\mathbf{r}, t)$, the carrier density N and the induced polarisation \mathbf{P} . The number of relevant dynamical variables characterises the system of coupled differential equations and thus the possible solutions of that nonlinear dynamical system [9]. Other quantities with very fast decay time scales adiabatically follow the slowly changing variables. Semiconductor-based single-mode lasers are known to be a prototype of a class-B laser with the dynamical variables $|E(t)|^2$ and $N(t)$ [52]. Typical solutions of this set of coupled nonlinear differential equations are represented by damped relaxation oscillations, a fixed point attractor. A class-A laser system can be derived by adiabatically eliminating the carrier inversion, mathematically specified by a partial differential equation known as the complex Ginzburg-Landau or complex Swift-Hohenberg equation. However, typical time scales in semiconductor-based active systems do not justify this approach.

Varshni band gap parameters [60],

$$\hbar\Omega_{ij,\mathbf{k}}(N, T_{\text{pl}}, T_{\text{lat}}) = E_{i,\mathbf{k}}^e + E_{j,-\mathbf{k}}^h + \delta E_{ij,\mathbf{k}}^{\text{SX}}(N, T_{\text{pl}}) + \delta E^{\text{CH}}(N, T_{\text{pl}}) + E_{\text{gap}}(T_{\text{lat}}), \quad (2.131)$$

$$E_{\text{gap}}(T_{\text{lat}}) = E_{\text{gap}}(T_{\text{lat}}^0) - \left(\frac{\alpha(T_{\text{lat}})^2}{\beta + T_{\text{lat}}} - \frac{\alpha(T_{\text{lat}}^0)^2}{\beta + T_{\text{lat}}^0} \right). \quad (2.132)$$

The Coulomb enhancement in Padé approximation [4, 48] is an approximative solution of nonlinear convolution integral equations for the polarisations $p_{ji,\mathbf{k}}(t)$. It is quantified by a complex, dimensionless factor

$$q_{ij,\mathbf{k}} = -\frac{i}{\hbar} \sum_{\mathbf{k}' \neq \mathbf{k}} V_{ijji}^{\text{sc}}(\mathbf{k} - \mathbf{k}') \frac{f_{ii,\mathbf{k}'}^e + f_{jj,-\mathbf{k}'}^h - 1}{i(\Omega_{ij,\mathbf{k}'} - \omega) + \gamma_{ij,\mathbf{k}'}^p}, \quad Q_{ij,\mathbf{k}}(\omega, N, T_{\text{pl}}) = \frac{1}{1 - q_{ij,\mathbf{k}}}. \quad (2.133)$$

Subsequently, we perform an adiabatic elimination of the polarisation variables in the semiconductor Bloch equations. After spectral summation, we can calculate the linear susceptibility kernel in frequency-domain

$$\chi(\omega, N, T_{\text{pl}}, T_{\text{lat}}) = \frac{\tilde{P}(\omega, N, T_{\text{pl}}, T_{\text{lat}}; t)}{\epsilon_0 \epsilon \tilde{E}(\omega; t)} = \frac{1}{\epsilon_0 \epsilon} \frac{N_{\text{QW}}}{L_{\text{ref}}} \times \\ - \sum_{i,j} \frac{1}{A} \sum_{\mathbf{k}} \frac{(\Omega_{ij,\mathbf{k}} - \omega) + i\gamma_{ij,\mathbf{k}}^p}{(\Omega_{ij,\mathbf{k}} - \omega)^2 + (\gamma_{ij,\mathbf{k}}^p)^2} \frac{1}{\hbar} |M_{ij}^{eh}|^2 (f_{ii,\mathbf{k}}^e + f_{jj,-\mathbf{k}}^h - 1) \cdot Q_{ij,\mathbf{k}}, \quad (2.134)$$

where the electric field amplitude is assumed to be constant over $1/\gamma^p$. In a last step, $\chi(\omega, N, T_{\text{pl}}, T_{\text{lat}})$ is inserted into the macroscopic field equations. With this approach active material properties and microscopic interactions and processes are effectively included into a macroscopic model. The advantage compared to common phenomenological models is that realistic device simulations can be performed. E.g., this computationally efficient model has been applied to study the transverse mode dynamics of (broad area) high-power semiconductor lasers [12, 36]. The validity of the model is restricted due to the applied approximations: Strong electric fields which lead to pronounced nonlinear behaviour, such as spectral carrier depletion, will violate the quasi-equilibrium assumption. The same holds for ultrashort pulse excitations which are shorter than the characteristic time scales associated with relaxation to quasi-equilibrium.

2.12 Conclusion

In this chapter we have derived the multi-subband semiconductor Bloch equations, a quantum mechanical description of the gain dynamics in low-dimensional systems, more precisely in quantum wells, based on the density matrix formalism. We have discussed the possibilities of band structure engineering of the optoelectronic properties in quantum

confined nanostructures, and introduced the basic concepts and physics of semiconductor heterostructures. The presented approach is formulated in momentum space and covers the relevant interactions in semiconductor-based optically active gain materials. It is associated with a diversity of time scales and nonlinearities. The interaction of light with semiconductor gain media within the semiclassical framework is modelled in the electric dipole approximation. The important many-body interactions, namely the screened Coulomb interaction and the scattering with phonons, involve the renormalisation of transition energies and the Coulomb enhancement of the Rabi frequency (screened Hartree-Fock terms), and the relaxation and dephasing processes. These many-body interactions have been presented together with other significant carrier loss channels in the context of a microscopic, band-resolved approach. The equations are derived both in a frequency-/time-domain formulation with split-off central frequency as well as in full time-domain. This novel full time-domain approach (without the usual rotating wave approximation) represents an accurate and spectrally broad modelling of the gain medium and offers the possibility to study sub-picosecond pulse interactions in semiconductor lasers. To our knowledge, the full time-domain semiconductor Bloch equations have not been reported before. We have shown how to couple the microscopic quantum theoretical description in momentum space with the macroscopic classical description in real space and have motivated further phenomenological terms that balance inhomogeneities. The dynamics of the gain medium is measured by the induced macroscopic polarisation, the carrier density, and the material dispersion. The models presented in this chapter will be applied to complex and realistic systems. However, the size of these laser systems may require an effective microscopic approach. Therefore, we have proposed the fitting of the complex dielectric susceptibility by only a few oscillators as an efficient method to reproduce the optoelectronic properties of the semiconductor gain medium.

3 Light Field Dynamics in Laser Cavities

3.1 Introduction—Macroscopic Maxwell Equations

The realistic modelling of a diode laser requires a spatially resolved consideration of the optical cavity, refractive index structure and laser fields, and a theoretical description of the optoelectronic properties of the semiconductor amplifier medium. Within a classical framework, the dynamics of the optical fields are governed by the macroscopic Maxwell equations (here written in a differential form and in the SI unit system) [69, 110]

$$\text{curl}\mathbf{E} + \partial_t\mathbf{B} = 0 \quad \text{Faraday's law,} \quad (3.1)$$

$$\text{div}\mathbf{B} = 0 \quad \text{absence of free magnetic poles,} \quad (3.2)$$

$$\text{div}\mathbf{D} = \rho \quad \text{Coulomb's law,} \quad (3.3)$$

$$\text{curl}\mathbf{H} - \partial_t\mathbf{D} = \mathbf{J} \quad \text{Ampère's law.} \quad (3.4)$$

The macroscopic electric and magnetic field quantities $\mathbf{E}(\mathbf{r}, t), \mathbb{R}^3 \times \mathbb{R} \rightarrow \mathbb{R}^3$ (electric field) and \mathbf{B} (magnetic induction) are defined as spatial averages over numerous atomic dimensions of the microscopic fields, which are governed by the vacuum Maxwell equations. Derived fields include the influence of the microscopic bound sources, and $\rho(\mathbf{r}, t)$ and \mathbf{J} describe the free macroscopic charge density and charge current density, respectively. The derived fields dielectric displacement \mathbf{D} and magnetic field \mathbf{H} can have complex multi-linear functional dependencies [69, 70]

$$\mathbf{D}[\mathbf{E}, \mathbf{B}] = \epsilon_0\epsilon\mathbf{E} + \mathbf{P}, \quad (3.5)$$

$$\mathbf{H}[\mathbf{E}, \mathbf{B}] = \frac{1}{\mu_0}\mathbf{B} - \mathbf{M}. \quad (3.6)$$

It is very challenging in theory and simulation of active devices to develop a comprehensive picture of the material properties, namely of the induced macroscopic electric \mathbf{P} and magnetic \mathbf{M} polarisations as dynamical material responses to an applied electromagnetic field. In general, the nonlinear functionals may be expanded in a Volterra series, as product of convolution integrals [5, 6]

$$P_i[\mathbf{E}] = \sum_{n=1}^{\infty} \int_{t_0}^t \dots \int_{t_0}^t dt_1 \dots dt_n \epsilon_0 \epsilon \chi_{i;j_1 \dots j_n}^{(n)}(\mathbf{r}, t - t_1, \dots, t - t_n) E_{j_1}(\mathbf{r}, t_1) \dots E_{j_n}(\mathbf{r}, t_n). \quad (3.7)$$

This approach assumes causality, invariance under translations in time and spatial locality. We note that the Fourier transforms of the tensorial susceptibility kernels $\chi_{i;j_1\dots j_n}^{(n)}(\mathbf{r}, t - t_1, \dots, t - t_n)$ to frequency domain lead to the measurable nonlinear susceptibility coefficients $\chi^{(n)}(\mathbf{r}, -\omega, \omega_1, \dots, \omega_n)$ [7]. In the general case, the permittivity or susceptibility are dispersive, absorbing, inhomogeneous, anisotropic and nonlinear material properties. The active material response is noninstantaneous. Maxwell equations (3.1)–(3.4) and the material response (3.5) form a closed set of equations. A solution is possible for arbitrary refractive index structures and cavity geometries, but because of the finite analysis windows correct boundary conditions of Dirichlet, von Neumann, combined type, or periodic boundary conditions have to be specified.

For describing the optical properties of semiconductor lasers it is a common ansatz to apply some reasonable simplifications and approximations to the macroscopic Maxwell equations. One typically assumes the absence of free field sources ($\rho = 0$ and $\mathbf{J} = 0$) and regards nonmagnetic materials $\mathbf{M} = 0$. Therefore only two quantities measure the passive and active material response in equation (3.5): $\epsilon(\mathbf{r}) \in \mathbb{R}$, which may have a fairly complex spatial structure in novel monolithic semiconductor devices, denotes the permittivity of the host background medium. $\mathbf{P}(\mathbf{r}, t)$ is the induced polarisation of the active gain material. For a semiconductor lasing medium the passive background refractive index $n_{\text{background}}(\lambda) = \sqrt{\epsilon}$ takes into account resonant excitations of the lattice with the strong bound inner electrons. It quantifies the linear, static, instantaneous material response¹. A typical value for a InGaAlAs-based device is ≈ 3.5 . In general, the permittivity is a rank-two tensor, a 3×3 matrix, but often a scalar dependence is assumed. The induced polarisation \mathbf{P} describes the gain and induced refractive index change. It contains the dynamical nonlinear interaction of the laser fields (with photon energies of about the band gap, few eV) with the charge carriers in the conduction and valence bands. In this work, one of the main foci is the detailed modelling of the induced material properties. One way to classify the various semiconductor laser models discussed in literature is the level of description of the induced polarisation in the active zone [37]: from the microscopic semiconductor Bloch equations to very simple phenomenological two-level gain models. An overview is given in FIGURE 1.1. From the above set of partial differential equations (3.1)–(3.4), and (3.5), one can deduce a full-vectorial wave equation for the electric field with the induced polarisation as source term

$$\text{grad}(\text{div}\mathbf{E}) - \nabla^2\mathbf{E} + \frac{\epsilon}{c^2}\partial_t^2\mathbf{E} = -\frac{1}{\epsilon_0 c^2}\partial_t^2\mathbf{P}. \quad (3.8)$$

The auxiliary condition of transversality, that is $\text{div}\mathbf{D} = 0$, leads to

$$\epsilon_0\epsilon\text{div}\mathbf{E} + \epsilon_0\text{grad}\epsilon \cdot \mathbf{E} + \text{div}\mathbf{P} = 0, \quad \mathbf{P} = 0 \rightarrow \text{div}\mathbf{E} = -\frac{1}{\epsilon}\text{grad}\epsilon \cdot \mathbf{E}. \quad (3.9)$$

¹Refractive index variations of the host or background material as a result of nonlinear optical effects (such as the third-order optical Kerr nonlinearity) will be disregarded. Thus, $n_{\text{background}}$ specifies the (passive) static and linear response to applied electromagnetic fields.

The Maxwell curl equations are a set of two coupled first order partial differential equations for the electric and magnetic field quantities. This is equivalent to a decoupled formulation second order for the electric or magnetic field, respectively.

In addition to the time-domain approach, diode laser systems can be characterised in the mode picture, i.e. in frequency domain: We study the passive optical eigenvalue problem, that means $\mathbf{P} = 0$, assume a time-harmonic behaviour $\mathbf{E} \propto \exp(-i\omega t)$ and transform the problem to Fourier space

$$\frac{1}{\epsilon} \nabla \times (\nabla \times \mathbf{E}) = -\frac{1}{\epsilon} \left(\text{grad} \left(\frac{1}{\epsilon} \mathbf{E} \cdot \text{grad} \epsilon \right) + \nabla^2 \mathbf{E} \right) - \frac{\omega^2}{c^2} \mathbf{E} = 0, \quad (3.10)$$

$$\nabla \times \left(\frac{1}{\epsilon} \nabla \times \mathbf{H} \right) = \frac{1}{\epsilon} (\text{grad}(\text{div} \mathbf{H}) - \nabla^2 \mathbf{H}) - \frac{1}{\epsilon^2} (\text{grad} \epsilon) \times (\text{curl} \mathbf{H}) - \frac{\omega^2}{c^2} \mathbf{H} = 0. \quad (3.11)$$

The above linear partial differential equations together with the geometry, $\epsilon(\mathbf{r})$ and correct boundary conditions determine the eigenfrequencies and optical field distributions within the resonator cavity, the so-called stationary cold-cavity modes. In many applications vector $\mathbf{A}(\mathbf{r}, t)$ and scalar Φ electromagnetic potentials are introduced to simplify the solution of the two homogeneous macroscopic Maxwell equations

$$\mathbf{B} = \text{curl} \mathbf{A}, \quad \mathbf{E} = -\text{grad} \Phi - \partial_t \mathbf{A}. \quad (3.12)$$

The arbitrariness in the choice of the potentials connected with the gauge invariance of the physical, that means measurable fields under gauge transformations can be restricted by demanding the transverse Coulomb gauge [69]

$$\text{div} \mathbf{A} = 0, \quad \Phi = 0. \quad (3.13)$$

We attain the following Helmholtz equation for the vector potential

$$\left(\frac{1}{\epsilon} \nabla^2 + \frac{\omega^2}{c^2} \right) \mathbf{A} = 0. \quad (3.14)$$

The full-vectorial wave equation or corresponding Helmholtz eigenvalue problem can be solved by various numerical methods [111]. In the case of metallic boundary conditions or an infinite analysis region (with periodic boundary conditions) we find a complete set of eigenfunctions with real eigenvalues, as we have a linear Hermitian differential operator. The cold-cavity modes represent standing waves or travelling plane waves², respectively. For general dielectric cavities and open boundary conditions the solutions have complex-valued frequencies and therefore lose energy across the boundary of the problem space. The completeness and orthogonality of the solutions cannot be proven.

Different laser models vary in and can be classified on the basis of how the optical fields are described and the level of approximations applied [111], ranging from the full-vectorial wave equation (without any approximations) to simple, spatially not resolved

²More precisely, the stationary solutions in periodic systems can be written as the product of a phase factor (plane wave) with a unit cell-periodic function $\exp(i\mathbf{k} \cdot \mathbf{r}) u_{\mathbf{k}}^{\omega}(\mathbf{r})$ (Bloch theorem [5]).

rate equation approaches (see FIGURE 1.2). In the following sections we will introduce two models: The transverse scalar wave equation model obtained by a paraxial approximation is suitable to the numerical simulation of edge-emitting semiconductor laser and amplifier structures. The full time-domain Maxwell equations, on the other hand, allow us to investigate problems which imply a broad range of relevant frequencies or complex dielectric structures.

3.2 Paraxial Approximation—Transverse Wave Equation

In this section an optical model for a broad area edge-emitting laser or amplifier structure with a simple Fabry-Pérot resonator geometry and a multi-layered dielectric slab waveguide structure is developed. Typical dimensions of such high-power semiconductor devices are: the stripe width of the current contact in the transverse x -direction (around $100\ \mu\text{m}$), the length of the resonator in the propagation z -direction (some $100\ \mu\text{m}$ to several mm), and the height of the zone with embedded active materials in lateral y -direction, that is in the direction of the grown layer structure (around $100\ \mu\text{m}$). The actual waveguide structure is typically a few hundred nm thick [2]. For more details see FIGURE 3.1. The aim of the subsequent considerations is to derive an approximated optical wave equation with source term for such a type of laser configuration and device size. Due to the fact that a simulation of the full-vectorial wave equation is only feasible for micrometer-sized active structures, such as microdisk or microgear lasers [13, 14], we will derive a scalar transverse wave equation applying the paraxial, effective index, rotating wave and slowly varying amplitude approximations.

In symmetric slab optical waveguides with embedded active quantum wells in the core layer and different differential gain coefficients for TE and TM linear polarised light [4], the transverse electric polarisation is normally predominant. We can assume $E_y = 0$. With this approximation, the wave equation (3.8) and transversality condition (3.9) read

$$\partial_x \partial_z E_z - \partial_y^2 E_x - \partial_z^2 E_x + \frac{\epsilon}{c^2} \partial_t^2 E_x + \frac{1}{\epsilon_0 c^2} \partial_t^2 P_x = 0, \quad (3.15)$$

$$\partial_z \partial_x E_x - \partial_y^2 E_z - \partial_x^2 E_z + \frac{\epsilon}{c^2} \partial_t^2 E_z + \frac{1}{\epsilon_0 c^2} \partial_t^2 P_z = 0, \quad (3.16)$$

$$\epsilon_0 \epsilon (\partial_x E_x + \partial_z E_z) + \epsilon_0 (\partial_x \epsilon) E_x + \epsilon_0 (\partial_z \epsilon) E_z + \partial_x P_x + \partial_z P_z = 0. \quad (3.17)$$

In order to gain simple solutions, which serve as basis of an expansion ansatz for solving the equations (3.15)–(3.17), we do not take into account the nonlinear dynamical polarisation and neglect any transverse or longitudinal dielectric structure. Then we get

$$\partial_x \partial_z E_z - \partial_z^2 E_x - \partial_y^2 E_x + \frac{\epsilon(y)}{c^2} \partial_t^2 E_x = 0, \quad (3.18)$$

$$\partial_z \partial_x E_x - \partial_x^2 E_z - \partial_y^2 E_z + \frac{\epsilon(y)}{c^2} \partial_t^2 E_z = 0, \quad (3.19)$$

$$\partial_x E_x + \partial_z E_z = 0. \quad (3.20)$$

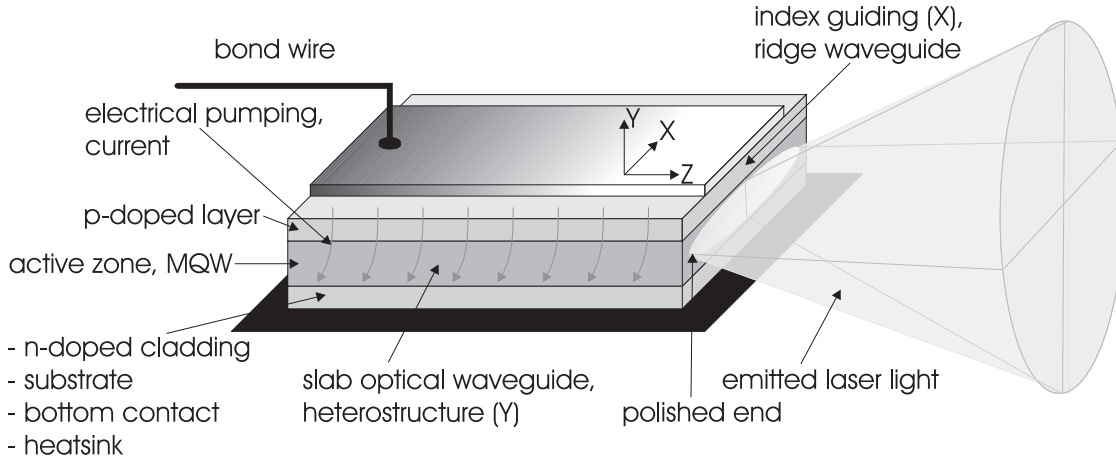


FIGURE 3.1: Semiconductor Fabry-Pérot edge-emitting laser structure: We recognise the optical resonator, a slab waveguiding heterostructure, the active gain medium (in our case semiconductor multi quantum wells), and the electrical carrier pumping mechanism. More complicated contact profiles, e.g. multi-stripe lasers [37, 112] or tapered semiconductor optical amplifiers [106], have been proposed. Novel designs like distributed feedback (DFB) lasers with longitudinal single-mode operation or multi-section lasers [113] have been suggested. These rather large and consequently high-power output devices suffer from poor beam quality, transverse multi-mode behaviour and spatio-temporal instabilities [3, 36]. An expansion of the electric fields in forward and backward travelling plane waves and the subsequent application of the paraxial, slowly varying amplitude and rotating wave approximations are a well justified approach [37]. We investigate the transverse multi-mode dynamics and optical filamentation in broad area edge-emitting lasers in CHAPTER 5, by applying the transverse scalar optical wave equation (3.37).

The solutions of the above system of partial differential equations with periodic boundary conditions are given by transverse electric (TE) plane waves which propagate forward and backward in the longitudinal direction $E_x \propto \exp(\pm i\omega t) \exp(\pm ik_0 n_{\text{eff}} z)$, $E_z = 0$, $\omega = ck_0$. The impact of the lateral optical waveguide structure is accounted for by the introduction of an effective index in the phase velocity term. In the above equations we perform the replacement $(-c^2 \partial_y^2 + \epsilon(y) \partial_t^2) E_{x|z} \rightarrow n_{\text{eff}}^2 \partial_t^2 E_{x|z}$. n_{eff} is the refractive index a travelling plane wave experiences in the layer structure. This approach is called the effective index approximation. It reduces the dynamical problem to a two-dimensional one. For the full problem (3.15)–(3.17) we choose an ansatz that decomposes the electromagnetic fields into slowly varying field amplitudes, and fast-oscillating phase factors which are represented by the above complete set of orthogonal eigenfunctions (related to the eigenfrequencies of the resonator). Furthermore, we assume longitudinal single-mode

operation³, monochromaticity with a positive frequency and obtain

$$E_{x|z}(\mathbf{r}, t; \omega) \rightarrow \tilde{E}_{x|z}(x, z, t)\phi(y)e^{-i\omega t}\zeta(z), \mathbb{R}^3 \times \mathbb{R} \rightarrow \mathbb{C}, \quad (3.21)$$

$$P_{x|z}(\mathbf{r}, t; \omega) \rightarrow P_{x|z}[\tilde{E}_{x|z}](x, z, t)\Theta(y)\phi(y)e^{-i\omega t}\zeta(z). \quad (3.22)$$

The expansion modes in the above product ansatz are specified by spatially delocalised plane waves

$$\zeta(z) = e^{ik_0 n_{\text{eff}} z}, \quad k_0 = \frac{\omega}{c}. \quad (3.23)$$

Effectively, a partial Fourier transformation to frequency and to momentum space has been carried out. In the ansatz (3.22) we have implicitly made a further approximation, the rotating wave approximation (RWA). The total electric field at frequency ω is a superposition of plane waves travelling to the left and to the right with amplitudes $\tilde{E}_{x|z}^{\pm}(x, z, t) \in \mathbb{C}$

$$E_{x|z}(\mathbf{r}, t; \omega) = \phi(y) \cdot \frac{1}{2} \left[e^{-i\omega t} (\tilde{E}_{x|z}^+ \zeta(z) + \tilde{E}_{x|z}^- \zeta^*(z)) + \text{conjugate complex} \right]. \quad (3.24)$$

To evaluate the material functional $\mathbf{P}[\mathbf{E}]$, counter-rotating parts and terms with phase factors which oscillate with multiples of the phase factor of the electric field amplitude are neglected. Mathematically speaking

$$\mathbf{P}[\mathbf{E}] \rightarrow \tilde{P}_{x|z}^+(x, z, t)\Theta(y)\phi(y)e^{-i\omega t}\zeta(z), \quad \tilde{P}_{x|z}^-(x, z, t) \approx P_{x|z}[\tilde{E}_{x|z}^+](x, z, t). \quad (3.25)$$

The function $\phi(y)$ records the stationary lateral field profile, which is determined by the slab optical waveguide and refractive index structure in y -direction. $\Theta(y)$ filters out the active layers. That means, the quantity is one at the position of the quantum wells, the areas where the optical field is amplified by stimulated emission, and zero for all other layers.

Additionally, a smallness parameter $f \ll 1$ is introduced as a measure to quantify the deviations from a plane wave solution, which is an eigenfunction of the passive problem in an infinite slab optical waveguide. The consistent expansion of the electric and polarisation field amplitudes in this parameter reads

$$\tilde{E}_{x|z}(x, z, t) = f^0 E_{x|z}^{(0)} + f^1 E_{x|z}^{(1)} + f^2 E_{x|z}^{(2)} + \dots, \quad (3.26)$$

$$\tilde{P}_{x|z}(x, z, t) = f^2 \cdot (f^0 P_{x|z}^{(0)} + f^1 P_{x|z}^{(1)} + f^2 P_{x|z}^{(2)} + \dots). \quad (3.27)$$

This results in an infinite hierarchy of coupled wave equations for the transverse and longitudinal field components. The paraxial approximation, based on the separation of time and length scales together with the consistent expansion ansatz, represents a systematic method to truncate this hierarchy and to decouple the transverse from the longitudinal problem. In lowest order, a closed equation for the transverse field dynamics

³This is achieved in DFB or DBR laser diodes by an additional periodic grating structure.

will be obtained. The usual paraxial approach [114] considers the propagation of a light beam with a Gaussian profile of width w , and introduces a characteristic longitudinal length of diffraction $l = k_0 n_{\text{eff}} w^2$ and a characteristic propagation time $t = l n_{\text{eff}} / c$. The expansion parameter is the ratio $w/l = 1/(k_0 n_{\text{eff}} w) \ll 1$, and we associate the various terms in the wave equation with different powers of f : The electric field amplitude as envelope of a wave packet starts with power f^0 . The derivation ∂_x of field amplitudes are considered to be order f^1 , and the derivations ∂_z, ∂_t of field amplitudes are associated with f^2 . The amplitudes are assumed to vary little on the time scale of the period of one optical cycle and on the length scale of the wavelength of the longitudinal mode. Variations in transverse direction are one order higher, but still smaller than the fast-oscillating phase factors. This type of slowly varying amplitude approximation (SVAA) capitalises on the separation of the time and length scales of the slow amplitude and fast phase dynamics

$$|\partial_t \tilde{E}_{x|z}| \ll |\omega \tilde{E}_{x|z}|, \quad |\partial_z \tilde{E}_{x|z}| \ll |k_0 n_{\text{eff}} \tilde{E}_{x|z}|. \quad (3.28)$$

In the limit $f \rightarrow 0$ or in the order $\mathcal{O}(f^0)$ travelling plane waves have to fulfil the system of wave equation (3.15)+(3.16) and the auxiliary divergence-free condition (3.17). This justifies to start the expansion of the polarisation (3.27) with f^2 . In addition, we impose the following ansatz for the dielectric constant, which is a sum of contributions only dependent on a single coordinate

$$\epsilon(x, y, z) \approx \epsilon(y) + f^2 \epsilon(x) \approx (n(y) + \delta n_{\text{pas}}(x))^2 \approx \epsilon(y) + f^2 2n(y) \delta n_{\text{pas}}(x). \quad (3.29)$$

We apply the paraxial approximation and insert the above expansions into the equations (3.15)–(3.17), and obtain for the transverse part up to the order $\mathcal{O}(f^3)$

$$\begin{aligned} \mathcal{O}(f^0) : 0 &= -E_x^{(0)} \frac{\partial_y^2 \phi}{\phi} + k_0^2 n_{\text{eff}}^2 E_x^{(0)} - \frac{\epsilon(y)}{c^2} \omega^2 E_x^{(0)} \\ \mathcal{O}(f^1) : &+ ik_0 n_{\text{eff}} \partial_x E_z^{(0)} - E_x^{(1)} \frac{\partial_y^2 \phi}{\phi} + k_0^2 n_{\text{eff}}^2 E_x^{(1)} - \frac{\epsilon(y)}{c^2} \omega^2 E_x^{(1)} \\ \mathcal{O}(f^2) : &+ ik_0 n_{\text{eff}} \partial_x E_z^{(1)} - E_x^{(2)} \frac{\partial_y^2 \phi}{\phi} + k_0^2 n_{\text{eff}}^2 E_x^{(2)} - i2k_0 n_{\text{eff}} \partial_z E_x^{(0)} - \frac{\epsilon(y)}{c^2} \omega^2 E_x^{(2)} \\ \mathcal{O}(f^2) : &- \frac{\epsilon(y)}{c^2} i2\omega \partial_t E_x^{(0)} - \frac{\epsilon(x)}{c^2} \omega^2 E_x^{(0)} - \frac{1}{\epsilon_0 c^2} \omega^2 P_x^{(0)} \Theta(y) \\ \mathcal{O}(f^3) : &+ ik_0 n_{\text{eff}} \partial_x E_z^{(2)} + \partial_x \partial_z E_z^{(0)} - E_x^{(3)} \frac{\partial_y^2 \phi}{\phi} + k_0^2 n_{\text{eff}}^2 E_x^{(3)} - i2k_0 n_{\text{eff}} \partial_z E_x^{(1)} \\ \mathcal{O}(f^3) : &- \frac{\epsilon(y)}{c^2} \omega^2 E_x^{(3)} - \frac{\epsilon(y)}{c^2} i2\omega \partial_t E_x^{(1)} - \frac{\epsilon(x)}{c^2} \omega^2 E_x^{(1)} - \frac{1}{\epsilon_0 c^2} \omega^2 P_x^{(1)} \Theta(y), \end{aligned} \quad (3.30)$$

and for the longitudinal part of the wave equation

$$\begin{aligned}
\mathcal{O}(f^0) : 0 &= -E_z^{(0)} \frac{\partial_y^2 \phi}{\phi} - \frac{\epsilon(y)}{c^2} \omega^2 E_z^{(0)} \\
\mathcal{O}(f^1) : &+ ik_0 n_{\text{eff}} \partial_x E_x^{(0)} - E_z^{(1)} \frac{\partial_y^2 \phi}{\phi} - \frac{\epsilon(y)}{c^2} \omega^2 E_z^{(1)} \\
\mathcal{O}(f^2) : &+ ik_0 n_{\text{eff}} \partial_x E_x^{(1)} - E_z^{(2)} \frac{\partial_y^2 \phi}{\phi} - \partial_x^2 E_z^{(0)} - \frac{\epsilon(y)}{c^2} \omega^2 E_z^{(2)} - \frac{\epsilon(y)}{c^2} i2\omega \partial_t E_z^{(0)} \\
\mathcal{O}(f^2) : &- \frac{\epsilon(x)}{c^2} \omega^2 E_z^{(0)} - \frac{1}{\epsilon_0 c^2} \omega^2 P_z^{(0)} \Theta(y) \\
\mathcal{O}(f^3) : &+ ik_0 n_{\text{eff}} \partial_x E_x^{(2)} + \partial_z \partial_x E_x^{(0)} - E_z^{(3)} \frac{\partial_y^2 \phi}{\phi} - \partial_x^2 E_z^{(1)} - \frac{\epsilon(y)}{c^2} \omega^2 E_z^{(3)} \\
\mathcal{O}(f^3) : &- \frac{\epsilon(y)}{c^2} i2\omega \partial_t E_z^{(1)} - \frac{\epsilon(x)}{c^2} \omega^2 E_z^{(1)} - \frac{1}{\epsilon_0 c^2} \omega^2 P_z^{(1)} \Theta(y). \tag{3.31}
\end{aligned}$$

The auxiliary transversality condition $\text{div} \mathbf{D} = 0$ (3.17) gives

$$\begin{aligned}
\mathcal{O}(f^0) : 0 &= \epsilon(y) ik_0 n_{\text{eff}} E_z^{(0)} \\
\mathcal{O}(f^1) : &+ \epsilon(y) \partial_x E_x^{(0)} + \epsilon(y) ik_0 n_{\text{eff}} E_z^{(1)} \\
\mathcal{O}(f^2) : &+ \epsilon(y) \partial_x E_x^{(1)} + \epsilon(y) ik_0 n_{\text{eff}} E_z^{(2)} + \epsilon(y) \partial_z E_z^{(0)} + \epsilon(x) ik_0 n_{\text{eff}} E_z^{(0)} \\
\mathcal{O}(f^2) : &+ (\partial_x \epsilon(x)) E_x^{(0)} + \frac{1}{\epsilon_0} ik_0 n_{\text{eff}} P_z^{(0)} \Theta(y) \\
\mathcal{O}(f^3) : &+ \epsilon(y) \partial_x E_x^{(2)} + \epsilon(x) \partial_x E_x^{(0)} + \epsilon(y) ik_0 n_{\text{eff}} E_z^{(3)} + \epsilon(y) \partial_z E_z^{(1)} + \epsilon(x) ik_0 n_{\text{eff}} E_z^{(1)} \\
\mathcal{O}(f^3) : &+ (\partial_x \epsilon(x)) E_x^{(1)} + \frac{1}{\epsilon_0} \partial_x P_x^{(0)} \Theta(y) + \frac{1}{\epsilon_0} ik_0 n_{\text{eff}} P_z^{(1)} \Theta(y). \tag{3.32}
\end{aligned}$$

In order $\mathcal{O}(f^0)$ we extract a one-dimensional eigenvalue problem with the eigenvalues n_{eff} and eigensolutions $\phi(y)$

$$\left[\frac{\partial_y^2 \phi(y)}{\phi(y)} + k_0^2 (\epsilon(y) - n_{\text{eff}}^2) \right] = 0. \tag{3.33}$$

Assuming that the refractive index of the active core zone is higher than the one of the surrounding cladding layers, $n_{\text{act}} > n_{\text{eff}} > n_{\text{cl}}$, the solution of the above eigenvalue problem describes a concentration of the electric field amplitude onto the active semiconductor layers due to optical guiding by total internal reflection. A simple double heterostructure with a thickness d_{act} of the active zone confines both the optical mode and the charge carriers to the same layer. The smallest eigenvalue is determined by the characteristic equation $\sqrt{n_{\text{act}}^2 - n_{\text{eff}}^2} \tan(k_0 d_{\text{act}} / 2 \sqrt{n_{\text{act}}^2 - n_{\text{eff}}^2}) - \sqrt{n_{\text{eff}}^2 - n_{\text{cl}}^2} = 0$. The related eigenfunction $\phi(y)$ within the active layer is given by $\cos(k_0 \sqrt{n_{\text{act}}^2 - n_{\text{eff}}^2} y)$, and the exponential decaying fields in the cladding layers by $\exp(-k_0 \sqrt{n_{\text{eff}}^2 - n_{\text{cl}}^2} (|y| - d_{\text{act}}/2))$. Considering the carrier confinement, the reduction of the thickness of the active layer

and of the width of the quantum wells appears advantageous in order to improve device performance parameters, e.g. lower the lasing threshold. This, however, reduces the coupling of the gain medium to the optical mode as quantified by the confinement factor Γ_y of the optical waveguide, which will be defined later on. Due the fact that the optical confinement is associated with a length scale of the magnitude of the optical wavelength, and the carrier quantum confinement with the nanometer scale, more complicated heterostructures, e.g. the separate confinement heterostructure and large optical cavity configuration, have been proposed. This allows the optical confinement to be separated from the quantum confinement of the active laser centres (see FIGURE 2.2). It is possible to generalise the eigenvalue problem to more spatial dimensions. As long as an ansatz $\epsilon(x, y, z) \approx \epsilon(x) + \epsilon(y) + \epsilon(z)$ is reasonable, a product of one-dimensional confinement eigenfunctions will be the solution. With the split-off of the stationary lateral mode profile, the dynamical problem is reduced to an effective two-dimensional one in (x, z) . The lateral layer structure is accounted for by an effective refractive index n_{eff} and a lateral confinement factor Γ_y . The amplitude $E_x^{(0)}$ is still undetermined, and we set $E_z^{(0)} = 0$. This exactly corresponds to the situation of a TE linear polarised plane wave propagating in z -direction as required in the $f \rightarrow 0$ limit.

An evaluation of the series expansion in order $\mathcal{O}(f^1)$ couples transverse with longitudinal field components

$$\partial_x E_x^{(0)} + ik_0 n_{\text{eff}} E_z^{(1)} = 0. \quad (3.34)$$

$E_x^{(1)}$ remains undetermined. In the next order we are able to derive a closed equation for the transverse field dynamics. The transverse part of the wave equation in $\mathcal{O}(f^2)$ is then given by

$$ik_0 n_{\text{eff}} \partial_x E_z^{(1)} \phi(y) - \left(i2k_0 n_{\text{eff}} \partial_z + i \frac{2\epsilon(y)k_0}{c} \partial_t + \epsilon(x)k_0^2 \right) E_x^{(0)} \phi(y) = \frac{k_0^2}{\epsilon_0} P_x^{(0)} \Theta(y) \phi(y). \quad (3.35)$$

By multiplying this equation with $\int_{-\infty}^{\infty} dy \phi(y)$ and integrating over the lateral direction, the lateral confinement factor Γ_y appears

$$\Gamma_y = \frac{\int_{-\infty}^{\infty} dy \Theta(y) |\phi(y)|^2}{\int_{-\infty}^{\infty} dy |\phi(y)|^2}. \quad (3.36)$$

Γ_y is a measure for the overlap of the optical mode or confinement function $\phi(y)$ with the active zone, which is the region where the electromagnetic field is amplified or absorbed. We employ the coupling of the longitudinal with the transverse field components (3.34) and can truncate the infinite hierarchy of the coupled wave equations. We introduce the notations $\tilde{E} = E_x^{(0)}$ and $\tilde{P} = P_x^{(0)}$. The transverse wave equation for the forward and backward propagating fields, in paraxial approximation, for a longitudinal single-mode edge-emitting laser structure may now be expressed by

$$\left(\frac{n^2}{cn_{\text{eff}}} \partial_t \pm \partial_z - i \frac{1}{2k_0 n_{\text{eff}}} \partial_x^2 - ik_0 \frac{n}{n_{\text{eff}}} \delta n_{\text{pas}}(x) \right) \tilde{E}^{\pm}(x, z, t) = i \frac{k_0 \Gamma_y}{\epsilon_0 2n_{\text{eff}}} \frac{N_{\text{QW}}}{L_{\text{ref}}} \tilde{P}^{\pm}(x, z, t). \quad (3.37)$$

The coupling to the active medium has been redefined $\Gamma_y \tilde{P}^\pm \rightarrow \Gamma_y N_{\text{QW}}/L_{\text{ref}} \tilde{P}^\pm$ (see FIGURE 2.6). The field amplitudes are defined as complex-valued quantities ($\mathbb{R}^2 \times \mathbb{R} \rightarrow \mathbb{C}$). To sum up, the above partial differential equation (3.37) describes the temporal evolution, propagation and diffraction of a transverse electric field amplitude \tilde{E} , with a possible ridge waveguide structure in transverse direction, and driven by the nonlinear dynamical induced electric polarisation \tilde{P} . A typical value for the refractive index-guiding profile is $\delta n_{\text{pas}}(x) \approx 0.003$. Although small, this quantity has a strong influence on the stability and transverse mode dynamics. The transverse mode profile is not only determined by the transverse waveguide structure but also by the carrier pump profile (gain-guiding) [2], see equation (5.3). The carried out approximations to derive the above paraxial wave equation (3.37) impose some limits on this model: The assumption of plane wave expansion functions as solution of the passive optical problem and the application of the slowly varying amplitude and rotating wave approximations are contradictory to the longitudinal multi-mode operation, micrometer-sized active devices, or ultrashort (sub-picosecond) pulse propagation.

A solution of (3.37) requires the specification of initial conditions and of boundary conditions, for example the reflection of the optical fields at the facets of the resonator

$$\tilde{E}^+(0) = \sqrt{R_l} \tilde{E}^-(0), \quad (3.38)$$

$$\tilde{E}^-(L) = \sqrt{R_r} \tilde{E}^+(L). \quad (3.39)$$

L denotes the length of the cavity, R_l and R_r are the intensity reflectivities of the resonator structure. One may apply a further approximation called the mean-field approximation [115] by introducing averaged field amplitudes within the cavity. The longitudinal averaged field amplitudes are then defined by

$$\tilde{E}(x, t) = \langle \tilde{E}^\pm(x, z, t) \rangle_z = \frac{1}{L} \int_0^L dz |\zeta(z)|^2 \tilde{E}^\pm(x, z, t) \rightarrow \frac{1}{L} \int_0^L dz \tilde{E}^\pm(x, z, t). \quad (3.40)$$

The longitudinal resonator structure has been taken into account by introducing a spatially averaged decay term

$$\pm \partial_z \tilde{E}^\pm(x, z, t) \rightarrow \gamma_{\text{resonator}} \tilde{E}(x, t), \quad \gamma_{\text{resonator}} = -\frac{\ln(\sqrt{R_l R_r})}{2L}. \quad (3.41)$$

A longitudinal confinement factor $\Gamma_z = \Gamma_r \mathcal{V}_z$ as well as a filling factor $\mathcal{V}_z = \int_0^L dz \Theta(z)/L$ ($\mathcal{V}_z = L_{\text{act}}/L$) express the longitudinal overlap between field and active gain sections.

3.3 Full Time-Domain Maxwell Equations

In the last section we have derived a model that is suitable to describe the transverse multi-mode dynamics in a longitudinal single-mode high-power broad area laser or amplifier structure. In this section we aim to derive an optical model which allows us to

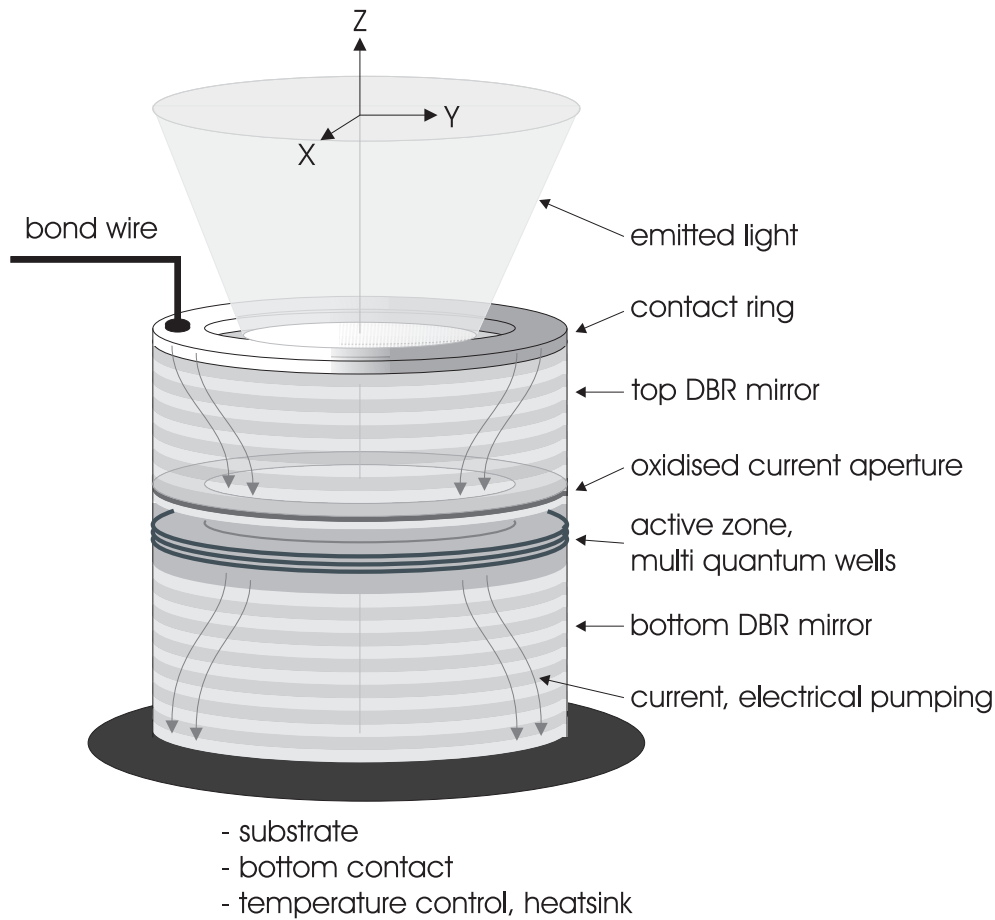


FIGURE 3.2: Simplified schematic (from [12]) of a vertical cavity surface-emitting laser (VCSEL): VCSEL are engineered by sandwiching active optical gain elements, such as semiconductor multi quantum wells, between highly reflecting dielectric multi-layered structures, so-called distributed Bragg reflectors (DBR). This laser structure may also be characterised as a one-dimensional photonic crystal [20] with a $n \cdot \lambda/2, n \in \mathbb{N}$, defect cavity. Advantages of this design are the circular output beams (easy in-coupling of optical signals into fibres), low divergence, longitudinal single-mode operation (one strong localised laser or defect mode), and the relatively inexpensive manufacturing costs. The compact size of these devices and the small lengths of the gain or amplification regions cause the rather low-power output of some mW and explain the importance of spontaneous emission as additive process [11, 108]. From a modelling point of view, the sub-wavelength refractive index structures and the discrepancy of the defect (cold-cavity) or laser mode from the delocalised plane wave assumption of the previous section demand for a modification of the paraxial wave model [12] and the development of novel approaches, such as models based on the full time-domain Maxwell equations. VCSEL devices with periodically structured defects are investigated in SECTION 6.1.

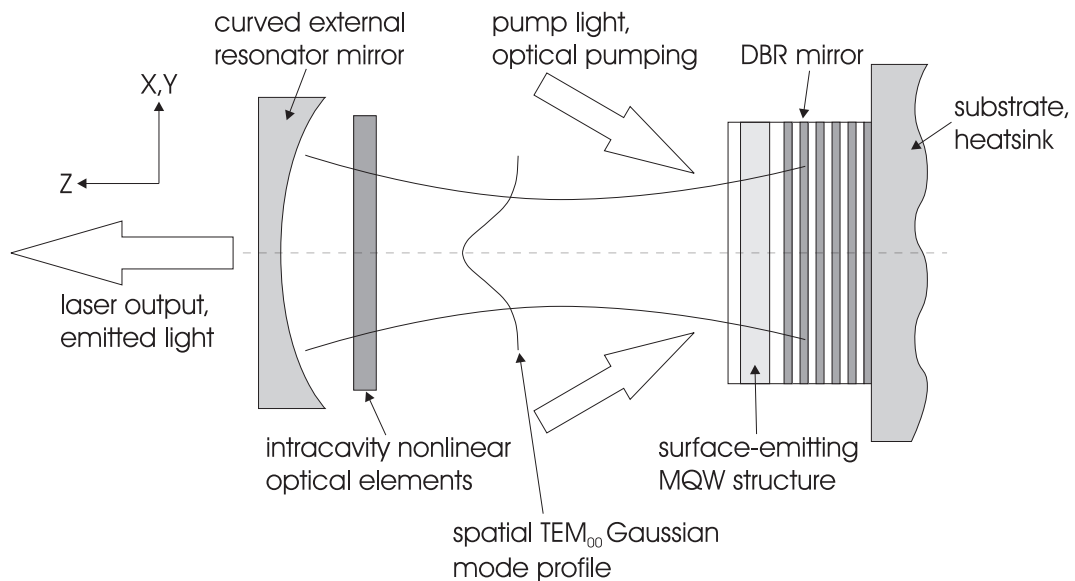


FIGURE 3.3: Vertical external cavity surface-emitting laser structure (VECSEL): One Bragg mirror stack of a VCSEL is replaced by an external resonator [16]. The structure is optically pumped (no doping required). The aim is to combine the near-diffraction-limited beam quality of a VCSEL with the scalability to a high-power output laser device in continuous wave operation [17]. Moreover, the possibility to place additional nonlinear elements into the external cavity configuration, e.g. semiconductor saturable absorber mirrors (SESAM) for passive mode-locking [32, 116], or nonlinear crystals for frequency conversion, is attractive. Starting from the three-dimensional full-vectorial Maxwell equations, we focus on the longitudinal propagation direction and assume stationary profiles in the perpendicular directions. The curved mirror results in a highly preferred transverse TEM_{00} beam profile. The spatio-temporal dynamics of the electromagnetic fields can thus be qualified by the Maxwell curl equations in one dimension. The other directions are effectively included via confinement factors $\Gamma_{x,y}(z)$, which are the overlap integrals of the transverse mode profiles with the active media, and by loss terms. Optically pumped VECSEL are explored in SECTION 6.2.

consider problems or devices which are characterised by a very broad range of relevant frequencies, longitudinal multi-mode behaviour, and spatially strong localised cold-cavity modes as typical for nanometer- or micrometer-sized cavities [13, 14] or refractive index structures [77, 117]. Examples of such active structures are vertical (external) cavity surface-emitting lasers (FIGURE 3.2 and FIGURE 3.3). It is obvious that approximations like the rotating wave or the slowly varying amplitude approximation can no longer be applied as these assumptions are only correct for a small spectral range around a central frequency. A model based on the two Maxwell curl equations and the material response (3.5) allows us to explore characteristics of novel laser structures such as vertical extended cavity surface emitting lasers (VECSEL), or processes of femtosecond pulse propagation, reshaping and generation in semiconductor structures. The layer or refractive index structure $\epsilon(z)$ is an important factor in such problems and will be

taken into consideration without any approximations. For devices with simple geometry, the influence of the two perpendicular directions can be disregarded in the dynamical interplay of the various longitudinal frequency components. Thus, we can reduce our dynamical problem to sets of coupled differential equations with one spatial degree of freedom, the longitudinal propagation z -direction. For the optical fields ($\mathbb{R} \times \mathbb{R} \rightarrow \mathbb{R}^2$) we obtain from (3.1)–(3.4)

$$\partial_z E_x + \partial_t B_y = 0, \quad (3.42)$$

$$\frac{1}{\mu_0} \partial_z B_y + \partial_t D_x = 0; \quad (3.43)$$

$$\partial_z E_y - \partial_t B_x = 0, \quad (3.44)$$

$$\frac{1}{\mu_0} \partial_z B_x - \partial_t D_y = 0. \quad (3.45)$$

The material response is given by

$$\mathbf{D}(z, t) = \epsilon_0 \epsilon(z) \mathbf{E}(z, t) + \Gamma_{x,y}(z) \frac{N_{\text{QW}}(z)}{L_{\text{ref}}} \mathbf{P}(z, t). \quad (3.46)$$

The two Maxwell div equations are satisfied with the assumption of transverse polarisation. In the case of linear polarised light we can identify two decoupled subsets $(E_x|D_x|P_x, B_y)$ and $(E_y|D_y|P_y, B_x)$. Indeed, in configurations with a pronounced propagation direction and with a rotational symmetry in the perpendicular plane, a formulation in left and right circular polarised optical fields⁴ is much more adapted [118]. Typically absorbing boundary conditions are used. This means, that at the boundary of the spatial region of interest there should be no reflection of an out-going wave. Mur suggested a simple scheme for such boundary conditions [111, 119]. For more details see the APPENDIX A.

In summary, the one-dimensional equations (3.42)–(3.46) are, in contrast to the paraxial transverse wave equation, formulated using real-valued variables. Thus, the electric polarisation, which describes the dynamical response of the gain material, has to be transformed to a formulation in \mathbb{R} (see SECTION 2.5). The presented model links a very comprehensive mapping of the optoelectronic properties of the semiconductor gain medium, e.g. the asymmetric gain spectra and a diversity of optical nonlinearities, with a description of the sub-wavelength passive structure and the optical fields including the fast-oscillating carrier wave. The approach is valid for a huge spectral range, however, due to computational effort, the model is limited to micrometer-sized active devices.

3.4 Conclusion

The propagation, diffraction and reflection of electromagnetic fields inside laser devices can be either modelled by the use of the macroscopic Maxwell curl equations or by some

⁴We can generate these fields by superposing the two linear polarised field components of equal amplitude with a constant relative phase shift of $\pm\pi/2$. This is only possible for a single frequency.

derived approximated wave equations. The induced macroscopic polarisation acts as source term of the laser fields (see CHAPTER 2). In this chapter we have developed two different models to account for the optical problem: Applying the slowly varying amplitude, rotating wave and effective index approximations, and utilising the separation of time and length scales together with a consistent expansion ansatz (paraxial approximation), a transverse scalar wave equation model has been obtained. This model is suitable to the numerical simulation of high-power and large area edge-emitting semiconductor laser and amplifier structures. A second model based on the full time-domain Maxwell curl equations is a full-vectorial wave equation model. It allows us to study problems which imply a very broad range of relevant frequencies or spatially strong localised laser modes. However, this approach is limited to micrometer-sized active devices. To our knowledge, a model combining the Maxwell curl equations with a band-resolved description of the semiconductor gain dynamics within the finite-difference time-domain framework has not been reported and implemented before.

4 Semiconductor Laser Fundamentals

4.1 Calculation of Scattering Rates

4.1.1 Microscopic Scattering Rates in Semiconductor Quantum Wells

The screened Coulomb interaction between the charge carriers and the coupling of the carriers to the various quantised modes or excitations of the lattice (phonons) are two of the relevant scattering processes for semiconductor two-component plasmas. A microscopic approach is based on the generalised quantum Boltzmann collision integrals (2.83)+(2.86) in second Born approximation, which takes into account out-scattering as well as in-scattering contributions [4]

$$\begin{aligned} \partial_t n_{ii,\mathbf{k}}^e \Big|_{\text{relax}} &= -2\Gamma_{ii,\mathbf{k}}^{ee,\text{out}} \{n_{\mathbf{k}}^o\} n_{ii,\mathbf{k}}^e + 2\Gamma_{ii,\mathbf{k}}^{ee,\text{in}} \{n_{\mathbf{k}}^o\} (1 - n_{ii,\mathbf{k}}^e) \\ &= -2 \left(\Gamma_{ii,\mathbf{k}}^{ee,\text{out}} \{n_{\mathbf{k}}^o\} + \Gamma_{ii,\mathbf{k}}^{ee,\text{in}} \{n_{\mathbf{k}}^o\} \right) n_{ii,\mathbf{k}}^e + 2\Gamma_{ii,\mathbf{k}}^{ee,\text{in}} \{n_{\mathbf{k}}^o\} \end{aligned} \quad (4.1)$$

$$\begin{aligned} &\approx -\gamma_{ii,\mathbf{k}}^e \{f_{\mathbf{k}}^o\} (n_{ii,\mathbf{k}}^e - f_{ii,\mathbf{k}}^e) \approx -\gamma_{ii,\mathbf{k}}^{e(\text{ph})} \{f_{\mathbf{k}}^e, n_{\text{ph}}\} (n_{ii,\mathbf{k}}^e - f_{ii,\mathbf{k}}^e(T_{\text{lat}})) \\ &\quad - \gamma_{ii,\mathbf{k}}^{ee(\text{cc})} \{f_{\mathbf{k}}^e\} (n_{ii,\mathbf{k}}^e - f_{ii,\mathbf{k}}^e(T_{\text{pl}}^e)) - \gamma_{ii,\mathbf{k}}^{eh(\text{cc})} \{f_{\mathbf{k}}^o\} (n_{ii,\mathbf{k}}^e - f_{ii,\mathbf{k}}^e(T_{\text{pl}}^h)), \end{aligned} \quad (4.2)$$

$$\begin{aligned} \partial_t p_{ji,\mathbf{k}} \Big|_{\text{relax}} &\approx - \left(\Gamma_{ii,\mathbf{k}}^{ee,\text{out}} \{f_{\mathbf{k}}^o\} + \Gamma_{ii,\mathbf{k}}^{ee,\text{in}} \{f_{\mathbf{k}}^o\} + \Gamma_{jj,\mathbf{k}}^{hh,\text{out}} \{f_{\mathbf{k}}^o\} + \Gamma_{jj,\mathbf{k}}^{hh,\text{in}} \{f_{\mathbf{k}}^o\} \right) p_{ji,\mathbf{k}} \\ &= -\gamma_{ij,\mathbf{k}}^p \{f_{\mathbf{k}}^o\} p_{ji,\mathbf{k}} = -\frac{\gamma_{ii,\mathbf{k}}^e \{f_{\mathbf{k}}^o\} + \gamma_{jj,\mathbf{k}}^h \{f_{\mathbf{k}}^o\}}{2} p_{ji,\mathbf{k}}. \end{aligned} \quad (4.3)$$

The above equations and the definitions of the scattering matrices (2.84)+(2.85) and (2.87)+(2.88) [51, 64] reflect the highly complex and nonlinear dependence of the microscopically calculated relaxation rates on the carrier distribution functions. For more details see SECTION 2.8. Here, individual scattering processes are analysed and in the summation the single interaction process is weighted with the appropriate measure, e.g. scattering with small momentum transfer is favoured. This is in contrast to the simple approach of phenomenologically defined scattering times, which is associated with the concepts of baths and reservoirs to describe the exponential relaxation of a system [4]. Semiconductor-based gain materials incorporate a hierarchy of carrier relaxation times, which may cause a loss of coherence. Slower relaxation times are connected with recombination and loss channels of the macroscopic carrier density, but the carrier-carrier scattering is the most dominant mechanism [120] responsible for the dephasing of the interband polarisation (4.3).

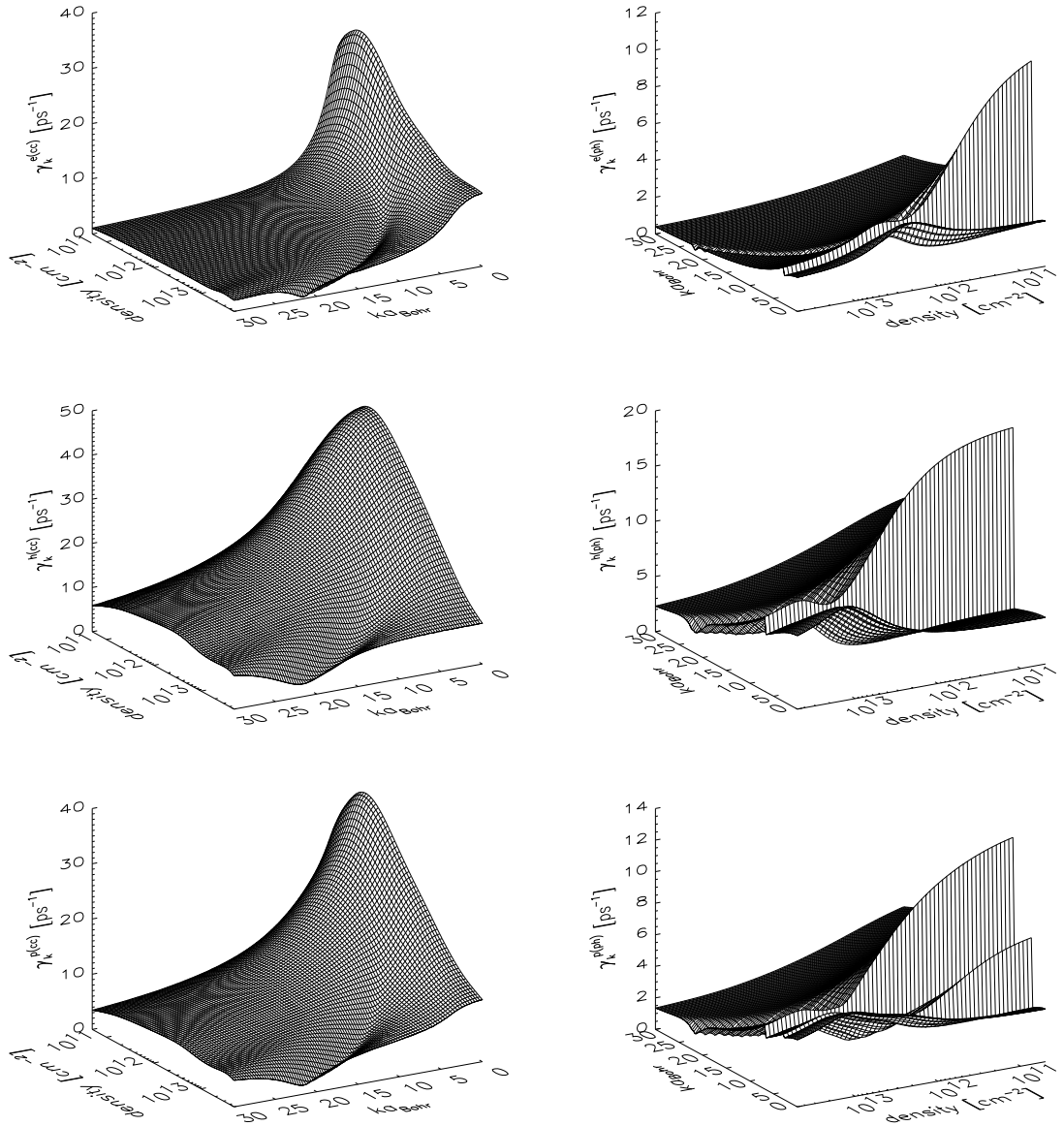


FIGURE 4.1: Calculated momentum relaxation rates of the electron (top) and hole (middle) distribution functions and dephasing rates of the interband polarisation (bottom) versus the carrier sheet density $N \in [5 \cdot 10^{10} \text{ cm}^{-2}, 5 \cdot 10^{13} \text{ cm}^{-2}]$ and the carrier momentum vector $k \cdot a_{\text{Bohr}} \in [0, 30]$. Depicted are the scattering rates due to the carrier-carrier, screened Coulomb interaction (left column) and for the Fröhlich interaction with longitudinal optical phonons (right column). The dielectric function is specified by the Lindhard formula (2.94) in the effective plasmon pole approximation (2.97)+(2.98).

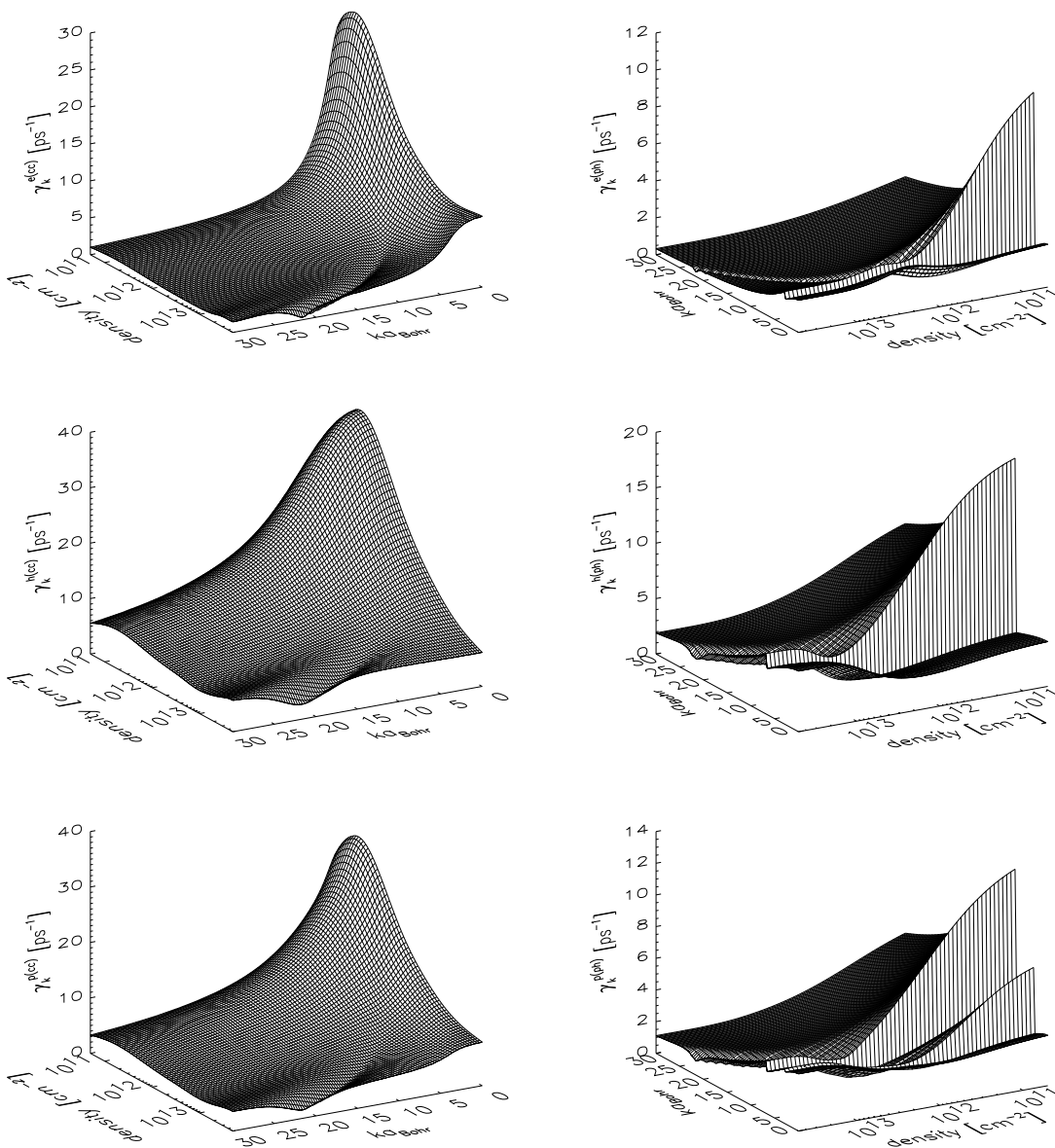


FIGURE 4.2: Same as FIGURE 4.1, but applying the simple, free-carrier dispersion model (2.96) to consider plasma screening.

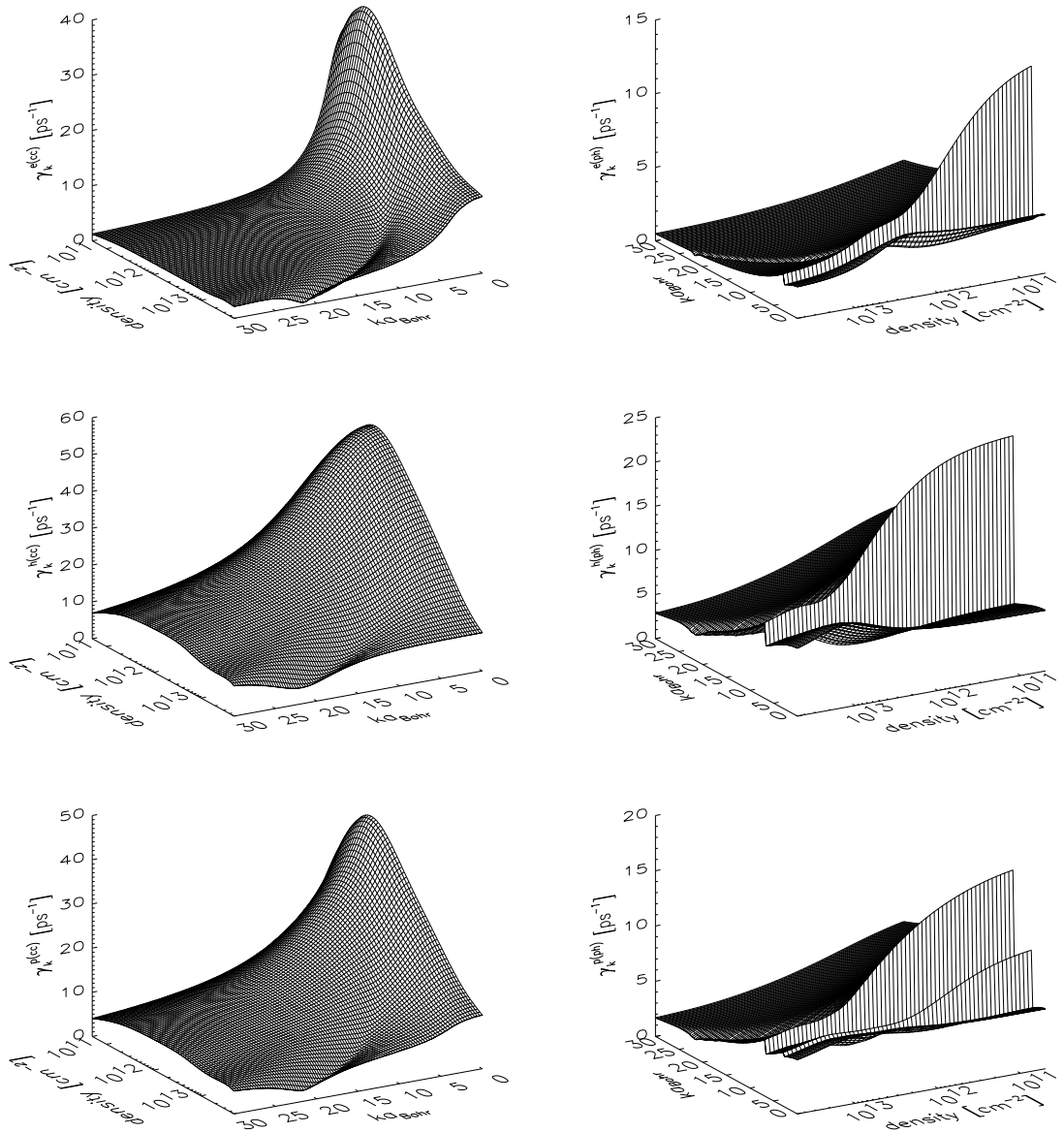


FIGURE 4.3: Same as FIGURE 4.1, but the temperature $T = T_{\text{pl}} = T_{\text{l-o}} = T_{\text{lat}}$ has been increased from 300 K to 400 K. Microscopic scattering rates reveal complex functional dependencies on (k, N, T) .

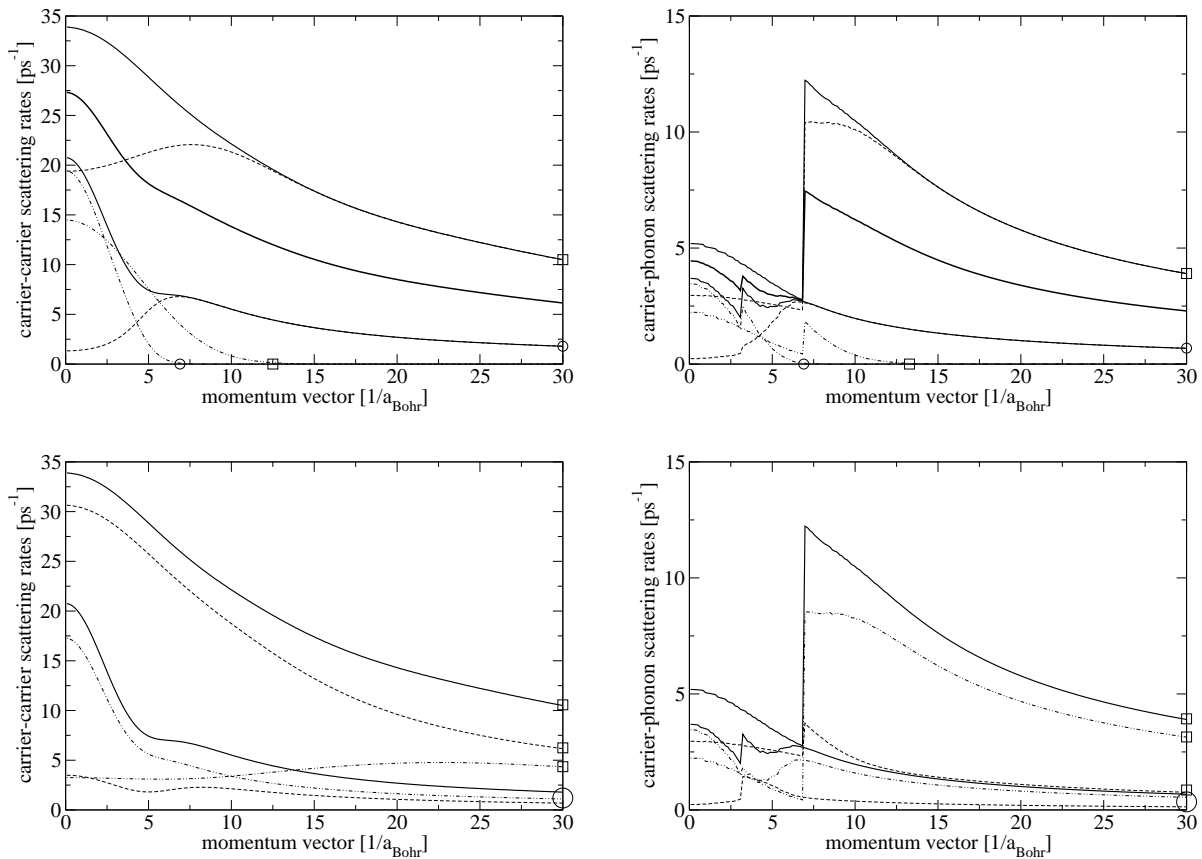


FIGURE 4.4: The graphs give a more detailed picture of the various contributions to the carrier-carrier (left) and carrier-phonon (right) scattering rates at $T = 300 \text{ K}$ and a density of $N = 2 \cdot 10^{12} \text{ cm}^{-2}$ (screening model as in FIGURE 4.1) of the electron (circle) and hole (square) distribution functions and the interband polarisation (top graphs, no symbol). (Top) For higher q the out-scattering processes (dashed lines) are more significant than the in-scattering contributions (dot-dashed). (Bottom left) We compare electron-electron and hole-hole scattering (dashed) with electron-hole interactions (dot-dashed lines). (Bottom right) Carrier-phonon scattering under absorption (dashed) and emission (dot-dashed) of a longitudinal optical phonon with $\hbar\omega_{\text{LO}} = 36 \text{ meV}$.

Due to the computational effort involved in the calculation of correlation contributions, the evaluation of scattering integrals together with a spatially resolved modelling of laser structures on a time window of several nanoseconds is not feasible. Instead, we evaluate the scattering matrices with quasi-equilibrium distribution functions $\{f_{\mathbf{k}}^{\circ}, n_{\text{ph}}\}$, compute the characterising relaxation rates (see (4.2)+(4.3)) for various parameter sets $\gamma_{\mathbf{k}}(N, T_{\text{pl}}, T_{\text{lat}})$, and use these precalculated values in the time-domain simulations. This approach of lookup tables [36, 53] is extended and modified to describe multi-subband quantum well structures [107]. In quantum confined structures the effective rates also depend on structural parameters. The relaxation rate approximation neglects scattering mediated by polarisation terms and applies a linearisation (see (4.2)+(4.3)) around the quasi-equilibrium state using the principle of detailed balance. This approach is sufficiently accurate, as long as the electromagnetic fields are not too strong, and scattering processes are studied on time scales longer than a characteristic relaxation time.

FIGURES 4.1–4.4 show results of the calculation of the scattering rates for a GaAs quantum well of 5 nm width (single-subband case). For every parameter tuple (k, N) , the scattering matrices (2.84)+(2.85) and (2.87)+(2.88), respectively, are calculated for each individual scattering process, and subsequently the summation over all possible processes is evaluated. The sharp structures in the graphs of the scattering rates due to the interaction of carriers with longitudinal optical phonons are induced by the onset of the possibility of out-scattering processes associated with the emission of a phonon (or in-scattering processes under absorption of a phonon). The threshold conditions are given by $k \geq \sqrt{2m/\hbar^2} \cdot \hbar\omega_{\text{LO}}$ and thus dependent on the mass of the scattered particles. As can be clearly seen, the dephasing rates of the interband polarisation correspond to the average values of the relaxation rates of the electron and hole distribution functions. The diverse constituent parts in the calculations of the scattering matrices exhibit very different, partly contrariwise shifts with changing (k, N, T) : The static inverse screening length κ (2.95) increases and hence the strength of the interaction, the screened potential (2.93) decreases with increasing density and decreasing temperature. Scattering processes with small momentum transfers are favoured. Other important factors are the number of scattering partners (initial states), unoccupied final states have to be available, and band filling effects. In the case of the Fröhlich interaction the phonon occupation number rises with increasing temperature. FIGURES 4.4 compares the different scattering contributions: We see that $\gamma_{\mathbf{k}}^{hh(cc)} > \gamma_{\mathbf{k}}^{he(cc)}, \gamma_{\mathbf{k}}^{eh(cc)} > \gamma_{\mathbf{k}}^{ee(cc)}$. Momentum relaxation processes which cause a redistribution of energy and establish quasi-equilibria characterised by N, T_{pl}^e for the electrons and by N, T_{pl}^h for the holes and scattering processes which couple the two subsystems occur on time scales of the same order of magnitude. This relation suggests a common plasma temperature T_{pl} , see SECTION 2.11.

4.1.2 Extension to the Multi-Subband Case

Intrasubband and intersubband relaxation rates play an important role in the optoelectronic properties of semiconductor laser devices. The electrical pumping of quantum confined active structures by carrier capture [63, 104] or intersubband transitions mediated by many-body interactions can be modelled by the multi-subband Boltzmann

collision integrals [121, 122]. These processes are essential for the operation of novel devices such as quantum cascade lasers [34] or infrared detectors. The scattering matrices for the screened Coulomb interactions (in the electron-electron case) are defined by

$$\begin{aligned} \Gamma_{i_1 i_1, \mathbf{k}}^{ee, \text{out}} &= \frac{\pi}{\hbar} \sum_{\mathbf{k}', \mathbf{q}} \sum_{i_2, i_3, i_4} \delta(-E_{i_1, \mathbf{k}}^e - E_{i_2, \mathbf{k}'}^e + E_{i_3, \mathbf{k}'+\mathbf{q}}^e + E_{i_4, \mathbf{k}-\mathbf{q}}^e) |V_{i_1 i_2 i_3 i_4}^{\text{sc}}(\mathbf{q})|^2 \\ &\times n_{i_2 i_2, \mathbf{k}'}^e (1 - n_{i_3 i_3, \mathbf{k}'+\mathbf{q}}^e) (1 - n_{i_4 i_4, \mathbf{k}-\mathbf{q}}^e), \end{aligned} \quad (4.4)$$

$$\begin{aligned} \Gamma_{i_1 i_1, \mathbf{k}}^{ee, \text{in}} &= \frac{\pi}{\hbar} \sum_{\mathbf{k}', \mathbf{q}} \sum_{i_2, i_3, i_4} \delta(-E_{i_1, \mathbf{k}}^e - E_{i_2, \mathbf{k}'}^e + E_{i_3, \mathbf{k}'+\mathbf{q}}^e + E_{i_4, \mathbf{k}-\mathbf{q}}^e) |V_{i_1 i_2 i_3 i_4}^{\text{sc}}(\mathbf{q})|^2 \\ &\times (1 - n_{i_2 i_2, \mathbf{k}'}^e) n_{i_3 i_3, \mathbf{k}'+\mathbf{q}}^e n_{i_4 i_4, \mathbf{k}-\mathbf{q}}^e. \end{aligned} \quad (4.5)$$

The out-scattering and in-scattering processes (for electrons) due to the Fröhlich interaction can be calculated by

$$\begin{aligned} \Gamma_{i_1 i_1, \mathbf{k}}^{ee, \text{out}} &= \frac{\pi}{\hbar} \sum_{\mathbf{q}, q_z} \sum_{i_2} \sum_{\pm} \delta(-E_{i_1, \mathbf{k}}^e + E_{i_2, \mathbf{k}-\mathbf{q}}^e \pm \hbar\omega_{l-o}) |\gamma_{i_1 i_2}(\mathbf{q}, q_z)|^2 \\ &\times (1 - n_{i_2 i_2, \mathbf{k}-\mathbf{q}}^e) \left(n_{\text{ph}, \mathbf{q}, q_z} + \frac{1}{2} \pm \frac{1}{2} \right), \end{aligned} \quad (4.6)$$

$$\begin{aligned} \Gamma_{i_1 i_1, \mathbf{k}}^{ee, \text{in}} &= \frac{\pi}{\hbar} \sum_{\mathbf{q}, q_z} \sum_{i_2} \sum_{\pm} \delta(-E_{i_1, \mathbf{k}}^e + E_{i_2, \mathbf{k}-\mathbf{q}}^e \mp \hbar\omega_{l-o}) |\gamma_{i_1 i_2}(\mathbf{q}, q_z)|^2 \\ &\times n_{i_2 i_2, \mathbf{k}-\mathbf{q}}^e \left(n_{\text{ph}, \mathbf{q}, q_z} + \frac{1}{2} \pm \frac{1}{2} \right). \end{aligned} \quad (4.7)$$

To understand the carrier and energy relaxation from non-equilibrium distribution functions, it is beneficial to investigate the strength of the interactions, which are mainly determined by the form factors (see FIGURE 4.5), and to group the scattering processes into different categories. FIGURE 4.6 shows the different types of scattering processes. The symmetry of the electronic envelope functions in a symmetric confinement potential results in a reduction of the number of nonzero form factors (2.59). The relevant processes are those weighted with $|V_{i_1 i_2 i_3 i_4}^{\text{sc}}(\mathbf{q})|^2$ in which the combinations of involved subband numbers satisfy the restrictive condition $\text{mod}(i_1 + i_2 + i_3 + i_4, 2) = 0$. Thereby, \mathbf{q} is the transfer momentum vector between two interacting particles i_1, i_2 with $i_1 \rightarrow i_4, i_2 \rightarrow i_3$, $E_{i_1, \mathbf{k}} - E_{i_4, \mathbf{k}-\mathbf{q}}$ the transferred energy. A total of 8 categories of electron-electron interactions (in two subbands) and 16 different scattering contributions in equations (4.4) and (4.5) have to be considered [124]: (A) $V_{1111}^{\text{sc}}, V_{2222}^{\text{sc}}$ describe purely intrasubband processes with an occupation and energy redistribution within a subband. (B) In $V_{1221}^{\text{sc}}, V_{2112}^{\text{sc}}$ electrons from different subbands interact, which reflects intrasubband transitions. This allows for an energy density equalisation. (C) In $V_{1212}^{\text{sc}}, V_{2121}^{\text{sc}}$ the particles are initially in different subbands (intersubband interactions) and undertake intersubband, exchange transitions. (D) Here, the intrasubband interactions $V_{1122}^{\text{sc}}, V_{2211}^{\text{sc}}$ result in intersubband transitions. There is both, an energy and a net occupation transfer between the subbands. Electron-hole and hole-hole scattering processes can be classified in an analogous way, and the consideration of intersubband and intrasubband scattering rates mediated

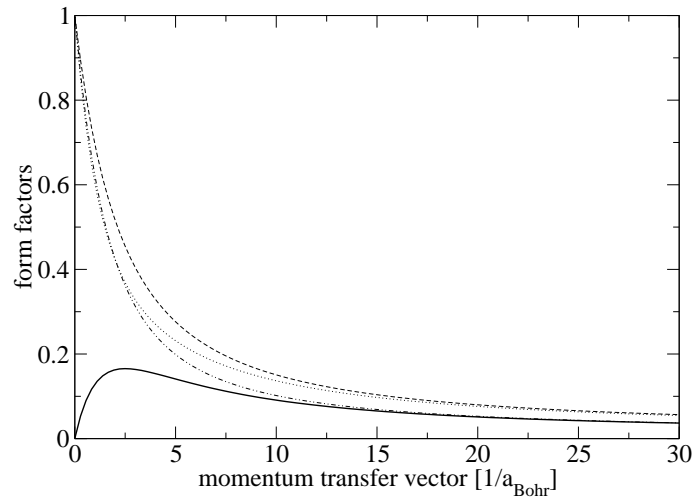


FIGURE 4.5: The form factors as defined in (2.59) determine the relative strength of the different classes of scattering processes in semiconductor quantum wells, primarily there is a distinction (for small q) between intrasubband transitions with $F(q \rightarrow 0) = 1$, such as F_{1111} (dashed), F_{1221} (dot-dashed) or F_{2222} (dotted), and intersubband transitions with $F(q \rightarrow 0) = 0$, weighted with the factor F_{1122} . At this $i_1 \rightarrow i_4$ in $F_{i_1 i_2 i_3 i_4}(q)$ labels the transition we are considering.

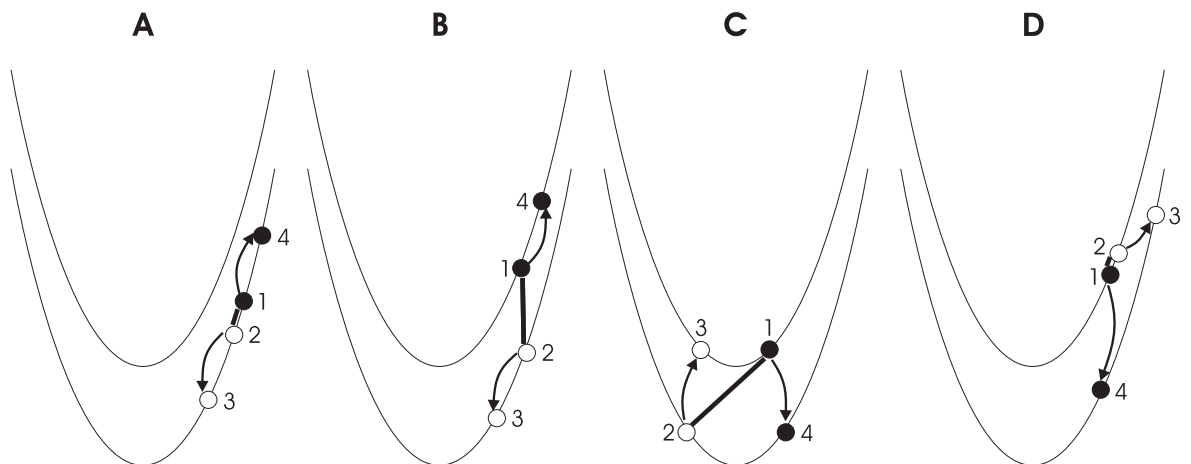


FIGURE 4.6: Classification of allowed out-scattering processes mediated by the screened Coulomb interaction [123, 124] involving the lowest two electron subbands. The investigated structure is a single, symmetric GaAs quantum well of 20 nm width.

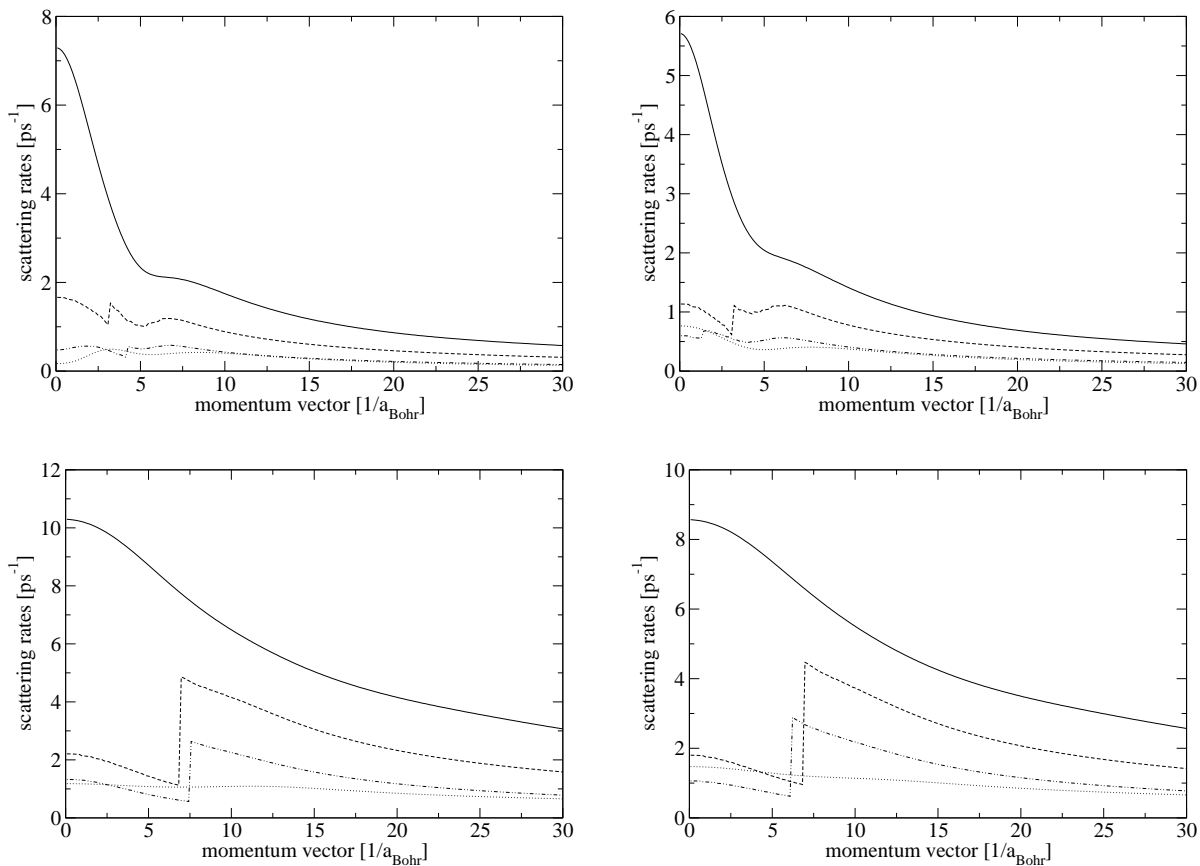


FIGURE 4.7: Momentum scattering rates of the electron (top) and hole (bottom) distribution functions at $T = 300$ K and at a carrier density of $N = 4 \cdot 10^{12} \text{ cm}^{-2}$ in a single quantum well of 20 nm width. Plotted are the microscopically calculated rates for the lower (left column) and upper (right column) subbands. In the graphs we analyse the various contributions, to specify we distinguish between carrier-carrier interactions involving intrasubband (solid lines) and intersubband (dotted) transitions, as well as intrasubband (dashed) and intersubband (dot-dashed) transitions caused by the Fröhlich interaction.

by the interaction with phonons is straightforward. The rates of the different categories of scattering processes characterise and give a measure of the time scales of the redistribution of carriers and energy in a multi-subband system starting from non-equilibrium distributions. The processes (A) lead to an equalisation separately for each subband, (B) and (C) couple the different subbands and involve an energy transfer. The scattering processes described by (D) are the only ones which make possible a relaxation to a single overall Fermi-Dirac distribution.

The scattering times of the different categories of scattering processes are calculated in FIGURE 4.7. Compared to the scattering rates calculated for the single-subband case in FIGURE 4.4 (with a quantum well width of 5 nm) the relaxation times in the multi-subband case are increased by a factor of approximately 3. This can be explained by

the reduced interaction strengths mainly given by the form factors and by the increased effect of screening for higher densities; in a broader quantum well the electronic wave functions are less localised. A comparison of the influence of different screening models in the calculations of the scattering rates, from the dynamical dielectric function in random phase approximation to the static, long-wavelength approach, can be found in [124]. The threshold conditions for the sharp structures in the carrier-phonon relaxation rates are modified by the offsets in intersubband transitions. The graphs clearly show that intraband scatterings due to the screened Coulomb interactions represent the dominant contributions. Typical rates are 200 fs (intrasubband), 1 ps (interaction with longitudinal phonons) and 2 ps (intersubband) for the electrons and 100 fs, 500 fs, 1 ps for the holes, respectively. These results conflict with the concept of separate temperatures for the carriers and the lattice in multi-subband or multi-level systems. We estimate the typical carrier capture time from the electrically or optically pumped wetting structures into a quantum confined active structure, for instance a quantum well or a quantum dot, to be a few picoseconds. The interaction strengths are weakened due to the reduced overlap of wetting layer states and the final state in the quantum confined structure.

4.2 Calculations of Quantum Well Laser Gain

The optoelectronic properties of semiconductor quantum well structures are modelled in this work within the semiclassical framework [10]. Quantum mechanically derived expressions of the semiconductor gain response are coupled to (and are the sources of) the optical waves and propagating laser fields by adding a term for the induced polarisation or complex susceptibility. The investigation of these local gain properties of active media and the calculation of important laser parameters allow quantitative predictions of the performance characteristics of diode laser structures [3, 4, 25].

Gain properties and typical laser parameters, as computed from a realistic description of the quantum confined semiconductor amplifier medium including energy and field renormalisations as well as correlation contributions [23, 24, 49–51, 125], are shown and discussed in FIGURES 4.15–4.20. An approximation to these spectra and a mapping of typical behaviours to a n -oscillator model with few fitting parameters [12, 41, 54, 55] in combination with a spatially resolved model for the electromagnetic fields can be a numerically efficient tool to investigate the dynamics of lasers [96, 126] and amplifiers [55]. Other approaches are more suitable to simulate large area active laser devices, such as broad area lasers [37, 127] or tapered amplifiers [106], along with the effects of optical nonlinearities, spectral hole burning or nonlinear gain saturation, but require some approximations of the dynamical and band-resolved description of the gain material. FIGURES 4.8–4.14 show optical gain spectra and important laser parameters as implemented in the latter approach.

In order to calculate the quantum well laser gain spectra, we start with a mode expansion of the electric field and the induced macroscopic polarisation in forward travelling

plane waves

$$E(z, t) = \frac{1}{2} E_{\text{env}}(z; \omega) e^{i\Phi(z; \omega)} e^{-i\omega t} e^{ik_0 n_{\text{eff}} z} + \text{conjugate complex}, \quad E_{\text{env}}, \Phi \in \mathbb{R}, \quad (4.8)$$

$$P_{\text{env}}(z; \omega) = \sum_{i,j} \frac{2}{A} \sum_{\mathbf{k}} M_{ij}^{eh} \tilde{p}_{ji, \mathbf{k}}, \quad E_{\text{env}} \leftarrow \frac{\Gamma N_{\text{QW}} d_{\text{QW}}}{L_{\text{ref}}} \frac{1}{d_{\text{QW}}} \frac{P_{\text{env}}}{\epsilon_0}. \quad (4.9)$$

Applying the slowly varying amplitude approximation and the rotating wave approximation, the amplitude and phase dynamics is given by (3.37) for the complex-valued electric field amplitude, or equivalently by

$$\partial_z E_{\text{env}}(z) = -\frac{k_0}{\epsilon_0 2n_{\text{eff}}} \frac{\Gamma N_{\text{QW}} d_{\text{QW}}}{L_{\text{ref}}} \frac{1}{d_{\text{QW}}} \text{Im}(P_{\text{env}}(z)) = g_{\text{mod}}(\omega) E_{\text{env}}(z), \quad (4.10)$$

$$E_{\text{env}}(z) \partial_z \Phi(z) = \frac{k_0}{\epsilon_0 2n_{\text{eff}}} \tilde{\Gamma} \frac{1}{d_{\text{QW}}} \text{Re}(P_{\text{env}}(z)), \quad \tilde{\Gamma} = \frac{\Gamma N_{\text{QW}} d_{\text{QW}}}{L_{\text{ref}}} \quad (4.11)$$

for the real-valued electric field envelope E_{env} and phase shift $\partial_z \Phi$. Note that by the expansion ansatz (4.8) a partial transformation to Fourier space has been performed. The optical field and semiconductor gain medium are coupled by the modal gain $g_{\text{mod}}(\omega)$ and carrier-induced refractive index change $\delta n(\omega)$ as properties of the dielectric susceptibility response. The refractive index change on the other hand is related to the phase shift by

$$e^{i\Phi(z; \omega)} e^{ik_0 n_{\text{eff}} z} = e^{ik_0 (n_{\text{eff}} + \delta n(\omega)) z} \rightarrow \partial_z \Phi(\omega) = k_0 \delta n(\omega). \quad (4.12)$$

We note that not the phase shift itself but phase shift changes influence the light field dynamics of broader laser structures. This is quantified by the linewidth enhancement or anti-guiding factor¹ α

$$\alpha = -\frac{d(\partial_z \Phi)/dN}{dg_{\text{mod}}/dN}. \quad (4.13)$$

The modal amplitude gain, which in the simplest case is the amplification of a monochromatic travelling plane wave with frequency ω and $k_0 n$, is connected to the semiconductor material gain by $g_{\text{mod}}(\omega) \propto \Gamma_r \mathcal{V}_z \tilde{\Gamma} g(\omega)|_{n \rightarrow n_{\text{eff}}}$. The coupling term $\mathcal{V}_z \tilde{\Gamma}$ filters out active regions². The gain characteristics are now computed in the quasi-equilibrium approximation: The band-resolved, k -dependent carrier populations $n_{ii, \mathbf{k}}^e, n_{jj, -\mathbf{k}}^h$ and the interband

¹A dominant feature of semiconductor-based active materials is the strong coupling between amplitude and phase dynamics [1, 2, 4, 48], quantified by the α factor. Consequences are a rather large laser linewidth (a typical value is given by 100 MHz), poor beam quality [3, 8, 36], and the occurrence of filamentation effects in semiconductor lasers [128–132]. In contrast to (asymmetric) multi-level or band-resolved descriptions, for a homogeneously broadened two-level active gain material we obtain a density independent value of $\alpha = (\Omega_0 - 2\pi c/\lambda)/\gamma^P$ (or in our full time-domain approach $\alpha = (\Omega_0^2 + (\gamma^P)^2 - \omega^2)/(2\gamma^P \omega)$, respectively). Thus, for commonly applied parameters index-guiding is suppressed in phenomenological models as $\alpha \approx 0$.

²A typical number for an edge-emitting, quantum well-based lasing structure is 0.05. For quantum dot or other nanometer-sized active structures the coupling and consequently amplification are reduced due to much smaller filling factors \mathcal{V}_z in propagation direction.

polarisation amplitudes $\tilde{p}_{ji,\mathbf{k}}$ are assumed to adiabatically follow temporal variations of the slower macroscopic variables N, T, E_{env} according to the slaving principle [10]. The driving physical processes are the ultrafast scattering and dephasing with typical relaxation times of about 50 fs. In the small signal or linear regime, where nonlinear saturation and spectral hole burning can be neglected, these relaxation processes result in electron and hole quasi-equilibrium Fermi-Dirac distributions³ $f_{ii,\mathbf{k}}^e, f_{jj,-\mathbf{k}}^h$. From the free-carrier susceptibility [4] we can derive

$$g_{\text{mod}}(\lambda) = \Gamma_z \tilde{\Gamma} \frac{\pi}{\epsilon_0 n_{\text{eff}} \lambda} \frac{1}{d_{\text{QWA}}} \sum_{\mathbf{k}} \frac{\gamma_{\mathbf{k}}^p}{(\Omega_{\mathbf{k}} - 2\pi c/\lambda)^2 + (\gamma_{\mathbf{k}}^p)^2} \frac{1}{\hbar} |M^{eh}|^2 (f_{\mathbf{k}}^e + f_{-\mathbf{k}}^h - 1), \quad (4.14)$$

$$\partial_z \Phi(\lambda) = -\Gamma_z \tilde{\Gamma} \frac{\pi}{\epsilon_0 n_{\text{eff}} \lambda} \frac{1}{d_{\text{QWA}}} \sum_{\mathbf{k}} \frac{\Omega_{\mathbf{k}} - 2\pi c/\lambda}{(\Omega_{\mathbf{k}} - 2\pi c/\lambda)^2 + (\gamma_{\mathbf{k}}^p)^2} \frac{1}{\hbar} |M^{eh}|^2 (f_{\mathbf{k}}^e + f_{-\mathbf{k}}^h - 1), \quad (4.15)$$

where we only consider the transitions $\tilde{p}_{11,\mathbf{k}}$. Gain spectra strongly depend on macroscopic parameters like the carrier density or temperature and on the optical frequency

$$\begin{aligned} \hbar \Omega_{\mathbf{k}}(N, T_{\text{pl}}, T_{\text{lat}}) &= (E_{\mathbf{k}}^e + E_{-\mathbf{k}}^h + E_{\text{gap}})(T_{\text{lat}}) + \delta E_{\mathbf{k}}^{\text{SX}}(N, T_{\text{pl}}) + \delta E^{\text{CH}}(N, T_{\text{pl}}), \\ f_{\mathbf{k}}^e(N, T_{\text{pl}}), f_{-\mathbf{k}}^h(N, T_{\text{pl}}), \gamma_{\mathbf{k}}^p(N, T). \end{aligned} \quad (4.16)$$

Some results of calculations of quantum well laser gain, applying the free-carrier theory, are presented in the following FIGURES 4.8–4.14. The investigated structure is a single GaAs/AlGaAs quantum well of 5 nm width with only one relevant interband polarisation term $\tilde{p}_{11,\mathbf{k}}$. However, a generalisation, as required for broader quantum confined structures with several subbands or bound states, is straightforward by adding a summation over all oscillators with non-vanishing dipole matrix elements or oscillator strengths.

From the simulations in FIGURE 4.8 we can extract a transparency carrier density, that is $g_{\text{mod}}(N > N_{\text{transparency}}) > 0$, of approximately $1.54 \cdot 10^{12} \text{ cm}^{-2}$. The slowly decaying tails in the gain spectra, and the fact that the material is not transparent below the band gap is related to the treatment of the dephasing. The correct microscopic inclusion of nondiagonal collision contributions would remove this problem [4] as the dielectric susceptibility response is not just the summation over independent, driven harmonic oscillators, but the various terms will cancel each other out. In our simulations of spatio-temporal dynamics of active semiconductor structures a term $\sum_{\mathbf{k}} \sum_{\mathbf{k}'}$ is numerically too expensive, and we have also disregarded these contributions in the computation of local properties of the gain material. We proceed as follows: For each tuple (N, T) we solve the electronic confinement problem, which determines the eigensolutions of the quantum

³The spectrally local depletion of the band-resolved inversion through spectral hole burning [37,40,106] or the spectrally selective carrier generation through optical pumping [15–17, 133, 134] play important roles in the propagation of ultrashort pulses in semiconductor optical amplifiers (see SECTIONS 6.4+6.5), in high-speed modulation of lasers, or in multi-mode operation. In these situations nonlinear saturation and non-equilibrium gain cannot be disregarded [73].

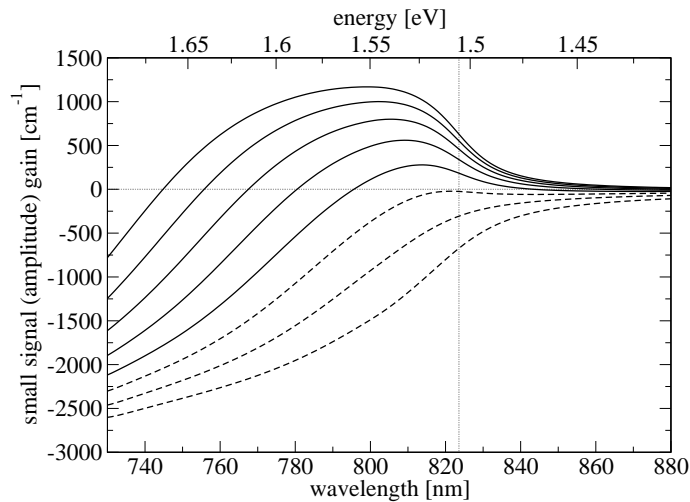


FIGURE 4.8: Small signal amplitude gain $g(\lambda, E; N, T)$ versus optical wavelength or energy for various carrier sheet densities $N \in \{0.5 \cdot 10^{12} \text{ cm}^{-2} \dots 4 \cdot 10^{12} \text{ cm}^{-2}\}$ at room temperature $T = 300 \text{ K}$ and $\tilde{\Gamma} = 1$, $\Gamma_z = 1$, $n_{\text{eff}} = n_{\text{background}}$.

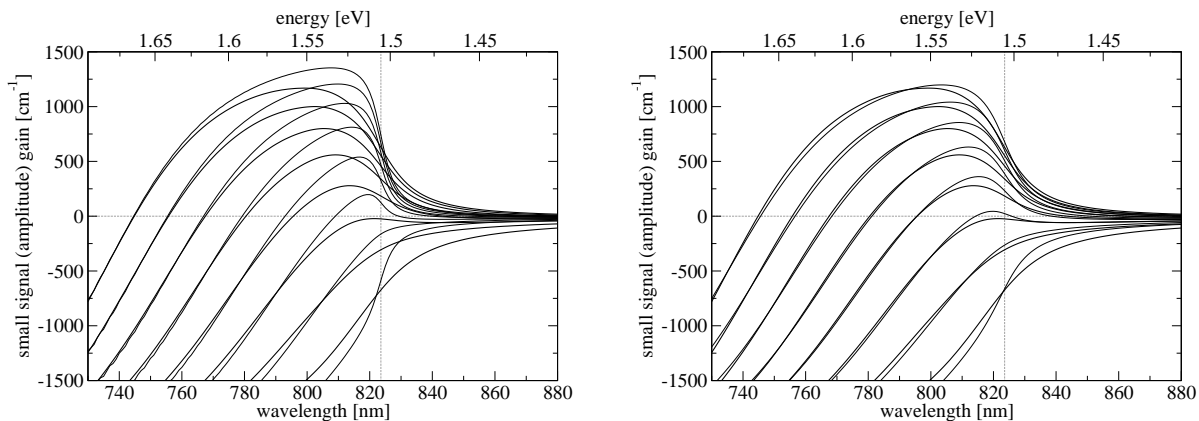


FIGURE 4.9: Comparison of gain spectra calculated from a model comprising microscopically determined scattering and dephasing rates $\gamma_{\mathbf{k}}^p(N, T)$ as input parameters with the more simple free-carrier approach with a constant phenomenological homogeneous broadening (thin line) of the individual transitions, that means of the Lorentzian oscillators.

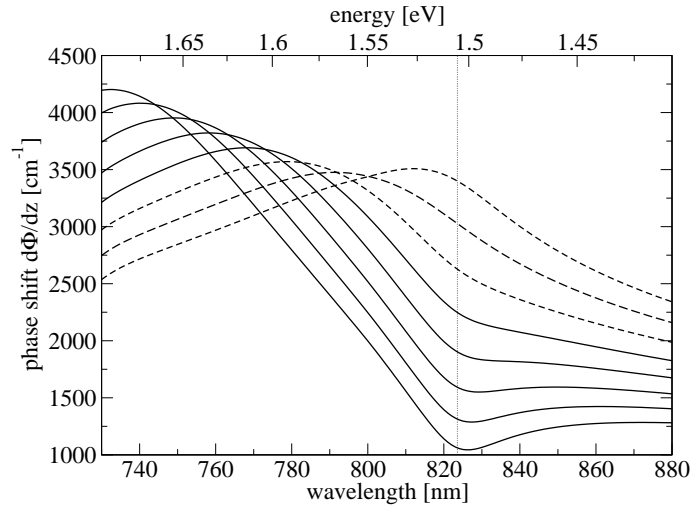


FIGURE 4.10: Induced phase shift or change of the refractive index. For energies near the band gap and $\lambda = 820$ nm, we obtain from the calculation of $\partial_z \Phi$ applying the relation (4.12) as typical value of the refractive index change $\Delta(\delta n)(1.5 \cdot 10^{12} \text{ cm}^{-2} \rightarrow 3 \cdot 10^{12} \text{ cm}^{-2}) = -0.0136$ (with a coupling factor of $\Gamma_r \mathcal{V}_z \tilde{\Gamma} = 1$).

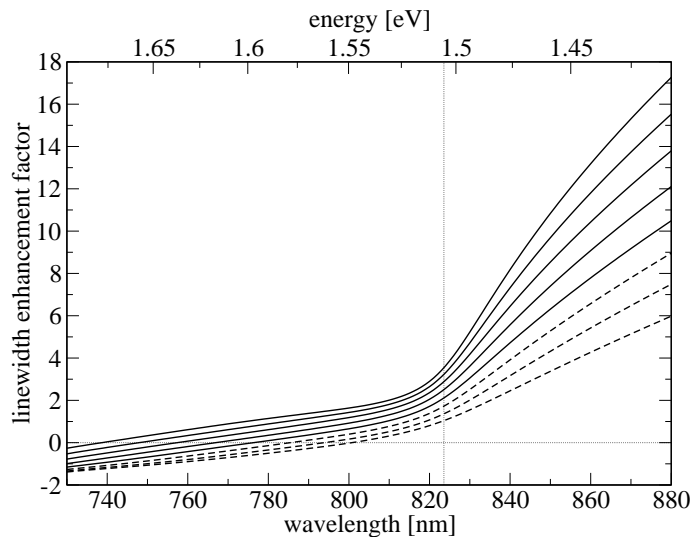


FIGURE 4.11: Linewidth enhancement or anti-guiding factor. At $\lambda = 820$ nm, we can extract $\alpha(1.5 \cdot 10^{12} \text{ cm}^{-2}) = 1.38$ and $\alpha(3 \cdot 10^{12} \text{ cm}^{-2}) = 2.36$.

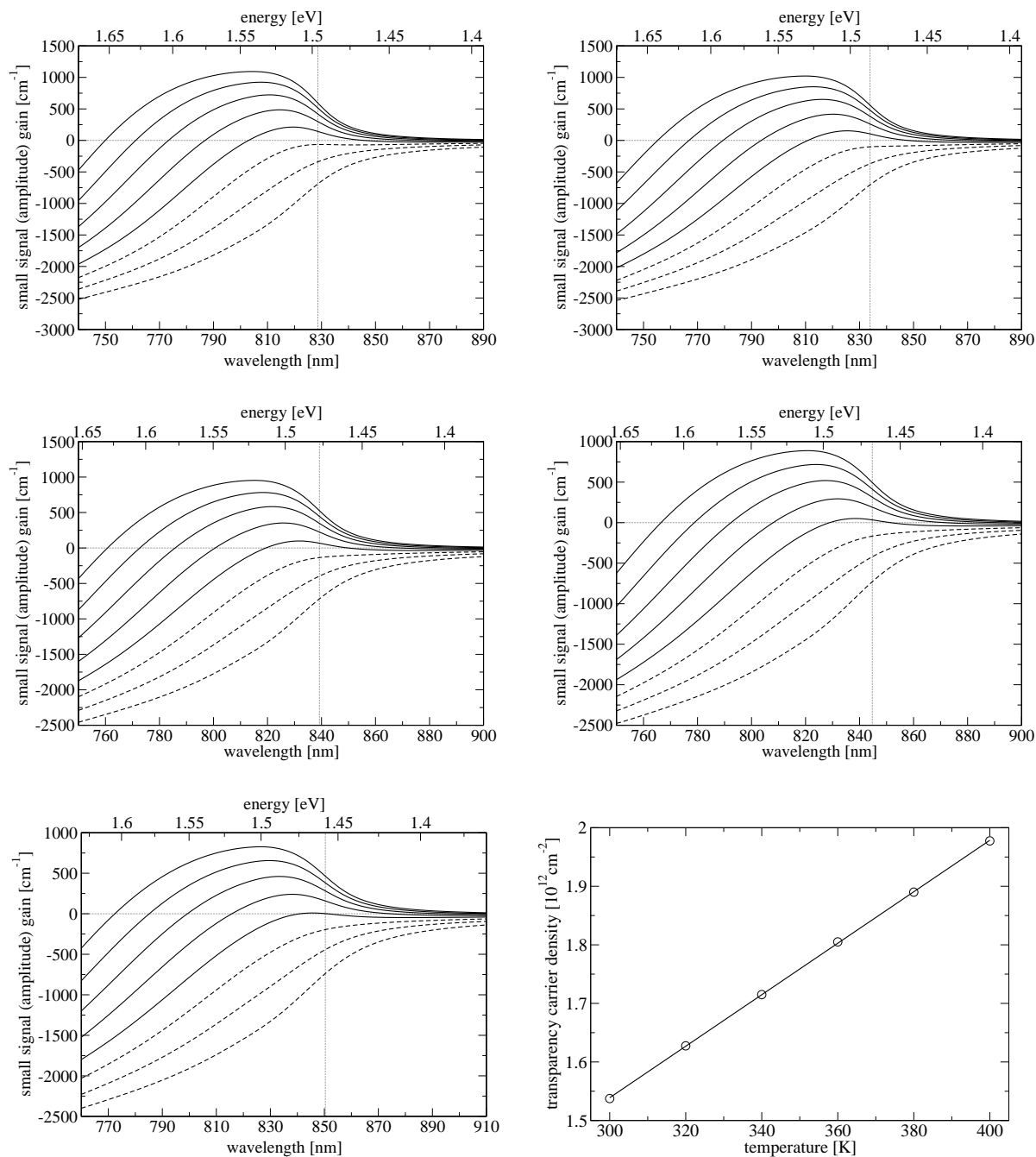


FIGURE 4.12: Modification of gain spectra with increasing plasma and lattice temperature $T \in \{320 \text{ K} \dots 400 \text{ K}\}$: The transparency carrier density increases linearly with temperature. Other properties of these small signal gain curves are depicted and discussed in FIGURES 4.13+4.14.

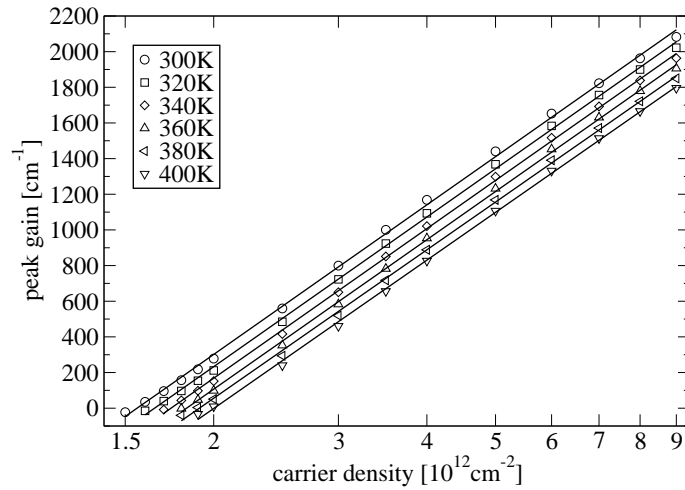


FIGURE 4.13: Peak gain versus carrier sheet density (of the quantum well) for various temperatures $T = T_{\text{pl}} = T_{\text{lat}} \in \{300 \text{ K} \dots 400 \text{ K}\}$. Depicted are the microscopically calculated gain measures (symbols) and the logarithmic curve fits, which take into account the sublinear dependence of the small signal gain on the inversion $N - N_{\text{transparency}}$ at higher densities, according to $g_{\text{peak}}(N, T) = g_0(T) \cdot \ln(N/N_{\text{transparency}}(T))$ with the fitting parameters transparency density $N_{\text{transparency}}(T)$ and the slope $g_0(T)$ (which only slightly varies with temperature). We can extract $g_0(300 \text{ K}) = 1210 \text{ cm}^{-1}$.

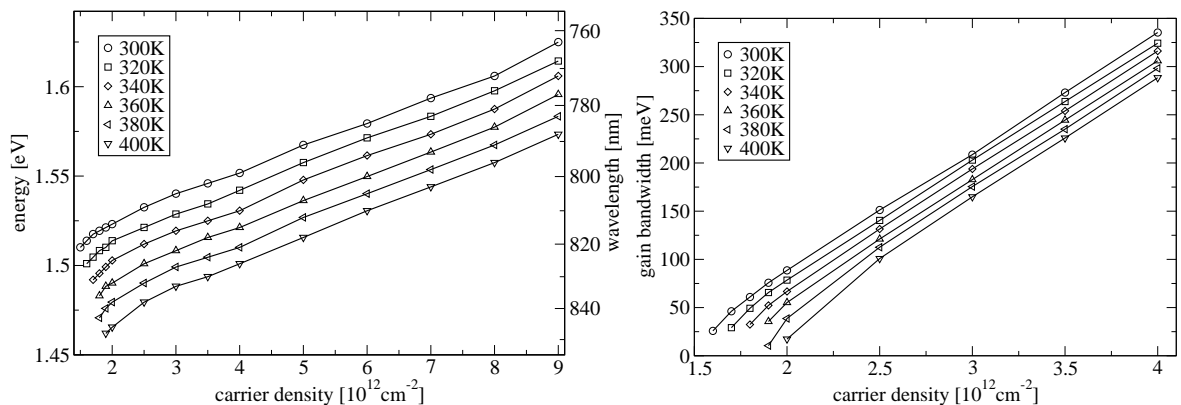


FIGURE 4.14: Frequency at the gain peak versus carrier density for various temperatures (left); the shift to higher frequencies with increasing density is caused by the effect of band filling. The available positive gain bandwidth is depicted on the right and we can estimate [4] a dependence of the spectral width of positive gain on $\propto \mu = \mu_e + \mu_h$.

well structure, calculate microscopic scattering rates $\gamma_{\mathbf{k}}^p(N, T)$ (see SECTION 4.1), and then weight the various contributions or oscillators in (4.14)+(4.15) with the electronic density of states ρ_k^{2D} of the quasi two-dimensional system.

FIGURE 4.9 illustrates the importance of relaxation rates and homogeneous broadenings in the calculations of the laser gain. These critical input parameters strongly determine the shape and magnitude of the calculated gain spectra [23]. The peak gain decreases with increasing rates γ^p . The results obtained from calculations with constant rates of 10 ps^{-1} (left) and 20 ps^{-1} (right) considerably differ from the calculations (4.14). The inclusion of realistic microscopic dephasing times and broadenings hence represents a significant improvement for the prediction of gain and carrier-induced refractive index change spectra.

In evaluating equation (4.15) there is a problem with the convergence of the integral. Absolute phase shifts are not of importance, and we have the freedom to choose a reference value. Thus, we could reinterpret the formula and include the shifts from the term -1 into the background refractive index of the host material [36]. Another possibility is to relate the changes of the refractive index $\Delta(\delta n)$ at two different carrier densities to the variations Δg_{mod} by the Kramers-Kronig transformation [5, 69, 70].

The graphs in FIGURE 4.11 reveal the strong dependence of α on the frequency and the carrier density. The implementation of this coupling between amplitude and phase dynamics by the use of a constant factor, like it is common in phenomenological semiconductor laser models [52, 73, 113, 135, 136], is therefore a problematic approach.

By incorporating renormalisation effects such as the variation of the transition energies and the field renormalisation (shift of the optical Rabi frequencies) in the screened Hartree-Fock approximation we obtain

$$\begin{aligned} g_{\text{mod}}(\lambda) + i\partial_z\Phi(\lambda) &= i\frac{k_0}{\epsilon_0 2n_{\text{eff}}}\Gamma_r \mathcal{V}_z \tilde{\Gamma} \frac{1}{d_{\text{QW}}}\frac{P_{\text{env}}}{E_{\text{env}}} = \frac{1}{A} \sum_{\mathbf{k}} (g_{\text{mod},\mathbf{k}} + i(\partial_z\Phi)_{\mathbf{k}}) \quad (4.17) \\ &= \Gamma_r \mathcal{V}_z \tilde{\Gamma} \frac{\pi}{\epsilon_0 n_{\text{eff}} \lambda} \frac{1}{d_{\text{QW}} A} \sum_{\mathbf{k}} \frac{\gamma_{\mathbf{k}}^p - i(\Omega_{\mathbf{k}} - 2\pi c/\lambda)}{(\Omega_{\mathbf{k}} - 2\pi c/\lambda)^2 + (\gamma_{\mathbf{k}}^p)^2} \frac{1}{\hbar} |M^{eh}|^2 (f_{\mathbf{k}}^e + f_{-\mathbf{k}}^h - 1) \cdot \frac{1}{1 - q_{\mathbf{k}}}. \end{aligned}$$

Many-body Hamiltonians, more precisely the screened Coulomb interaction, lead to a change of transition energies $\delta E_{\mathbf{k}}^{\text{SX}} = \delta E_{\mathbf{k}}^{e,\text{SX}} + \delta E_{-\mathbf{k}}^{h,\text{SX}}, \delta E^{\text{CH}}, \hbar\Omega_{\mathbf{k}}$ and a modified material susceptibility function. The induced polarisation can be expanded in orders of V^{sc} . The Padé approximation [48] reinterprets this as a geometrical series followed by a resummation. This high density approximation introduces the complex-valued dimensionless factors $q_{\mathbf{k}}(\lambda), Q_{\mathbf{k}}(\lambda) = 1/(1 - q_{\mathbf{k}}(\lambda))$ which are given by

$$q_{\mathbf{k}}(\lambda) = -\frac{i}{\hbar} \sum_{k'} V_{k,k'}^{\text{sc}} \frac{\gamma_{k'}^p - i(\Omega_{k'} - 2\pi c/\lambda)}{(\Omega_{k'} - 2\pi c/\lambda)^2 + (\gamma_{k'}^p)^2} (f_{k'}^e + f_{k'}^h - 1). \quad (4.18)$$

The angular integrations of the screened Coulomb potential to $V_{k,k'}^{\text{sc}}(N, T_{\text{pl}})$ have to be evaluated numerically. The small signal gain spectra in the screened Hartree-Fock approximation can be related to the results computed by the free-carrier theory, see

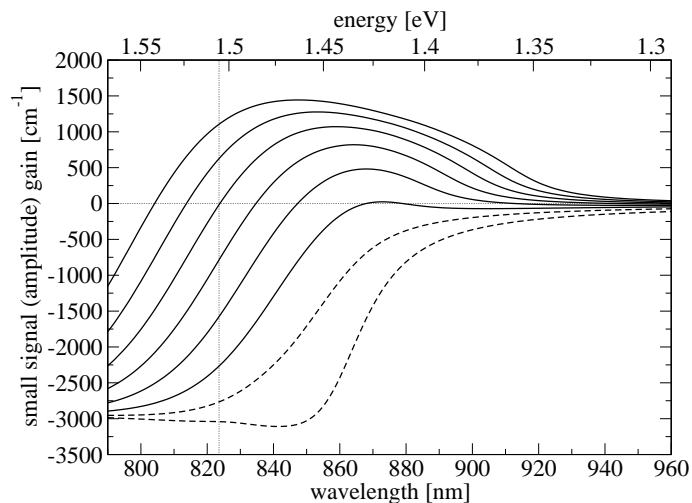


FIGURE 4.15: Same as FIGURE 4.8, but with renormalisation effects from many-body interactions as per (4.17). The signatures of the Coulomb effects are the existence of resonances below the band gap (excitons), plus an enhancement of the continuum optical spectrum [4].

equations (4.14)+(4.15), to obtain

$$\begin{aligned}
 g_{\text{mod}}(\lambda) + i\partial_z\Phi(\lambda) &= \frac{1}{A} \sum_{\mathbf{k}} \left(g_{\text{mod},\mathbf{k}}^{\text{FCT}} \cdot \text{Re}(Q_{\mathbf{k}}) - (\partial_z\Phi)_{\mathbf{k}}^{\text{FCT}} \cdot \text{Im}(Q_{\mathbf{k}}) \right) \\
 &\quad + i\frac{1}{A} \sum_{\mathbf{k}} \left((\partial_z\Phi)_{\mathbf{k}}^{\text{FCT}} \cdot \text{Re}(Q_{\mathbf{k}}) + g_{\text{mod},\mathbf{k}}^{\text{FCT}} \cdot \text{Im}(Q_{\mathbf{k}}) \right). \quad (4.19)
 \end{aligned}$$

Some results of the calculation of quantum well laser gain in the screened Hartree-Fock approximation including energy and field renormalisations are shown in FIGURES 4.15–4.20. In addition to the steps described above for a non-interacting electron-hole plasma, we do have to evaluate the plasma screening, calculate the Coulomb potentials $V_{k,k'}^{\text{sc}}(N, T_{\text{pl}})$, and compute the integrals of the renormalisation terms $\delta E_{\mathbf{k}}^{\text{SX}}, \delta E_{\mathbf{k}}^{\text{CH}}, q_{\mathbf{k}}, Q_{\mathbf{k}}$.

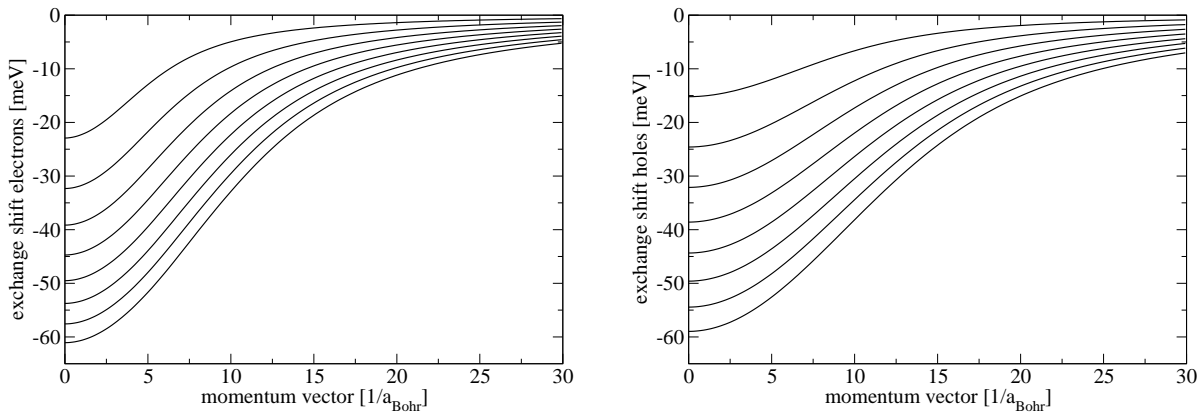


FIGURE 4.16: Exchange shifts (renormalisation of particle energies) $\delta E_{\mathbf{k}}^{e,SX}$ (left graph) and $\delta E_{-\mathbf{k}}^{h,SX}$ (right) versus the carrier momentum vector for various carrier sheet densities $N \in \{0.5 \cdot 10^{12} \text{ cm}^{-2} \dots 4 \cdot 10^{12} \text{ cm}^{-2}\}$. Moreover, spectral positions are modified by the Debye shift $\delta E^{\text{CH}}(1.5 \cdot 10^{12} \text{ cm}^{-2}) = -22.3 \text{ meV}$, $\delta E^{\text{CH}}(3 \cdot 10^{12} \text{ cm}^{-2}) = -27 \text{ meV}$.

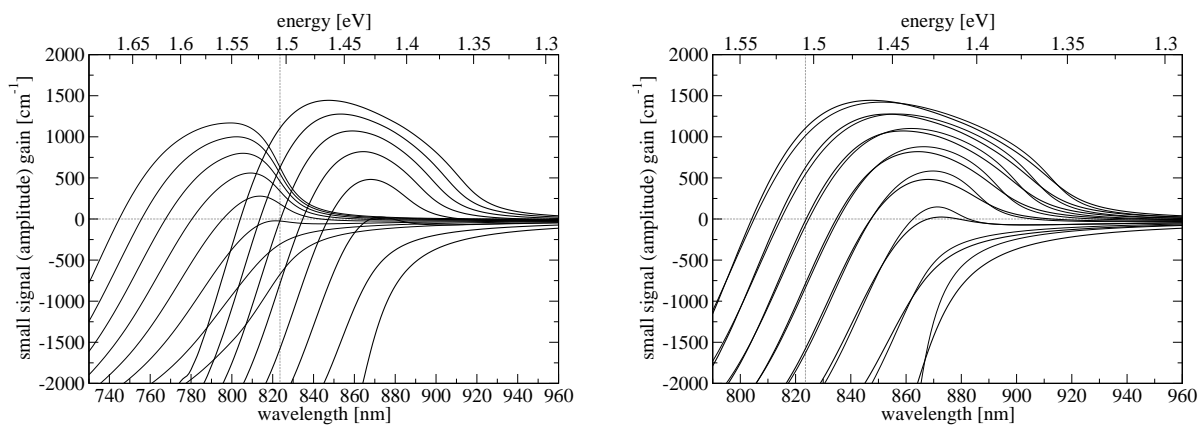


FIGURE 4.17: The interband Coulomb enhancement results in a reshaping and an increase of the magnitude of amplification or absorption, most noticeable at low carrier densities. Energy renormalisation causes a spectral shift. This can be seen in the left picture in comparison to results neglecting many-body effects (thin line). (Right) Gain calculations assuming a constant broadening of the Lorentzian line shapes of 20 ps^{-1} clearly differ from our numerical results which incorporate microscopically determined dephasing times.

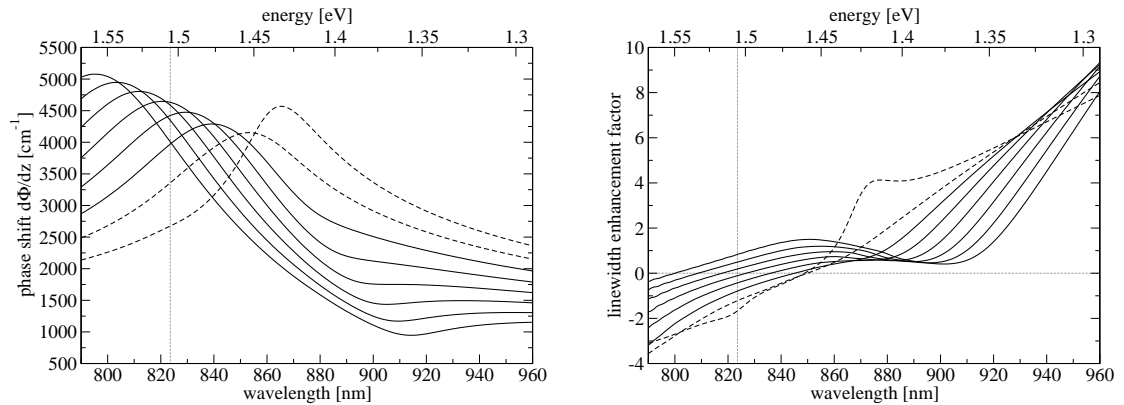


FIGURE 4.18: Same as FIGURE 4.10 (left diagram) and FIGURE 4.11 (right graph), but including renormalisation effects. The spectra are more structured. At an optical wavelength of 870 nm we can extract a refractive index change of $\Delta(\delta n)(1.5 \cdot 10^{12} \text{ cm}^{-2} \rightarrow 3 \cdot 10^{12} \text{ cm}^{-2}) = -0.0128$ ($\Gamma_r \mathcal{V}_z \tilde{\Gamma} = 1$), and anti-guiding factors of $\alpha(1.5 \cdot 10^{12} \text{ cm}^{-2}) = 0.62$, $\alpha(3 \cdot 10^{12} \text{ cm}^{-2}) = 0.81$.

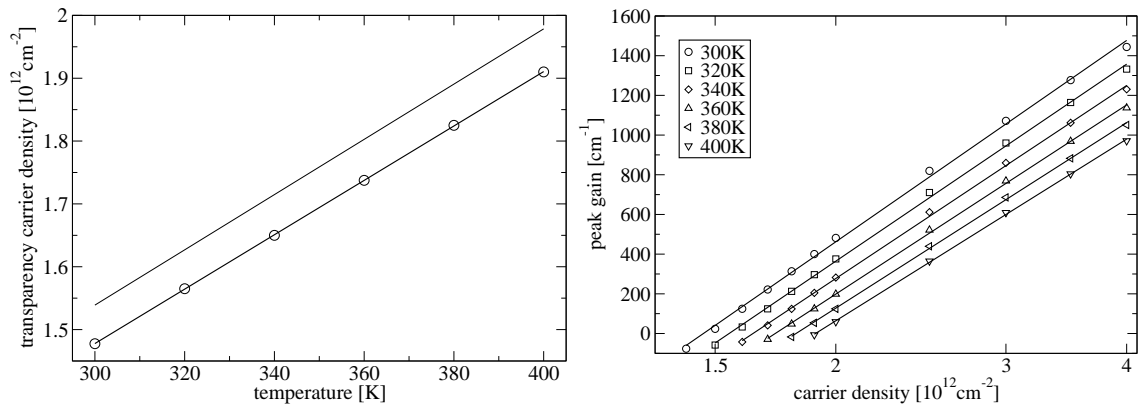


FIGURE 4.19: (Left) Transparency carrier density versus temperature. The thin line gives a comparison to results obtained from free-carrier theory. (Right graph) As FIGURE 4.13: The effect of Coulomb enhancement or interband attraction leads to an increased peak gain, the slope measures are given by $g_0(300 \text{ K}) = 1464 \text{ cm}^{-1}$ (an increase of approximately 20%) and $g_0(400 \text{ K}) = 1321 \text{ cm}^{-1}$. Band filling effects cause the gain rollover and reduction of the differential gain as the carrier density increases.

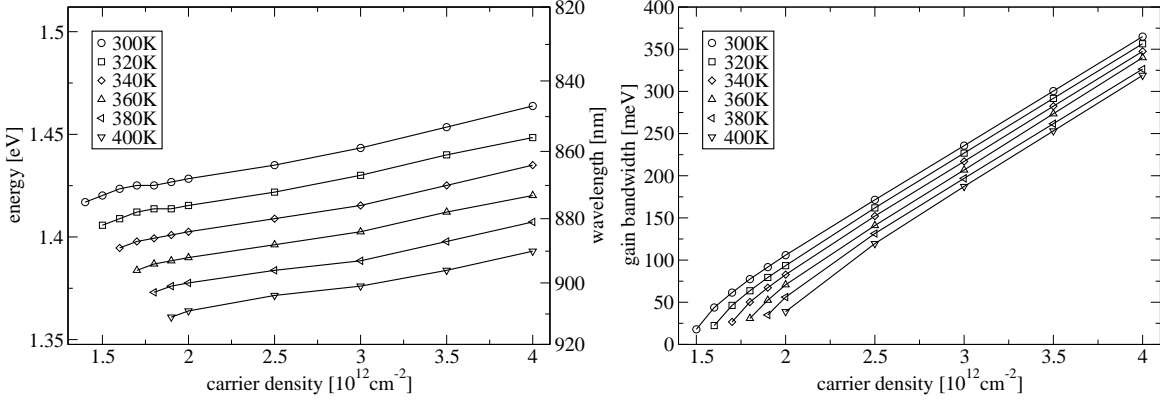


FIGURE 4.20: As FIGURE 4.14: Both, band filling and Coulomb enhancement cause a blue shift of the frequencies at peak gain which exceeds the opposing red shift due to energy renormalisations (left). The available gain bandwidth is not affected significantly when many-body interactions are considered (right).

4.3 Relaxation Oscillations

In this section high frequency relaxation oscillations, which are typical in semiconductor laser systems, are investigated, and important laser parameters and terminology are introduced [1–3]. The damped relaxation oscillations are a transient dynamical behaviour [9] which dominate when a semiconductor laser diode is switched on or off, or perturbed during operation by the modulation or fluctuations of parameters, e.g. the pump current, by optical injection [137] or by optical feedback [52]. The starting point of our considerations are the semiconductor laser rate equations⁴, a set of equations for the complex-valued electric field amplitude in slowly varying amplitude approximation (3.37) and for the carrier density (2.122)

$$\frac{n^2}{cn_{\text{eff}}}\partial_t\tilde{E} = -\gamma_{\text{resonator}}\tilde{E} + i\kappa\tilde{P} + ik_0\frac{n}{n_{\text{eff}}}\delta n_{\text{pas}}\tilde{E}, \quad \kappa = \frac{k_0}{\epsilon_0 2n_{\text{eff}}}\frac{\Gamma N_{\text{QW}}}{L_{\text{ref}}}\Gamma_r\mathcal{V}_z, \quad (4.20)$$

$$\partial_t N = -\frac{1}{2\hbar}\text{Im}(\tilde{P}^* \cdot \tilde{E}) - \Gamma^{\text{nr}}N - \Gamma_N^{\text{sp}} - \Gamma_N^{\text{Auger}} + \Lambda. \quad (4.21)$$

Spatial degrees of freedom and physical effects like diffraction and transverse index- and gain-guiding, spatial hole burning (self-focussing) or carrier diffusion will not be explicitly considered. Instead, they are treated by introducing effective parameters, such as a phenomenological optical loss rate $\gamma_{\text{resonator}}$ (or a resonator Q-factor), and the confinement and filling factors as measures of the spatial overlap between field mode and

⁴A derivation starting from Maxwell or the laser cavity equations [14] shows the basic assumptions and thus limitations of this approach: The cold-cavity modes, which are the eigensolutions of the associated Helmholtz eigenvalue problem, have to form an orthonormal, complete basis system. This is essential for superposition and projection operations and implies metallic or periodic boundary conditions. The field profiles for the active structure are assumed to be identical with the cold-cavity modes, and only longitudinal single-mode operation is considered.

quantum confined active structures. The semiconductor susceptibility response can be obtained by adiabatically eliminating the induced polarisations, which leads to

$$\tilde{P} = \epsilon_0 \epsilon \chi(\omega, N) \tilde{E}, \quad G(\omega, N) = -\epsilon_0 \epsilon \text{Im}(\chi(\omega, N)), \quad (4.22)$$

$$\epsilon_0 \epsilon \chi = - \sum_{i,j} \frac{1}{A} \sum_{\mathbf{k}} \frac{1}{i(\Omega_{ij,\mathbf{k}} - \omega) + \gamma_{ij,\mathbf{k}}^p} \frac{i}{\hbar} |M_{ij}^{eh}|^2 (f_{ii,\mathbf{k}}^e + f_{jj,-\mathbf{k}}^h - 1) \cdot Q_{ij,\mathbf{k}}. \quad (4.23)$$

We can separate the amplitude and phase dynamics⁵ by the ansatz $\tilde{E} = E_{\text{env}} \exp(i\Phi) \rightarrow \partial_t \Phi = cn_{\text{eff}}/n^2 \kappa \epsilon_0 \epsilon \text{Re}(\chi(\omega, N)) + c/nk_0 \delta n_{\text{pas}}$, and end up with a reduced set of variables $|\tilde{E}(t)|^2$ and $N(t)$ and the rate equations of a class-B laser system

$$\partial_t |\tilde{E}|^2 = -2 \frac{cn_{\text{eff}}}{n^2} (\gamma_{\text{resonator}} - \kappa G) |\tilde{E}|^2, \quad (4.24)$$

$$\partial_t N = \Lambda - \Gamma_{\text{nr}} N - \Gamma_N^{\text{sp}} - \Gamma_N^{\text{Auger}} - \frac{1}{2\hbar} G |\tilde{E}|^2. \quad (4.25)$$

The condition 'gain equals optical losses' determines the threshold carrier density and together with the rates of the various carrier loss channels the for lasing required threshold current. Above laser threshold, the steady state solution of the inversion is independent of the pump power. This phenomenon is called density pinning or gain clamping and prevents multi-mode lasing operation (see CHAPTER 5)

$$G(\omega, N_{\text{threshold}}) = \frac{\gamma_{\text{resonator}}}{\kappa} \rightarrow N_{\text{st}} = N_{\text{threshold}} \geq N_{\text{transparency}}, \quad (4.26)$$

$$\Lambda_{\text{threshold}} = \Gamma_{\text{nr}} N_{\text{st}} + \Gamma_{N_{\text{st}}}^{\text{sp}} + \Gamma_{N_{\text{st}}}^{\text{Auger}}, \quad \tilde{\Lambda} = \Lambda - \Lambda_{\text{threshold}}. \quad (4.27)$$

This means that above threshold all additional pumping is converted into light emission. The slope efficiency of the light-current curve, which is the conversion factor injected carriers to emitted photons, is thus constant

$$|\tilde{E}|_{\text{st}}^2 = \frac{2\hbar \tilde{\Lambda}}{G(N_{\text{threshold}})} = \frac{2\hbar \tilde{\Lambda} \kappa}{\gamma_{\text{resonator}}}, \quad \partial_{\tilde{\Lambda}} |\tilde{E}|_{\text{st}}^2 = \frac{2\hbar \kappa}{\gamma_{\text{resonator}}}. \quad (4.28)$$

A linear stability analysis of the fixed point attractor $(N_{\text{threshold}}, |\tilde{E}|_{\text{st}}^2)$ in reduced phase space quantifies how the laser system reacts to perturbations and gives the oscillation period $T_{\text{ro}} = 2\pi/\sqrt{\Omega_{\text{ro}}^2 - \Gamma_{\text{ro}}^2}$ and damping Γ_{ro} of the relaxation oscillations

$$\lambda_{\pm} = -\Gamma_{\text{ro}} \pm i\sqrt{\Omega_{\text{ro}}^2 - \Gamma_{\text{ro}}^2}, \quad (4.29)$$

$$\Gamma_{\text{ro}} = \frac{1}{2} \left(\Gamma_{\text{nr}} + \partial_N \Gamma_N^{\text{sp}} + \partial_N \Gamma_N^{\text{Auger}} + \frac{\tilde{\Lambda} \kappa}{\gamma_{\text{resonator}}} \partial_N G \right) \Big|_{N_{\text{st}}}, \quad (4.30)$$

$$\Omega_{\text{ro}} = \sqrt{2 \frac{cn_{\text{eff}}}{n^2} \tilde{\Lambda} \kappa \partial_N G|_{N_{\text{st}}}}. \quad (4.31)$$

⁵In broad area lasers the coupling between amplitude and phase dynamics, measured by the α factor, leads to filamentation and instabilities as the result of competing gain- and induced index-guiding. For more details see CHAPTER 5. These and other phase sensitive effects cannot be neglected in spatially extended systems.

In the following we will compare this theoretical results with simulations of the spatio-temporal dynamics in edge-emitting lasers applying the paraxial model (see FIGURES 4.21+4.22), and in vertical cavity surface-emitters modelled within the full time-domain approach (see FIGURES 4.23+4.24). In both cases, the gain medium is formed of several active layers of GaAs (quantum wells) and will be modelled by the microscopic, band-resolved semiconductor Bloch equations. We see that starting from noise or spontaneous emission the electric field amplitude is rising exponentially as energy stored in the carrier subsystem is transformed into the optical laser field. Then the carrier density is eaten up by the light field and eventually falls below threshold ($\delta N = N - N_{st} < 0$). The lasing breaks down. The electrical pumping pushes the inversion back above the threshold value, and the behaviour repeats: Intensity and the carrier density oscillate around their steady state solution with a constant phase shift of $\pi/2$. In the main, our simulations and the theoretical calculations show a very close agreement apart from small deviations due to the spatial degree of freedom and diffraction and diffusion processes (in edge-emitting structures, see FIGURES 4.21+4.22). Also there are difficulties in determining the effective parameters n_{eff} , $\gamma_{\text{resonator}}$, $\Gamma_z = \Gamma_r \mathcal{V}_z$ in surface-emitters or microcavity lasers due to the problem to define an effective length of the structure. In FIGURE 4.23 the switch-on dynamics of a VECSEL is numerically studied. In order to fit the transient dynamical behaviour, which is shown in our full time-domain simulations with values $\Gamma_{\text{ro}} = 2.54 \cdot 10^9 \text{ s}^{-1}$ and $T_{\text{ro}} = 260 \text{ ps}$, we would set $\kappa = 6.9 \cdot 10^{23} \text{ VC}^{-1} \text{ m}^{-1}$ ($\Gamma N_{\text{QW}}/L_{\text{ref}}\Gamma_z = 5.4 \cdot 10^6 \text{ m}^{-1}$ and $n_{\text{eff}} = 3.41$) and $\gamma_{\text{resonator}}c/n_{\text{eff}} = 8.3 \cdot 10^{10} \text{ s}^{-1}$.

Relaxation oscillations are a transient dynamical feature before steady state lasing operation sets in within a cavity. In an amplifier structure we treat the field intensity (or envelope amplitude) not as a dynamical variable but as given parameter. Here, we introduce the saturation intensity

$$|\tilde{E}|_{\text{sat}}^2 = \frac{2\hbar \left(\Gamma^{\text{nr}} + \partial_N \Gamma_N^{\text{sp}} + \partial_N \Gamma_N^{\text{Auger}} \right)}{\partial_N G} \Bigg|_{N_{\text{transparency}}} \quad (4.32)$$

and solve for the stationary steady state value of the carrier density

$$N - N_{\text{transparency}} = \frac{\Lambda - \Gamma^{\text{nr}} N_{\text{transparency}} - \Gamma_{N_{\text{transparency}}}^{\text{sp}} - \Gamma_{N_{\text{transparency}}}^{\text{Auger}}}{\left(\Gamma^{\text{nr}} + \partial_N \Gamma_N^{\text{sp}} + \partial_N \Gamma_N^{\text{Auger}} \right) \Big|_{N_{\text{transparency}}}} \frac{1}{1 + |\tilde{E}|^2/|\tilde{E}|_{\text{sat}}^2}. \quad (4.33)$$

This large signal effect is visible both in absorption and amplification. The gain compression or saturation [4] increases with increasing field intensity as the available carriers and gain are reduced.

For a more simple characterisation of the gain material we consider a homogeneously broadened two-level system (or macroscopic semiconductor gain model) with the susceptibility response $\epsilon_0 \epsilon \chi = -1 / (i(\Omega - \omega) + \gamma^P) i/\hbar |M^{eh}|^2 2(N - N_{\text{transparency}})$, which assumes a linear dependence of the gain on the carrier density $\partial_N G(\omega, N) = G_0(\omega)$,

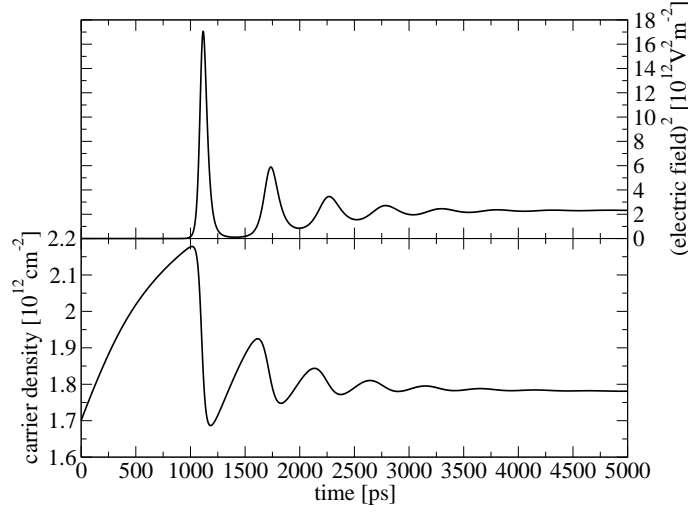


FIGURE 4.21: Damped relaxation oscillations in an edge-emitting, single-mode semiconductor laser structure; depicted are the electric field amplitude squared $|\tilde{E}|^2$ (at the top) and the carrier density (at the bottom) recorded at the centre of the device versus time. The lasing structure is characterised by the waveguide properties $n_{\text{eff}} = 3.51$ (with $n_{\text{act}} = 3.59$, $d_{\text{act}} = 250$ nm, $n_{\text{cl}} = 3.45$), $\Gamma N_{\text{QW}}/L_{\text{ref}} = 5.2 \cdot 10^6 \text{ m}^{-1}$ and $\gamma_{\text{resonator}}c/n_{\text{eff}} = 2.68 \cdot 10^{10} \text{ s}^{-1}$, the coupling factor $\kappa c/n_{\text{eff}} = 5.5 \cdot 10^{31} \text{ VC}^{-1}\text{s}^{-1}$, $\Gamma_z = 1$, $\Gamma^{\text{nr}} = 2 \cdot 10^8 \text{ s}^{-1}$ and $N_{\text{transparency}}(815 \text{ nm}) = 1.54 \cdot 10^{12} \text{ cm}^{-2}$. With the above derived theory (4.20)–(4.31) we can estimate for the stationary solution $N_{\text{threshold}} = 1.7 \cdot 10^{12} \text{ cm}^{-2}$, $\Lambda_{\text{threshold}} = 7.935 \cdot 10^{20} \text{ cm}^{-2}\text{s}^{-1}$, $|\tilde{E}|_{\text{st}} = 1.85 \cdot 10^6 \text{ Vm}^{-1}$, and for the damped relaxation oscillations at a pumping of two times threshold $\Gamma_{\text{ro}} = 2.64 \cdot 10^9 \text{ s}^{-1}$ and $T_{\text{ro}} = 406$ ps.

$G(\omega, N) = G_0(\omega)(N - N_{\text{transparency}})$. Furthermore, we sum up all carrier loss channels to an effective loss rate Γ^{eff} . The stationary solution above lasing threshold is given by

$$N_{\text{threshold}} = N_{\text{transparency}} + \frac{\gamma_{\text{resonator}}}{\kappa G_0}, \quad \Lambda_{\text{threshold}} = \Gamma^{\text{eff}} N_{\text{threshold}}, \quad |\tilde{E}|_{\text{st}}^2 = \frac{2\hbar\tilde{\Lambda}\kappa}{\gamma_{\text{resonator}}}. \quad (4.34)$$

The decay rate and frequency of the damped relaxation oscillations are quantified by

$$\Gamma_{\text{ro}} = \frac{1}{2} \left(\Gamma^{\text{eff}} + \frac{\tilde{\Lambda}\kappa G_0}{\gamma_{\text{resonator}}} \right), \quad \Omega_{\text{ro}} = \sqrt{2 \frac{cn_{\text{eff}}}{n^2} \tilde{\Lambda}\kappa G_0}, \quad (4.35)$$

and the gain saturation behaviour is described by

$$|\tilde{E}|_{\text{sat}}^2 = \frac{2\hbar\Gamma^{\text{eff}}}{G_0}, \quad G(\omega, |\tilde{E}|^2) = \frac{G_0(\omega)(\Lambda - \Gamma^{\text{eff}} N_{\text{transparency}})}{\Gamma^{\text{eff}}} \frac{1}{1 + |\tilde{E}|^2/|\tilde{E}|_{\text{sat}}^2}. \quad (4.36)$$

The physical cause of the gain compression is the depletion or the decrease of the macroscopic carrier density due to hole burning in an amplifier structure or the increase of N in an absorber, respectively (see SECTIONS 6.4+6.5). We note, that an applied light intensity (optical pumping) cannot induce a transition from absorption to amplification as $|\tilde{E}|^2 \rightarrow \infty : N \rightarrow N_{\text{transparency}}, G \rightarrow 0$.

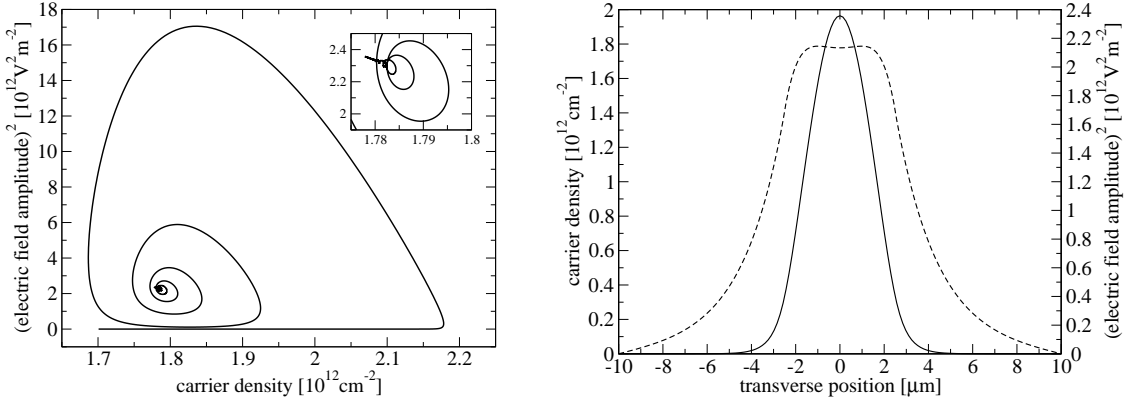


FIGURE 4.22: Reduced phase space diagram [14] (left graph), and transverse electric field amplitude and carrier density profiles at time 10 ns (right). The variations of the simulation results (based on a set of partial differential equations) from the theoretical calculations are caused by the processes of diffraction of the optical fields, a transverse gain- and index-guiding (by a dielectric structure), for more details see equation (3.37), and the diffusion of carriers in the laser with a $5 \mu\text{m}$ broad current contact. Therefore, crossings of the trajectory in the reduced phase space occur, the stationary transverse profiles are not been reached even after 10 ns, and the threshold carrier density and necessary current for lasing are higher (by reason that diffraction can be reinterpreted as additional optical loss channel). However, applying $N_{\text{threshold}}$ and $\gamma_{\text{resonator}}$ as fitting parameters we do get a nearly perfect match of theory and simulation.

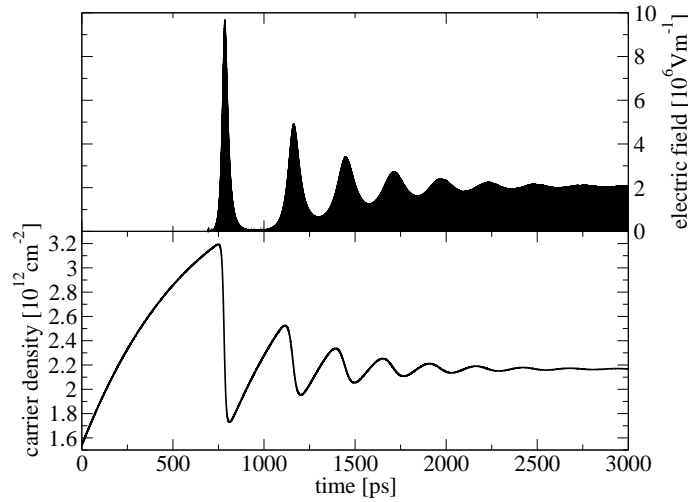


FIGURE 4.23: Damped relaxation oscillations in a vertical cavity surface-emitting semiconductor laser structure (VCSEL); depicted are the absolute value of the electric field including the carrier wave as well as the electric field envelope $E_{\text{env}} = |\tilde{E}|$ (at the top) and the carrier sheet density (at the bottom) versus time. The fixed point attractor of the nonlinear (class-B laser) system is specified by $N_{\text{st}} = 2.167 \cdot 10^{12} \text{ cm}^{-2}$ and $|\tilde{E}|_{\text{st}} = 2.10 \cdot 10^6 \text{ V m}^{-1}$. Other relevant parameters include $\Lambda = 2 \cdot \Lambda_{\text{threshold}}$ and the carrier loss channels $\Gamma^{\text{nr}} = 1 \cdot 10^9 \text{ s}^{-1}$ and Γ_N^{sp} according to (2.48).

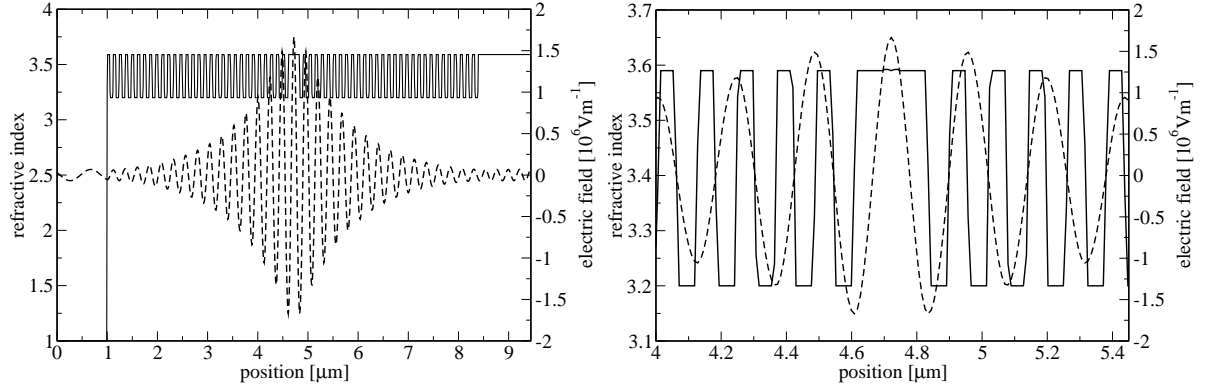


FIGURE 4.24: Refractive index structure and longitudinal electric field profile (snapshot at time point 3 ns). Between a top and a bottom highly reflective Bragg mirror a defect of length λ is enclosed, at the maxima of the modes active quantum well layers are positioned. The electromagnetic field is enhanced over the active quantum confined structures, for this reason the laser mode strongly differs from a delocalised plane wave. The calculations of the overlap or filling factor, average refractive index and the optical losses are critical because thereby it is necessary to identify an effective length of the lasing structure (in particularly of the DBR mirror).

4.4 Quantisation of Light

Together with the semiclassical approach, presented in CHAPTER 2, a phenomenological loss term accounting for spontaneous emission has been introduced into the semiconductor carrier dynamics. A full quantum theoretical treatment of the electromagnetic fields will motivate this loss factor and analyse the impact of spontaneous emission on the dynamics of the optical fields itself. In analogy to the evaluations in CHAPTER 2, we work in lowest order of the Taylor expansion of the Wigner distribution functions. By applying a plane wave expansion one can specify the Hamilton operators in second quantisation by

$$H_{\text{light}} = \sum_{p,\mathbf{q}} E_{p,\mathbf{q}}^b b_{p,\mathbf{q}}^\dagger b_{p,\mathbf{q}}, \quad E_{p,\mathbf{q}}^b = \hbar\omega_{p,\mathbf{q}}, \quad \omega_{p,\mathbf{q}} = \omega_{\mathbf{q}} = \frac{c}{n}q, \quad (4.37)$$

$$\mathbf{E} = \sum_{p,\mathbf{q}} i \sqrt{\frac{\hbar\omega_{p,\mathbf{q}}}{2\epsilon_0\epsilon V}} (b_{p,\mathbf{q}} e^{i\mathbf{q}\cdot\mathbf{r}} - b_{p,\mathbf{q}}^\dagger e^{-i\mathbf{q}\cdot\mathbf{r}}) \mathbf{e}_{p,\mathbf{q}}, \quad \mathbf{g}_{p,\mathbf{q}} = i \sqrt{\frac{\hbar\omega_{p,\mathbf{q}}}{2\epsilon_0\epsilon V}} \mathbf{M}_{ij}^{eh} \cdot \mathbf{e}_{p,\mathbf{q}}, \quad (4.38)$$

$$H_{\text{carrier-light}} = - \sum_{i,j,\mathbf{k}} \sum_{p,\mathbf{q}} \left[\mathbf{g}_{p,\mathbf{q}} b_{p,\mathbf{q}} c_{i,\mathbf{k}}^\dagger d_{j,-\mathbf{k}}^\dagger + \mathbf{g}_{p,\mathbf{q}}^* b_{p,\mathbf{q}}^\dagger d_{j,-\mathbf{k}} c_{i,\mathbf{k}} \right], \quad (4.39)$$

where only the resonant terms in the interaction Hamiltonian have been considered. Then, the following dynamical equations can be deduced for the carrier correlations

$n_{ii,\mathbf{k}}^e, n_{jj,-\mathbf{k}}^h, p_{ji,\mathbf{k}}$ and for $\langle b_{p,\mathbf{q}} \rangle$ and the photon distribution $n_{p,\mathbf{q}}^b$

$$\partial_t n_{ii,\mathbf{k}}^e = \frac{i}{\hbar} \sum_j \sum_{p,\mathbf{q}} \left(\mathbf{g}_{p,\mathbf{q}} \langle b_{p,\mathbf{q}} c_{i,\mathbf{k}}^\dagger d_{j,-\mathbf{k}}^\dagger \rangle - \mathbf{g}_{p,\mathbf{q}}^* \langle b_{p,\mathbf{q}}^\dagger d_{j,-\mathbf{k}} c_{i,\mathbf{k}} \rangle \right), \quad (4.40)$$

$$\partial_t p_{ji,\mathbf{k}} = -i\Omega_{ij,\mathbf{k}} p_{ji,\mathbf{k}} - \frac{i}{\hbar} \sum_{p,\mathbf{q}} \mathbf{g}_{p,\mathbf{q}} \langle b_{p,\mathbf{q}} (c_{i,\mathbf{k}}^\dagger c_{i,\mathbf{k}} + d_{j,-\mathbf{k}}^\dagger d_{j,-\mathbf{k}} - 1) \rangle, \quad (4.41)$$

$$\partial_t \langle b_{p,\mathbf{q}} \rangle = -i\omega_{p,\mathbf{q}} \langle b_{p,\mathbf{q}} \rangle + \frac{i}{\hbar} \sum_{i,j} \mathbf{g}_{p,\mathbf{q}}^* \sum_{\mathbf{k}} p_{ji,\mathbf{k}}, \quad (4.42)$$

$$\partial_t n_{p,\mathbf{q}}^b = \partial_t \langle b_{p,\mathbf{q}}^\dagger b_{p,\mathbf{q}} \rangle = \frac{i}{\hbar} \sum_{i,j,\mathbf{k}} \left(\mathbf{g}_{p,\mathbf{q}}^* \langle b_{p,\mathbf{q}}^\dagger d_{j,-\mathbf{k}} c_{i,\mathbf{k}} \rangle - \mathbf{g}_{p,\mathbf{q}} \langle b_{p,\mathbf{q}} c_{i,\mathbf{k}}^\dagger d_{j,-\mathbf{k}}^\dagger \rangle \right). \quad (4.43)$$

The semiclassical description would be the result of a factorisation of the above dynamical equations (4.40)–(4.43). Instead, we solve the field-dipole correlations dynamics $\partial_t \langle b_{p,\mathbf{q}} c_{i,\mathbf{k}}^\dagger d_{j,-\mathbf{k}}^\dagger \rangle$ by a formal integration similar to the methods applied in SECTION 2.8⁶. An equivalent formulation of the quantum noise dynamics and spontaneous emission based on a space-space representation of these field-dipole correlations is given in [138]. In order to truncate the hierarchy and to close the system of equations, the expectation values must be factorised. This leads to the following additional terms entering the dynamical equations for the carrier and photon distributions and accounting for the influence of spontaneous emission

$$\partial_t n_{ii,\mathbf{k}}^e : - \sum_j \gamma_{ij,\mathbf{k}}^{\text{sp}} n_{ii,\mathbf{k}}^e n_{jj,-\mathbf{k}}^h, \quad \gamma_{ij,\mathbf{k}}^{\text{sp}} = \frac{2\pi}{\hbar} \sum_{p,\mathbf{q}} \frac{1}{\hbar} \delta(\Delta\Omega_{ij,\mathbf{k}}) \mathbf{g}_{p,\mathbf{q}} \mathbf{g}_{p,\mathbf{q}}^* = \frac{2n(\Omega_{ij,\mathbf{k}})^3 |M_{ij}^{eh}|^2}{3\hbar\epsilon_0\pi c^3}, \quad (4.44)$$

$$\partial_t n_{p,\mathbf{q}}^b : + \gamma_{p,\mathbf{q}}^{\text{sp}}, \quad \gamma_{p,\mathbf{q}}^{\text{sp}} = \frac{2\pi}{\hbar} \sum_{i,j} \sum_{\mathbf{k}} \frac{1}{\hbar} \delta(\Delta\Omega_{ij,\mathbf{k}}) \mathbf{g}_{p,\mathbf{q}} \mathbf{g}_{p,\mathbf{q}}^* n_{ii,\mathbf{k}}^e n_{jj,-\mathbf{k}}^h, \quad (4.45)$$

$$\sum_{i,j} \frac{1}{A} \sum_{\mathbf{k}} \gamma_{ij,\mathbf{k}}^{\text{sp}} n_{ii,\mathbf{k}}^e n_{jj,-\mathbf{k}}^h = \frac{1}{A} \sum_{p,\mathbf{q}} \gamma_{p,\mathbf{q}}^{\text{sp}} = \sum_p \int d\omega S_p(\omega) = \sum_p \int d\lambda \tilde{S}_p(\lambda), \quad (4.46)$$

$$S_p(\omega) = \sum_{i,j} \frac{n(\omega_{p,\mathbf{q}})^3}{3\hbar\epsilon_0\pi^2 c^3} \frac{1}{A} \sum_{\mathbf{k}} |M_{ij}^{eh}|^2 \frac{\gamma_{ij,\mathbf{k}}^p}{(\Omega_{ij,\mathbf{k}} - \omega_{p,\mathbf{q}})^2 + (\gamma_{ij,\mathbf{k}}^p)^2} n_{ii,\mathbf{k}}^e n_{jj,-\mathbf{k}}^h. \quad (4.47)$$

A steady state solution for the photon distribution is given by the amplified spontaneous emission spectra (4.48). Contrary to the semiclassical approach the gain $g_{p,\mathbf{q}}^{\text{mod}}$ is smaller than the optical losses of the resonator $\tilde{\gamma}_{\text{resonator}}$. Indeed, spontaneous emission occurs with a rate $\gamma_{p,\mathbf{q}}^{\text{sp}}$ into the laser mode p, \mathbf{q} which we assumed to be a plane wave with wavenumber q and polarisation p . Microcavity structures show a large fraction of spontaneous emission emitted into the laser mode, qualified by a high β coupling factor.

⁶ $\partial_t \langle b_{p,\mathbf{q}} c_{i,\mathbf{k}}^\dagger d_{j,-\mathbf{k}}^\dagger \rangle = -i/\hbar (E_{p,\mathbf{q}}^b - \hbar\Omega_{ij,\mathbf{k}}) \langle b_{p,\mathbf{q}} c_{i,\mathbf{k}}^\dagger d_{j,-\mathbf{k}}^\dagger \rangle + i/\hbar \sum_{i',j',\mathbf{k}'} \mathbf{g}_{p,\mathbf{q}}^* \langle c_{i,\mathbf{k}}^\dagger d_{j,-\mathbf{k}}^\dagger d_{j',-\mathbf{k}'} c_{i',\mathbf{k}'} \rangle + i/\hbar \sum_{p',\mathbf{q}'} \mathbf{g}_{p',\mathbf{q}'}^* \langle b_{p',\mathbf{q}'}^\dagger b_{p,\mathbf{q}} (c_{i,\mathbf{k}}^\dagger c_{i,\mathbf{k}} + d_{j,-\mathbf{k}}^\dagger d_{j,-\mathbf{k}} - 1) \rangle$ specifies the time evolution of this correlation as the sum of expectation values of products of four operators.

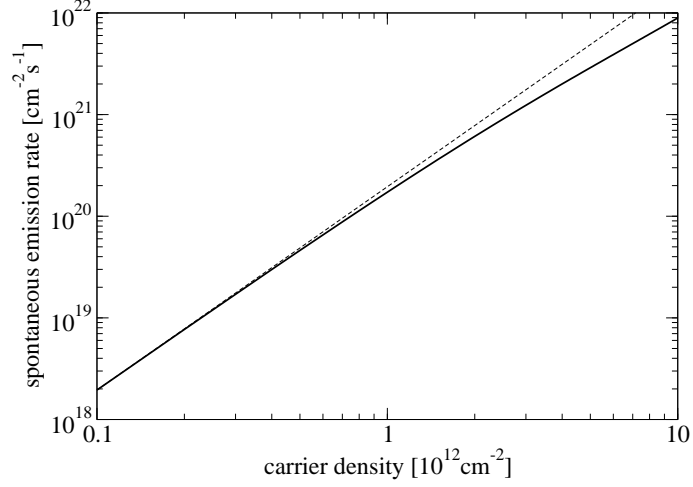


FIGURE 4.25: Total spontaneous emission or radiative recombination rate Γ_N^{sp} versus carrier density. At low carrier densities the usually assumed ansatz $\partial_t N = -BN^2$ [88] represents a relatively good fit (dashed line), and we can extract $B = 1.95 \cdot 10^{-4} \text{ cm}^2 \text{ s}^{-1}$. For higher densities there are considerable deviations as a result of the Pauli exclusion principle for fermionic particles (as described by the Fermi-Dirac distribution functions). The radiative recombination rate Γ_N^{sp} is obtained from the spontaneous emission spectra, see FIGURE 4.26, by $\Gamma_N^{\text{sp}} = \sum_{p=\text{TE, TM}} \int d\lambda \tilde{S}_p(\lambda)$.

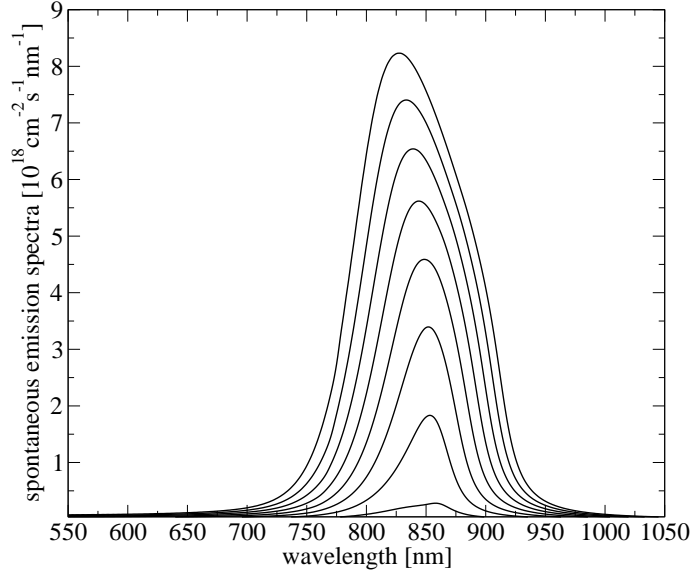


FIGURE 4.26: Spontaneous emission or luminescence spectra $\tilde{S}_{\text{TE}}(\lambda)d\lambda$ for TE-polarisation for various carrier sheet densities $N \in \{0.5 \cdot 10^{12} \text{ cm}^{-2} \dots 4 \cdot 10^{12} \text{ cm}^{-2}\}$ at room temperature $T = 300 \text{ K}$. Many-body effects are included via microscopically calculated scattering or dephasing rates $\gamma_{\mathbf{k}}^p(N, T)$, Coulomb renormalisation effects are incorporated by renormalised transition frequencies $\Omega_{ij, \mathbf{k}}$ and Coulomb enhancement, within the framework of the Padé approximation, by $Q_{ij, \mathbf{k}}$. Only bound quantum well states are considered (system is a single GaAs/AlGaAs quantum well of 5 nm width).

In theory this could offer the possibility of thresholdless lasers. Generally, there is a modification of spontaneous emission by the dielectric structure or cavity [11, 42, 43, 139]

$$\begin{aligned} \partial_t n_{p,\mathbf{q}}^b &= 2 (g_{p,\mathbf{q}}^{\text{mod}} - \tilde{\gamma}_{\text{resonator}}) n_{p,\mathbf{q}}^b + \gamma_{p,\mathbf{q}}^{\text{sp}}, \quad \tilde{\gamma}_{\text{resonator}} = \frac{cn_{\text{eff}}}{n^2} \gamma_{\text{resonator}}, \\ n_{p,\mathbf{q}}^b &= \frac{\gamma_{p,\mathbf{q}}^{\text{sp}}}{2 (\tilde{\gamma}_{\text{resonator}} - g_{p,\mathbf{q}}^{\text{mod}})}, \end{aligned} \quad (4.48)$$

$$g_{p,\mathbf{q}}^{\text{mod}} = \Gamma_z \tilde{\Gamma} \frac{1}{\hbar^2} \sum_{i,j,\mathbf{k}} \mathbf{g}_{p,\mathbf{q}} \mathbf{g}_{p,\mathbf{q}}^* \frac{\gamma_{ij,\mathbf{k}}^p}{(\Omega_{ij,\mathbf{k}} - \omega_{p,\mathbf{q}})^2 + (\gamma_{ij,\mathbf{k}}^p)^2} (n_{ii,\mathbf{k}}^e + n_{jj,-\mathbf{k}}^h - 1). \quad (4.49)$$

An in-depth consideration of resonator effects requires the incorporation of phase sensitive quantities, such as $\langle b_{p,\mathbf{q}} b_{p,\mathbf{q}} \rangle$ and $\langle b_{p,\mathbf{q}}^\dagger b_{p,\mathbf{q}}^\dagger \rangle$. In the set of equations of motion, this phase sensitivity is mediated by the coupling to the interband polarisation terms $p_{ji,\mathbf{k}}$. In the end, the resonator structure spectrally redistributes the electromagnetic fields originating from spontaneous emission $\gamma_{p,\mathbf{q}}^{\text{sp}}$ itself [108]. In a one-dimensional Fabry-Pérot cavity the steady state solution for the photon distribution $n_{p,q}^b$ can be calculated from the condition [36]

$$E_{p,q^-} = f_{p,q} E_{p,q^+} \cos(\varphi_{p,q}) + E_{p,q}^{\text{sp}} \rightarrow n_{p,q}^b = \gamma_{p,q}^{\text{sp}} \cdot \mathcal{F} [g_{p,q}^{\text{mod}}, \varphi_{p,q}, \gamma_{\text{resonator}}, T_{\text{resonator}}]. \quad (4.50)$$

The feedback coefficient $f_{p,q}$ and the phase shift $\varphi_{p,q}$ are computed for one round trip with period $T_{\text{resonator}}$. Furthermore, the quantum mechanical fluctuation-dissipation theorem allows for the description of spontaneous emission by the addition of Langevin noise operators or forces (and connected Gaussian-Markovian stochastic processes) in spatially homogeneous systems⁷.

4.5 Thermodynamics of Semiconductor Lasers

In microcavity lasers such as V(E)CSEL structures the heat dissipation from the active nanostructures to the ambient is seriously hindered. Heating and thermal effects become more pronounced and problematic in microlasers and ever more complicated structured active devices as the thermal rollover limits the maximum output power [12, 91, 106]. Because of the time scales of the macroscopic balancing processes, we do not work within a time-domain approach but rather use iterative solvers to obtain the thermal steady state solution: On basis of a thermodynamic model we balance the carrier density and energy density flows according to the various sources and sinks. Applied approximations comprise the assumption of Fermi-Dirac distributions (no spectral hole burning), an

⁷A generalisation of the quantum theory of light for open or spatially inhomogeneous systems is rather critical [44, 47]. One approach is to make an expansion in the exact eigenmodes of the total system, including resonator and external electromagnetic fields, that is to say, system and bath [45, 46]. The required mode projection of the electromagnetic fields however conflicts with the application of the Langevin approach [8] in a full time-domain scheme or in a mathematical description build on partial differential equations.

adiabatic elimination of the interband polarisations, single optical polarisation, and no explicit treatment of the spatial degrees of freedom. In dependence on the macroscopic variables carrier sheet density N , common plasma temperature T_{pl} for the electrons and the holes, and lattice temperature T_{lat} , the electronic band structure is calculated by $E_{\text{gap}}(T_{\text{lat}}, N, T_{\text{pl}})$ (Debye shift included), $E_{ii,\mathbf{k}}^{e,\text{SX}}(N, T_{\text{pl}})$, $E_{jj,-\mathbf{k}}^{h,\text{SX}}(N, T_{\text{pl}})$, $E_{ij,\mathbf{k}}^{\text{SX}}(N, T_{\text{pl}})$. The diverse carrier loss channels and the coupling of the carrier subsystem to the laser fields are balanced by a pumping term Λ_N (for more details see SECTION 2.11)

$$\begin{aligned} \Lambda_N = & \Gamma^{\text{nr}} N + \sum_{i,j} \frac{1}{A} \sum_{\mathbf{k}} \gamma_{ij,\mathbf{k}}^{\text{sp}}(N, T) f_{ii,\mathbf{k}}^e(N, T_{\text{pl}}) f_{jj,-\mathbf{k}}^h(N, T_{\text{pl}}) + \Gamma_N^{\text{Auger}}(T) \\ & + \sum_{i,j} \frac{1}{A} \sum_{\mathbf{k}} \sum_{\mathbf{q}} \tilde{g}_{ij,\mathbf{k}}^{\mathbf{q}} n_{\mathbf{q}}^b. \end{aligned} \quad (4.51)$$

Here, $\gamma_{ij,\mathbf{k}}^{\text{sp}}$ is calculated using the Weißkopf-Wigner theory (2.48). A crucial point is not to treat Auger recombination [2] by phenomenological parameters, but rather address these Coulomb mediated scattering processes on a microscopic level (similar to the considerations (2.83)–(2.85)) by $\Gamma_N^{\text{Auger}}(T)$, $\Gamma_U^{\text{Auger}}(T)$ [87,108]. The coupling of the inversion to the photon distribution is quantified by

$$\tilde{g}_{ij,\mathbf{k}}^{\mathbf{q}} = \frac{\omega_{\mathbf{q}}}{\epsilon_0 \epsilon V} \frac{|\mathbf{M}_{ij}^{eh}|^2}{\hbar} \frac{\gamma_{ij,\mathbf{k}}^p}{(\Omega_{ij,\mathbf{k}} - \omega_{\mathbf{q}})^2 + (\gamma_{ij,\mathbf{k}}^p)^2} (f_{ii,\mathbf{k}}^e + f_{jj,-\mathbf{k}}^h - 1). \quad (4.52)$$

A similar equation can be obtained for the plasma energy density $U(N, T_{\text{pl}}) = U^e + U^h$

$$\begin{aligned} \Lambda_U = & \Gamma^{\text{nr}} U + \sum_{i,j} \frac{1}{A} \sum_{\mathbf{k}} \gamma_{ij,\mathbf{k}}^{\text{sp}}(N, T) f_{ii,\mathbf{k}}^e(N, T_{\text{pl}}) f_{jj,-\mathbf{k}}^h(N, T_{\text{pl}}) E_{ij,\mathbf{k}}^{\text{SX}}(N, T_{\text{pl}}) \\ & + \Gamma_U^{e,\text{Auger}}(T) + \Gamma_U^{h,\text{Auger}}(T) + \sum_{i,j} \frac{1}{A} \sum_{\mathbf{k}} \sum_{\mathbf{q}} \tilde{g}_{ij,\mathbf{k}}^{\mathbf{q}} E_{ij,\mathbf{k}}^{\text{SX}}(N, T_{\text{pl}}) n_{\mathbf{q}}^b \\ & + \sum_i \frac{1}{A} \sum_{\mathbf{k}} \gamma_{ii,\mathbf{k}}^{e(\text{ph})}(N, T) (f_{ii,\mathbf{k}}^e(N, T_{\text{pl}}) - f_{ii,\mathbf{k}}^e(N, T_{\text{lat}})) E_{ii,\mathbf{k}}^{e,\text{SX}}(N, T_{\text{pl}}) \\ & + \sum_j \frac{1}{A} \sum_{\mathbf{k}} \gamma_{jj,-\mathbf{k}}^{h(\text{ph})}(N, T) (f_{jj,-\mathbf{k}}^h(N, T_{\text{pl}}) - f_{jj,-\mathbf{k}}^h(N, T_{\text{lat}})) E_{jj,-\mathbf{k}}^{h,\text{SX}}(N, T_{\text{pl}}). \end{aligned} \quad (4.53)$$

Finally, we have to balance the energy density flows into and out of the lattice subsystem. The energy density transfer (thermalisation) plasma to the lattice is mediated by phonons

$$\begin{aligned} \sigma_{\text{th}} \frac{T_{\text{lat}} - T_{\text{amb}}}{d_{\text{amb}} d_{\text{act}}} = & \Gamma^{\text{nr}} (U(N, T_{\text{pl}}) + N E_{\text{gap}}(T_{\text{lat}}, N, T_{\text{pl}})) \frac{N_{\text{QW}}}{L_{\text{ref}}} \\ & + \sum_i \frac{1}{A} \sum_{\mathbf{k}} \gamma_{ii,\mathbf{k}}^{e(\text{ph})}(N, T) (f_{ii,\mathbf{k}}^e(N, T_{\text{pl}}) - f_{ii,\mathbf{k}}^e(N, T_{\text{lat}})) E_{ii,\mathbf{k}}^{e,\text{SX}}(N, T_{\text{pl}}) \frac{N_{\text{QW}}}{L_{\text{ref}}} \\ & + \sum_j \frac{1}{A} \sum_{\mathbf{k}} \gamma_{jj,-\mathbf{k}}^{h(\text{ph})}(N, T) (f_{jj,-\mathbf{k}}^h(N, T_{\text{pl}}) - f_{jj,-\mathbf{k}}^h(N, T_{\text{lat}})) E_{jj,-\mathbf{k}}^{h,\text{SX}}(N, T_{\text{pl}}) \frac{N_{\text{QW}}}{L_{\text{ref}}}. \end{aligned} \quad (4.54)$$

The behaviour of the solution can now be studied by variation of the independent parameter N . An evaluation of the balance equations for the density flows (4.51), and the energy density flows (4.53)+(4.54) determines $\Lambda_N \rightarrow I_{\text{pump}}, T_{\text{pl}}$ and T_{lat} . As final result we obtain the photon distribution in dependence on the state of the active semiconductor structure $n_{\mathbf{q}}^b(N, T_{\text{pl}}, T_{\text{lat}})^8$. In our approach, the pumping fields (an optical pumping scheme is implemented [16, 33]) are coupled to the active gain structures in a semiclassical way

$$\Lambda_N = - \sum_{i,j} \frac{1}{A} \sum_{\mathbf{k}} \frac{|\mathbf{M}_{ij}^{eh} \cdot \tilde{\mathbf{E}}_{\text{pump}}|^2}{2\hbar^2} \frac{\gamma_{ij,\mathbf{k}}^p}{(\Omega_{ij,\mathbf{k}} - \omega_{\text{pump}})^2 + (\gamma_{ij,\mathbf{k}}^p)^2} (f_{ii,\mathbf{k}}^e + f_{jj,-\mathbf{k}}^h - 1), \quad (4.55)$$

and similar for the energy density pump Λ_U . The pump intensities are given by $I_{\text{pump}} = \epsilon_0 \sqrt{\epsilon c} |\tilde{\mathbf{E}}_{\text{pump}}|^2 / 2$. This explains the thermal rollover in V(E)CSEL or general microcavity laser structures. The previously described operating principles of gain clamping and density pinning are not justified. With a rise in temperature the available gain is reduced, which has to be compensated by a higher carrier density. However, with increasing temperature and carrier density (or pumping) the carrier loss processes of spontaneous emission and particularly Auger recombination are of more and more relevance, and the thermal load per absorbed photon rises. The active nanostructures in microlasers are comparatively small-sized compared with millimeter-sized edge-emitting structures. A higher carrier density and pumping is necessary to compensate the reduced gain as the amplification $\propto \exp(g_{\text{mod}} L_{\text{act}})$ is determined by the length of the active structures. With that, losses and temperature effects are strongly enhanced.

In addition to the intrinsic temperature dependence of the gain, thermally induced refractive index changes will contribute to a further reduction of the effective or modal gain and eventually cause thermal rollover [15, 33]. The shift of the optical thickness and consequently of the microcavity resonance with a typical value of $+0.1 \text{ nmK}^{-1}$ results in a mismatch between the antinodes of the mode and the active gain elements (in a resonant periodic gain structure), and in an increasing offset between resonance frequency and gain peak. A typical value of the band gap and gain shift is $+0.3 \text{ nmK}^{-1}$. A detuning at room temperature of gain peak and microcavity resonance can improve the high-power, high temperature operation of V(E)CSEL [105].

4.6 Conclusion

In this chapter we have considered the local properties of the active laser gain medium. The resonator structure and spatial effects are accounted for by the introduction of

⁸In contrast to the quantum mechanical approach presented above, there is no contribution from spontaneous emission to the laser intensity in the semiclassical limit. The lasing wavelength is determined by the spectral position for which first the constraint $g_{\mathbf{q}_l}^{\text{mod}}(N, T_{\text{pl}}, T_{\text{lat}}) = \tilde{\gamma}_{\text{resonator}}^{\mathbf{q}_l}$ is fulfilled. The coupling between the classical electric field amplitude and a semiconductor gain material is characterised by the replacement $\sum_{\mathbf{q}} \tilde{g}_{ij,\mathbf{k}}^{\mathbf{q}} n_{\mathbf{q}}^b \rightarrow \tilde{g}_{ij,\mathbf{k}}(\omega_{\mathbf{q}_l})$ (with an expression for $\tilde{g}_{ij,\mathbf{k}}(\omega_{\mathbf{q}_l}) \propto |\tilde{E}|^2$ similar to (4.55)).

effective parameters. We calculate realistic input parameters for the analysis of spatio-temporal laser dynamics, which improves our models quantitatively. The following insights have been gained applying this approach:

- Microscopic scattering and dephasing rates for the screened Coulomb and the Fröhlich interactions in GaAs quantum well systems have been calculated for various carrier sheet densities and temperatures. These effective measures enter our simulations of spatio-temporal laser dynamics in form of lookup tables. The different contributions have been analysed, and we have specified typical values for each process. We have justified the concept of a common plasma temperature and identified carrier-carrier scattering as dominant contribution to the ultrafast optical dephasing.
- We have computed the optical gain properties and important laser parameters of semiconductor amplifier media. We have performed the analyses for a realistic description of the quantum confined semiconductor gain medium including many-body interactions and correlation contributions (as starting point for our fitting ansatz of the susceptibility), as well as for a more simple approach in which renormalisation effects have been neglected (as implemented in the dynamical band-resolved models). The numerical results are in good agreement with experimental findings. The inclusion of realistic microscopic dephasing times and broadenings provide a significant improvement for the prediction of gain and carrier-induced refractive index change spectra.
- We have analysed the strongly damped high frequency relaxation oscillations in semiconductor laser systems. This transient dynamical behaviour is dominant when a laser is switched-on or perturbed during operation by modulation or fluctuations of parameters or by optical injection. We have compared simulations of the spatio-temporal dynamics in edge-emitters and in surface-emitting structures with theoretical calculations. We have found the concept of density pinning and a classification as class-B laser system to be well justified.
- We have touched the problem of a quantum theoretical treatment of the electromagnetic field dynamics in semiconductor laser systems and discussed the microscopic evaluation of the processes of spontaneous emission.
- We have developed a thermodynamic model, which balances the flows (the various sinks and sources) of the macroscopic carrier density, the common plasma temperature and for the lattice temperature. This allows us to investigate the performance characteristics and to analyse thermal rollover of diode lasers. We have identified the invalidity of the concept of the pinning of the density (above lasing threshold) in microcavity lasers, and subsequent the rapid increase of Auger recombination with increasing density and temperature as the main contributions to thermal rollover. We also show that the process of spontaneous emission is an important factor in these laser structures.

5 Transverse Multi-Mode Laser Dynamics

5.1 Introduction—Effects of Spatial Degrees of Freedom

The in CHAPTER 4 discussed semiconductor laser principles of density pinning and gain clamping (at their threshold values) and the selection mechanism due the spectral dependence of the material gain prevent the coexistence of laser modes within the semiclassical framework. Single-mode operation and a stable, steady state output signal are expected. The competition between the various modes for the available carrier inversion and gain is won, according to the principle of survival of the fittest as derived from nonlinear dynamics [9] and synergetics [10], by the fundamental mode. This mode is the first to fulfil the condition 'modal gain equal optical losses' on increasing the pump and carrier density. In contrast to this analysis, experimental and numerical studies [112, 132, 140] of wide-aperture edge-emitting diode lasers (broad area lasers¹) show several mode families from the interplay between longitudinal and higher order transverse modes². This coexistence of multiple modes in semiconductor lasers is due to the (in the above considerations neglected) spatial degrees of freedom and inhomogeneous broadenings. Multi-mode behaviour originates from the mechanisms of spatial and spectral hole burning, as well as due to spontaneous emission [3, 112]. The interaction of the field with different spatial regions of the inversion distribution (as the various modes are driven by separated and independent carrier baths) allows multi-mode behaviour. In analogy, for a sufficiently large frequency spacing between modes, the different laser modes can couple to individual

¹The scaling of the output power of edge-emitting lasers (up to around 10 Watt in continuous wave operation) is achievable by the broadening of the current contact and of the aperture of the waveguide (typical stripe widths are 50–500 μm). But, this broad area lasers suffer from the deterioration of coherence properties, beam quality and profile, broad multi-lobed far-field patterns, and from dynamical optical filamentation and spatio-temporal instabilities in the near-field [36, 37, 106, 130, 132]. That is caused by the excitation of higher order transverse modes and self-focussing effects in large-aperture structures. Concepts to overcome this (geometrical) instability are proposed by multi-stripe laser arrays [37, 112], by current profiling (inhomogeneous pumping) [36, 131], or the control and stabilisation of spatio-temporal emission by delayed optical feedback [132].

²In a waveguide or cavity structure a laser mode is defined as the spatial pattern of the electromagnetic field or the intensity distribution, characterised by its eigenfrequency and a decay rate, from the coupling to the surrounding free space modes, and driven by a source term (the induced electric polarisation or material gain). Demanding stationarity, due to the fact that (integrated over the spatial coordinates) the optical losses are balanced by the gain, active or laser modes can be computed from the Maxwell equations specifying applicable, absorbing boundary conditions. These modes do not necessarily form a complete set of orthonormal functions. A less strict definition understands a laser mode as the spatial field profile at a specified frequency.

polarisations and electron-hole pairs of the inhomogeneously broadened gain material. The spontaneous formation of spatio-temporal patterns (in the quasi-periodic or regular regime) develops as the result of the superposition or interference of all excited laser modes. Nonlinear mode coupling, optical nonlinearities (self-focussing) and time-varying carrier and refractive index profiles lead to higher spatio-temporal complexity.

The mode structure of a typical edge-emitting diode laser device can be estimated as follows. The frequency spacing of standing waves in a Fabry-Pérot laser cavity with the application of metallic (or periodic) boundary conditions is specified by

$$\Delta k_{\text{lo}} = \frac{\pi}{L} \rightarrow \Delta \omega_{\text{lo}} = \frac{c}{n_{\text{eff}}} \Delta k_{\text{lo}} = \frac{\pi c}{n_{\text{eff}} L} \rightarrow \Delta \lambda_{\text{lo}} = \frac{\lambda^2}{2\pi c} \Delta \omega_{\text{lo}} = \frac{\lambda^2}{2n_{\text{eff}} L}. \quad (5.1)$$

Typical values (using the parameters $L = 1 \text{ mm}$, $n_{\text{eff}} = 3.5122$, $\lambda = 815 \text{ nm}$) for the longitudinal mode spacing are $\Delta \omega_{\text{lo}} = 268 \cdot 10^9 \text{ s}^{-1}$, $\Delta \lambda_{\text{lo}} = 0.1 \text{ nm}$. A similar condition for the higher order transverse modes, corresponding to the same longitudinal mode resonance, gives the estimate

$$k = \sqrt{k_{\text{lo}}^2 + k_{\text{tr}}^2} \approx k_{\text{lo}} + \frac{k_{\text{tr}}^2}{2k_{\text{lo}}}, \quad \Delta k_{\text{tr}} = \frac{\pi}{W} \rightarrow \Delta \omega_{\text{tr}} = \frac{c\lambda}{4\pi n_{\text{eff}}^2} \Delta(k_{\text{tr}}^2) \rightarrow \Delta \lambda_{\text{tr}}. \quad (5.2)$$

Typical values (with $W = 50 \mu\text{m}$) for the mode separation of the first four transverse modes are $\Delta \omega_{\text{tr}} = 18.7 \cdot 10^9 \text{ s}^{-1}$, $31.1 \cdot 10^9 \text{ s}^{-1}$, $43.6 \cdot 10^9 \text{ s}^{-1}$. Higher order transverse modes possess higher frequencies than the fundamental mode. Each mode creates a carrier (and intensity) grating with a lattice constant of $2\pi/(2k_{\text{lo}}) = \lambda_{\text{lo}}/(2n_{\text{eff}})$ and $\lambda_{\text{tr}}/(2n_{\text{eff}})$, respectively.

We have seen that multi-mode behaviour originates from hole burning and the separation of carrier baths. Consequently, processes which are coupling the different spatial (or spectral) regions counteract the mechanisms behind multi-mode operation. For spectral hole burning such processes include scattering and homogeneous broadening. Spatial hole burning, carrier depletion and inversion inhomogeneities are balanced by carrier diffusion³.

The electric field (envelope) distributions and lasing frequencies are determined by gain-guiding as well as by the effective refractive index profile $n_{\text{eff}} + \delta n_{\text{pas}}(x) + \delta n[N(x)]$

³For an edge-emitting diode laser structure, applying the one-dimensional Maxwell semiconductor Bloch model in full time-domain, we have computed the output spectra with a realistic value of the ambipolar carrier diffusion constant of $D_N = 10 \text{ cm}^2 \text{ s}^{-1}$ and with artificially switched-off diffusion, respectively: The laser spectrum of the device with switched-off diffusion (this means that the inversion baths of the different modes are decoupled) shows a multitude of peaks, connected with the different longitudinal modes, with constant $\Delta \omega_{\text{lo}}$. Because of the high spatial frequency of the intensity and carrier grating associated with longitudinal modes, carrier inhomogeneities created by longitudinal spatial hole burning are washed out on a picosecond time scale ($\propto D_N(2k_{\text{lo}})^2$). Consequently, our simulations reveal that carrier diffusion drastically reduces the number of excited longitudinal modes, for shorter structures even to single-mode operation.

(both quantified by the specified inversion distribution $N(x)$) [2, 141]

$$\begin{aligned} \partial_x^2 \tilde{E}(x; \omega_{\text{mode}}) = & 2k_0 n_{\text{eff}} \left(i(-\kappa \epsilon_0 \epsilon \text{Im}(\chi(\omega_{\text{mode}})) [N(x)] - \gamma_{\text{resonator}}) \right. \\ & \left. - (\kappa \epsilon_0 \epsilon \text{Re}(\chi(\omega_{\text{mode}})) [N(x)] + \frac{n}{n_{\text{eff}}} k_0 \delta n_{\text{pas}}(x)) \right) \tilde{E}(x; \omega_{\text{mode}}). \end{aligned} \quad (5.3)$$

In a self-consistent approach, the transverse carrier profile is the result of diffusion, electrical pumping, carrier loss channels, and stimulated recombination, depletion by spatial hole burning and gain saturation. At regions where the optical intensity is high, the gain and carrier-induced refractive index change are saturated as a result of spatial hole burning. With decreasing carrier density the effective index increases, governed by the anti-guiding factor α . Due to these optical nonlinearities, a mode creates its own confining waveguide. The importance of the local dynamics (in contrast to the mode picture) is rising for increasing stripe width and/or pumping. The process of self-focussing creates tightly focussed spots in the intensity, i.e. so-called optical filaments.

5.2 Transverse Instabilities in Broad Area Lasers

This section investigates the transverse instability, multi-mode behaviour and the formation of optical filamentation in semiconductor lasers. In particular, we analyse above which stripe width the regime of single-mode, continuous wave operation in the fundamental mode becomes unstable. We also identify the main control parameters and the physical mechanisms that lead to these instabilities. We calculate the growth rates of the self-modulated solutions (with transverse wavenumber $k_{\text{tr}} = k$). Optical nonlinearities due to carrier depletion by hole burning, and the nonlinear interaction between the electromagnetic field and the gain material (qualified by $g(x)$ and $\delta n(x)$), are included in our calculations. The starting point for our analysis are the transversally resolved Maxwell semiconductor Bloch equations in paraxial and mean-field approximation. We apply an adiabatic elimination of the induced polarisation variables (see (4.20)+(4.21)) and obtain

$$\begin{aligned} \frac{n^2}{cn_{\text{eff}}} \partial_t \tilde{E}(x, t) = & (-\gamma_{\text{resonator}} - \kappa \epsilon_0 \epsilon \text{Im}(\chi(N))) \tilde{E} + i \frac{1}{2k_0 n_{\text{eff}}} \partial_x^2 \tilde{E} \\ & + i \left(\kappa \epsilon_0 \epsilon \text{Re}(\chi(N)) + \frac{n}{n_{\text{eff}}} k_0 \delta n_{\text{pas}}(x) \right) \tilde{E}, \end{aligned} \quad (5.4)$$

$$\begin{aligned} \sigma = & \frac{cn_{\text{eff}}}{n^2} \frac{1}{2k_0 n_{\text{eff}}}, \quad \tilde{E} = E_{\text{env}} e^{i\Phi}, \\ \partial_t N(x, t) = & \frac{\epsilon_0 \epsilon}{2\hbar} \text{Im}(\chi(N)) |\tilde{E}|^2 - \Gamma^{\text{eff}} N + \Lambda(x) + D_N \partial_x^2 N, \\ \Gamma^{\text{eff}} = & \Gamma_{N_{\text{st}}}^{\text{eff}} = \Gamma^{\text{nr}} + \partial_N \Gamma_N^{\text{sp}} + \partial_N \Gamma_N^{\text{Auger}} \Big|_{N_{\text{st}}}. \end{aligned} \quad (5.5)$$

A linear stability analysis of the stationary and spatially homogeneous (translation invariance assumed) solution ($E_{\text{st}}, \Phi = -\omega_{\Phi} t + \Phi_0, N_{\text{st}}$) is performed. The exponential decay or growth rates in time of oscillatory perturbations ($\delta E, \delta E^*, \delta N$), characterised by

a wavevector k (and with an intensity and carrier density grating of $2k$, and $D = 4D_N$), are calculated from

$$\partial_t \delta E = -i\sigma k^2 \delta E + \frac{cn_{\text{eff}}}{n^2} \kappa \epsilon_0 \epsilon \left(-\partial_N \text{Im}(\chi) + i\partial_N \text{Re}(\chi) \right) \Big|_{N_{\text{st}}} E_{\text{st}} \delta N, \quad (5.6)$$

$$\partial_t \delta N = \frac{\epsilon_0 \epsilon}{2\hbar} \text{Im}(\chi(N_{\text{st}})) E_{\text{st}} (\delta E + \delta E^*) + \left(\frac{\epsilon_0 \epsilon}{2\hbar} \partial_N \text{Im}(\chi) \Big|_{N_{\text{st}}} E_{\text{st}}^2 - \Gamma^{\text{eff}} - Dk^2 \right) \delta N. \quad (5.7)$$

Using the ansatz $\delta E, \delta E^*, \delta N \propto \exp(\lambda t)$ an eigenvalue problem is derived, which leads to the following characteristic cubic equation

$$\begin{aligned} & (\sigma^2 k^4 + \lambda^2) \left(\frac{\epsilon_0 \epsilon}{2\hbar} \partial_N \text{Im}(\chi) \Big|_{N_{\text{st}}} E_{\text{st}}^2 - \Gamma^{\text{eff}} - Dk^2 - \lambda \right) \\ & + 2 \frac{\epsilon_0 \epsilon}{2\hbar} \text{Im}(\chi(N_{\text{st}})) E_{\text{st}}^2 \frac{cn_{\text{eff}}}{n^2} \kappa \epsilon_0 \epsilon \left(-\lambda \partial_N \text{Im}(\chi) + \sigma k^2 \partial_N \text{Re}(\chi) \right) \Big|_{N_{\text{st}}} = 0, \end{aligned} \quad (5.8)$$

with the eigenvalues $\lambda_1 \in \mathbb{R}$ and $\lambda_{2,3} \in \mathbb{C}$ (conjugate complex). Analysis of equation (5.8) [36, 37] reveals that for realistic semiconductor diode laser parameters $\text{Re}(\lambda_{2,3}) < 0, \forall k$ and $\lim_{k \rightarrow \infty} \text{Re}(\lambda_{2,3}) = 0$. Thus, in order to ensure the stability of transverse modes with high wavenumbers, a numerical diffusion term $D_x \partial_x^2 \tilde{E}$ [36] of an elliptic character is added to (5.4), as we discuss in APPENDIX A. Instabilities occur for $\text{Re}(\lambda) > 0$; a conditional equation for k_{crit} follows from $\text{Re}(\lambda_1) = 0$

$$\begin{aligned} & \sigma^2 k^4 \left(\frac{\epsilon_0 \epsilon}{2\hbar} \partial_N \text{Im}(\chi) \Big|_{N_{\text{st}}} E_{\text{st}}^2 - \Gamma^{\text{eff}} - Dk^2 \right) \\ & + 2\sigma k^2 \frac{\epsilon_0 \epsilon}{2\hbar} \text{Im}(\chi(N_{\text{st}})) E_{\text{st}}^2 \frac{cn_{\text{eff}}}{n^2} \kappa \epsilon_0 \epsilon \partial_N \text{Re}(\chi) \Big|_{N_{\text{st}}} = 0, \end{aligned} \quad (5.9)$$

$$\begin{aligned} k_{\text{crit}}^2 &= \frac{\epsilon_0 \epsilon / (2\hbar) \partial_N \text{Im}(\chi) \Big|_{N_{\text{st}}} E_{\text{st}}^2 - \Gamma^{\text{eff}}}{2D} \\ &+ \sqrt{\frac{(\Gamma^{\text{eff}} - \epsilon_0 \epsilon / (2\hbar) \partial_N \text{Im}(\chi) \Big|_{N_{\text{st}}} E_{\text{st}}^2)^2}{(2D)^2} + \frac{(\epsilon_0 \epsilon)^2 \text{Im}(\chi) E_{\text{st}}^2 cn_{\text{eff}} / n^2 \kappa \partial_N \text{Re}(\chi) \Big|_{N_{\text{st}}}}{\hbar D \sigma}}. \end{aligned} \quad (5.10)$$

Unstable eigenvalues are found for a band of wavenumbers with $0 < k < k_{\text{crit}}$. The interpretation of this is that there is no stable stationary and spatially homogeneous solution and that, independent of the electrical pumping and the width of the lasing structure, spatio-temporal instabilities arise. However, transverse boundary conditions and the unpumped margin stripes stabilise the system, and the oscillatory perturbations can only develop in structures with $W > W_{\text{crit}}$. For typical semiconductor gain materials and laser parameters we may approximate (5.10) by

$$k_{\text{crit}} \approx \sqrt{\frac{2\tilde{\Lambda} cn_{\text{eff}} / n^2 \kappa \alpha \left(-\epsilon_0 \epsilon \partial_N \text{Im}(\chi) \Big|_{N_{\text{st}}} \right)}{\sigma \left(\Gamma^{\text{eff}} - \epsilon_0 \epsilon / (2\hbar) \partial_N \text{Im}(\chi) \Big|_{N_{\text{st}}} E_{\text{st}}^2 \right)}}. \quad (5.11)$$

For an edge-emitting diode laser operating at $\Lambda = 2\Lambda_{\text{threshold}}$, $\tilde{\Lambda} = \Lambda - \Lambda_{\text{threshold}}$, and assuming the parameters specified in FIGURE 4.21, the critical wavevector and critical

width (of the transverse spatially extended structure) are given by

$$k_{\text{crit}} = 2 \cdot 10^{-4} \text{ nm}^{-1} \rightarrow W_{\text{crit}} \approx \frac{\pi}{k_{\text{crit}}} = 15.7 \text{ } \mu\text{m}.$$

The main control parameters are given by the stripe width, the electrical pumping Λ , the anti-guiding factor α , the differential gain and the various carrier loss channels. W_{crit} is decreasing for increasing electrical pumping but remains nearly constant for higher values of the pump [36]. The transverse instability is promoted by increasing the width of the current contact or likewise by increasing the pumping. Another important dependency is represented by the linewidth enhancement factor α ; carrier-induced refractive index changes are destabilising and breaking up the transverse modes and producing filaments. Quantum dot gain systems with reduced amplitude-phase coupling are known to improve laser beam quality as optical filamentation is suppressed in these structures [29, 93, 95].

5.3 Simulations—Different Dynamic Emission Regimes

In this section we numerically verify the analytical predictions (5.2) and (5.10) by applying a microscopic (transverse) spatially resolved model. The model incorporates a density matrix approach to the optoelectronic properties of the quantum well gain medium, and incloses a diversity of time scales and optical nonlinearities. The electromagnetic field dynamics is calculated by integrating the Maxwell wave equation in paraxial approximation. Different degrees of spatio-temporal complexity and several dynamic emission regimes can be distinguished depending on the stripe width as the main control parameter. In particular, we identify continuous wave operation, regular or quasi-periodic operation and irregular behaviour.

We note that the analysis of spatio-temporal emission dynamics is carried out in analogy to the experimental streak camera technique, which permits the measurement of integrated field intensity traces with a maximum resolution of 10 ps [132, 140]. Numerically, we calculate the instantaneous optical intensity as well as on-the-fly computations of (over few ten picoseconds) time-averaged transverse profiles

$$\langle |\tilde{E}(x, t)|^2 \rangle_T = \frac{1}{N+1} \sum_{t=t_0}^{t_0+N\Delta t} |\tilde{E}(x, t)|^2, \quad \langle N(x, t) \rangle_T = \frac{1}{N+1} \sum_{t=t_0}^{t_0+N\Delta t} N(x, t). \quad (5.12)$$

This averaging allows to eliminate the mode beating dynamics with characteristic frequencies of $\Delta\omega_{\text{mode}} - \Delta\omega_{\text{mode}'}$. Furthermore, the placement of a spectrometer into the experimental setup for near-field measurements allows a spectral decomposition of the spatio-temporal laser emission dynamics. Our theoretical approach in the same way assumes a linear expansion in transverse modes $\tilde{E}_{\text{mode}}(x; \omega_{\text{mode}})$ with the coefficients $c_{\text{mode}} \in \mathbb{C}$. We interpret transverse modes as spectrally filtered spatial near-field patterns or field distributions, which can be extracted from the electric field amplitude time

series by projection or spectral filtering (with $\omega_{\text{mode}} = \omega - \Delta\omega_{\text{mode}}$)

$$e^{-i\omega t} \cdot \tilde{E}(x, t) = e^{-i\omega t} \cdot \sum_{\text{mode}} e^{+i\Delta\omega_{\text{mode}} t} c_{\text{mode}} \tilde{E}_{\text{mode}}(x; \omega_{\text{mode}}), \quad (5.13)$$

$$c_{\text{mode}} \tilde{E}_{\text{mode}}(x; \omega_{\text{mode}}) = \frac{1}{N+1} \sum_{t=t_0}^{t_0+N\Delta t} e^{-i\Delta\omega_{\text{mode}} t} \tilde{E}(x, t). \quad (5.14)$$

In this context, the Karhunen-Loève decomposition should be mentioned, which extracts a complete set of orthonormal laser modes from the eigenvalue problem of the Hermitian covariance matrix (space-space correlations) $C_{ij} = 1/T \int_{t=t_0}^{t_0+T} dt \delta \tilde{E}^*(x_i, t) \delta \tilde{E}(x_j, t)$, $\delta \tilde{E}(x, t) = \tilde{E}(x, t) - \langle \tilde{E}(x, t) \rangle_T$ [37, 112].

The most important simulation parameters are summarised in the following table:

important simulation parameters (GaAs/AlGaAs quantum well lasers)	
<i>electronic properties of the semiconductor gain material [60]:</i>	
band gap energy $E_{\text{gap}}(T = 300 \text{ K})$	1.424 eV
Varshni band gap parameters:	
$E_{\text{gap}}(T = 0 \text{ K}), \alpha, \beta$	1.517 eV, $5.5 \cdot 10^{-4} \text{ eVK}^{-1}$, 225 K
effective electron mass m_e	$0.067 m_0$
effective hole mass m_h	$0.330 m_0$
width of quantum wells d_{QW}	5 nm
Bohr radius a_{Bohr}	13.777 nm
dipole matrix element M^{eh}	0.3 enm
effective polarisation dephasing constant γ^p	20 ps^{-1}
nonradiative recombination time $1/\Gamma^{\text{nr}}$	5 ns
Auger recombination coefficient Γ^{Auger}	$2.5 \cdot 10^{-18} \text{ cm}^4 \text{ s}^{-1}$
energy of longitudinal optical phonons $\hbar\omega_{\text{LO}}$	36 meV
(electrical) pump efficiency η	0.5
pumping Λ	$2\Lambda_{\text{threshold}}$
ambipolar carrier diffusion constant D_N	$10 \text{ cm}^2 \text{ s}^{-1}$
<i>optical and geometrical properties of the dielectric waveguide:</i>	
laser wavelength λ	815 nm
resonator/laser cavity length L	1 mm
width of current contact, stripe width W	$5 \dots 100 \mu\text{m}$
width of unpumped margin stripes W_{margin}	$7.5 \mu\text{m}$
thickness of active layer d_{act}	250 nm
transverse index-guiding $\delta n_{\text{pas}}(x)$	$-3 \cdot 10^{-3}$
intensity reflectivities R_l, R_r	0.95, 0.3
resonator loss $\gamma_{\text{resonator}} c/n_{\text{eff}}$	0.0268 ps^{-1}
dielectric constant ϵ	12.89
effective refractive index $n_{\text{eff}} (n_{\text{act}}, n_{\text{cl}})$	3.5122 (3.590, 3.452)
confinement factor $\Gamma_y N_{\text{QW}}/L_{\text{ref}}$	$5.2 \mu\text{m}^{-1}$

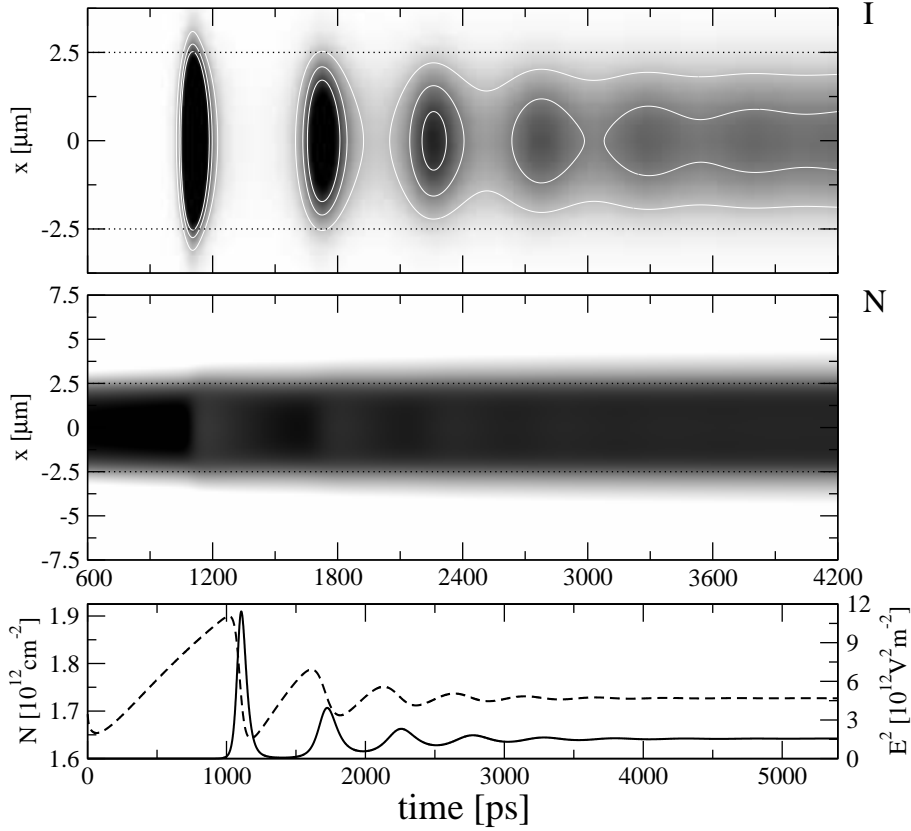


FIGURE 5.1: Transverse single-mode switch-on dynamics of a $5\ \mu\text{m}$ broad edge-emitting semiconductor diode laser structure: Depicted are the optical near-field intensity (top), the carrier sheet density (middle), and the (over the stripe width) spatially averaged electric field amplitude squared (solid line; bottom) and carrier inversion (dashed; bottom). The transverse field profiles ($x, z = L, t$) are linearly coded in grey scales with dark/black corresponding to high values and white to low intensities or carrier densities, respectively. Device parameters are specified in FIGURE 4.21; other important characteristics quantify the index-guiding by a ridge waveguide structure $\delta n_{\text{pas}}(\text{stripe}) = 0, \delta n_{\text{pas}}(\text{margin}) = -3 \cdot 10^{-3}$, the ambipolar carrier diffusion $D_N = 10\ \text{cm}^2\text{s}^{-1}$, and the width of the unpumped margin stripes $W_{\text{margin}} = 7.5\ \mu\text{m}$. Our simulations show stable transverse single-mode operation after a few nanoseconds.

FIGURES 5.1+5.2 give an insight into the transient dynamic regime of damped high frequency relaxation oscillations and transverse single-mode operation (characterised by the Gaussian fundamental mode) for a broad area laser structure with $W = 5\ \mu\text{m}$. We find a very close agreement between these numerical results, applying the paraxial transverse wave equation model with a microscopic approach to the dynamical polarisation response, and the theoretical description of the transient dynamic regime of damped relaxation oscillations, for more details see SECTION 4.3.

Increasing the stripe width to $16\ \mu\text{m}$ (see FIGURES 5.3+5.4), and to $50\ \mu\text{m}$ (FIGURES

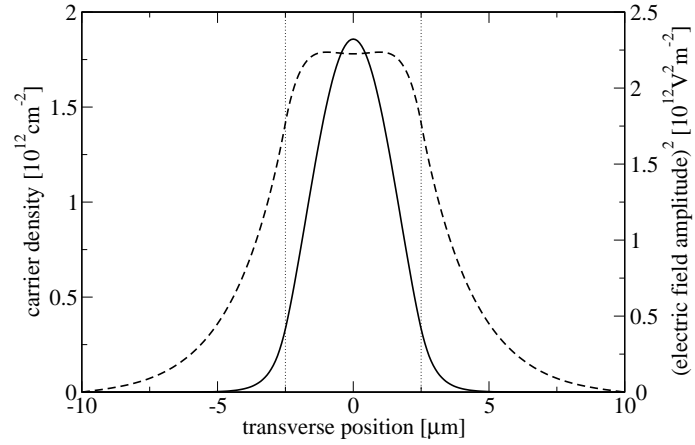


FIGURE 5.2: (Transverse) Electric field amplitude and carrier density profiles at 5 ns. An electric field amplitude squared of $|\tilde{E}|^2 = 2 \cdot 10^{12} \text{ V}^2 \text{ m}^{-2}$ translates in the investigated laser structure with GaAs/AlGaAs quantum wells to an intensity of $\approx 1 \text{ MW cm}^{-2}$.

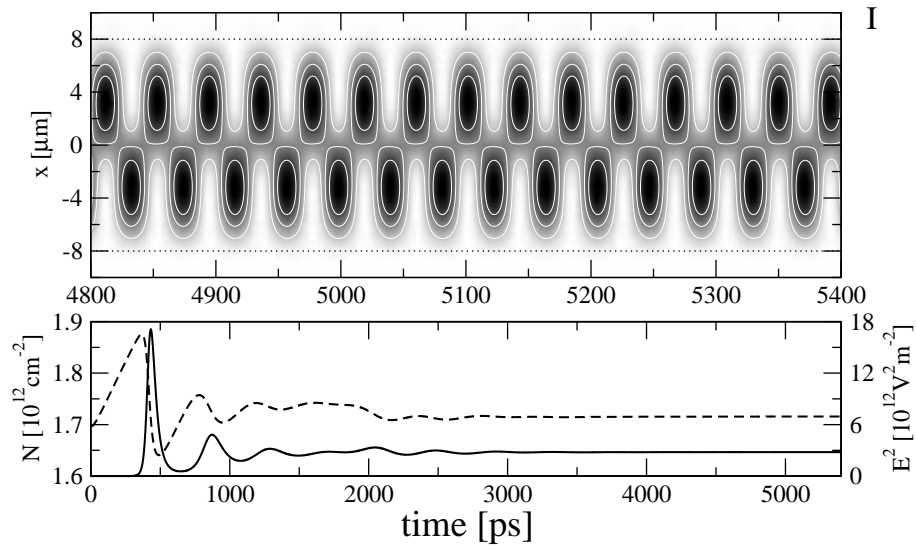


FIGURE 5.3: Spatio-temporal emission dynamics of a $16 \mu\text{m}$ wide diode laser structure for moderate pumping $\Lambda = 2\Lambda_{\text{threshold}}$.

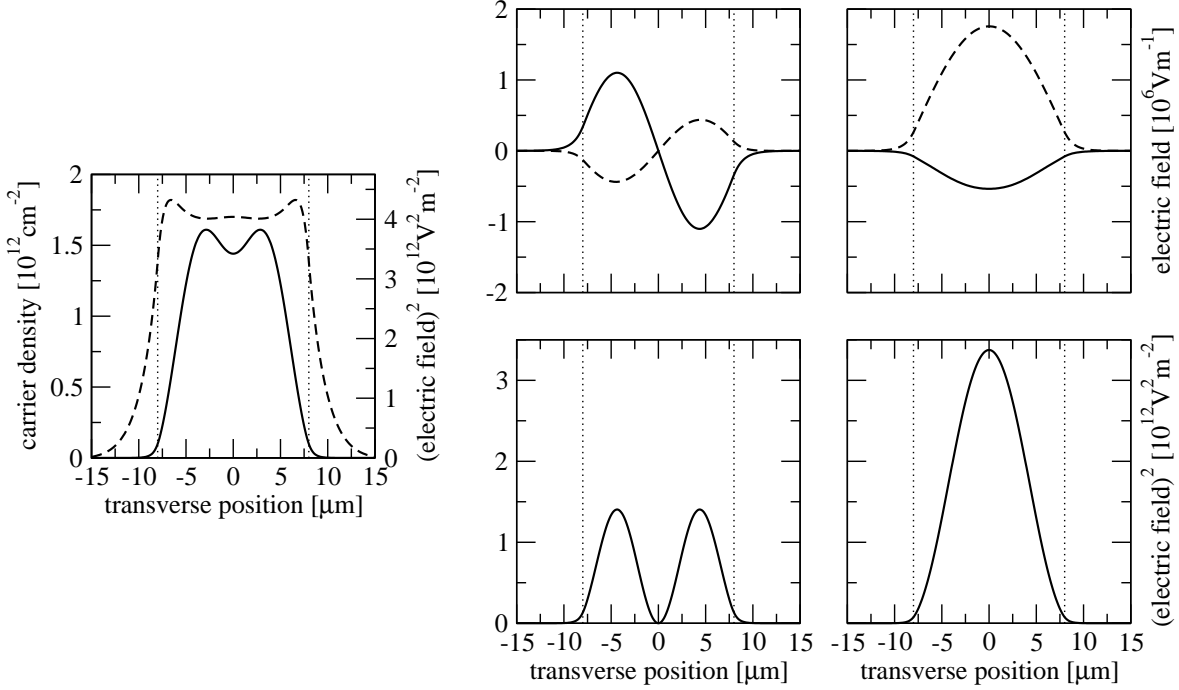


FIGURE 5.4: (Left graph) Transverse profiles of the carrier density $\langle N(x, t) \rangle_T$ (dashed) and of the electric field amplitude squared $\langle |\tilde{E}(x, t)|^2 \rangle_T$ (solid line) averaged over the time interval $t \in [3.6 \text{ ns}, 5.4 \text{ ns}]$ ($T = 1.8 \text{ ns}$). The real and imaginary components (top; solid and dashed lines, respectively) and the absolute values squared (bottom) of the transverse active laser modes $c_{\text{mode}} \tilde{E}_{\text{mode}}(x; \omega_{\text{mode}})$, as numerically determined from spectral filtering (projection) operations according to (5.14), are depicted: fundamental, symmetric mode with the oscillation frequency $\omega_0 = 2.31066 \cdot 10^{15} \text{ s}^{-1}$, $\lambda_0 = 815.2005 \text{ nm}$ (right column), and first order transverse eigenmode (antisymmetric) $\omega_1 = 2.31081 \cdot 10^{15} \text{ s}^{-1}$, $\lambda_1 = 815.1469 \text{ nm}$ (middle).

5.5+5.6), higher order modes show up supported by the carrier, gain and refractive index profiles. The spatio-temporal emission can be characterised in the mode picture as superposition and beating of several transverse modes (as spectrally filtered spatial near-field distributions). Spatio-temporal patterns evolve on picosecond time scales. The optical field dynamics can be projected, using (5.14), onto laser eigenmodes. The simulations shown in FIGURE 5.3 reveal an alternating right-left pulsing of the optical intensity with a time period of 41.3 ps. We also note that this quasi-periodic or regular spatio-temporal dynamics is a non-transient behaviour; a constant electrical pumping level is applied, and we see from the graph at the bottom that after $\approx 3 \text{ ns}$ the integrated intensity as well as density are constant. The spectral decomposition of the near-field pattern (cf. FIGURE 5.4) shows that in addition to the (Gaussian) fundamental mode a higher order transverse mode (with a higher eigenfrequency) is excited. The beating and superposition of these two modes with different spatial distributions (and hence carrier baths), symmetries and oscillation frequencies (because of the additional component k_{tr})

result in the high frequency switching of the output intensity. FIGURE 5.4 shows the carrier and spectrally filtered field profiles. The coexistence and interaction of two modes with $\Delta\lambda = 0.0536$ nm, $\Delta\nu = 24.19$ GHz and $|c_0|/|c_1| = 1.537$ induce a high frequency oscillation of the optical intensity between the left-hand and right-hand edges of the pumped region (stripe width $W = 16$ μm), for more details see FIGURE 5.3. We see that the two modes interact with different spatial regions of the inversion distribution. Our simulations demonstrate the dependence of spatio-temporal emission dynamics on the stripe width of a semiconductor broad area laser. The dynamic regime of single-mode operation and damped relaxation oscillations (class-B laser system) becomes unstable at a critical parameter of $W_{\text{crit}} = 16$ μm , which is in close agreement with theoretical predictions from (5.11). The mode analysis allows for the characterisation of spatio-temporal complexity and an estimate of the number of dynamical degrees of freedom. We note that in our simulations of transverse multi-mode laser dynamics, the induced polarisation variables are not adiabatically eliminated, unlike in [12, 36, 37, 140], as a consequence the spectral variation of the gain (and the dispersion) acts as natural mode selection mechanism.

The results shown in FIGURE 5.6 further support the validity of the mode picture. We find (for $W = 50$ μm) seven dominant modes (and associated peaks in the laser output spectrum $\sum_x |\tilde{E}(x, \Delta\omega)|^2$). The numerically computed properties of these higher order transverse modes—field distributions, laser frequencies $\Delta\omega_{\text{mode}}$, and symmetries (in respect of the transverse coordinate x)—confirm in the main the simple analytical estimates derived in (5.2). We note small asymmetries and deviations of the extracted modes from perfect distributions (see e.g. $\text{Re}(c_1 \tilde{E}_1(x; \omega_1))$), and that $\langle |\tilde{E}(x, t)|^2 \rangle_T$ slightly differs from the summed modal intensities $\sum_{\text{mode}} |c_{\text{mode}}|^2 |\tilde{E}_{\text{mode}}(x; \omega_{\text{mode}})|^2$. We note that the mode analysis assumes the linear superposition of the various spectral contributions, and it is based on spectral filtering using Fourier transformation. The transverse density, gain and refractive index profiles, supporting the various laser modes, can be well approximated as flat (constant) over the pumped, active area [141]. Our time-domain approach enables the investigation of temporal changes in the mode structure as the effect of the slow carrier and/or temperature dynamics (e.g. spatial transport processes) and therefore changing gain $g[N(x, t), T(x, t)]$ and index profiles $\delta n[N(x, t), T(x, t)]$ [12].

FIGURE 5.11 gives an insight into the microscopic carrier and gain dynamics of a 50 μm wide broad area laser with two optically active electron and two hole subbands. As the imprints of the optical field dynamics we see spectral hole burning in the carrier distribution functions $\delta n_k^\circ(t) = n_k^\circ(t) - f_k^\circ[N(t)]$, and interband polarisations $|p_{11,k}(t)|, |p_{22,k}(t)|$.

In FIGURES 5.7+5.8—important laser parameters include $W = 16$ μm , $\Lambda = 4\Lambda_{\text{threshold}}$, and $\delta n_{\text{pas}} = 0$ —a spontaneous symmetry breaking occurs and the laser intensity gradually migrates to one edge of the stripe. We interpret this irregular dynamic behaviour as a consequence of the high linewidth enhancement factor and the strong carrier-induced changes of the refractive index $\delta n[N(x)]$ in semiconductor-based active structures. We find a spatio-temporal instability resulting in the spontaneous breaking of the symmetry and a drift of the intensity profile to one edge of the stripe in combination with con-

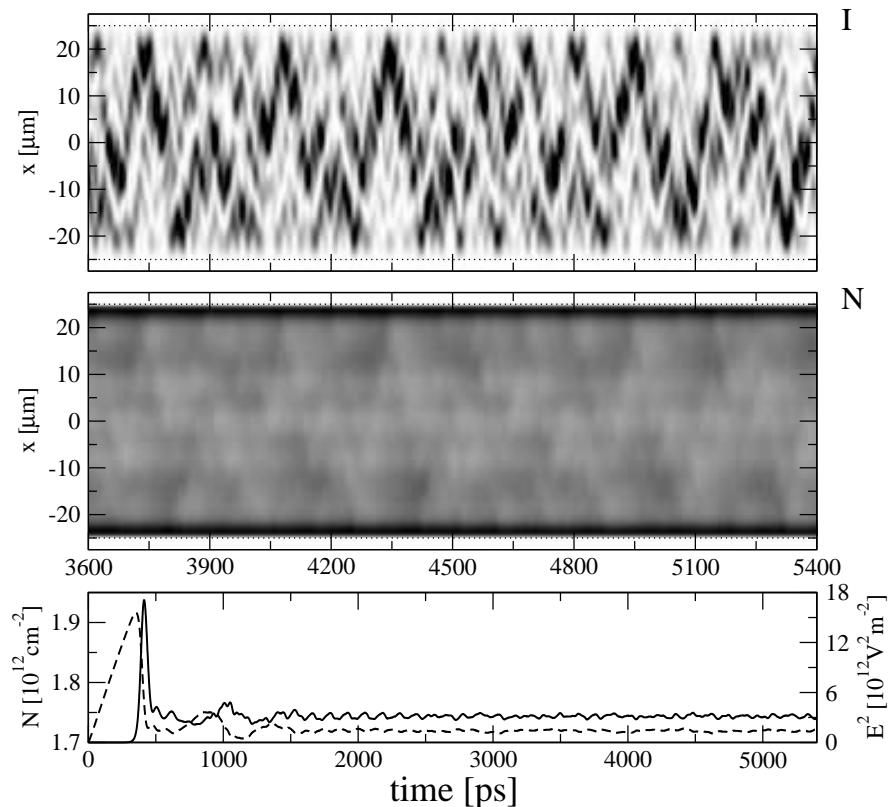


FIGURE 5.5: Same as FIGURE 5.1, but for a $50\ \mu\text{m}$ wide edge-emitting semiconductor laser. The calculation of the spatially resolved output spectrum $|\tilde{E}(x, \Delta\omega)|^2$ and a spectral decomposition of the electric field amplitude time dynamics, based on equation (5.14) (see FIGURE 5.6), shows that the observed spatio-temporal behaviour may be explained in the mode picture by the coexistence of several transverse field patterns, i.e. active laser modes (quasi-periodic regime).

tinuously decreasing integrated output power [112, 140]. The laser emission jumps back to the centre of the stripe, and a large pulse can be seen simultaneously in the laser output. The gradual migration of the intensity distribution and the asymmetric emission demonstrate the impact of the strong amplitude-phase coupling and high linewidth enhancement factor in active semiconductor devices. An accumulation of carriers not only increases the local optical gain but also leads to a repulsion of the optical field because of counteracting anti-guiding by the carrier-induced refractive index changes of the waveguide properties.

As another result of the strong amplitude-phase coupling, mediated by the α factor, a spot of the intensity creates its own confining waveguide (self-focussing) induced by optical nonlinearities. With increasing stripe width ($W = 100\ \mu\text{m}$) the influence of local dynamics is rising, and spatio-temporal instabilities and dynamical optical filamentation deteriorate the laser emission characteristics (see FIGURES 5.9+5.10). With increasing stripe width we note an increase in the spatio-temporal complexity and a gained im-

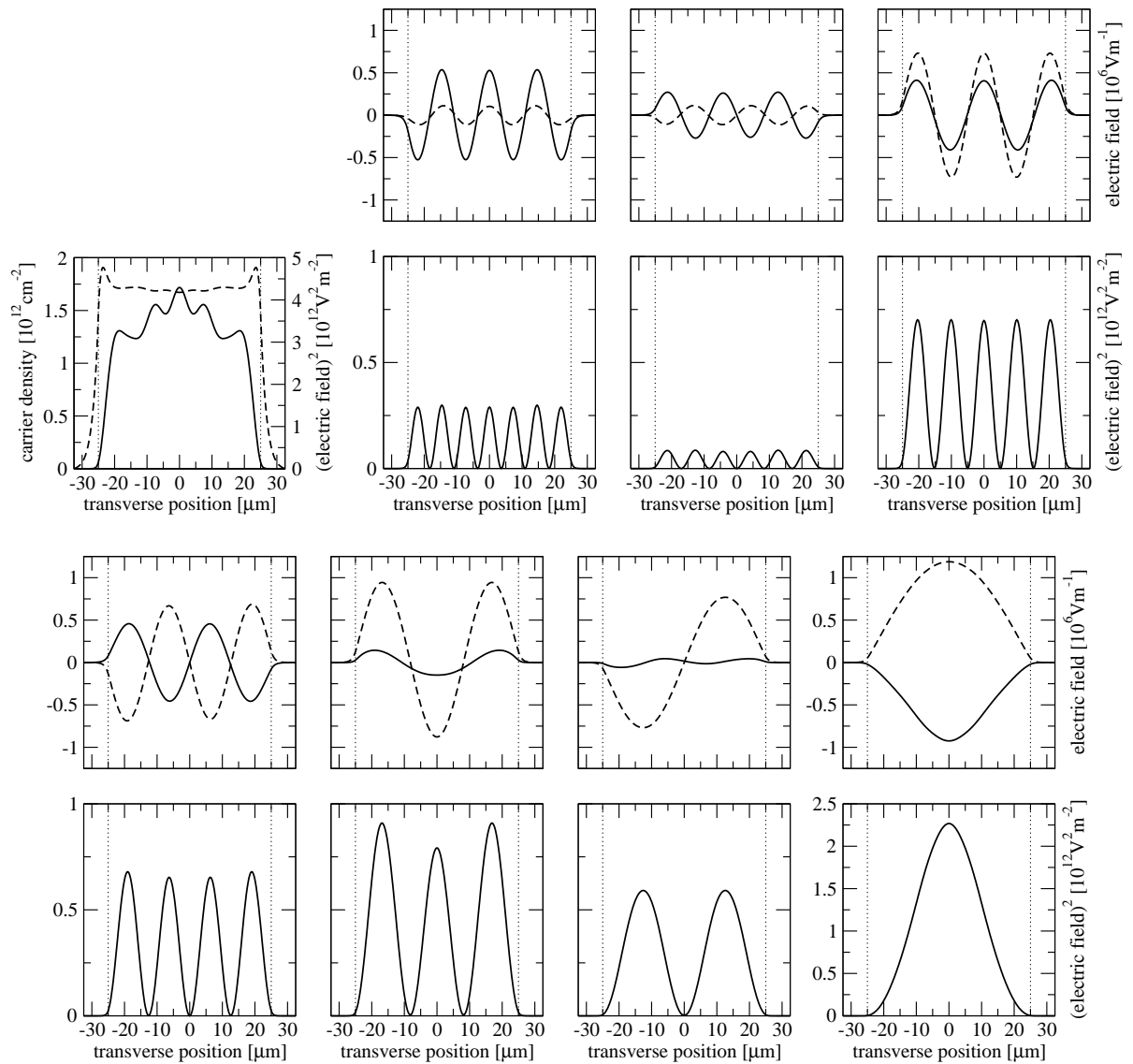


FIGURE 5.6: As FIGURE 5.4, but for a broad area laser structure with a stripe width of $50 \mu\text{m}$. Spatio-temporal emission is characterised by time-averaged transverse profiles and by the projection of the (complex) electric field amplitude dynamics onto the laser eigenmodes (for more details see (5.13)+(5.14)).

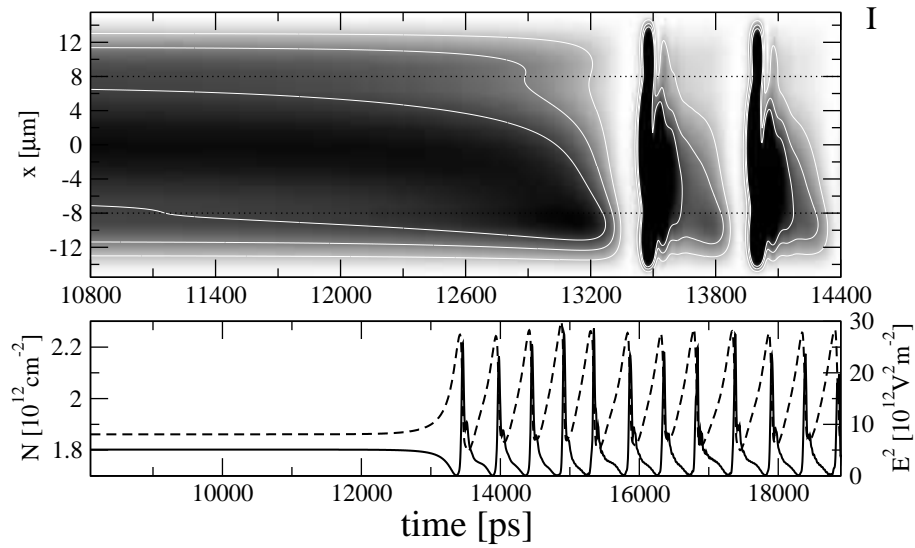


FIGURE 5.7: As in FIGURE 5.3, but at higher pumping levels $\Lambda = 4\Lambda_{\text{threshold}}$ and without a built-in rectangular index-guiding (by a ridge waveguide structure).

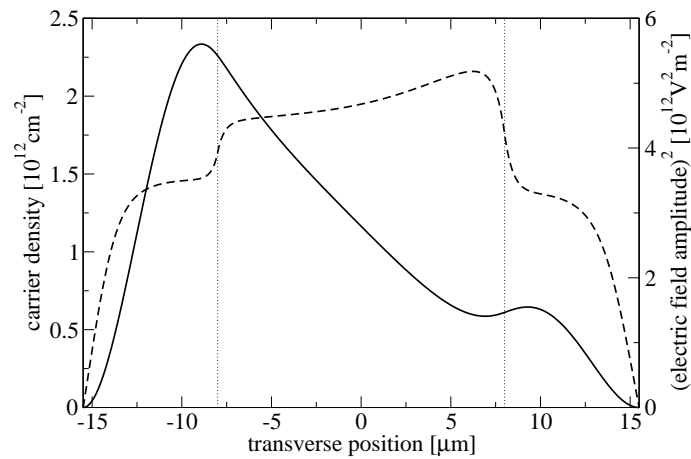


FIGURE 5.8: Transverse electric field amplitude and inversion profiles at $t = 13.2$ ns.

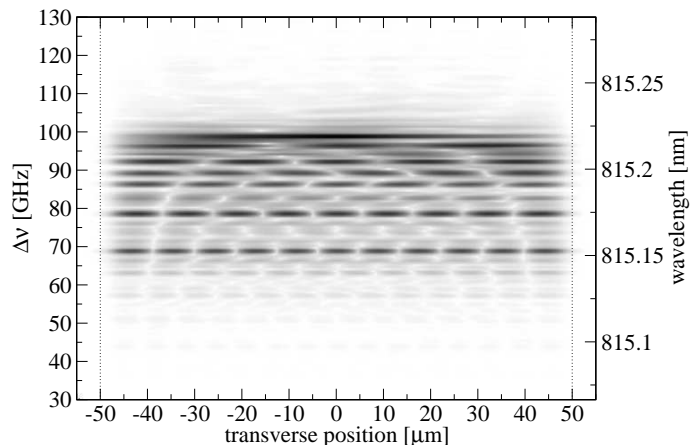


FIGURE 5.9: Spatially resolved output spectrum of a $100\ \mu\text{m}$ wide diode laser computed by Fourier transforms of the electric field amplitude time series (applying a Hann window filter [142]); depicted is the spectral electric field $|\tilde{E}(x, \lambda)|$ ($\nu = c/815\ \text{nm} - \Delta\nu$).

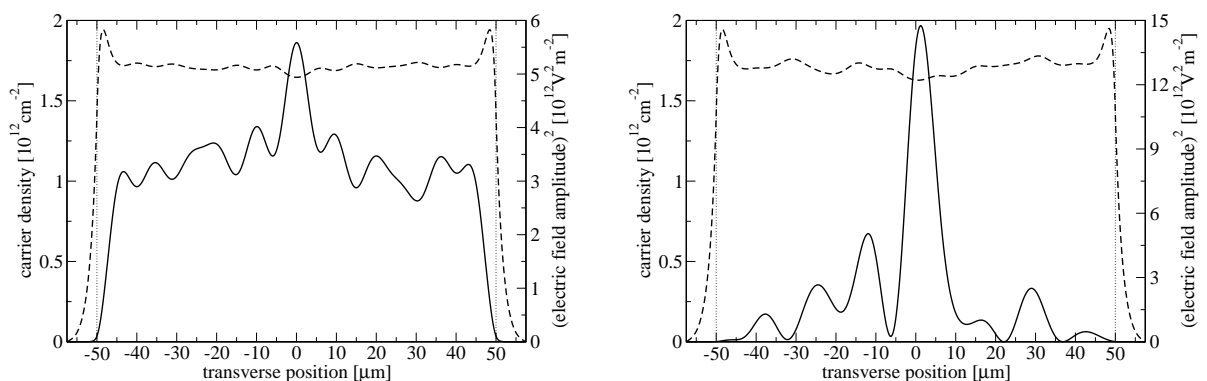


FIGURE 5.10: Depicted are the transverse profiles of the carrier sheet density (dashed) and of the electric field amplitude squared (solid line) averaged over the time interval $t \in [3.6\ \text{ns}, 5.4\ \text{ns}]$ (left graph), and at the time point $t = 5\ \text{ns}$ (right).

portance of local dynamics. The spatio-temporal emission dynamics becomes irregular and the mode resonances spectrally strongly broadened (FIGURE 5.9). The noticeable asymmetries in the left graph of FIGURE 5.10 implies that for a $100\ \mu\text{m}$ broad area laser, optical filamentation and local dynamics dominate global correlations or modes. A two-dimensional visualisation of the spatial distribution of the intracavity intensity $I(x, z, t) \propto |\tilde{E}^+(x, z, t)|^2 + |\tilde{E}^-(x, z, t)|^2$ shows the dynamics of these filamentary structures. We see the formation, interaction, breakup and longitudinal propagation (diagonal and mainly parallel to the optical axis) of optical filaments [37, 112]. Our simulations feature the intrinsic time scale of the cavity round trip time $\tau = 2Ln_{\text{eff}}/c = 23.43\ \text{ps}$.

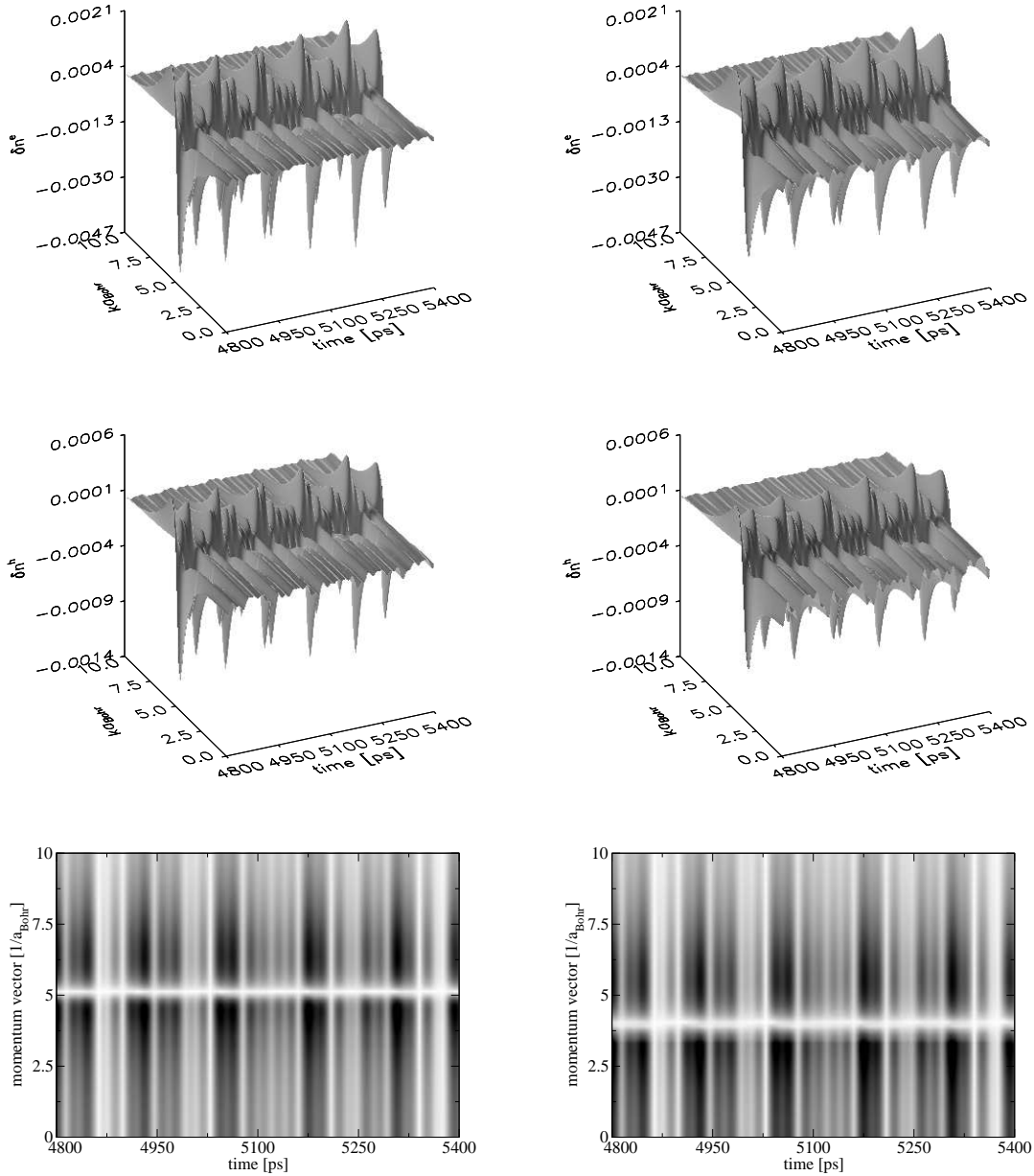


FIGURE 5.11: Microscopic, band-resolved carrier dynamics in a semiconductor broad area laser. Depicted are the non-equilibrium Wigner distributions for the electron (top) as well as hole subbands (middle), and of the induced interband polarisations (at the bottom); recorded at the position $x = 0, z = L$. The properties of the lower electron and hole subbands are plotted on the left, for the upper, optically active subbands at the right. The investigated structure contains 20 nm wide GaAs/AlGaAs quantum wells (in all other graphs in this section $d_{\text{QW}} = 5$ nm). Other simulation parameters include $k_{\text{cut-off}} = 30/a_{\text{Bohr}}$ and a resolution of 201 momentum grid points.

5.4 Conclusion

In this chapter we have applied the paraxial wave equation model in order to theoretically and numerically investigate the transverse multi-mode dynamics and optical filamentation in broad area edge-emitting laser structures. We demonstrate that with increasing stripe width and/or higher pumping powers, the gain and effective refractive index profiles become large enough to support multiple transverse laser modes. Local structures, so-called optical filaments, are focussed spots in the intensity and arise from the nonlinear optical effect of self-focussing. This multi-mode and filamentation behaviour together with the self-organised, spontaneous formation of spatio-temporal patterns, a known phenomenon in nonlinear dynamics, originate from optical nonlinearities due to hole burning, the carrier and gain dynamics, and the selective depletion of the density by the various transverse modes. The interactions of the optical field with different domains of the gain material, with different spatial (transverse degree of freedom) and spectral (inhomogeneous broadening) regions of the population inversion, result in the coexistence of multiple modes. A quantitative understanding of the impacts of carrier diffusion, gain- and index-guiding, gain saturation and self-focussing is achieved. We have presented a linear stability analysis of the transverse instability to identify the main control parameters as the stripe width, the pumping and the linewidth enhancement factor. Numerical simulations of spatio-temporal dynamics support this interpretation. Depending on the stripe width, different degrees of spatio-temporal complexity and several dynamic emission regimes have been distinguished. An eigenmode analysis of the numerically calculated complex optical field envelopes enables us to extract the lasing frequencies and the active modes, by means of discrete, spatially resolved Fourier transforms of the near-field.

6 Longitudinal Multi-Mode Laser Dynamics

6.1 VCSEL with Resonant Periodic Gain and Refractive Index Structures

Microcavity [13] or more generally micrometer-sized active laser and amplifier structures offer a couple of advantages compared to commonly used (sub-) millimeter-sized active optical elements. Examples are the strong optical confinement, large quality factors and long photon lifetimes, the low lasing thresholds, and the strong coupling of active materials with photons. These features make them attractive as compact coherent laser sources and efficient small amplifiers in photonic integrated circuits. However, most of these structures have very limited output powers and very low single-pass amplification due to the relative small size of the active gain sections. For example, a typical VCSEL structure only contains few quantum wells. In order to improve the performance of VCSEL, the overlap between the quantum-confined gain elements and the quasi-standing wave pattern can be optimised by placing the quantum wells at the antinodes of the cavity mode. The number and position of the antinodes is thereby controlled by the optical thickness of the microcavity [11, 15]. Using a resonant periodic gain structure a maximum relative longitudinal confinement factor of $\Gamma_r = 2$ can be achieved [11]. The longitudinal confinement factor Γ_z is defined in (6.3). $E_{\text{mod}}(z)$ describes the electric field profile as the stationary solution of the wave equation or of the Helmholtz equation

$$D(z, t) = \epsilon_0 \epsilon(z) E(z, t) + \left(\Gamma_{x,y} \frac{N_{\text{QW}}}{\Delta z} \right) (z) P(z, t), \quad (6.1)$$

$$\left(\partial_z^2 - \frac{\epsilon(z)}{c^2} \partial_t^2 \right) E(z, t) = \frac{1}{\epsilon_0 c^2} \left(\Gamma_{x,y} \frac{N_{\text{QW}}}{\Delta z} \right) (z) \partial_t^2 P(z, t), \quad (6.2)$$

$$\Gamma_z = \frac{\int_L dz E_{\text{mod}}^2(z) \Theta(z)}{\int_L dz E_{\text{mod}}^2(z)} = \mathcal{V}_z \Gamma_r = \frac{L_{\text{act}}}{L} \Gamma_r. \quad (6.3)$$

A further improvement of active micrometer-sized laser and optical amplifier elements can be achieved by incorporating photonic band gap materials or photonic crystal structures with high refractive index contrasts [20]. This allows to control modes and photons at the length scale of the optical wavelength [18, 19].

In the following we study the photonic band edge band gap laser, which employs gain enhancement using photonic crystal structures: We analyse asymmetric (one-

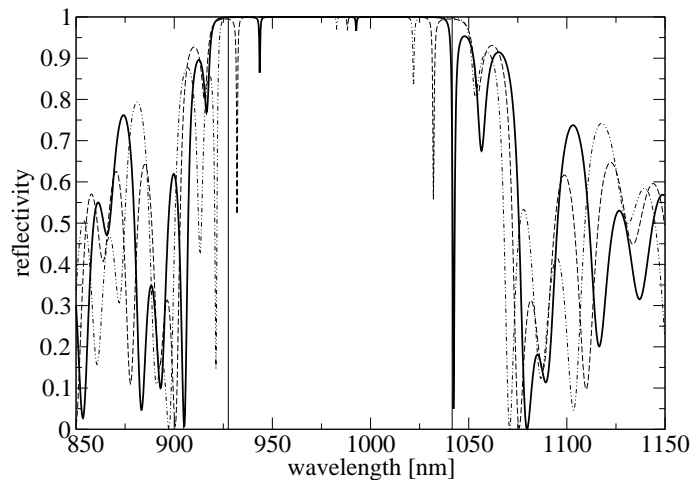


FIGURE 6.1: Reflectivity spectra of an asymmetric VCSEL structure (thick line) composed of a $13 \cdot \lambda/2$ point defect (microcavity) embedded in dielectric Bragg mirror stacks of $\lambda/4$ layers (the top DBR mirror consists of 15 pairs and the bottom DBR, grown on the substrate, of 25 pairs), and spectra of two lasing structures with an additional periodic refractive index and gain structure configuration (dashed and dot-dashed). The edges of the photonic stop band of the Bragg mirror with periodicity a_{Bragg} are for comparison plotted as thin lines (for more details see FIGURE 6.2). The active laser device operates at frequencies of resonant cavity or defect modes (within the cavity dips).

dimensional) VCSEL structures which comprise dielectric Bragg mirror stacks of $\lambda/4$ layers, an embedded resonant periodic gain structure with quantum wells placed at the antinodes of the defect modes, and an additional periodic refractive index structure $n(z) = n(z + Z)$. The device structure is depicted in FIGURE 6.7. Graded index layers (GRIN) are used to improve the carrier capture from barrier layers into the quantum wells [63]. The passive refractive index structures are characterised by the reflectivity spectra, see FIGURE 6.1. The first stop band generated by distributed Bragg reflectors and dips at wavelengths of resonant cavity modes are clearly visible.

To gain a deeper insight into the gain enhancement mechanism, we analyse the individual elements of the laser device and identify the functions of the various components. The infinite long Bragg mirror (see FIGURE 6.2) as well as periodic gain and refractive index structures (in FIGURES 6.3+6.4) with periodicity a_{Bragg} and a_{pgs} , respectively, are reinterpreted as one-dimensional photonic crystals. A common approach in discussing the properties of periodic photonic systems is to normalise the eigenfrequencies and wavevectors by the fundamental length of the crystal (because of the linearity of the basic equations, the results are scalable with the geometry). The frequencies are depicted in units of $2\pi c/a$ [20]. In a homogeneous material of uniform refractive index n_{average} the light cone is specified (for the dimensionless quantities wave number and frequency) by the relation $\omega = k/(2n_{\text{average}})$. At the edges of the Brillouin zone the modes in a homogeneous refractive index configuration show a twofold degeneracy, the perturbation through a periodic refractive index structure causes a splitting and the occurrence of a

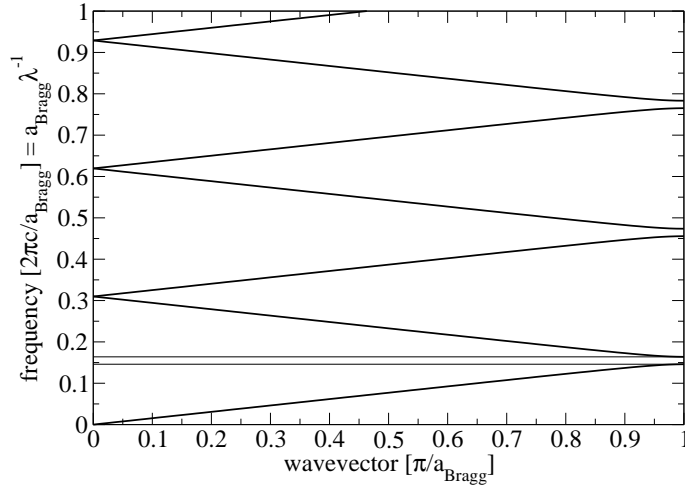


FIGURE 6.2: Band structure diagram calculated for an infinite long AlGaAs/GaAs Bragg mirror structure [143]: The unit cell of the photonic crystal consists of two layers (with refractive indices of $n = 2.96, 3.55$) and is characterised by a lattice constant of $a_{\text{Bragg}} = 152 \text{ nm}$. Considering the symmetry of the layer system and the fact that for $k > \pi/a_{\text{Bragg}}$ modes may be folded back by a reciprocal lattice vector into the first Brillouin zone, it is sufficient to consider $k \in [0, \pi/a_{\text{Bragg}}]$ [20]. Similar to the properties of electrons in a solid described by electronic band structure diagrams [5] band gaps occur at π/a_{Bragg} (i.e. there are no propagating solutions for frequencies within the band gaps). The periodic index structure acts as a frequency-selective filter, i.e. it functions as mirror for wavelengths within the band gaps.

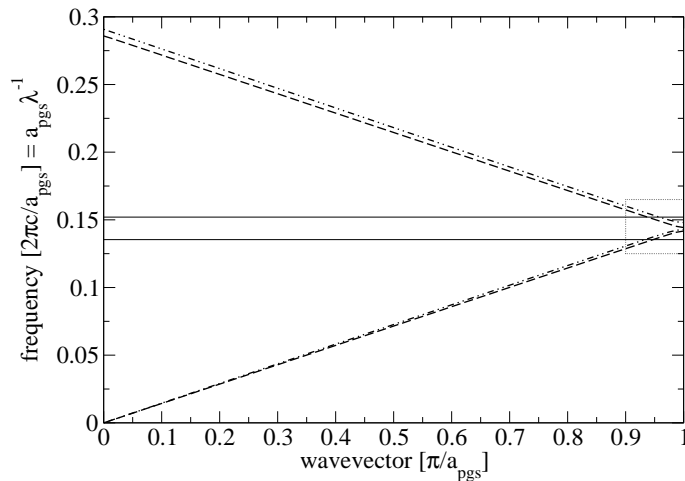


FIGURE 6.3: Band structure diagram of infinite long periodic (graded) index structures with $a_{\text{pgs}} = 141 \text{ nm}$ and different refractive index contrasts Δn [143]. In an actual device these structures are enclosed within an asymmetric Bragg mirror configuration. A more detailed graph of the band structure near π/a_{pgs} (showing flat dispersion curves near the photonic band edges) is given in FIGURE 6.4.

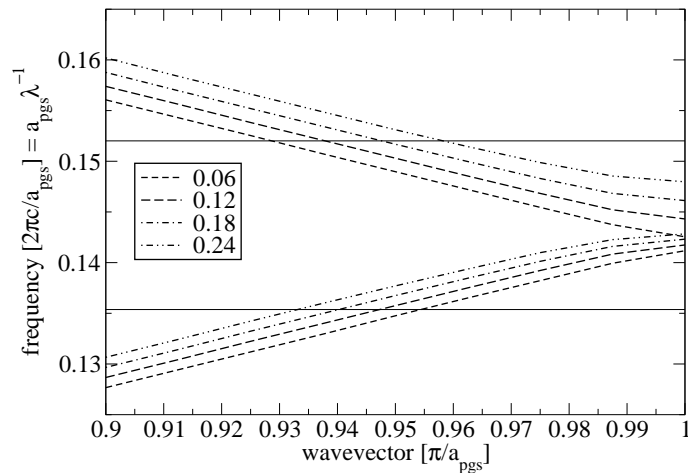


FIGURE 6.4: Resonant periodic gain and GRIN structures, and Bragg mirror stop band (plotted as thin lines).

frequency interval where the optical density of states is zero. In the lower branch the maxima of the standing waves are in the higher index material, whereas in the upper branch the modes are mainly localised in the lower dielectric material [20]. FIGURE 6.4 shows an increasing photonic band gap and a shift of the eigenfrequencies to higher values on decreasing the average dielectric constant n_{average} and increasing Δn . We consider structures with different index contrasts (as the depths of the GRIN is altered). At the band edges the dispersion is flat associated with a zero group velocity. Of special interest is the region near the long-wavelength side of the band gap, where the maxima of the standing wave patterns are localised in the high index material at active gain elements. Thus, this photonic crystal provides the effective gain enhancement for the photonic band edge modes. The slow down of propagating waves is associated with more gain per unit length. FIGURE 6.2 shows the band structure of an infinite long dielectric Bragg mirror. For a range of frequencies the eigenvalues and the group velocities are purely imaginary, which corresponds to evanescent waves. For normalised frequencies of the photonic band edge modes equal to $a_{\text{pgs}}/\lambda \approx 0.142$, this photonic crystal acts as a mirror. A photonic band edge band gap laser is composed of two photonic crystal structures: In the finite-sized VCSEL the flat dispersion curves near the photonic band edges in the band structure diagrams of the inner GRIN are used for lasing operation. The photonic band gap provided by the surrounding photonic crystal minimises the losses of the laser mode.

In summary, operating the laser at frequencies of $a_{\text{pgs}}/\lambda \approx 0.142$ and controlling the optical modes by exploiting the special properties of photonic band gap materials improves the performance of the laser device. The periodic GRIN pattern stimulates the band edge enhancement of the effective gain and an optimum overlap between the laser mode and the resonant periodic gain structure. The DBR suppresses the optical losses of photonic band edge modes [18, 19, 144]. We note that the refractive index contrasts of the analysed periodic structures are relatively low. Thus, to achieve the special proper-

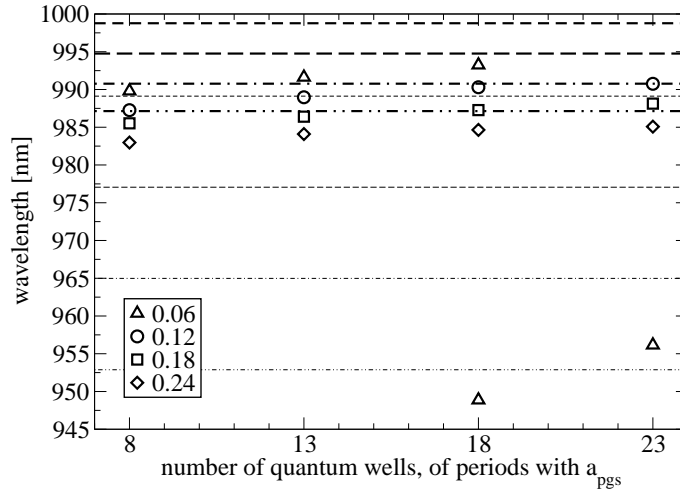


FIGURE 6.5: Operating wavelength of the laser device: Plotted are the edges of the band structure diagram FIGURE 6.3 (with the lower branches as thick lines) and the active laser frequencies as computed using the FDTD method (symbols). With an increasing number of quantum wells and periods of the index structure with a lattice constant of a_{pgs} the frequencies of the lower band edges as the limits are approached. The concept of the photonic band edge laser [18, 144] is to capitalise on the special properties of the singularities in the band structure diagrams, and it is based upon gain enhancement by an increased localisation of the modes over the active quantum confined structures [11, 15] and a more efficient interaction of photons with an active material in a photonic crystal structure. The two deviating wavelengths around 950–955 nm are linked to a different cavity dip.

ties offered by photonic band gap materials and to reach the limits of the infinitely long structures a certain number of periods of the crystals are required.

We next test the above discussed control of photons by periodic refractive index structures and the mode and gain enhancement in these novel VCSEL structures. The numerical simulation of real, finite-sized samples and the calculations of the operating wavelengths (see FIGURE 6.5) and threshold carrier densities (see FIGURE 6.6) demonstrate the significant improvements. FIGURE 6.7 shows that the specified concepts of effective gain enhancement become more distinctive with increasing number of periods of the finite structure and increasing refractive index contrasts.

Recently, a two-dimensional photonic crystal slab laser structure based on the concept of photonic band edge lasing [144] assisted by a photonic band gap has been demonstrated [18]. Its design is based on the enhancement of the effective gain in periodic systems $\epsilon(\mathbf{r}) = \epsilon(\mathbf{r} + \mathbf{R})$ (\mathbf{R} describes a lattice vector) by the singularities of the optical density of states at points of zero group velocity at the photonic band edges [19], either from confinement or periodicity. As a consequence, the photon dispersion relations $\omega(\mathbf{k})$ close to the band gaps become more flat, and the group velocity is reduced. The

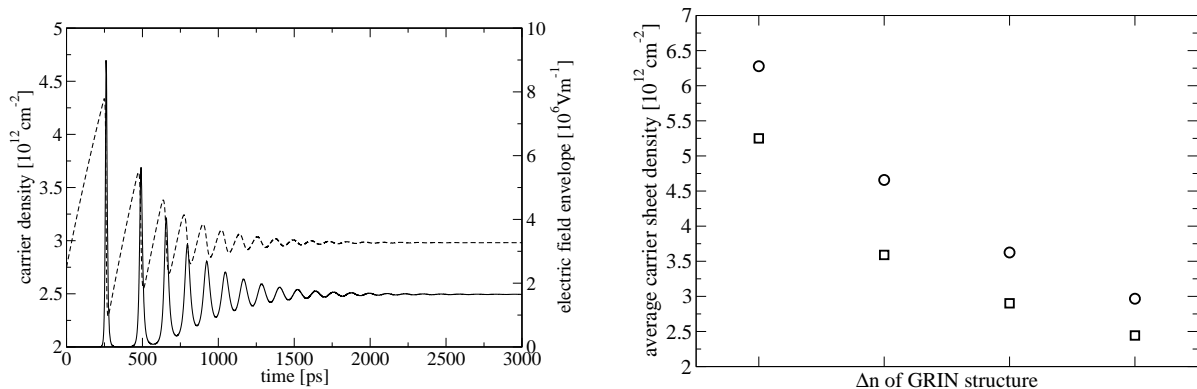


FIGURE 6.6: Carrier sheet density (dashed) and electric field envelope (solid line) at the position of the gain elements versus time (in picoseconds). The simulations show typical relaxation oscillations of the semiconductor-based class-B laser system (for more details see SECTION 4.3) towards the steady state characterised by N_{st} and $(E_{\text{env}})_{\text{st}}$. In the right diagram we show the averaged stationary (threshold) carrier density in the quantum wells for a periodic gain and refractive index structure with 13 (circles) and 18 (squares) periods. The photonic band edge laser design optimises the mode and gain enhancement [11, 18, 144] and consequently reduces the threshold for lasing.

thresholds for lasing decrease as the photons in the photonic crystal can interact with the active quantum well material more efficiently (i.e. for a lengthy period) and the coupling between cavity mode and gain material is enhanced (see FIGURES 6.6+6.7). To recapitulate, the wave is slowed down and experiences an increased gain per unit length. In a real sample, the periodic photonic crystal structures are finite-sized, and the group velocities at the band edges are small but nonzero. Consequently, the laser modes represent quasi-standing waves and optical losses occur. An outer photonic crystal region maximises the quality factor of the photonic band edge mode. Both types of laser, utilising 1D (our VCSEL device) and 2D photonic crystal structures, are examples of photonic band edge band gap lasers [18]. Finite-difference full time-domain simulations of the lasing frequencies and thresholds and of the field profiles fully support the theory of gain enhancement. We note that some of the functional ingredients are also implemented in conventional distributed feedback (DFB) lasers, which are structures with very low index contrasts.

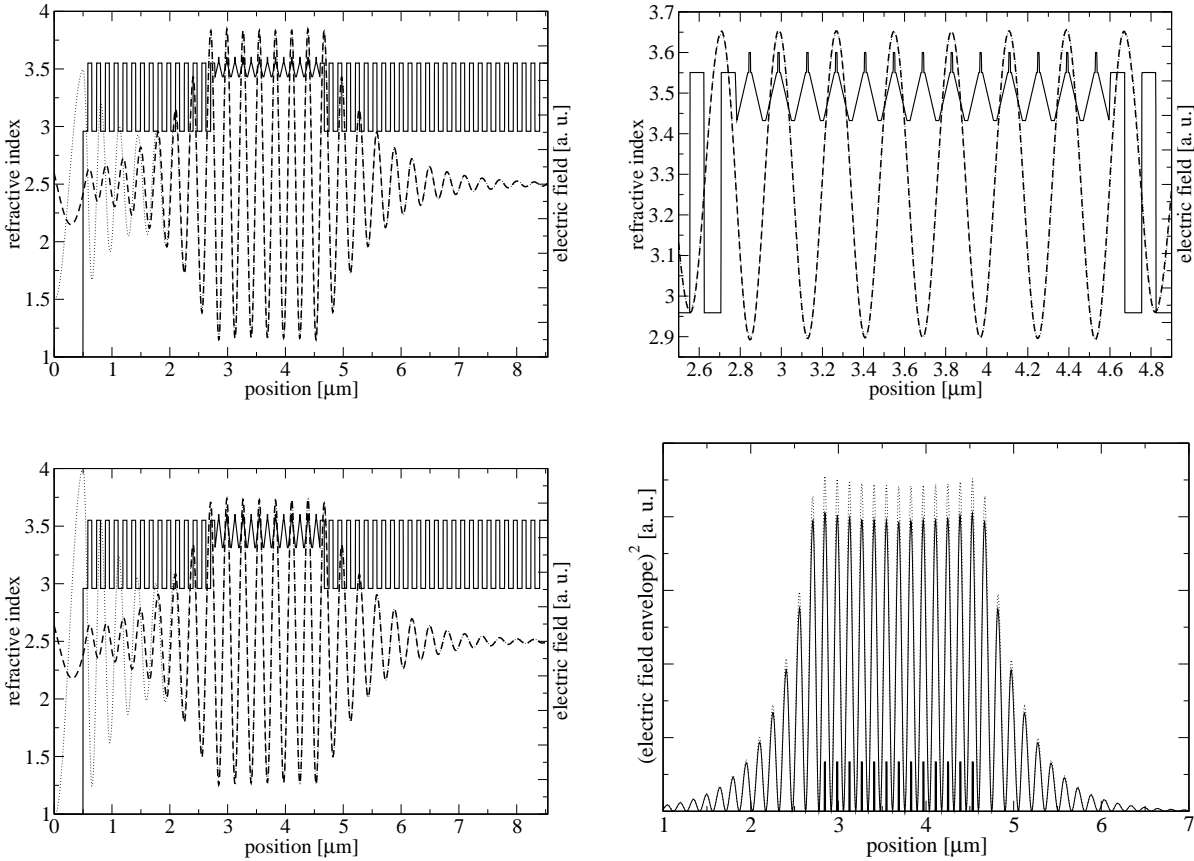


FIGURE 6.7: Electric field profile and refractive index structure for a configuration with $\Delta n = 0.12$ (at the top) and for $\Delta n = 0.24$ (bottom). The laser mode is becoming more strongly confined over the active quantum wells with increasing contrast of the GRIN structure (see bottom right graph). In the left column we compare the electric field profiles of the laser system simulated using the finite-difference full time-domain model (dashed lines) with transfer matrix calculations [11, 139, 145] (dotted lines) of the passive structure. We note the very close agreement between laser mode and cold-cavity mode. The discrepancies of the profiles in the left Bragg mirror are due to different boundary conditions and excitations. In the full time-domain solver sources of the electromagnetic field are placed in the defect cavity and absorbing boundary conditions are applied. The transfer matrix method starts with the constraint of an out-going wave at the right boundary, a to the right travelling plane wave, and calculates the reflected and transmitted components at every layer surface. Consequently, for passive structures and real-valued dielectric constants there are at the left boundary to the left and to the right travelling wave components. We note that in finite length structures the mode enhancement is not uniform over the pattern, but highest near the centre of the periodic index structure [144].

6.2 Optically Pumped VECSEL

A modified version of the VCSEL structure is the vertical external cavity surface-emitting laser (VECSEL). A simplified schematic of this novel type of laser structure is shown in FIGURE 6.8. VECSEL are bridging the gap between semiconductor diode lasers and optically pumped solid-state lasers [33]: An external laser cavities enforces the optical output in low divergence, circular TEM_{00} beams. Optical pumping techniques offer power scalability by the increase of the active, pumped area. With this, a combination of continuous wave high-output power and near-diffraction-limited beam quality can be achieved [16, 17]. The use of semiconductor gain materials renders the possibilities of band gap engineering and semiconductor processing technologies. Also, complex optical layer structures can be grown. The optical pumping scheme and external mirror configuration permit high-power operation by an increase in the size of the active region (a uniform carrier distribution over a large aperture is achieved) without the occurrence of transverse multi-mode dynamics. Mode beating effects, instabilities and filamentation and large beam divergence are known to limit the performance of broad area lasers [36, 37, 106, 130], and wide-aperture surface-emitters [12, 131]. The open structure of the VECSEL allows to introduce nonlinear optical elements into the cavity. The ready access to the lasing mode is exploited for applications such as passive mode-locking using semiconductor saturable absorber mirrors (SESAM) or frequency doubling by nonlinear crystals [16, 17, 33]. An inherent drawback of the external mirror design is that the optical setup is less compact and requires the precise alignment of multiple discrete components. A monolithically integrated device structure, a so-called microchip VECSEL, may offer a

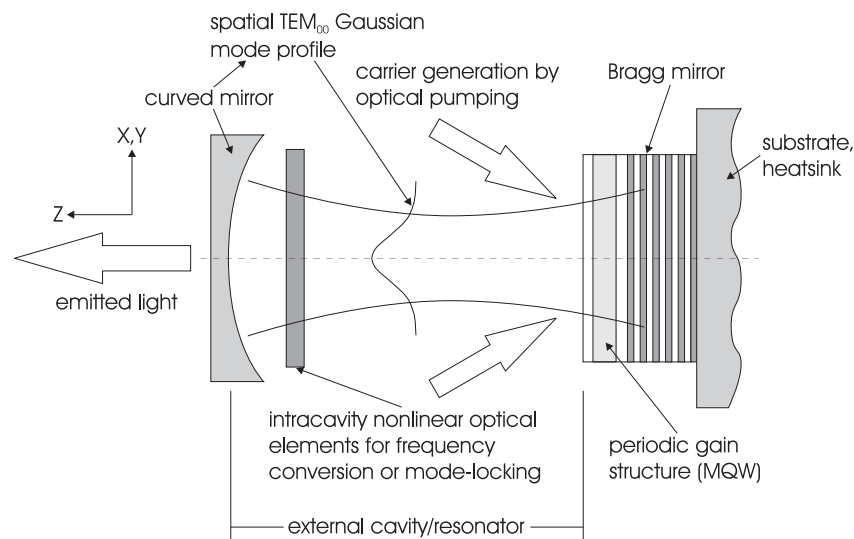


FIGURE 6.8: Simplified schematic of an optically pumped vertical external cavity surface-emitting semiconductor laser structure [15–17, 33, 86, 133, 134, 146, 147]. The optoelectronic device (coherent light source) comprises a resonator, defined by a dielectric Bragg reflector and an external cavity with a curved mirror, a resonant periodic gain structure, an optical pumping mechanism, and intracavity nonlinear optical elements.

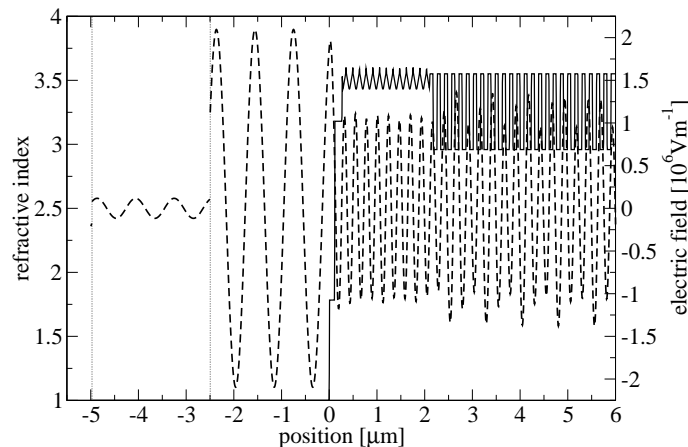


FIGURE 6.9: Refractive index structure of a realistic vertical extended cavity surface-emitting laser device, and snapshot of the electric field profile including the carrier wave (lasing has not yet set in). The points of discontinuity in the electric field profile are connected to the positions where the external optical fields (that are to the right travelling plane wave components) are injected into the active structure: The continuous wave optical pump is realised at $-2.5 \mu\text{m}$ (with parameter $E_{\text{env}} = 2 \cdot 10^6 \text{ Vm}^{-1}$, which translates to an intensity of approximately 2 MWcm^{-2} and, assuming a Gaussian transverse intensity profile with a FWHM of $50 \mu\text{m}$, to a pump power of few 10 W). A delayed optical feedback boundary condition is implemented at $\approx -5 \mu\text{m}$ to mimic external cavities of some cm length. We note the exponential decay of the electric field (the pump) over the periodic gain and the graded index layer structure (with $\Delta n = 0.12$, for more details see FIGURE 6.7).

solution to this problem [134]. A more detailed diagram of a realistic VECSEL structure plus the numerical implementation of optical pumping and of the external cavity (via the longitudinal delayed optical feedback boundary conditions, see APPENDIX A) is depicted in FIGURE 6.9. We note the resonant periodic gain and graded refractive index structures as analysed in SECTION 6.1. The actual laser sub-cavity is coupled to the external resonator by means of an anti-reflection coating (for the pump). The Bragg mirror is not highly reflective for the pump wavelength of 808 nm . In transverse or radial direction static field profiles are assumed. In our effective longitudinal, one-dimensional model, the structures and physical processes in radial direction are accounted for by radial averaging and the introduction of effective parameters, e.g. the transverse confinement factor $\Gamma_{x,y}(z)$. In conclusion, the increased power performance (scalable to continuous wave output powers of some 10 W) of this novel type of surface-emitting semiconductor laser structure is accomplished by the adaptation of optical pumping technologies originally developed for solid-state laser systems. Optically pumped VECSEL convert (with reasonable efficiency) low beam quality optical pump power from multi-mode high-power diode laser bars into near-diffraction-limited, circularly symmetric output beams of the fundamental transverse mode [33]. This combination of high-output power and good beam quality (in continuous wave operation or mode-locked) together with the compact

semiconductor-based design is attractive for a wide range of industrial applications such as materials processing, leading edge projection and display technologies (laser TV), spectroscopy or high-bandwidth telecommunication.

In the following, the various functional constituent parts of this novel laser type will be specified [16, 17, 33, 133, 134]. Capabilities, key design aspects and operating principles will be analysed.

Semiconductor wafer design and external laser cavity: A vertical extended cavity surface-emitting laser basically resembles a VCSEL structure (see FIGURE 6.7), however, one of the DBR mirrors is replaced by a transparent (wide band gap) window layer and an external spherical mirror. Typical values for the radius of curvature are 50 mm, a cavity length of few cm, and an optical mode diameter on the chip of some 100 μm . A VECSEL works like a diode-pumped thin disk solid-state laser, but replaces the disk with a surface-emitting semiconductor active mirror structure, which comprises of a Bragg mirror and an active region consisting of an array of quantum wells. The utilisation of semiconductor gain materials offers a flexible choice of laser emission wavelength. Epitaxy and processing technologies allow for the realisation of sub-wavelength index and gain structures. The quantum wells can be positioned periodically (at half-wavelengths intervals) in the antinodes of the laser standing wave. A resonant periodic gain structure is formed with $\Gamma_r \approx 2$. A one-dimensional photonic crystal involves the further enhancement of the effective gain for photonic band edge modes, for more details see SECTION 6.1. However, the enhancement of the effective modal gain by the longitudinal confinement factor proceeds at the expense of narrow spectral filter windows, as $\Gamma_r(\lambda)$ is peaked at the etalon resonances of the sub-cavity between Bragg mirror and the air surface. To be more tolerant to variations of the device structure and less temperature sensitive, and for applications that require a very broad gain bandwidth (e.g. mode-locking), the spectrum of $g_{\text{mod}}(\lambda)$ can be flattened as the etalon resonances are broadened and weakened by anti-reflection coatings¹, by double quantum well resonant periodic gain structures (wells are distributed in pairs) [15], or by using a relatively short active structure.

Optical pumping scheme: A main advantage of optical pumping is the possibility to define a uniform distribution of pump power over a broad active region (e.g. 200 μm diameter). This creates a controlled, homogeneous carrier profile over a large aperture. Also, undoped semiconductor materials can be used which reduces optical losses due to free carrier absorption and heat deposition. The optical pumping (pump optics is AR coated) occurs via interband transitions and the generation of electrons and holes in the pump-absorbing barrier material. Because of the broad pump bandwidth and the high densities, the pump light is converted into carriers within the barriers in a single pass. The carriers are diffusing and captured into the lasing states of the quantum wells and participate in stimulated emission [16]. An alternative approach is in-well pumping,

¹AR coatings are composed of transparent thin films, with multi-layers of contrasting refractive index and different thickness. The functionality is based on destructive interference. For a single-layer AR coating of thickness $\lambda/(4n_{\text{AR}})$ the optimum value is given by the geometric mean of the surrounding indices $n_{\text{AR}} = \sqrt{n_{\text{air}}n_{\text{sub}}}$. AR coating is also important for optical pumping.

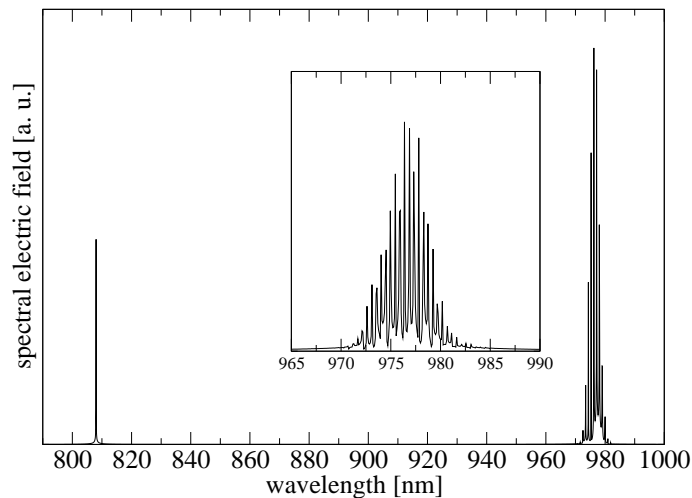


FIGURE 6.10: Spectral distribution of the electric field: The peaks in the spectrum are generated by optical pumping at $\lambda_{\text{pump}} = 808$ nm (from reflections) and by several longitudinal, external cavity laser modes at ≈ 975 nm. The simulated external resonator structure has a length of $L_{\text{cav}} = 0.5$ mm and 1 mm (in inset), respectively, which translates to a longitudinal mode spacing of $\Delta k = \pi/L_{\text{cav}} \rightarrow \Delta\lambda \approx \lambda^2/(2L_{\text{cav}})$. For the 1mm long external cavity configuration the multi-mode, continuous wave solution consists of approximately 20 longitudinal modes with mode spacing of ≈ 0.5 nm.

which reduces the heat generated within the chip as the quantum defect is minimised [146]. Due to low absorption multi-passing and a rather complicated optical setup with a resonant cavity for the pump light is required. An example of the optical intracavity field dynamics is given in FIGURE 6.10: The laser operates in a group of longitudinal, external cavity modes that fit in an etalon resonance within the mirror bandwidth. The optical pumping, carrier relaxation and lasing due to stimulated emission are characterised in FIGURE 6.11.

Thermal Design: High-power continuous wave operation of VECSEL requires the efficient heat removal from the resonant periodic gain structure or pumped region on a large area. As long as one can assume one-dimensional heat flow into the heatsink, the laser structure is power scalable. The heat can be either extracted through the DBR mirror, or a heat spreading plate technique can be applied [17]. Indeed, real optically pumped VECSEL devices suffer from the strong intrinsic temperature dependence of the semiconductor gain material², and the shift of the relative longitudinal confinement factor with temperature further reduces the effective gain. The maximum output power is ultimately limited by thermal rollover.

Intracavity nonlinear optical elements: Intracavity circulating powers in VECSEL devices frequently exceed the output power by a factor of approximately 50. For this reason,

²With higher pumping of the active region and rising temperature, the available material gain diminishes. To compensate for that the inversion has to increase (no density pinning from gain clamping). With higher carrier densities and temperatures the loss channels, mainly Auger recombination, become more important, and the thermal load per absorbed pump photon increases.

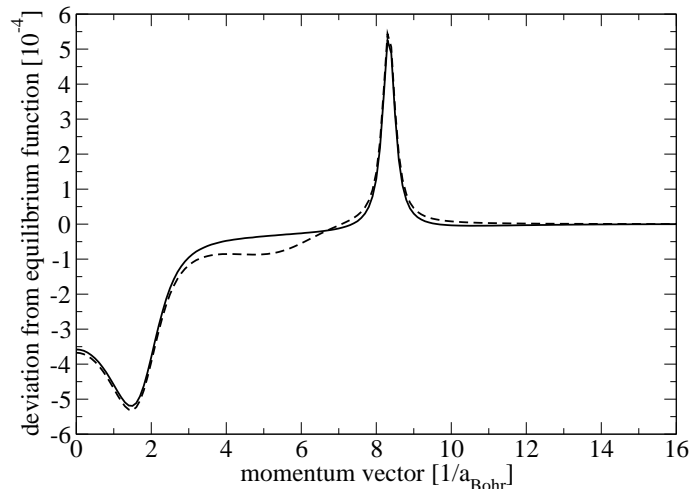


FIGURE 6.11: Spectral hole burning and spectral selective carrier generation originating from lasing and optical pumping, respectively; depicted are deviations of the actual distribution functions for the electrons (dashed) and holes (solid line) from the quasi-equilibrium Fermi-Dirac distributions. After a few nanoseconds the transient relaxation oscillations are damped out, and a quasi-stationary state is achieved. Carrier generation due to pumping into high energy states of the band structure (in-well pumping), momentum relaxation of carriers towards the Fermi-Dirac distribution and stimulated recombination from states near the band edge are in a dynamical balance. The active mirror contains a periodic structure of 8 nm wide (high gain, compressively strained) InGaAs/GaAs quantum wells (plus spacer, GRIN and stress compensation layers) and a high contrast GaAs/AlAs DBR. In this section, we assume $\gamma_k^e = \gamma_k^h$. The pumping wavelength is 808 nm.

physical processes based on the placement of nonlinear optical elements into the extended cavity are comparatively efficient, examples are nonlinear frequency conversion and the saturation of absorber elements. Applications include frequency doubling of infrared surface-emitters using nonlinear optical crystals to attain powerful and compact sources of coherent, single-mode light in the green and blue wavelength regions (which can be used for projection and display technologies). VECSEL structures are also attractive for ultrafast optical pulse generation using the the concept of passive mode-locking. This can be achieved by integrating semiconductor saturable absorber mirrors³ as developed for pulse generation in solid-state lasers. The broad gain bandwidth (the active laser sub-cavity has to be AR coated at the operating wavelength) and the high intracavity powers support the mode-locking process. Pulses generated by surface-emitting structures are typically less chirped than pulses from edge-emitters due to the comparatively short

³As the absorber section has to saturate at lower pulse intensities than the gain section, the effect of any resonant enhancement for the SESAM may also be taken into account, see SECTION 6.4. A cavity mode designed to be more tightly focussed on the SESAM than on the gain structure (in our one-dimensional model the mode area determines the coupling or overlap factor $\Gamma_{x,y}(z)$) helps to achieve the conditions for stable, self-starting mode-locking.

length of the highly nonlinear waveguide [17]. The self-starting pulse generation and pulse shaping mechanisms in passive mode-locked lasers take advantage of the various temporal regimes that can be distinguished in the evolution of non-equilibrium distributions generated by optical excitations (pulses) in semiconductor absorber materials (see SECTIONS 6.4+6.5).

6.3 Small Signal Gain Calculations

In this section we analyse the passing of an optical pulse through an active medium [14, 148], in order to verify the accuracy of the presented finite-difference full time-domain model including the Maxwell curl equations and the band-resolved semiconductor Bloch equations. Firstly, we probe a semiconductor optical amplifier structure (GaAs quantum wells) with a weak femtosecond pulse that is spectrally broad enough to scan the optical polarisation response of the gain medium. In the linear pulse propagation regime the probe pulses are sampling the optoelectronic properties of the semiconductor gain material without changing the state of the active gain medium. Hole burning effects, carrier depletion and saturation can therefore be neglected. Using a travelling wave approach the propagation of a pulse can be described by the following set of equations

$$E(z, t) = \frac{1}{2} E_{\text{env}}(z, t) e^{i\Phi(z, t)} e^{-i\omega t} e^{ik_0 n_{\text{eff}} z} + \text{conjugate complex}, \quad E_{\text{env}}, \Phi \in \mathbb{R}, \quad (6.4)$$

$$\left(\frac{n^2}{cn_{\text{eff}}} \partial_t + \partial_z \right) \tilde{E}(z, t) = i \frac{k_0 \Gamma}{\epsilon_0 2n_{\text{eff}}} \frac{N_{\text{QW}}}{L_{\text{ref}}} \tilde{P}(z, t), \quad \tilde{E} = E_{\text{env}} e^{i\Phi}, \quad \tilde{P} \in \mathbb{C}, \quad (6.5)$$

$$\tilde{E}_{\text{out}}(z; \omega) = \tilde{E}_{\text{in}}(\omega) e^{g_{\text{mod}}(\omega)z} e^{i(\partial_z \Phi)(\omega)z} = \tilde{E}_{\text{in}}(\omega) e^{g_{\text{mod}}(\omega)z} e^{ik_0 \delta n(\omega)z}. \quad (6.6)$$

The different pulse Fourier components are amplified or attenuated by a factor of $\exp(g_{\text{mod}}(\omega)z)$ and experience a phase shift quantified by $\exp(i(\partial_z \Phi)(\omega)z)$. The physical effects that result in changes of the pulse spectrum and shape include the linear gain, the gain dispersion, and the dispersion of the waveguide structure $n_{\text{eff}}(\omega)$ and the chromatic dispersion of the host or background material $n_{\text{background}}(\omega)$ [41]. The latter arises from high energy excitations and is typically qualified by empirical formula, e.g. the Sellmeier equation. Dispersion results in different spectral components of the optical pulse travelling at different velocities and manifests itself as temporal effect causing an increase of the length of an initially unchirped ultrashort pulse in time-domain. A measure for these phenomena is given by the group velocity dispersion $v_{\text{pulse}} = \partial_k \omega = v_{\text{phase}} / (1 - \lambda/n \partial_\lambda n)$. In the following simulations, although, we will solely consider the carrier-induced refractive index change dispersion. To calculate spectra within a model in frequency-/time-domain we would have to run a series of simulations with different central wavelengths (as the ansatz only gives correct results for a rather small bandwidth around the split-off frequency). Within our full time-domain approach we inject a probe pulse, record a time series of the electric field at a position z_L and subsequently perform a Fourier transformation. We note that, based on the fact that we have not split-off a reference phase, the electromagnetic field at a single time point does not reveal any information.

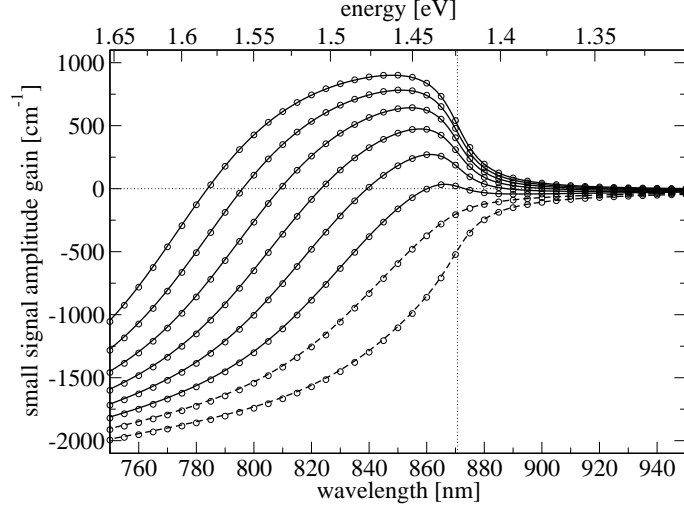


FIGURE 6.12: Small signal (electric field amplitude) gain spectra g_{mod} for various carrier sheet densities $N \in \{0.5 \cdot 10^{12} \text{ cm}^{-2} \dots 4 \cdot 10^{12} \text{ cm}^{-2}\}$ calculated from the full time-domain approach (lines) compared with results obtained from standard free-carrier theory (circles) according to equation (4.14) [149]. We inject a probe pulse (with parameters $E_0 = 1 \cdot 10^{-3} \text{ Vm}^{-1}$, $T_{\text{pulse}}^{\text{FWHM}}(E_{\text{env}}(t)) = 10 \text{ fs}$) into the semiconductor optical amplifier structure, and record the electric fields at the position z_L . Important simulation parameters comprise the dephasing constant $\gamma^p = 20 \text{ ps}^{-1}$, the electronic band gap $E_{\text{gap}}(\text{GaAs}) = 1.424 \text{ eV}$ and the waveguide properties $n_{\text{eff}} = n_{\text{background}} = 3.6$, $\Gamma N_{\text{QW}}/L_{\text{ref}} = 1/\Delta z = 1/6.556 \text{ nm}$. We assume a in propagation direction unstructured device, that is $\Gamma_r \mathcal{V}_z = 1$.

It is necessary to calculate a time series. For a semiconductor optical amplifier of length L_{act} we obtain the small signal amplitude gain from the relation

$$g_{\text{mod}} = \frac{1}{L_{\text{act}}} \ln \left(\frac{E_{\text{act}}(z_L, \lambda, N)}{E_{\text{pas}}(z_L, \lambda)} \right), \quad (6.7)$$

where E_{act} is the spectral electric field of the amplified pulse, and E_{pas} of a reference optical pulse (probing the passive structure). The induced refractive index change spectra can be extracted by

$$\partial_z \Phi = \frac{1}{L_{\text{act}}} \text{mod}(\Phi_{\text{act}}(z_L, \lambda, N) - \Phi_{\text{pas}}(z_L, \lambda), 2\pi). \quad (6.8)$$

We note that the electrical pumping term and the carrier loss processes are switched-off. The relevant spectral information is extracted from the simulation data (that are the time series of the amplified and of a reference pulse) by discrete Fourier transformations.

In summary, we can show that the full time-domain simulations (see FIGURES 6.12–6.14) agree well with analytical calculations. Furthermore, we extend our investigations to the propagation of sub-picosecond pulses in the nonlinear or saturation regime where theoretical approaches applying the slowly varying amplitude and the rotating wave approximations are known to be invalid. This will be discussed in the next sections.

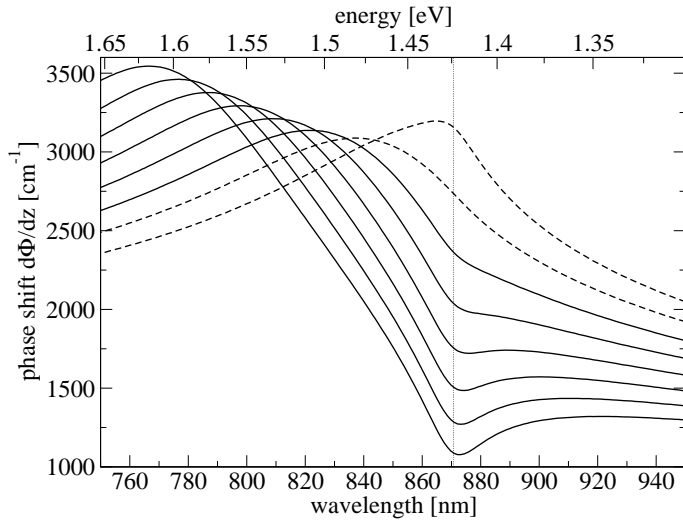


FIGURE 6.13: Induced phase shift $\partial_z\Phi$ or change of the refractive index $k_0\delta n = \partial_z\Phi$ versus optical wavelength or energy calculated from the (finite-difference) full time-domain model according to (6.8).

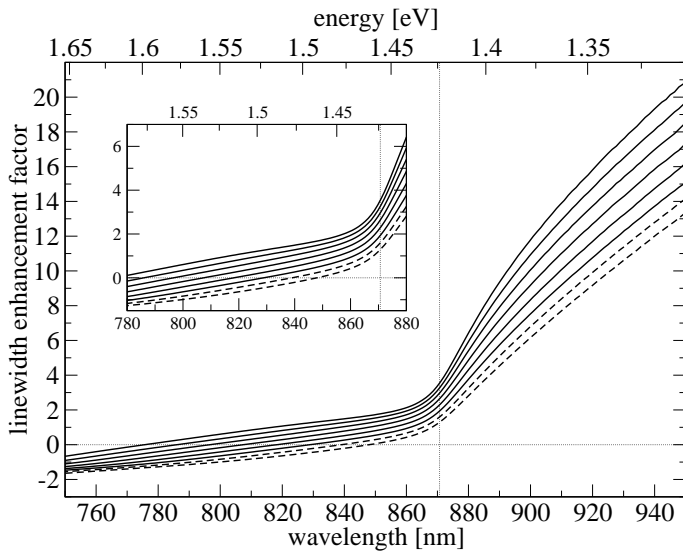


FIGURE 6.14: Anti-guiding or linewidth enhancement factor α . The very close agreement between the spectra calculated with the Maxwell semiconductor Bloch equations in full time-domain and the calculations depicted in FIGURES 4.9–4.11 is a verification for our novel approach.

6.4 Nonlinear Pulse Propagation

Semiconductor optical amplifiers (SOA) are essentially pumped, active structures without end mirrors but with fibres⁴ attached to both facets for the in- and out-coupling of electromagnetic fields. SOA are key components of all-optical networks, e.g. attractive as optical switches and regenerators. The amplification of optical signals is achieved through stimulated emission which causes transfer of the energy stored in the carrier subsystem of a semiconductor to the optical fields. However, the mode of operation is limited by pulse-induced changes of the gain medium and the carrier dynamics, and the large amplitude and phase nonlinearities as changes of the semiconductor gain feed back to the trailing part of the optical pulse. In this nonlinear or saturation regime, the amplitude gain or induced refractive index change becomes dependent on characteristics of the pulse, such the pulse shape, pulse width $T_{\text{pulse}}^{\text{FWHM}}(E_{\text{env}}(t))$ or spectral bandwidth $\Delta\nu_{\text{pulse}}^{\text{FWHM}}(E(t))$ and the peak amplitude E_0 . In addition, parameters of the amplifier structure, e.g. the length L_{act} or coupling strength to the active waveguide $\Gamma N_{\text{QW}}/L_{\text{ref}}$, have a strong influence. In the following, we investigate the (sub-) picosecond pulse interactions in SOA structures, namely the propagation and amplification of ultrashort optical pulses with hyperbolic secant pulse envelopes⁵. We model the injected pulses by

$$E(t) = E_{\text{env}}(t) \cdot \cos(\omega(t - t_0) + \Phi_0), \quad E_{\text{env}}(t) = E_0 \cdot \text{sech}(\gamma_{\text{pulse}}(t - t_0)), \quad (6.9)$$

$$T_{\text{pulse}}^{\text{FWHM}}(E_{\text{env}}(t)) = \frac{2 \ln(2 + \sqrt{3})}{\gamma_{\text{pulse}}}, \quad \Delta\nu_{\text{pulse}}^{\text{FWHM}}(E(t)) = \frac{2 \ln(2 + \sqrt{3}) \gamma_{\text{pulse}}}{\pi^2}, \quad (6.10)$$

$$T_{\text{pulse}}^{\text{FWHM}}(E_{\text{env}}^2(t)) = \frac{\ln(3 + \sqrt{8})}{\gamma_{\text{pulse}}}, \quad \nu_{\text{pulse}}^{\text{FWHM}}(E^2(t)) = \frac{\ln(3 + \sqrt{8}) \gamma_{\text{pulse}}}{\pi^2}, \quad (6.11)$$

$$\int_{-\infty}^{\infty} dt E_{\text{env}}(t) = E_0 \cdot \frac{\pi}{\gamma_{\text{pulse}}}, \quad \int_{-\infty}^{\infty} dt E_{\text{env}}^2(t) = E_0^2 \cdot \frac{2}{\gamma_{\text{pulse}}}. \quad (6.12)$$

In addition to the above discussed linear mechanisms of small signal gain and the various dispersions, and amplified spontaneous emission as broad bandwidth noise background, there are further important physical processes which cause changes of the pulse shape and the pulse spectrum during propagation in semiconductor amplifier structures for high electric fields and optical intensities. These nonlinear optical effects comprise the inelastic light scattering with different phonons (Brillouin, Raman) and the optical Kerr effect $n(\omega, I) = n(\omega) + \int d\omega' n_2(\omega, \omega') I(\mathbf{r}, t; \omega')$, which states that the index change of the host or background material is directly proportional to the electric field amplitude squared. The second order nonlinear refractive index n_2 is attributed to an instantaneously occurring nonlinear response $\chi^{(3)}$. A nonlinear polarisation is generated, which

⁴Laser sources and amplifier materials operating in the near infrared at wavelengths near to the (data) transmission windows of the silica fibres are preferable, more precisely that is at 1310 nm (minimal dispersion), 1550 nm (absorption minimal) and at around 850 nm (local minimum).

⁵Pulses with a Gaussian pulse shape, i.e. $E_{\text{env}}(t) = E_0 \cdot \exp(-\gamma_{\text{pulse}}^2(t - t_0)^2)$, are characterised in time- and frequency-domain by $T_{\text{pulse}}^{\text{FWHM}}(E_{\text{env}}(t)) = 2\sqrt{\ln 2}/\gamma_{\text{pulse}}$, $\Delta\nu_{\text{pulse}}^{\text{FWHM}}(E(t)) = 4\sqrt{\ln 2}\gamma_{\text{pulse}}$ and $\int_{-\infty}^{\infty} dt E_{\text{env}}(t) = E_0 \cdot \sqrt{\pi}/\gamma_{\text{pulse}}$.

in turn modifies a propagating pulse. It manifests itself temporally as self-phase modulation (dynamical frequency shift), and spatially as self-focussing counteracting optical diffraction. In the subsequent simulations we concentrate on the resonant optical transitions. The consideration of the distribution functions and of the macroscopic carrier density as dynamical variables in the band-resolved microscopic and macroscopic Bloch equations, respectively, and the physical effects of spectral and spatial hole burning represent an optical Kerr-type nonlinearity⁶. Our goal is to correlate the changes of the pulse shape and spectrum to the modifications of the microscopic and macroscopic state of the semiconductor gain medium. The pulse-induced changes of the gain material by induced emission or absorption generate non-equilibrium distributions. These and other relevant interactions and recovery mechanisms lead to a dynamical gain $g_{\text{mod}}(t)$ and phase shift $\partial_z \Phi \rightarrow \delta n(t)$, which in turn modify the temporal and spectral properties of the propagating optical pulse. Characteristic time scales of the various interaction processes in momentum and real space have to be compared to the pulse duration. This helps to determine which terms have a strong influence. For (sub-) picosecond optical pulses the carrier loss channels nonradiative recombination, spontaneous emission and Auger recombination, an electrical carrier pumping term Λ , and the transverse spatial degree of freedom⁷ and processes like diffraction and carrier diffusion may be neglected as these terms have only a marginal influence on the state of the active gain material on the sub-picosecond time scale. The mechanisms which essentially govern the (sub-) picosecond pulse interactions in quantum well-based SOA structures include hole burning or more general, the generation of non-equilibrium states of the gain medium by stimulated transitions, the propagation of the optical fields, and the partial recovery caused by Coulomb and phonon interactions.

In FIGURES 6.15–6.18 we analyse the interaction of 10 fs hyperbolic secant optical pulses with semiconductor amplifier and absorber elements in the saturation regime. The results are obtained by calculating averaged gain and carrier-induced refractive index change spectra according to (6.7) and (6.8) (FIGURES 6.15+6.17), and by characterising the input and output pulses in time- and frequency-domain (see FIGURES 6.16+6.18). An increasing electric field amplitude E_0 reads to higher instantaneous optical intensities and a larger time-integrated pulse energy of the excitation pulse. The spectra are flattening and the absolute value of the amplitude gain is reduced due to

⁶By applying an adiabatic elimination of the nonlinear polarisation we can specify the pulse-induced change of the inversion by $\partial_t N|_{\text{carrier-light}} = -1/(2\hbar)G|\tilde{E}|^2$. Assuming a linear gain model $G = G_0(N - N_{\text{transparency}})$, this depletion of the carrier density results in a change of the refractive index of $\Delta N \rightarrow \Delta(\delta n) \propto G_0\alpha I(\mathbf{r}, t)$. For most frequencies the refractive index increases with decreasing inversion.

⁷Taking into consideration the transverse spatial degree of freedom and transverse pulse profiles would have obvious implications: For high-intensity pulses the centre area of the pulse operates in the nonlinear regime connected with gain saturation and hole burning effects. At the (transverse) edges the pulse sees the linear gain. Consequently, an optical pulse is higher amplified at the edges and the spatial width of the transverse pulse profile is increasing. The refractive index depends on the inversion and thus on the optical intensity. The field components at the pulse edges will be, as a result of individual optical path lengths and group indices and self-focussing, time-shifted compared to the pulse centre [106].

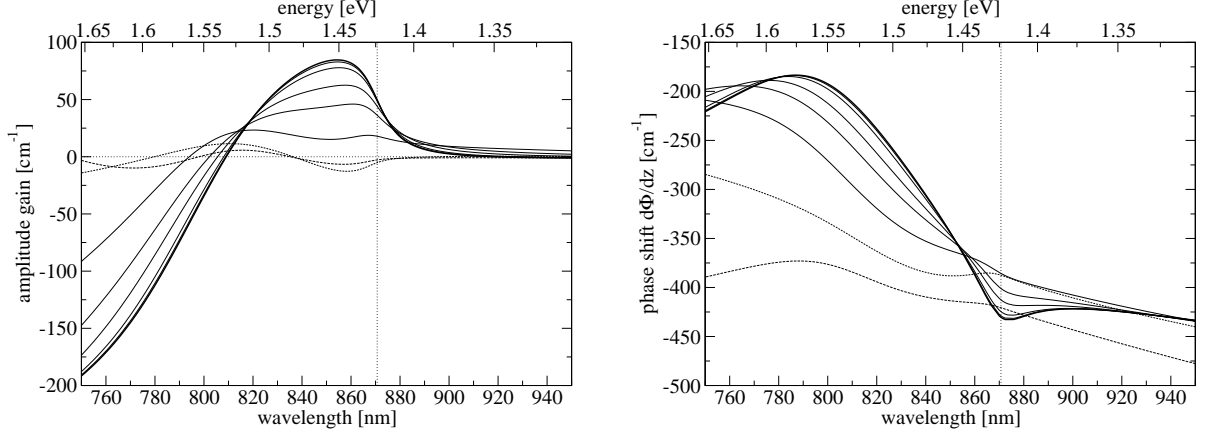


FIGURE 6.15: Propagation of 10 fs hyperbolic secant pulses (see (6.9)) in an active semiconductor optical amplifier (SOA) structure. Pulse and device parameters are: central wavelength $\lambda = 850$ nm, $N = 3 \cdot 10^{12}$ cm $^{-2}$, $\Gamma N_{\text{QW}}/L_{\text{ref}} = 1/50$ nm, $n_{\text{eff}} = 3.6$ and $L_{\text{act}} = 0.1$ mm. The amplitude gain (left) and induced refractive index change spectra (right) are calculated for various electric field amplitudes and pulse energies of the input pulse: $E_0 \leq 1 \cdot 10^7$ Vm $^{-1}$ (small signal gain or linear regime; displayed as thick line), $5 \cdot 10^7, 1 \cdot 10^8, 2 \cdot 10^8, 3 \cdot 10^8, 5 \cdot 10^8$ Vm $^{-1}$ (nonlinear saturation regime with carrier depletion due to hole burning effects; thin lines) and $E_0 = 1 \cdot 10^9, 2 \cdot 10^9$ Vm $^{-1}$ (pulse areas $M^{eh}/\hbar E_0 \cdot \pi/\gamma_{\text{pulse}}$ exceed π ; dashed).

hole burning and carrier depletion by induced emission in an amplifier element or as the result of an increased inversion by stimulated absorption within the saturable absorber. This effect is referred to as pulse-induced gain saturation. The generation of non-equilibrium distribution functions, the partial saturation recovery and the resulting ultrafast gain dynamics of $g_{\text{mod}}(t)$ and $\delta n(t)$ can be experimentally measured by pump-probe techniques. In the next section we implement these measurements numerically. To summarise, gain saturation is caused by the coupling of photons with the carrier system and the pulse-induced changes of $n_{\mathbf{k}}^{\circ}$ in momentum space and N in real space. In an amplifier the instantaneous available resonant carrier inversion is reduced. In an absorber (and in the electronic multi-level picture) the possible initial states of the pump transitions are depleted, whilst the final states are occupied due to stimulated absorption. A realistic modelling of few-cycle femtosecond pulse interactions in semiconductor materials gives a quantitative description of gain saturation and recovery. An in-depth treatment of the intraband relaxation and redistribution of carriers, more precisely of the scattering processes mediated by the Coulomb interaction must be included. Evidently, a description of carrier relaxation by the generalised quantum kinetic Boltzmann equations in the Markovian approximation (no memory effects) which also neglects nonlinear terms in the interband polarisations is deficient. A full treatment of many-body interactions and of the correlation contributions in the semiconductor Bloch equations without approximations is beyond an approach with microscopically precalculated relaxation rates. Such a treatment in combination with a spatially extended time-domain

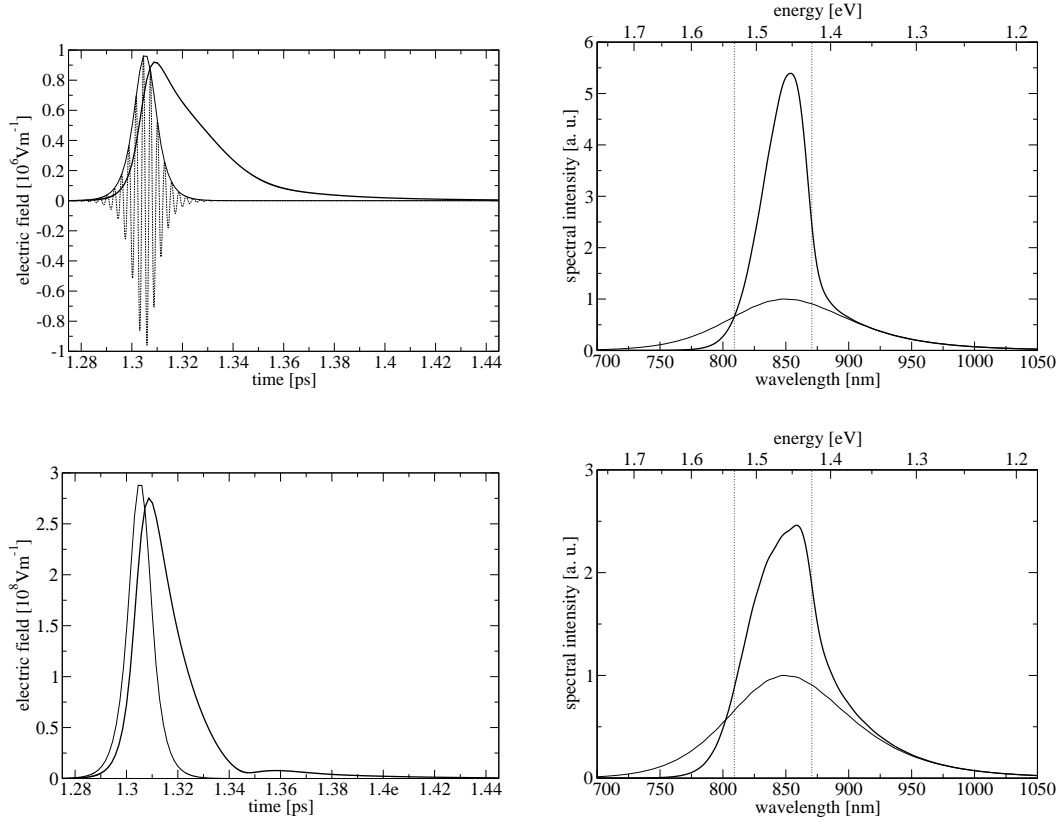


FIGURE 6.16: Depicted are the input or more precisely a reference pulse (thin line), which is probing the passive ($M^{eh} = 0$) waveguide structure, and the amplified pulse (as thick line) for pulse propagation experiments in SOA in the linear (top) and in the saturation regime (bottom). Within the time-domain picture the amplification of few femtosecond pulses is realised by a pronounced elongation of the trailing part of the optical pulse (caused by the fact that $T_{\text{pulse}}^{\text{FWHM}} < 1/\gamma^p$) and by an increase of the optical pulse energy $\propto \int dt |E_{\text{env}}(z, t)|^2$. The maximum value of the pulse envelope is not increased. We can also notice a small time delay of the amplified pulse by approximately 5 fs as a result of the noninstantaneous gain response to the pulse excitation. In frequency-domain the different spectral components of the optical pulse experience absorption (for high frequencies), amplification or transparency (for energies below the band edge), compare to FIGURE 6.15.

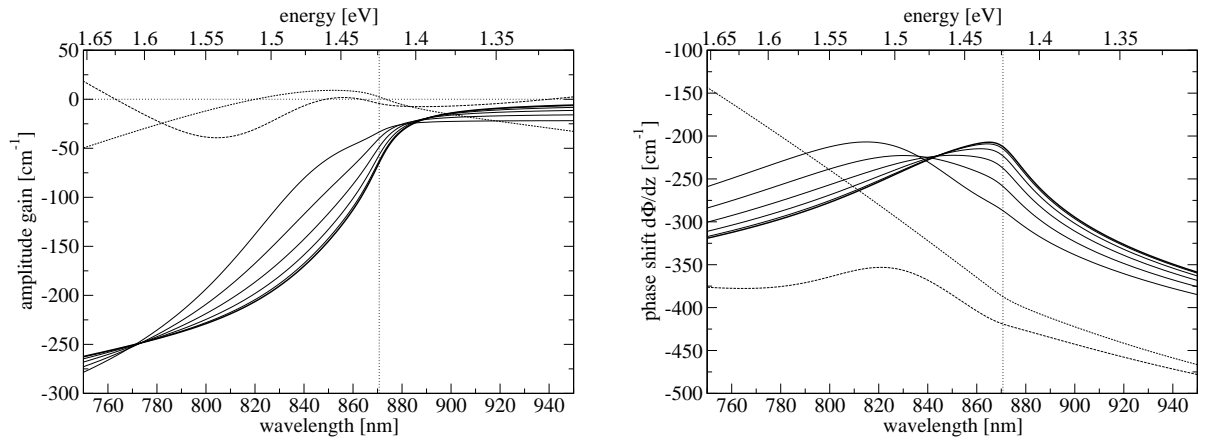


FIGURE 6.17: Same as FIGURE 6.15, but for a semiconductor absorber structure with $N = 0.5 \cdot 10^{12} \text{ cm}^{-2}$ (and we replace $E_0 = 5 \cdot 10^7 \text{ Vm}^{-1} \rightarrow 4 \cdot 10^8 \text{ Vm}^{-1}$).

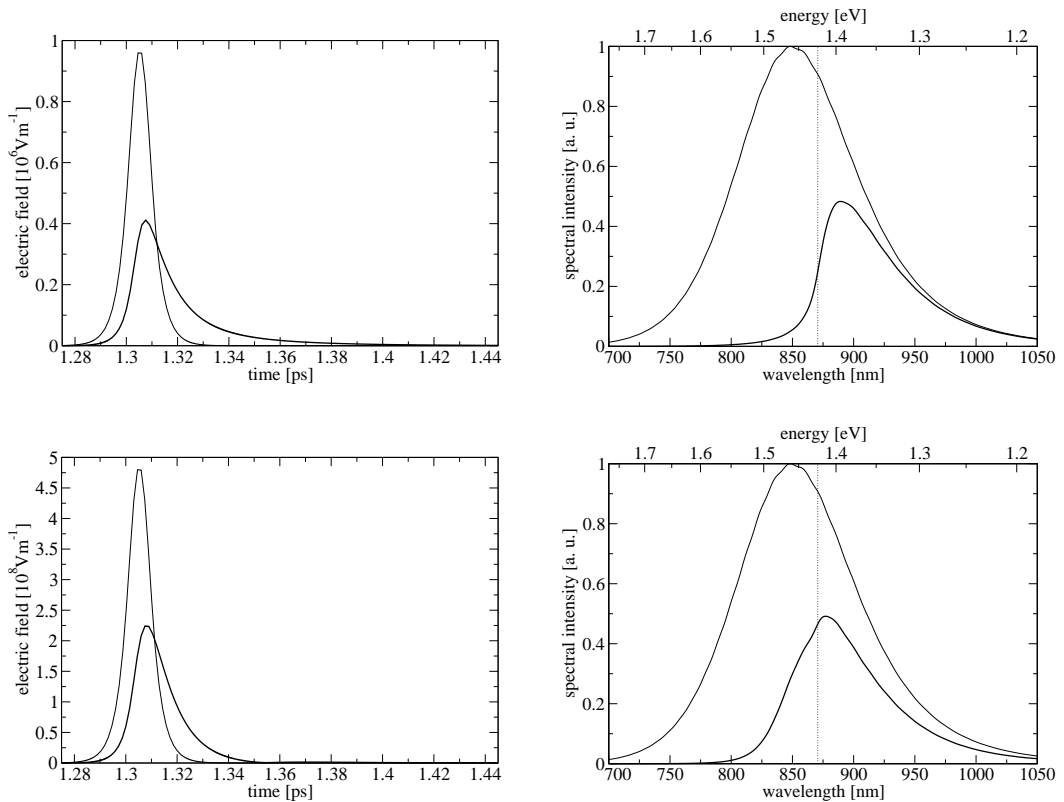


FIGURE 6.18: Same as FIGURE 6.16, but for the optical absorber structure (quantum wells). Pulse propagation in the linear and saturation regime is characterised in time-domain (left column) and in a frequency-domain picture (right). Here, spectral windows showing absorption and transparency can be identified.

approach involves a huge computational effort and is difficult to realise.

FIGURES 6.19–6.22 show the propagation and interaction of 1 ps electromagnetic pulses in semiconductor gain structures. When we cut an optical pulse into temporal segments we see that earlier parts of the pulse induce changes to the active gain material, such as modifications of the carrier distributions, the macroscopic carrier density and the available gain $g_{\text{mod}}(t)$ (dynamical saturation). Later segments of the pulse experience these modifications of the gain medium. Consequently, the amplification or absorption is larger at the leading edge of the pulse than for the trailing edge. This results in asymmetry of the amplified pulse envelope. Because of the large α factor in active semiconductor materials and the dependence of the refractive index on the intensity (optical Kerr-type nonlinearity) spectral changes occur as a result of self-phase modulation, and temporal changes are due to changes of the group index $n + \omega \partial_{\omega} n$. The temporal variation of the nonlinear phase leads to dynamical modulations of the instantaneous frequency $\omega_{\text{inst}}(t) = \partial_t \Phi$. In other words, due to nonlinearities and dispersion during propagation a chirp of the optical pulse arises. New frequency components are generated, and the spectrum becomes asymmetric and broadened. The cause of self-phase modulation is the density dependence of the refractive index change δn , the physical effects behind it are hole burning by stimulated emission and relaxation dynamics. Self-phase modulation (SPM) is classified according to the recovery times: Slow SPM depends on the time-integrated power of the input pulse, whereas fast SPM depends on the pulse and amplifier characteristics $T_{\text{pulse}}^{\text{FWHM}}(E_{\text{env}}(t))$, $\Delta\nu_{\text{pulse}}^{\text{FWHM}}(E(t))$, E_0 and L_{act} . This fast nonlinearity causes an inhomogeneous saturation of the modal gain due to the effect of spectral hole burning, but is only significant for very high field amplitudes or intensities. For moderate field amplitudes, there is no clear hole due to the large, dominant homogeneous broadening. In two-level or macroscopic gain descriptions, this nonlinear gain saturation is typically specified by the following phenomenological ansatz

$$g_{\text{mod}} = \frac{g_{\text{mod, small signal}}(\lambda, N)}{1 + \tilde{\epsilon}_{\text{sat}} E_0^2} \rightarrow g(z, t) = \frac{g_{\text{mod, small signal}}(\lambda, N)}{1 + \epsilon_{\text{sat}} S(z, t)}, \quad (6.13)$$

$$S(z, t) = \frac{1}{2} \epsilon_0 \epsilon \frac{|\tilde{E}(z, t)|^2}{\hbar \omega}, \quad \epsilon_{\text{sat}} = \frac{2\hbar\omega}{\epsilon_0 \epsilon} \tilde{\epsilon}_{\text{sat}}, \quad (6.14)$$

with the nonlinear gain coefficient ϵ_{sat} [73, 113] and the saturated gain being function of the instantaneous optical intensity. In FIGURES 6.19+6.21 we investigate nonlinear gain suppression and determine from our simulation data effective nonlinear gain coefficients ϵ_{sat} (by curve fitting). Results for optical amplifier structures, in which spectral depletion of resonant carriers saturates the gain, are shown in FIGURE 6.19: The picosecond pulses test the spectrally local (at around 850 nm) available gain. The saturation behaviour is hence determined by the intraband carrier dynamics (kinetics), mainly how fast a spectral hole in the distribution functions is refilled. Consequently, increasing the time constants of these intraband carrier relaxation processes (e.g. Coulomb scattering) by a factor of two will change the nonlinear gain coefficient. We find (dashed line) $\tilde{\epsilon}_{\text{sat}} = 1.4 \cdot 10^{-15} \text{ m}^2 \text{ V}^{-2} \rightarrow \epsilon_{\text{sat}} = 5.8 \cdot 10^{-24} \text{ m}^3$. Other in literature discussed

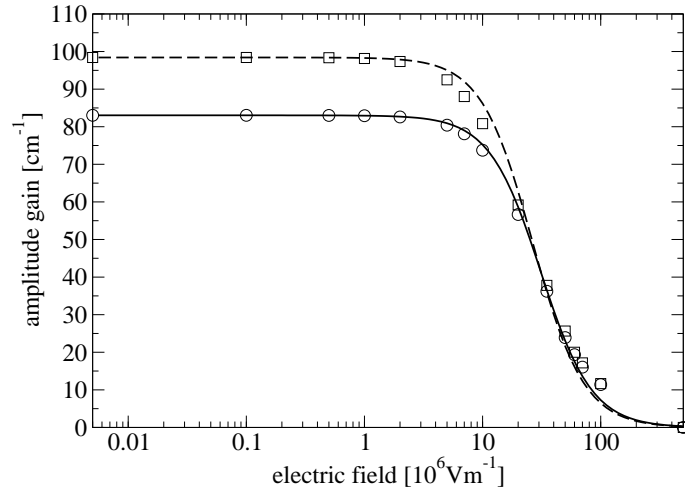


FIGURE 6.19: Nonlinear gain suppression in semiconductor optical amplifiers due to spectral (and spatial) hole burning, as result of the depletion of available resonant carriers for stimulated recombination processes. The propagation of 1 ps pulses in a structure as described in FIGURE 6.15 is simulated with the full time-domain model. Depicted are the saturated amplitude gain at 850 nm versus the electric field amplitude E_0 . The phenomenological ansatz according to (6.13) (thick line) is compared with the simulation data (circles), we can extract from nonlinear curve fitting $\tilde{\epsilon}_{\text{sat}} = 1.0 \cdot 10^{-15} \text{ m}^2 \text{ V}^{-2} \rightarrow \epsilon_{\text{sat}} = 4.2 \cdot 10^{-24} \text{ m}^3$.

mechanisms behind the gain power saturation [73] comprise the reduced instantaneous gain (as the consequence of finite effective recovery or scattering times of the phonon scattering processes) associated with carrier heating and heat-induced changes of the amplifier medium, and due to the depletion of the macroscopic carrier density through the coupling of carriers with photons. The associated recovery time scales of the processes balancing the various depletion mechanisms determine the thresholds from which saturation behaviour sets in. Typical values of these physical parameters (effective lifetimes) are given by $\tau_{\text{shb}} = 100 \text{ fs}$, $\tau_{\text{ch}} = 1 \text{ ps}$ and $\tau_{\text{macr}} = 500 \text{ ps}$. For saturable absorber elements, in which the saturation mechanism is the spectral selective carrier generation, simulation results of gain saturation are displayed in FIGURE 6.21.

In FIGURE 6.20 the simulated results of the propagation and amplification of 1 ps pulses in a SOA structure are shown: In the nonlinear regime asymmetries in the pulse shape and spectrum are observed. The dynamical saturation leads to a small shift of the pulse spectrum to longer wavelengths, and we see a pulse narrowing in frequency-domain. In an amplifier structure the leading edge of the optical pulse will experience more amplification than the trailing segments. The connected reshaping of the pulse shape (or envelope) results effectively in a temporal shift of the pulse peak (here by $\approx 50 \text{ fs}$) which can be reinterpreted as pulse advancement. In an analogous manner, we find a pulse slowdown for saturable semiconductor absorber elements (of $\approx 100 \text{ fs}$), see FIGURE 6.22. As this time advancement or delay is dependent on the carrier density and on the optical pulse properties, the propagation time is controllable and tunable [152]. The propagation

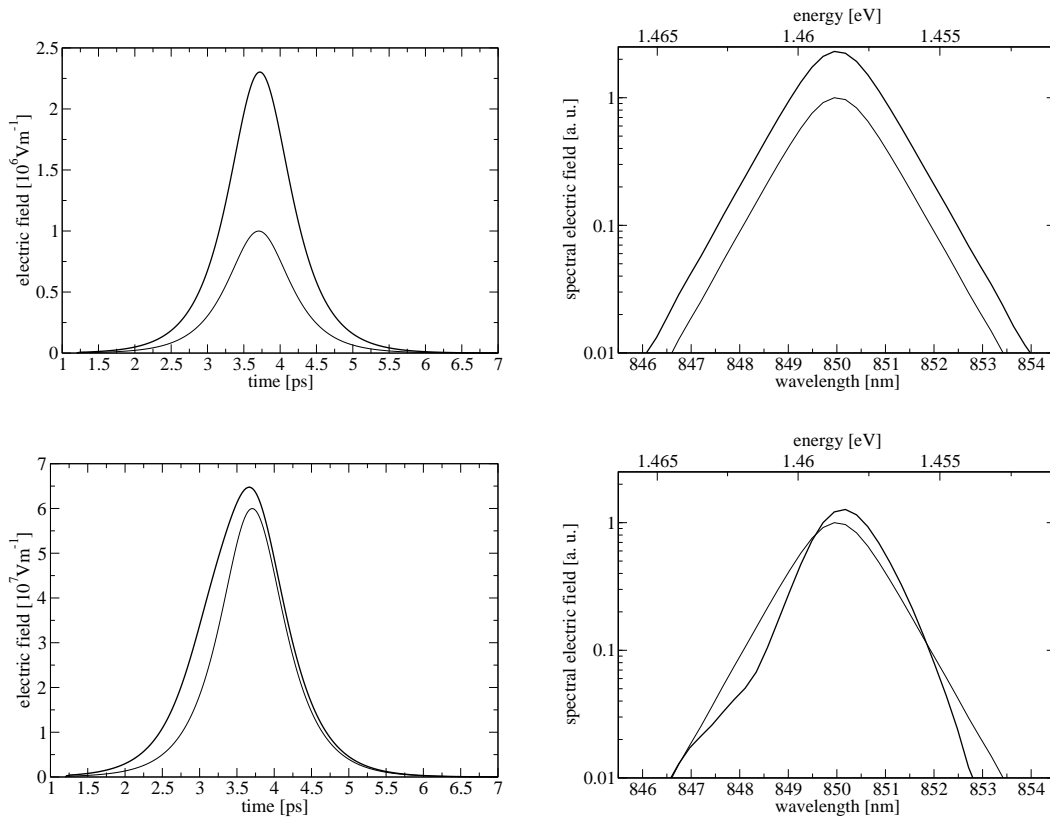


FIGURE 6.20: Amplification of picosecond pulses in an active semiconductor structure. In the linear regime (top) the output pulse is connected with the input pulse by the simple multiplication with a factor $\exp(g_{\text{mod}}(850 \text{ nm}, N)L_{\text{act}})$ (or in other words $\ln(E_{\text{out}}(\nu)) = \ln(E_{\text{in}}(\nu)) + g_{\text{mod}}(850 \text{ nm}, N)L_{\text{act}}$), pulse shape and spectrum remain unchanged. Possible processes which may change the pulse shape and spectrum in the linear regime include gain dispersion plus the dispersion linked with the background (or host) material or caused by the waveguide, refractive index structure. For high-intensity pulses (bottom) the effects of dynamical saturation behaviour and fast self-phase modulation (the modification of the refractive index by the optical pulse itself) [106], and consequently a time-dependent phase shift and temporally varying instantaneous frequency lead to a strong reshaping of pulses in time- and frequency-domain.

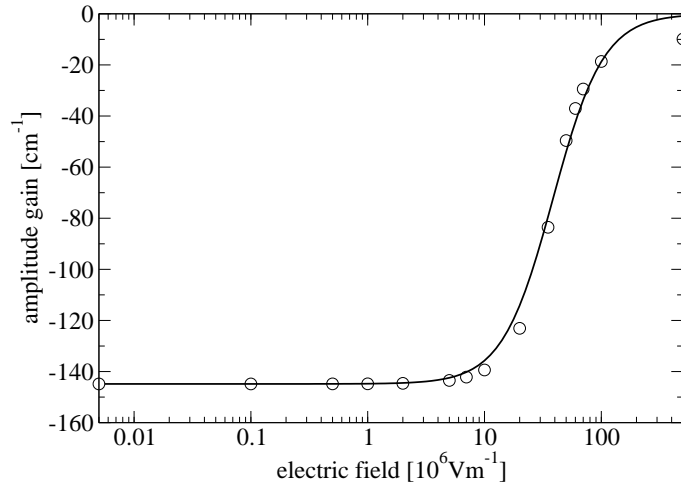


FIGURE 6.21: Same as FIGURE 6.19, but for a semiconductor optical absorber structure ($N = 0.5 \cdot 10^{12} \text{ cm}^{-2}$). From nonlinear curve fitting to the phenomenological description (6.13) we can extract $\tilde{\epsilon}_{\text{sat}} = 6.7 \cdot 10^{-16} \text{ m}^2 \text{ V}^{-2} \rightarrow \epsilon_{\text{sat}} = 2.7 \cdot 10^{-24} \text{ m}^3$. Semiconductor saturable absorber elements, embedded into a Bragg mirror structure, so-called semiconductor saturable absorber mirrors (SESAM) [32, 150], or as part of a multi-section laser device [113, 136], are the key elements of ultrashort laser pulse generators based on the concept of passive mode-locking [116, 151].

in an active semiconductor can also induce a strong chirp of the pulse [153]. The various segments of the pulse see different gain $g_{\text{mod}}(t)$ and individual refractive index changes $\delta n(t)$ due to spectral carrier depletion and subsequent intraband scattering processes, and because of hole burning and recovery by an effective macroscopic carrier pump term. Thus, the microscopic and macroscopic carrier state is varying over time, and likewise gain and refractive index are time-dependent. As consequence of this dynamical saturation behaviour we notice the following changes to the pulse shape and spectrum (the effects are more pronounced with increasing power): In time-domain the reshaping of the pulse envelope results in the sharpening of the trailing edge of the pulse, the pulse broadening and a shift towards negative times (pulse advancement). The pulse spectrum exhibits an asymmetric shift towards longer wavelengths, the propagation in the saturation regime imposes a chirp with the leading edge redshifted and the trailing edge of the pulse blueshifted. In a similar way, the nonlinear pulse interaction in a saturable absorber (FIGURE 6.22) shows a sharpening of the leading edge of the pulse, a pulse shortening in time-domain and a time delay (or pulse slowdown). In frequency-domain we find an asymmetric broadening to higher frequencies, the dynamical saturation imposes a positive (followed by a negative) chirp.

We note that the quantitative understanding of nonlinear pulse shaping in semiconductors is critical to applications such as passive mode-locking. The generation of ultrashort optical pulses by mode-locking of many longitudinal laser modes can be realised by active (loss modulation), passive (self-amplitude modulation) and hybrid techniques [1, 73, 151].

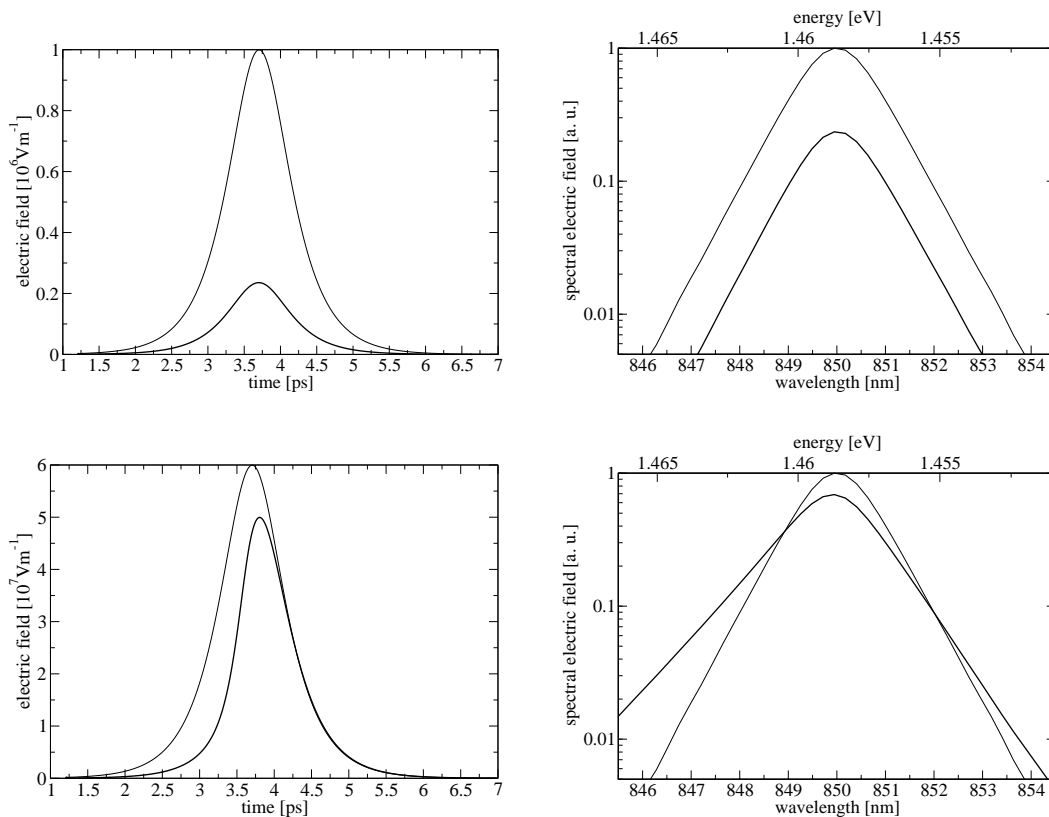


FIGURE 6.22: Propagation of picosecond pulses in a semiconductor optical absorber, analogue to FIGURE 6.20. The nonlinear dynamical saturation process in the absorber structure effectively sharpens the leading edge of the electromagnetic pulse and leads to a pulse shortening of the propagated pulse (thick line) compared to the input pulse. Contrariwise, in a semiconductor optical amplifier the leading edge of the pulse is stronger amplified and thus effectively the trailing edge sharpened. The combination of saturable absorber elements and gain sections offers the possibility of ultrafast pulse generation by passive mode-locking [33]. Furthermore, we notice as a result of pulse-induced changes of the gain medium a pulse broadening in frequency-domain and a shift of the pulse spectrum to shorter wavelengths.

The realisation of the concept of passive mode-locking based upon semiconductor saturable absorber elements capitalises on the existence of a variety of saturation energies and of very different time scales of saturation recovery in semiconductor-based absorber materials. For more details on the gain dynamics and recovery see SECTION 6.5. The physical processes with a lower saturation intensity (for a part of the absorption) and characterised by longer recovery times (the carriers are removed by interband recombination or macroscopic carrier loss processes) enable the self-starting of mode-locking from spontaneous emission or small fluctuations. The mechanism with the faster time scale, due to a partial recovery of the absorption when carriers thermalise by intraband relaxation or scattering, and higher saturation energy provide a reshaping mechanism of sub-picosecond pulses [32, 33]. To summarise, conditions for stable pulse generation by mode-locking in (monolithic) multi-section diode lasers can be specified [32, 33, 73, 151]: 1) The small signal gain of the amplifier section has to be bigger than the unsaturated losses of the absorber elements (self-starting). 2) The absorber elements must saturate faster, at lower pulse intensities than the gain section. This may be implemented by an adequate choice of cavity configurations and the dielectric multi-layer design. To enhance the optical fields over the quantum well-based (or more general quantum confined) absorber structures the saturable absorbers are often embedded into a Bragg mirror structure (SESAM) and thus the light focussed by the absorber cavity. 3) The loss recovery must take place more quickly than that of the gain section. With defect engineering, which involves the generation of defect states in the band gap which give rise to ultrafast carrier trapping into deep levels to deplete the bands [33], this goal can be achieved. In all, the slow absorber in conjunction with the dynamical gain saturation, the absorption exceeds the pulse amplification everywhere except near the peak of the optical pulse. As a consequence, the pulse will shorten due to amplification of the peak and attenuation of the edges as there is just an ultrashort net-gain window from the combined saturation of absorber and gain [33, 73]. Our approach to combine a material model which implies a variety of different time regimes and saturation mechanisms with the direct solution of Maxwell equations represents an improvement to known theoretical descriptions of passive mode-locking [96, 113, 116, 126, 136] and permits the optimisation of pulsed monolithic semiconductor lasers.

6.5 Ultrafast Gain Dynamics

In this section we analyse the femtosecond and picosecond dynamics of the gain $g_{\text{mod}}(t)$ and of the refractive index change $\delta n(t)$ by simulating and numerically rebuilding pump-probe experiments in which (high-intensity) pump and (weak) probe pulses with a variable, tunable time delay copropagate in the semiconductor optical amplifier structure. In our simulations we calculate the pulse interactions of 200 fs optical pulses with the SOA structure in the nonlinear or saturation regime. At the points in time of interest the whole microscopic and macroscopic state of the gain structure is recorded: $n_{\mathbf{k}}^{\circ}(z, t)$, $N(z, t)$, $\mathbf{p}_{\mathbf{k}}(z, t)$, $\partial_t \mathbf{p}_{\mathbf{k}}(z, t)$, $P(z, t)$. In an additional step, we impose a time delay, prepare the system into the appropriate recorded state and sample with a weak femtosecond probe

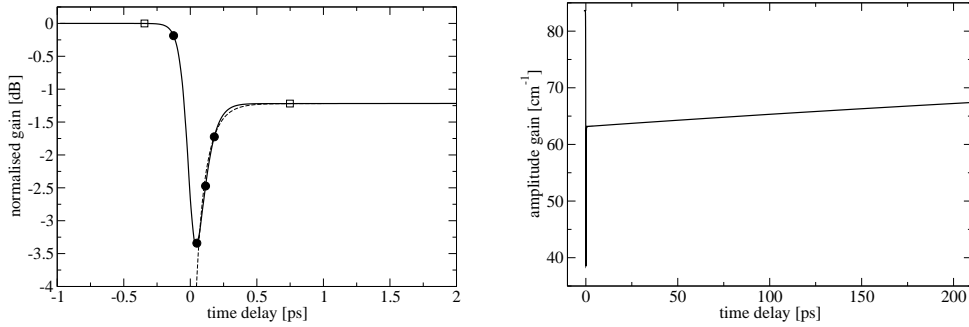


FIGURE 6.23: Pump-probe experiment of a semiconductor gain structure with carrier density of $N = 3 \cdot 10^{12} \text{ cm}^{-2}$ showing the ultrafast dynamics (recovery) of the gain. The pump pulse (central wavelength $\lambda = 850 \text{ nm}$, $T_{\text{pulse}}^{\text{FWHM}} = 200 \text{ fs}$, $E_0 = 5 \cdot 10^7 \text{ Vm}^{-1}$, hyperbolic secant pulse shape) generates an excitation, i.e. a modification of the state of the semiconductor amplifier medium (non-equilibrium distributions). Probe pulses sample the gain dynamics. Depicted are the normalised amplitude gain $10 \cdot \log(g_{\text{mod}}(t)/g_{\text{mod, small signal}})$ [dB] (left picture) or the gain (right) at 850 nm versus the delay time between pump and probe pulse. The power saturation of the gain originates from several depletion mechanisms of the available resonant carriers. Assuming an exponential decay of the various carrier excitations and exponential recovery of the gain, and the mechanisms to be independent, that is $g_{\text{mod, small signal}} - g_{\text{mod}}(t) = \Delta g_{\text{shb}} \exp(-t/\tau_{\text{shb}}) + \Delta g_{\text{ch}} \exp(-t/\tau_{\text{ch}}) + \Delta g_{\text{macr}} \exp(-t/\tau_{\text{macr}})$, we can identify the different time scales on which the gain recovers. The balancing of spectral depletion of carriers and spectral hole burning by Coulomb scattering occurs with a rate of approximately $1/\tau_{\text{shb}} = 11 \text{ ps}^{-1}$ (see fit, dashed line in left graph). The macroscopic carrier density recovers on the nanosecond scale. The rate is given by the effective pumping, the electrical pump minus the carrier loss channels (right picture). In FIGURE 6.24 we analyse the instantaneous gain at time points marked with circles (left) and with squares (right).

pulse the non-equilibrium carrier state of the amplifier medium to obtain $g_{\text{mod}}(t)$ and $\delta n(t)$. We calculate the time series of the probe pulse after passing through the gain material and perform a Fourier transformation to gain the instantaneous spectra.

The microscopic origin of the fast nonlinearities are spectral hole burning or the spectral selective generation of carriers, respectively, and the many-body Coulomb dynamics by intraband carrier relaxation and scattering (FIGURES 6.24+6.27). The recovery of the gain saturation is achieved by various mechanisms and physical effects, the different recovery rates are calculated for semiconductor optical amplifier structures in FIGURE 6.23 and for saturable absorbers in FIGURE 6.26. In FIGURE 6.25 the dependence of the gain dynamics and recovery on the central pulse frequency and peak amplitude, the pumping or macroscopic carrier density, and on the microscopic scattering rates is analysed in detail.

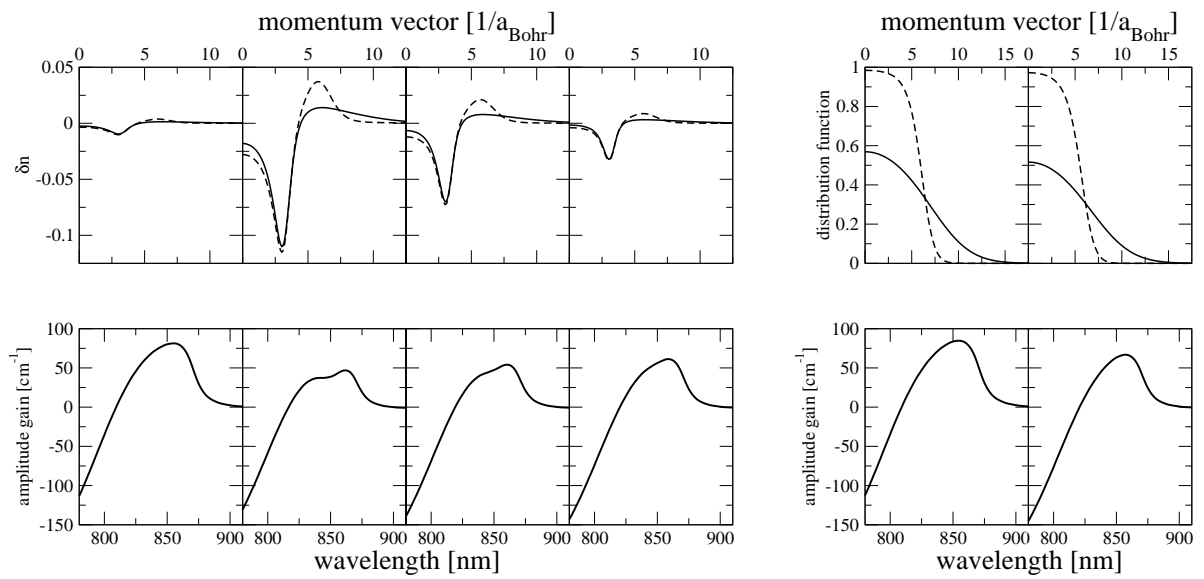


FIGURE 6.24: Gain saturation by spectral hole burning (leads to a reduced spectral inversion) and recovery due to carrier redistribution by Coulomb scattering processes (left, at the time points marked with circles in FIGURE 6.23). Slower gain dynamics by the depletion of the macroscopic inversion ($N = 3 \cdot 10^{12} \text{ cm}^{-2} \rightarrow 2.6 \cdot 10^{12} \text{ cm}^{-2}$) and the recovery due to an increase of the macroscopic density by carrier injection (right, squares). We plot the electron (dashed) and hole (solid line) distribution functions or the spectral deviations $\delta n_{\mathbf{k}}^{\circ} = n_{\mathbf{k}}^{\circ} - f_{\mathbf{k}}^{\circ}$ (at top) and the instantaneous gain spectra (bottom) for the six time points marked in FIGURE 6.23. For sub-picosecond pulse interactions the gain dynamics and the induced microscopic and macroscopic changes of the active material are determined by spectral carrier generation $g_{\mathbf{k}}$ or spectral hole burning, and by intraband carrier relaxation.

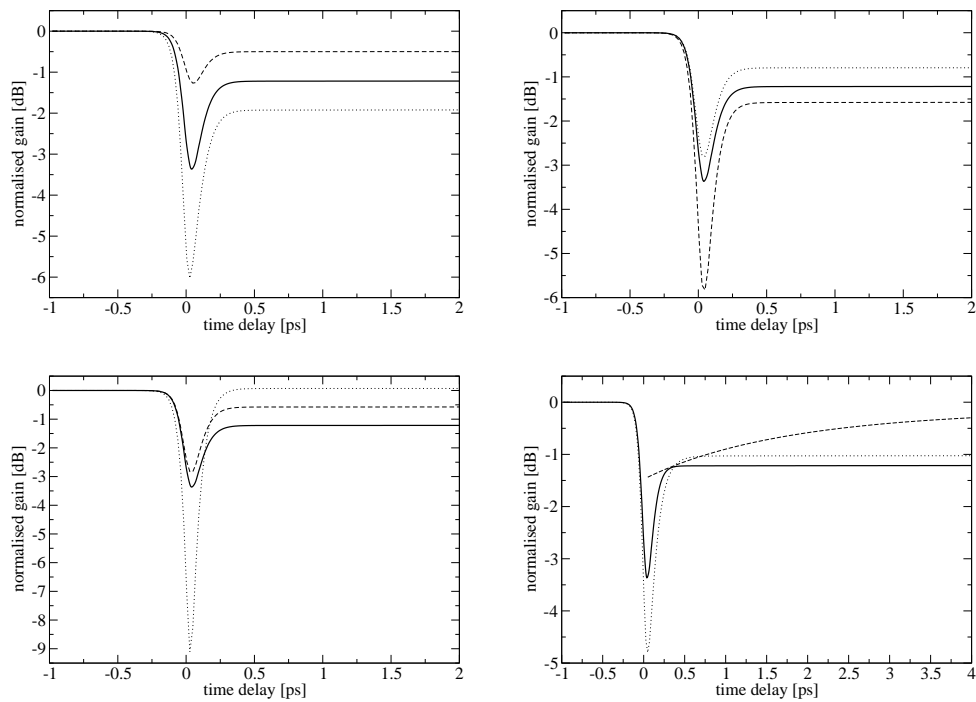


FIGURE 6.25: The excitation of the SOA medium as the response to the pump pulse, characterised in FIGURE 6.23, and the subsequent gain recovery is depicted as wide solid lines. The influence of parameters of the pulse and of the SOA structure on the gain recovery dynamics is analysed. (Top left) The gain saturation is more distinct with increasing electric field amplitude and energy of the pump pulse: $E_0 = 3 \cdot 10^7 \text{ Vm}^{-1}$ (dashed) and $7 \cdot 10^7 \text{ Vm}^{-1}$ (dotted). (Top right) We change the electrical pump or carrier density of the SOA, $N = 2 \cdot 10^{12} \text{ cm}^{-2}$ (dashed) and $4 \cdot 10^{12} \text{ cm}^{-2}$ (dotted), and the central wavelength of the pump pulse (bottom left) to $\lambda = 870 \text{ nm}$ (near the band edge, dashed line) and 810 nm (near transparency, dotted). (Bottom right) Shows the influence of the time scales of intraband relaxation processes. The Coulomb scattering rates are reduced by a factor of two (dotted). An additional relaxation process with a time constant of $\tau_{\text{ch}} = 2 \text{ ps}$, associated with the interaction of the electron-hole subsystem with phonons (with the lattice) and with carrier temperature relaxation, is taken into account.

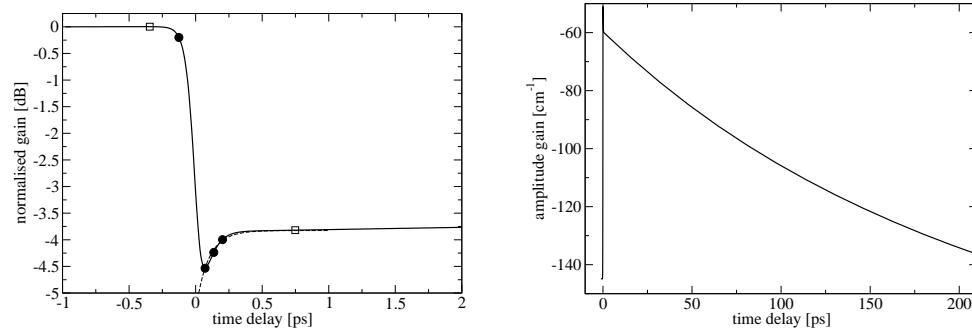


FIGURE 6.26: Same as FIGURE 6.23, but for a semiconductor absorber element (initial carrier density $N = 0.5 \cdot 10^{12} \text{ cm}^{-2} < N_{\text{transparency}}$). Curve fitting allows to extract effective rates of the gain (or better absorption) recovery $1/\tau_{\text{shb}} = 9.5 \text{ ps}^{-1}$ (left, dashed line) and $1/\tau_{\text{macr}} = 3.5 \text{ ns}^{-1}$ (right).

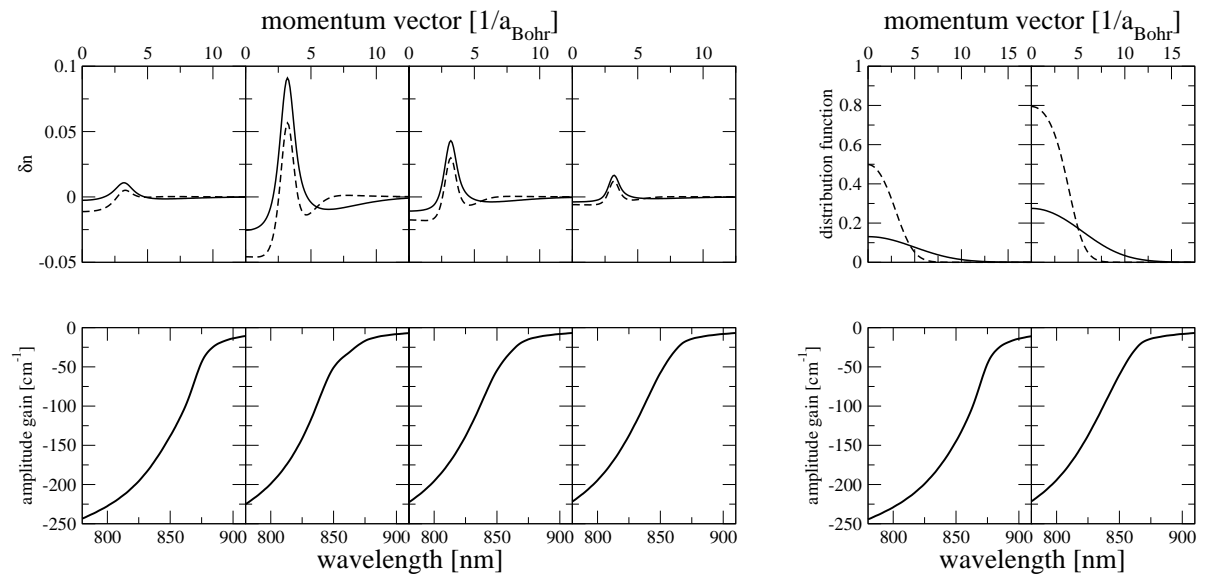


FIGURE 6.27: As FIGURE 6.24 the formation and the relaxation of optically excited, non-equilibrium distributions (left graph) by spectrally selective absorption (and carrier generation) and by the Coulomb interaction (which does not change the macroscopic carrier density), respectively, is shown. (Right) The macroscopic carrier generation and the absorber recovery due to various macroscopic carrier loss channels such as nonradiative and Auger recombination, spontaneous emission plus diffusion processes are analysed.

6.6 Chirped Pulse Amplification

In this section we extend the investigation of (sub-) picosecond pulse interactions with semiconductor gain materials to the propagation and amplification of pulses with a temporally varying nonlinear phase and time-dependent instantaneous frequency. More specifically, we simulate optical input pulses with a positive or negative linear chirp⁸

$$E(t) = E_{\text{env}}(t) \cdot \cos((\omega + \Delta\omega(t - t_0))(t - t_0) + \Phi_0), \quad (6.15)$$

$$\omega_{\text{inst}}(t) = \partial_t \Phi(t) = \omega + 2\Delta\omega(t - t_0). \quad (6.16)$$

So far we have characterised an optical pulse both in frequency-domain by calculating the spectrum and in time-domain by simulating the time series of the electric field envelope. This corresponds to time-integrated and spectrally integrated measurements, respectively. To gain a better understanding of the interaction of pulses with gain materials it is preferable to use an hybrid time-/frequency-domain approach. This involves both resolutions simultaneously, that is the spectrum or the instantaneous frequency versus time delay. The experimental technique to implement such measurements, the so-called frequency-resolved optical gating (FROG) method [153], measures the spectrogram

$$|E_g(\omega, \tau)|^2 \propto \left| \int_{-\infty}^{\infty} dt E_{\text{signal}}(t, \tau) e^{-i\omega t} \right|^2, \quad E_{\text{signal}}(t, \tau) = E(t) \cdot g(t - \tau), \quad (6.17)$$

by applying a gate function $g(t - \tau)$ with variable time delay τ . For ultrashort optical pulses the only available, however unknown gate function is the pulse itself. From our full time-domain simulations, in which the evolution of the electric field including the carrier wave is calculated, we can reproduce the various FROG measurements with different gate functions, for example the PG-FROG by using

$$E_{\text{signal}}(t, \tau) = E(t) |E_{\text{env}}(t - \tau)|^2. \quad (6.18)$$

We have seen that dynamical gain saturation, the intensity dependence of the refractive index, fast SPM and nonlinearities are of particular importance with decreasing pulse width and increasing peak power and instantaneous intensities. The amplification of pulses with femtosecond durations to extremely high energies and peak powers is crucial for a lot of applications, such as frequency conversion by means of nonlinear optical crystals. However, nonlinearities and the excess of the threshold of catastrophic optical damage, where the semiconductor gain material and the facets of the device take damage, limit the mode of operation. One proposal to overcome this problem is given by the chirped pulse amplification technique: The femtosecond pulses are chirped and consequently temporally stretched to pulse durations of several ten or more picoseconds by dispersive elements. This reduces the peak electric field amplitude E_0 and the

⁸A frequency chirp always increases the spectral width (for a given pulse length), or in other words, involves the increment of the time-frequency bandwidth product beyond the Fourier transform limit.

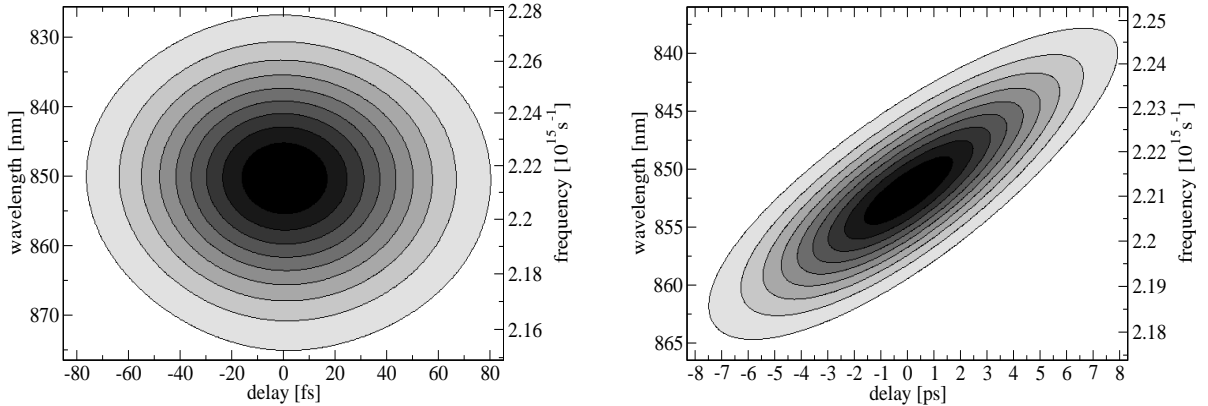


FIGURE 6.28: Calculated PG-FROG spectrograms $|E_g(\omega, \tau)|^2$, applying a gate function as specified in (6.18), of the amplified optical pulses for the 100 fs, unchirped input pulse (left) with $E_0 = 1 \cdot 10^8 \text{ Vm}^{-1}$, and for a 10 ps, positive linearly chirped pulse (right) with an identical pulse energy and spectrum. The relative spectrograms are linearly colour-coded in grey scales, dark/black corresponds to high values and white to low spectral intensities. The propagation and amplification of pulses in an active semiconductor material has induced asymmetries and small chirps. We note that the gradient of the PG-FROG spectrograms with time delay does not necessarily correspond to the instantaneous frequency $\omega_{\text{inst}}(\tau)$, but is dependent on the pulse shape and the applied gate function $g(t - \tau)$. (Right diagram) In the saturation regime there is a shift of the spectra to longer wavelengths (by approximately 2 nm) compared to the spectrum of the optical input pulse. For more details see FIGURE 6.30.

intensities. After the pulses have passed through the active media a compressor element (with opposite dispersion) temporally compresses the pulse by removing the chirp. FIGURE 6.29 illustrates that the fast Kerr-type nonlinearity is partially avoided and the electrical to optical energy conversion, the extraction of the in the carrier system stored energy, becomes more efficient: We have numerically analysed the amplification of the pulse energy, which is proportional to $\int_{-\infty}^{\infty} dt E_{\text{env}}^2(z, t) = \int_{-\infty}^{\infty} d\nu |E_{\nu}(z, \nu)|^2$, and the gain saturation in semiconductor-based amplifiers. A 10 ps pulse $E_0 = 1 \cdot 10^7 \text{ Vm}^{-1}$ is characterised by a maximal intensity of $I_0 = 0.5\epsilon_0\epsilon c/n \cdot E_0^2 \approx 50 \text{ MWcm}^{-2}$, a power of $P_0 = \int dA I_0(x, y) \approx 50 \text{ W}$ (FWHM $10 \mu\text{m}$), pulse energy of $\int dt P(t) \approx 0.4 \text{ nJ}$ and $\int dt E_{\text{env}}^2(t) \approx 750 \text{ V}^2\text{m}^{-2}\text{s}$. Plotted is the amplification of the pulse energy which corresponds to twice the amplitude gain g_{mod} . From nonlinear curve fitting to (6.13) we can extract the nonlinear saturation coefficient in the case of the 100 fs pulse (circles, dashed) as $2.31 \cdot 10^{-3} \text{ m}^2\text{V}^{-2}\text{s}^{-1}$. The application of the concept of chirped pulse amplification utilises the in the amplifier structure stored energy more effectively, suppresses nonlinear saturation effects, and prevents optical damage. An improvement by a factor of 2 to 3 is realised, and we find a saturation coefficient (solid line) of $9.85 \cdot 10^{-4} \text{ m}^2\text{V}^{-2}\text{s}^{-1}$. The main reasons for the improved performances are given by the less distinctive hole burning and gain saturation for smaller optical peak powers and by a partial recovery of the spectral inversion and of the gain for pulse lengths of the stretched pulses greater

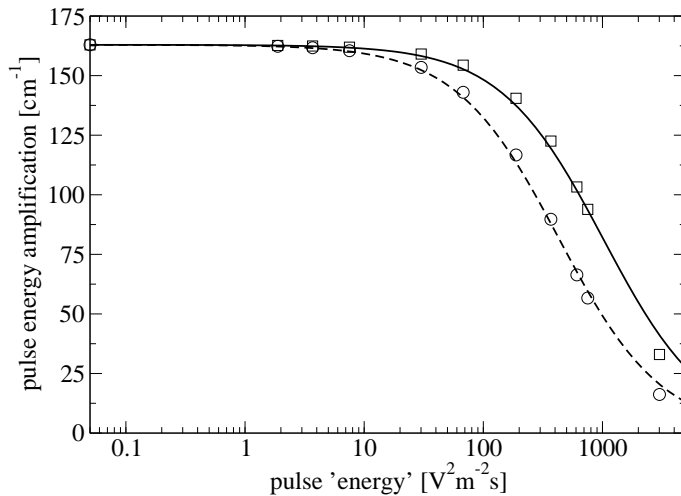


FIGURE 6.29: Amplification of optical pulses with Gaussian pulse shapes and a pulse duration of $T_{\text{pulse}}^{\text{FWHM}}(E_{\text{env}}(t)) = 100$ fs (unchirped) or 10 ps and showing a positive linear chirp (see (6.15)) of $\Delta\omega = 2.78 \cdot 10^{24} \text{ s}^{-2}$, respectively, in a SOA. Important parameters are $\lambda = 850$ nm, $N = 3 \cdot 10^{12} \text{ cm}^{-2} \approx 2N_{\text{transparency}}$, $\Gamma N_{\text{QW}}/L_{\text{ref}} = 1/50$ nm, $n_{\text{eff}} = 3.6$ and $L_{\text{act}} = 0.05$ mm. Using dispersive optical elements, such as diffraction grating-pairs for pulse stretching and compression, we can convert the two pulses into one another as both pulses feature the same pulse energy and spectrum.

than the time constants of recovery. Obviously, in a realisation of the chirped pulse amplification method the recompression step demands some considerations as not only the chirp from pulse stretching but also the extra dispersions arising from the interactions in the SOA structure have to be compensated.

As the intensities of the stretched and chirped pulses and the gain approach saturation, the amplified pulse spectrum will be frequency-shifted. For a positive chirped pulse, with the leading edge extracting energy preferentially and the trailing edge experiencing less amplification, the central wavelength is redshifted (FIGURE 6.30).

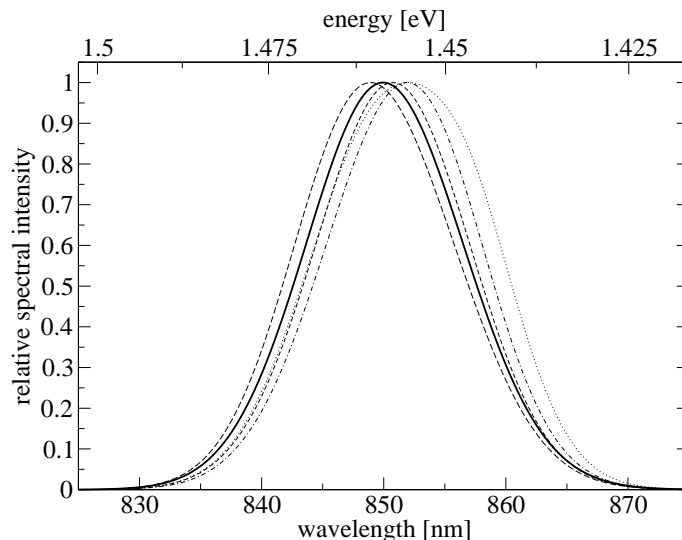


FIGURE 6.30: Relative spectral intensity $|E_\nu|^2$ versus wavelength (or energy): Depicted are the spectrum of the linearly chirped input pulse (as solid line) and the characterisations of various amplified (chirped) pulses in frequency-domain. With increasing pulse energy or electric field amplitude of the input pulse, $E_0 = 5 \cdot 10^6 \text{ Vm}^{-1}$ (dashed), $1 \cdot 10^7 \text{ Vm}^{-1}$ (dot-dashed) and $2 \cdot 10^7 \text{ Vm}^{-1}$ (dotted), we recognise an increasing shift of the spectra to longer wavelengths. This occurs because in the nonlinear or gain saturation regime the leading red edge of a pulse with positive linear chirp extracts energy from the semiconductor amplifier structure preferentially. The trailing blue edge is less amplified and consequently the spectrum is effectively redshifted. For a negative linearly chirped input pulse we observe a blueshift of the spectrum (long-dashed line).

6.7 Ultrashort Coherent Optical Pulse Interactions

The availability of high-intensity ultrashort optical pulses allows for the study of transient nonlinear coherent pulse propagation phenomena in active media [82, 83], such as self-induced transparency [154], pulse area theorem [81] or soliton solutions [155]. Common assumptions comprise the neglect of pumping terms and of decay or dephasing processes. Lifetimes greatly exceed the pulse duration, and the induced polarisation has a more or less infinite memory. Consequently, a coherent medium is considered with the sole relevant interaction being the electric dipole transitions. The interaction of an optical pulse with a resonant absorber (or amplifier) medium within the semiclassical framework can be analysed by solving the Maxwell and the exactly resonant two-level (or equivalent macroscopic) Bloch equations. However, an extension to inhomogeneous broadening of the two-level atomic system (with $\omega_0 \gg \Delta\omega_{\text{inh}} \gg \Delta\omega_{\text{pulse}}$) is possible [155]. The full time-domain model consists of the one-dimensional Maxwell curl equations (3.42)–(3.46)

and the macroscopic Bloch equations [14, 76]

$$\partial_z E_x + \partial_t B_y = 0, \quad \frac{1}{\mu_0} \partial_z B_y + \partial_t D_x = 0, \quad D_x = \epsilon_0 \epsilon E_x + \Gamma_{x,y} \frac{N_{\text{QW}}}{L_{\text{ref}}} P_x, \quad (6.19)$$

$$\partial_t^2 P + 2\gamma^P \partial_t P + \omega^2 P = -\frac{4\Omega(M^{eh})^2}{\hbar} E (N - N_{\text{transparency}}), \quad E \leftarrow \Gamma \frac{N_{\text{QW}}}{L_{\text{ref}}} \frac{P}{\epsilon_0}, \quad (6.20)$$

$$\partial_t N = \frac{1}{\hbar\Omega} E (\partial_t P + \gamma^P P) - \Gamma^{\text{nr}} N. \quad (6.21)$$

The results can then be compared to analytical descriptions of ultrashort coherent optical pulse propagation in a resonant medium [36, 154, 155]. A summary of common notations and known analytical results is presented below. We introduce the real-valued phase $\Phi(z, t)$ and envelope variables $E_{\text{env}}(z, t)$, which may also become negative, and rewrite the electric field as

$$E(z, t) = \frac{1}{2} E_{\text{env}}(z, t) e^{i\Phi(z, t)} e^{-i\omega_0 t} e^{ik_0 n_{\text{eff}} z} + \text{conjugate complex}, \quad E_{\text{env}}, \Phi \in \mathbb{R}. \quad (6.22)$$

We imply a similar expression for the induced polarisation. ω_0 is the carrier frequency and we assume $\Omega - \omega_0 = 0$ and $\omega_0 T_{\text{pulse}} \gg 1$. By applying the slowly varying envelope approximation (SVEA), the dynamics is given by the reduced Maxwell equations for a forward travelling wave, by the following partial differential equations [36]

$$\left(\frac{n^2}{cn_{\text{eff}}} \partial_t + \partial_z \right) E_{\text{env}}(z, t) = -\frac{k_0 \Gamma}{\epsilon_0 2n_{\text{eff}}} \frac{N_{\text{QW}}}{L_{\text{ref}}} \text{Im}(P_{\text{env}}(z, t)), \quad (6.23)$$

$$E_{\text{env}}(z, t) \left(\frac{n^2}{cn_{\text{eff}}} \partial_t + \partial_z \right) \Phi(z, t) = \frac{k_0 \Gamma}{\epsilon_0 2n_{\text{eff}}} \frac{N_{\text{QW}}}{L_{\text{ref}}} \text{Re}(P_{\text{env}}(z, t)), \quad (6.24)$$

which we consider in combination with the macroscopic Bloch equations⁹ in rotating wave approximation (RWA) (see SECTIONS 2.4+2.5).

The state of the two-level system is characterised by the Bloch pseudo-vector. We introduce a new variable $\theta(z, t)$ which is the net angle that this pseudo-vector has been turned through at a time t by an applied electric field envelope $E_{\text{env}}(z, t)$. It is also an expression for the area of the pulse developed up to time t (no explicit knowledge of $E_{\text{env}}(z, t)$ is required)

$$\theta(z, t) = \int_{-\infty}^t dt' \Omega_{\text{Rabi}}(z, t') = \frac{M^{eh}}{\hbar} \int_{-\infty}^t dt' E_{\text{env}}(z, t') \rightarrow \partial_t \theta(z, t) = \frac{M^{eh}}{\hbar} E_{\text{env}}(z, t). \quad (6.25)$$

⁹The above described macroscopic or two-level Bloch equations model may also be applied as efficient simulation tool [55, 126] to analyse millimeter-sized active semiconductor-based devices. To cover important properties of semiconductor gain materials we perform some changes to the atomic-like two-level approach: In (6.20) a nonlinear gain model (as for quantum wells) is introduced by $N - N_{\text{transparency}} = N_{\text{transparency}} (N/N_{\text{transparency}} - 1) \rightarrow N_{\text{transparency}} \ln(N/N_{\text{transparency}})$ and gain or absorption suppression, nonlinear saturation by $E \rightarrow E/(1 + \epsilon_{\text{sat}} S)$, with the photon density $S \propto E_{\text{env}}^2$ [73]. In (6.21) additional loss channels and carrier diffusion may be implemented.

The idea is to search for unique pulse shapes, for analytical solutions of the nonlinear problem (6.23)+(6.24) with dependency $(z, t) = t - z/v_{\text{pulse}}$. This condition reduces the problem to an ordinary differential equation, the so-called Mathieu equation $\partial_t^2 \theta(t) = \gamma_{\text{pulse}}^2 \sin(\theta(t))$, which also governs the motion of a pendulum initially angled in the non-equilibrium upward position (the solution describes exactly one rotation). The solution of this equation specifies a temporal soliton

$$E_{\text{env}}(z, t) = E_{\text{env}} \left(t - \frac{z}{v_{\text{pulse}}} \right), \quad \partial_t \Phi(z, t) = \text{constant}, \quad (6.26)$$

$$E_{\text{env}}(z, t) = E_0 \cdot \text{sech} \left(\gamma_{\text{pulse}} \left(t - \frac{z}{v_{\text{pulse}}} \right) \right), \quad E_0 = 2\gamma_{\text{pulse}} \frac{\hbar}{M^{eh}}, \quad (6.27)$$

$$v_{\text{pulse}} = \left(\frac{n^2}{cn_{\text{eff}}} + \frac{k_0 \Gamma}{\epsilon_0 2n_{\text{eff}}} \frac{N_{\text{QW}}}{L_{\text{ref}}} \frac{4\hbar}{E_0^2} 2(N_{\text{transparency}} - N_0) \right)^{-1} < v_{\text{phase}}. \quad (6.28)$$

The hyperbolic secant solution (6.27) is unattenuated and retains its shape. The pulse area theorem describes general properties of pulse propagation [81]. In the nonlinear regime the pulse area $\Theta(z)$ develops according to (6.31)

$$\Theta(z) = \lim_{t \rightarrow \infty} \theta(z, t), \quad (6.29)$$

$$\alpha = \pi \delta(\Omega - \omega_0) \frac{k_0 \Gamma}{\epsilon_0 2n_{\text{eff}}} \frac{N_{\text{QW}}}{L_{\text{ref}}} \frac{(M^{eh})^2}{\hbar} 2(N_{\text{transparency}} - N_0), \quad (6.30)$$

$$\partial_z \Theta(z) = -\alpha \sin(\Theta(z)), \quad (6.31)$$

$$\lim_{z \rightarrow \infty} \Theta(z) = \begin{cases} 2n\pi, n \in \mathbb{N}_0 & \alpha > 0 \\ (2n+1)\pi, n \in \mathbb{N}_0 & \alpha < 0 \end{cases}. \quad (6.32)$$

Consequently, in optical pulse configurations with $\Theta_0 = m\pi, m \in \mathbb{N}_0$ the pulse area is conserved in the coherent propagation problem, which means $\partial_z \Theta(z) = 0$. In an absorber medium with $\alpha > 0$ the asymptotic solutions (attractors) are given as even multiples of π where the branch number n is determined by the initial pulse area. Pulses with larger areas divide into n separate 2π pulses, and n solitons given by (6.27) are formed. In an amplifier the stable solutions are specified by odd multiples of π .

FIGURE 6.31 shows the propagation of a 2π pulse with hyperbolic secant pulse envelope shape (6.27) in an absorber: This optical pulse gives a complete transition of the carrier system from the ground state (in the terminology of a two-level system), i.e. $N_0 = N_{\text{transparency}} - \delta N$ in our approach, to the excited state $N_{\text{transparency}} + \delta N$. The properties of the optical excitation pulse are maintained. These transitions occur within one Rabi period, the optical pulse solution propagates distortionless as a solitary wave as though it were unaffected by the presence of the active nonlinear medium, as though the medium were transparent [76, 154, 155]. In the full time-domain simulations, a propagating sech-pulse enters a $360 \mu\text{m}$ long active, resonantly absorbing medium. The temporal evolutions of the electric field including the carrier wave (top) and of the macroscopic carrier density (bottom) are recorded at positions $0 \mu\text{m}$, $90 \mu\text{m}$, $180 \mu\text{m}$, $270 \mu\text{m}$ and

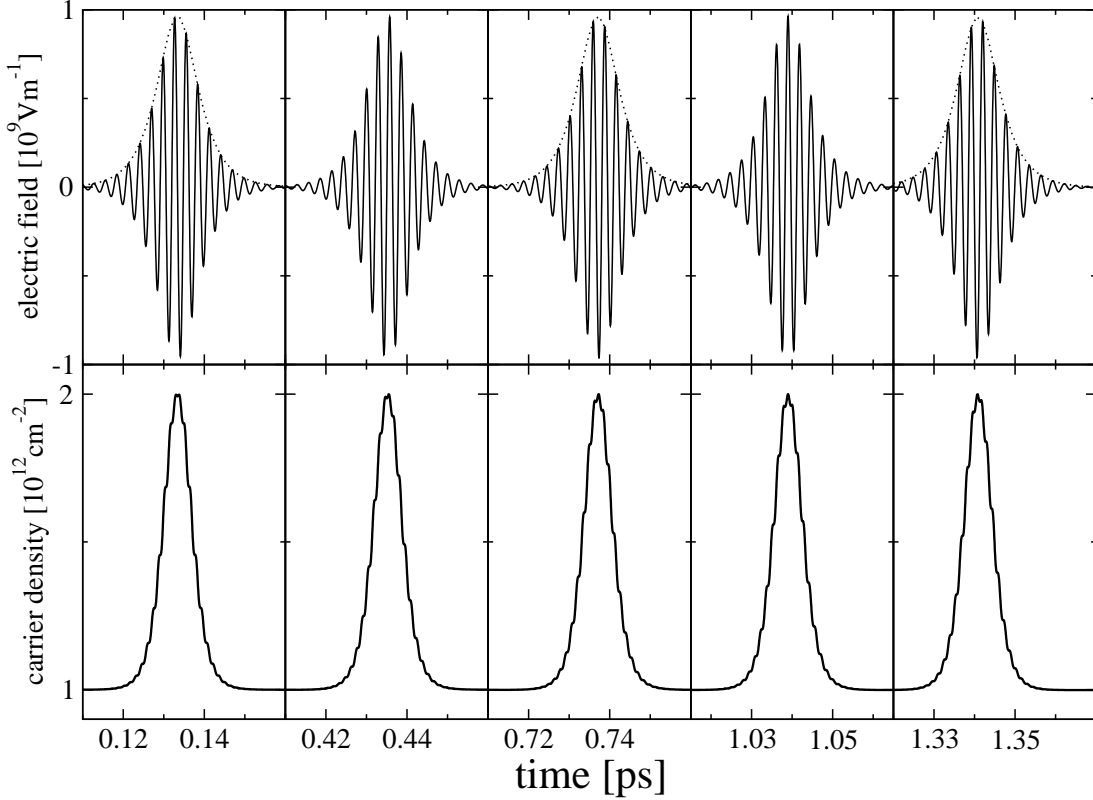


FIGURE 6.31: Self-induced transparency or propagation of a temporal soliton. Simulation parameters are set to $\gamma^P = 1 \cdot 10^9 \text{ s}^{-1}$, $\Gamma N_{\text{QW}}/L_{\text{ref}} = 1 \cdot 10^7 \text{ m}^{-1}$, $N_{\text{transparency}} = 1.5 \cdot 10^{12} \text{ cm}^{-2}$, $N_0 = 1 \cdot 10^{12} \text{ cm}^{-2}$, $n = n_{\text{eff}} = 1$, and $\gamma_{\text{pulse}} = 2.2 \cdot 10^{14} \text{ s}^{-1} \rightarrow T_{\text{pulse}}^{\text{FWHM}} = 12 \text{ fs}$.

$360 \mu\text{m}$ (from the left). The full time-domain Maxwell Bloch simulations [76, 80] essentially reproduce the known analytical results of self-induced transparency and pulse area theorem [81, 154, 155].

FIGURE 6.32 shows the resonant coherent interaction of pulses with different pulse areas Θ_0 with a two-level atomic system: A 2π pulse generates a complete excitation and subsequent deexcitation of the medium (top left) [14]. The coherent induced absorption of pulse energy during the first half of the pulse, the leading edge of the pulse putting energy into the medium by flipping the Bloch pseudo-vector, $\propto \int_{-\infty}^{z_0/v_{\text{pulse}}} dt E_{\text{env}}^2(z_0, t)$ is followed by the coherent induced emission of exactly the same amount of energy back into the light field during the second half [154]. The trailing edge of the optical pulse is flipping the Bloch vector back to its original position (Rabi flopping). The carrier density is displayed as wide solid line, the electric field with carrier wave (thin solid line) is phase shifted by $\pi/2$ versus the polarisation (dashed), as expected for a harmonic oscillator driven by a resonant excitation. The time-derivatives of the electric field play an essential role in the nonlinear evolution of the system, and the flattenings in the density profile appear where $|\partial_t E|$ takes its maximum value [76]. Apart from this additional cubic, polynomial-like features the numerical full time-domain simulations agree well with the

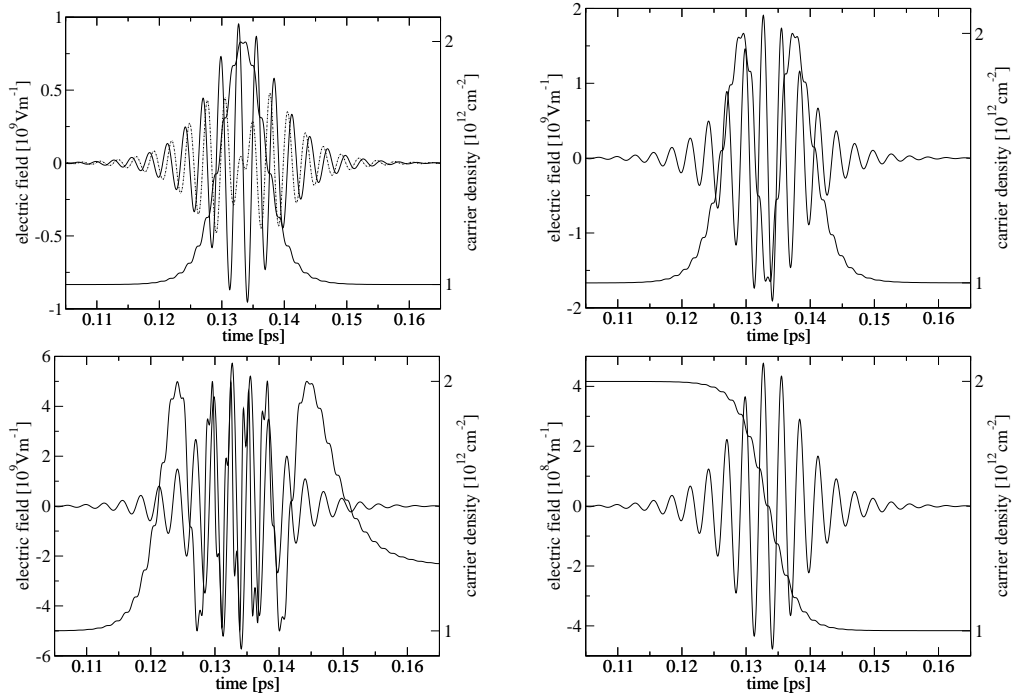


FIGURE 6.32: Resonant coherent interaction of pulses with different pulse areas Θ_0 (E_0 in (6.27) is varied) with a semiconductor structure described by the macroscopic gain model (6.20)+(6.21), which is equivalent to a two-level atomic system. Depicted are details of the temporal profiles at position $0 \mu\text{m}$ of pulse and active material (simulation parameters same as in FIGURE 6.31).

analytical results [14, 76, 80]. The same is true in the case of 4π pulses in an absorber medium with two symmetric transitions (top right), and for π pulse propagation in an amplifier medium with $N_0 = 2 \cdot 10^{12} \text{ cm}^{-2}$, displayed at bottom right. For larger pulse areas, we have numerically calculated a 12π pulse (bottom left), incomplete Rabi flops occur instead of an integer number. In [80] this is called the breakdown of the pulse area theorem due to carrier wave Rabi flopping, which manifests itself in strong carrier reshaping, electric field time-derivative effects and a subsequent production of higher spectral components in the travelling pulse. FIGURES 6.33+6.34 show further tests of the pulse area theorem.

An extension to an inhomogeneously broadened two-level atomic system is given in FIGURE 6.35, where we consider a band-resolved semiconductor absorber medium: The coupling between the different energy states of the band structure has been artificially switched-off (top). This means, we treat the absorber material as a purely inhomogeneously broadened ensemble of two-level systems. The temporal profiles are given at $0 \mu\text{m}$ (left) and at the end of the active region at $360 \mu\text{m}$ (right). The simulations show strong signatures of the above discussed nonlinear coherent resonant effects [155]. The impacts of the time-derivatives of the electric field seem to have changed, and the value of the carrier density at the upper reversal point of the Rabi flop is not equal

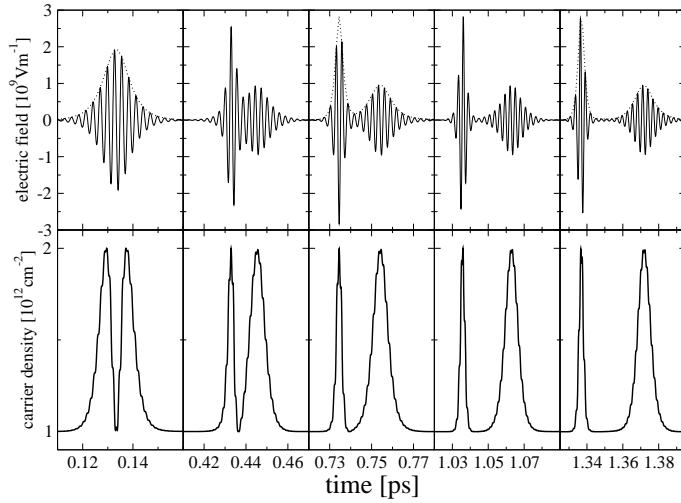


FIGURE 6.33: Test of the pulse area theorem: We analyse the propagation of a 4π pulse in a resonantly absorbing medium. The pulse divides into two separate 2π soliton pulses of the specific envelope shape given by (6.27) (having different amplitudes and durations T_{pulse}) which propagate at different group velocities (6.28). The velocity may be considerably less than the phase velocity of light in the medium cn_{eff}/n^2 . With the objective to shorten the required simulation time, the coupling parameter $\Gamma N_{\text{QW}}/L_{\text{ref}}$ has been increased by a factor of 5.

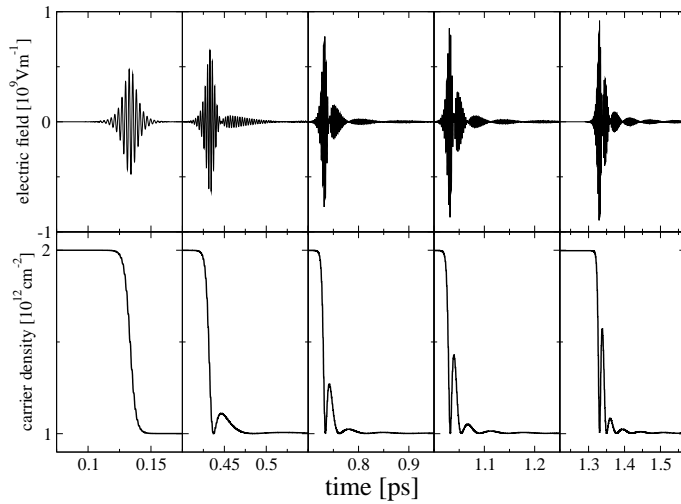


FIGURE 6.34: Propagation of a π pulse in a semiconductor amplifier: According to the area theorem both an increase of the pulse energy $\propto \int dt E_{\text{env}}^2(z, t)$ and maintaining the pulse area is possible if with increasing envelope the pulse duration is shortened (pulse compression). For a few-cycle pulse coherent stimulated emission from the medium back into the pulse may happen behind the main pulse (longer tail effects) and the pulse would split [156]. This pulse splitting, where sections with negative electric field envelopes and areas occur, is another possible mechanism of conserving the pulse area.

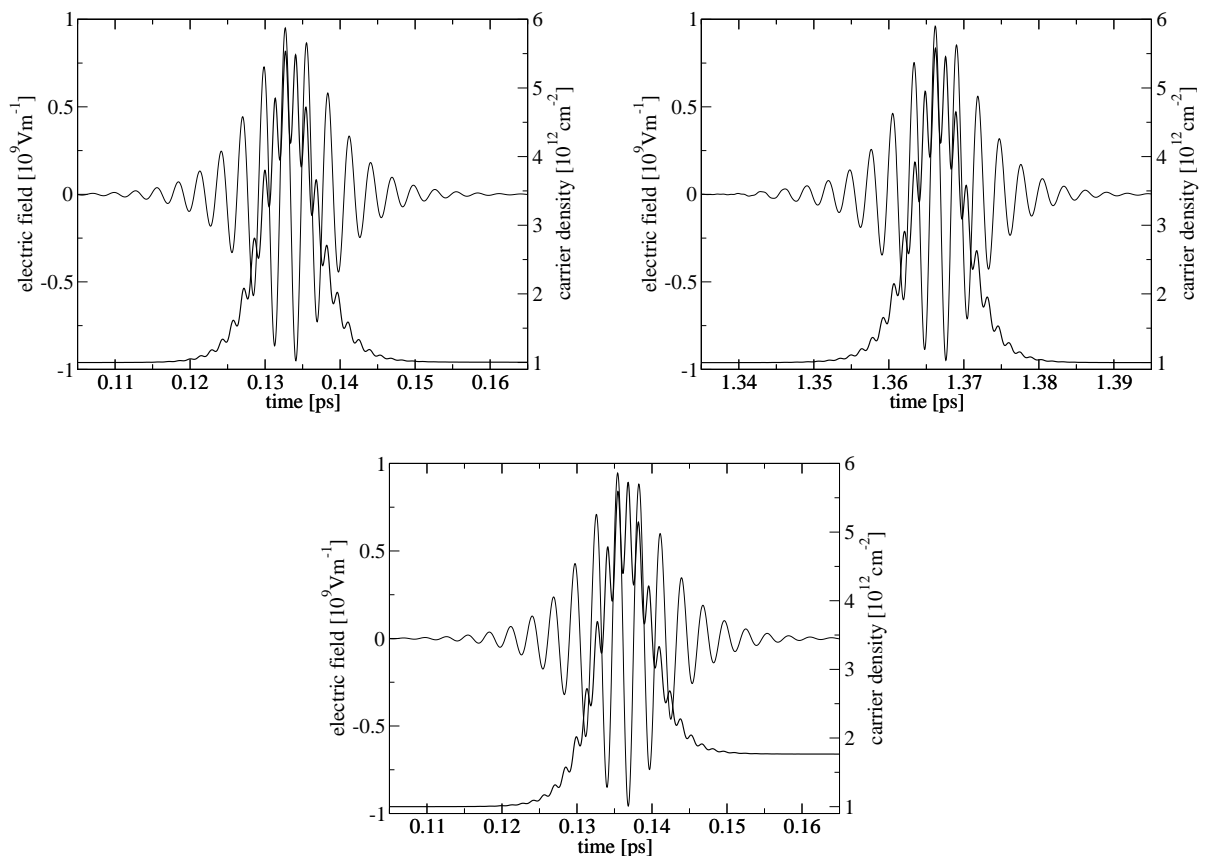


FIGURE 6.35: Interaction of 2π self-induced transparency pulses with a band-resolved semiconductor absorber medium.

$N_{\text{transparency}} + \delta N$. These deviations from analytical predictions can be explained by the huge inhomogeneous broadening associated with the band-resolved material model (the SVEA and RWA approximations are not applicable any more) and by the thereby implemented nonlinear gain characteristics $\propto (N - N_{\text{transparency}})$. We also study coherent pulse interactions in the case of dephasing processes, other relaxation and loss channels, and consequently homogeneous broadening represented by realistic parameters (bottom). Incomplete Rabi flops occur, ultrafast nonlinear propagation effects become less distinctive and disappear entirely for longer pulses. Depicted are the temporal evolutions at $0 \mu\text{m}$, contrary to all other simulations we have chosen $n = n_{\text{eff}} = 3.6$ and the length of the absorber region as $100 \mu\text{m}$.

6.8 Conclusion

In this chapter we have employed the full time-domain model, which combines the Maxwell curl equations and the semiconductor Bloch equations, in order to investigate the longitudinal multi-mode dynamics in novel surface-emitting laser structures and the nonlinear interaction of femtosecond and picosecond pulses with an optical gain medium.

In more detail:

- We have analysed VCSEL with embedded periodic gain and refractive index structures. The concept of the photonic band edge laser is to exploit the special properties of the singularities in the optical band structure diagrams, i.e. the band edges with flat dispersion. This laser is based on gain enhancement by an increased localisation of the modes over the active quantum confined structures and by the more efficient interactions of photons with the gain medium. The surrounding photonic band gap region suppresses optical losses. Our simulations of lasing frequencies, thresholds and field profiles quantitatively analyse photonic band edge band gap diode lasers and numerically validate the gain enhancement for band edge modes.
- Realistic optically pumped external cavity surface-emitting laser structures have been modelled. Our microscopic approach reveals the dynamical balance between carrier generation or pumping at high energy states in the band structure diagram, momentum relaxation of carriers towards the Fermi-Dirac distribution and stimulated recombination or lasing from states near the band edge. We show that the longitudinal multi-mode behaviour is composed of several external cavity modes.
- By probing the semiconductor gain medium with weak electromagnetic test pulses, we have found the analogy between these propagation experiments and small signal gain calculations assuming quasi-equilibrium.
- For high-intensity pulses, that is in the nonlinear or saturation regime, the pump pulses are modifying the gain material. We numerically investigate (sub-) picosecond pulse interactions with semiconductor structures and identify the microscopic origin of the fast nonlinearities, and specify the physical effects behind various saturation mechanisms. We also compute nonlinear gain coefficients and the different recovery rates. Group velocity dispersion, and the fast optical nonlinearities and self-phase modulation are the main causes of asymmetries in pulse temporal and spectral shape. The most critical parameters of gain recovery are the time constants of intra-band scattering and carrier redistribution. The reshaping of the pulse envelope (e.g. pulse slowdown or advancement, sharpening of edges, and change of pulse duration) and asymmetries in the pulse spectrum are discussed. To investigate the dynamics of the gain and the refractive index change pump-probe experiments are numerically reproduced. One technique for amplifying high-intensity pulses, which avoids these nonlinearities and increases the extractable energy from the active medium, is proposed by the chirped pulse amplification method.
- We have investigated nonlinear coherent pulse propagation phenomena in active gain media, such as the pulse area theorem or self-induced transparency. Our numerical full time-domain simulations with adjusted constants of decay and in particular of the dephasing processes agree well with analytical predictions, apart from the propagation of optical pulses with large pulse areas, or few-cycle pulses in amplifying materials. Coherent ultrafast nonlinear propagation effects become less distinctive if we apply a more realistic model of the quantum well gain material, loss channels, dephasing processes and homogeneous broadening.

A Discretisation Schemes and Numerical Implementations

The numerical treatment of partial differential equations implies a finite-difference discretisation scheme of the incorporated field amplitudes and differential operators in time and space. We are solely working on uniformly spaced (and rectangular) grids with the spatial and temporal steppings $\Delta x, \Delta z, \Delta t$ and introduce the following abbreviatory notation for a macroscopic field F

$$F(x, z, t) = F(x_0 + i\Delta x, z_0 + j\Delta z, t_0 + n\Delta t) = F_{i,j}^n. \quad (\text{A.1})$$

The various differential operators (up to second order in the investigated models) have to be transformed to finite-difference operators, for instance for the derivations with respect to the transverse coordinate by

$$\partial_x F(x, z, t) = \partial_x F_{i,j}^n \rightarrow \frac{1}{\Delta x} (F_{i+1/2,j}^n - F_{i-1/2,j}^n) \rightarrow \frac{1}{2\Delta x} (F_{i+1,j}^n - F_{i-1,j}^n), \quad (\text{A.2})$$

$$\partial_x^2 F(x, z, t) = \partial_x^2 F_{i,j}^n \rightarrow \frac{1}{(\Delta x)^2} (F_{i+1,j}^n - 2F_{i,j}^n + F_{i-1,j}^n), \quad (\text{A.3})$$

and for the temporal differential operator by

$$\partial_t F(x, z, t + \Delta t/2) = \partial_t F_{i,j}^{n+1/2} \rightarrow \frac{1}{\Delta t} (F_{i,j}^{n+1} - F_{i,j}^n). \quad (\text{A.4})$$

The correct centring of the time points and of the positions is absolute essential, which may demand for an additional averaging process.

For the active points on the spatial grid, the dynamical material response is represented on basis of the band-resolved semiconductor Bloch equations. Thereby, microscopic quantities $f(k, t)$ have to be discretised on an extra, equally spaced momentum grid

$$f(k, t) = f(k_0 + k\Delta k, t_0 + n\Delta t) = f_k^n. \quad (\text{A.5})$$

To evaluate integrals over the momentum grid (this can be found in the connection of macroscopic with the respective microscopic variables as a spectral summation, or in the scattering integrals) we do approximate the integrals as a sum of trapezoidal areas. In integrations of functions with singularities an adaptive scheme based on Gauss-Kronrod quadrature rules is applied [142].

A.1 Discretisation Scheme of the Transverse Wave Equation Model

In numerically solving a multi-dimensional partial differential equation the stability and accuracy, plus the complexity of the algorithm, that is to say, the number of iteration steps required to calculate the new field values, together with the spatial grid (this quantity chiefly determines the memory requirements) and temporal stepping are the most crucial parameters as one is still at the very limit of calculating capacities even on supercomputers for these extremely time-critical (and multi-physics, multi-scale) problems.

In the transverse scalar paraxial wave equation model, associated with an ambipolar diffusion equation for the carrier sheet density and a dynamical equation for the induced electric polarisation, the equation (3.37) for the complex optical field amplitude $\tilde{E}^+(x, z, t), \mathbb{R}^2 \times \mathbb{R} \rightarrow \mathbb{C}$, is the most critical part concerning numerical stability

$$\begin{aligned} \frac{n^2}{cn_{\text{eff}}} \partial_t \tilde{E}^+(x, z, t) &= \left(-\partial_z + i \frac{1}{2k_0 n_{\text{eff}}} \partial_x^2 + ik_0 \frac{n}{n_{\text{eff}}} \delta n_{\text{pas}}(x) \right) \tilde{E}^+ + i \frac{k_0 \Gamma_y}{\epsilon_0 2n_{\text{eff}}} \frac{N_{\text{QW}}}{L_{\text{ref}}} \tilde{P}^+ \\ \rightarrow a \partial_t E &= (-\partial_z + ib \partial_x^2 + ic(x)) E + idP = \mathcal{L}[E] + \mathcal{N}[E]. \end{aligned} \quad (\text{A.6})$$

On the right-hand side of the differential operator equation we have separated the linear terms in the electric field amplitude, denoted by $\mathcal{L}[E]$, from the nonlinear functional $\mathcal{N}[E] = ik_0 / (\epsilon_0 2n_{\text{eff}}) \Gamma_y N_{\text{QW}} / L_{\text{ref}} P[E]$ which turns out to be not too critical for the stability of the numerical method. The different numerical schemes can now be classified by the way the linear part of the right-hand side of the equation is treated [142]. A simple explicit scheme in which one uses the field values at the old time n is straightforward

$$a \frac{E_{i,j}^{n+1} - E_{i,j}^n}{\Delta t} = \mathcal{L}[E^n] + \mathcal{N}[E_{i,j}^n], \quad (\text{A.7})$$

but the algorithm is not stable for too large time steps Δt . On the other hand, one could evaluate this linear term fully implicit at the new time point $n + 1$, consequently one calculates $\mathcal{L}[E^{n+1}]$ (E^{n+1} represents a vector with $N_{\text{cells}} = N_x \cdot N_z$ elements). This numerical scheme is unconditionally stable but it would require in the case of a two-dimensional grid the inversion of a huge matrix ($N_{\text{cells}} \times N_{\text{cells}}$) at every time step. Evidently one has to find a compromise between stability and accuracy and the simplicity of the algorithm. The proposed Hopscotch method [157] is introducing some implicit character into a predominantly explicit scheme. For a two-dimensional spatial grid, which can be visualised by a chessboard with white and black squares, all white fields are solved explicitly. The remaining (in-between) black fields are then solved implicitly

$$a \frac{E_{i,j}^{n+1} - E_{i,j}^n}{\Delta t} = -\frac{E_{i,j+1}^{n+1} - E_{i,j-1}^{n+1}}{2\Delta z} + ib \frac{E_{i+1,j}^{n+1} - 2E_{i,j}^{n+1} + E_{i-1,j}^{n+1}}{(\Delta x)^2} + ic_i E_{i,j}^{n+1} + \mathcal{N}[E_{i,j}^n]. \quad (\text{A.8})$$

As the electric fields on four of the five integration stencil points have already been calculated in the explicit half step (as all neighbours of a black square are white squares)

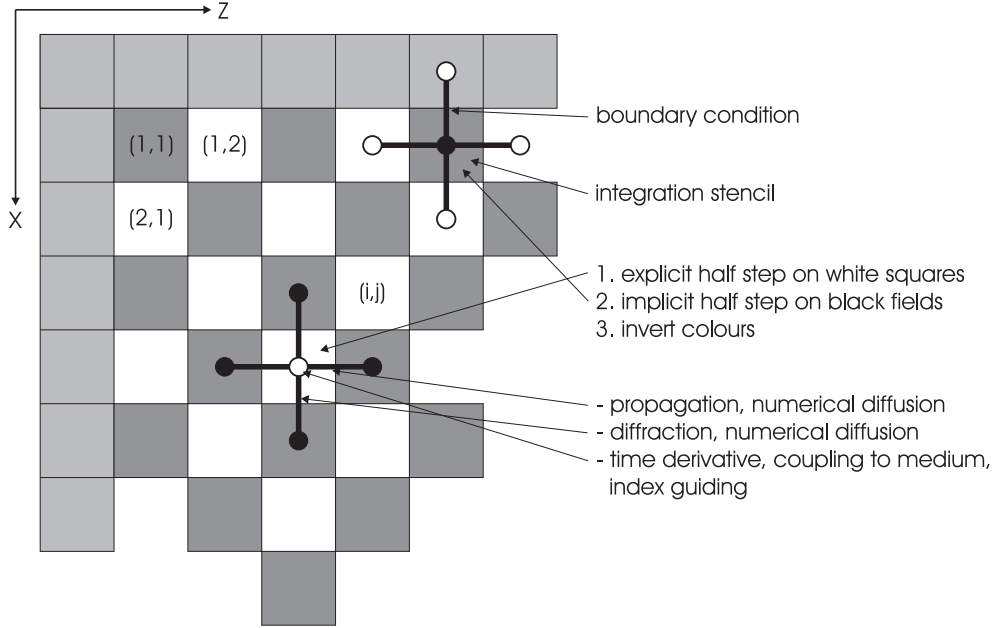


FIGURE A.1: Hopscotch method: The diagram (from [12]) shows the two-dimensional spatial grid with white and black squares (the colour is linked to the explicit and implicit scheme, respectively) and the discretisation of the various differential operators of the scalar transverse wave equation. The ambipolar diffusion equation of the macroscopic charge carrier density is numerically solved in synchronism with the wave equation. An additional momentum grid is attached to each active field to compute the band-resolved semiconductor gain and carrier dynamics.

the nonlocal elements in the above expression are in the end evaluated explicitly (see FIGURE A.1). In the following integration step the colours are inverted. With the Hopscotch method one does not have to solve a matrix-valued problem, the implicit character (and for this reason necessary inversion) arises only locally. The method is very efficient and stable, reasonable accurate, and memory requirements are low due to the fact that there is no need for introducing helping fields in the algorithm. One remaining problem occurs because of the hyperbolic character of the propagation term $-\partial_z E$ which can lead to numerical instabilities [36]. This problem can be solved by adding a very small numerical diffusion, terms with elliptic character which are stabilising the equation¹

$$+ D_x \partial_x^2 E_{i,j} + \frac{n^2}{cn_{\text{eff}}} \frac{D_z}{\Delta t} (E_{i,j+1} - 2E_{i,j} + E_{i,j-1}). \quad (\text{A.9})$$

Before numerically solving the partial differential equations for the macroscopic fields

¹Another ansatz called the Lax-Wendroff discretisation scheme suggests a spatial averaging of the field amplitudes $E_{i,j}^n = 1/2(E_{i,j+1}^n + E_{i,j-1}^n)$. This induces an additional (dissipative) term of elliptic character on the right-hand side which stabilises the algorithm but also strongly changes and thus corrupts the solution of the partial differential equation, for example a propagating pulse will numerically elapse.

$E_{i,j}, N_{i,j}$ we do consider the stiff system of ordinary differential equations which models the dynamical material response. For the white squares we choose an explicit method, for the black fields an implicit discretisation is opted for, and it turns out to be sufficient to treat all nonlinear terms (in the dynamical variables) in a fully explicit way without losing accuracy. Most of the computing time is spent in the time integrations of the semiconductor material part, but the algorithm for the system of ordinary differential equations is straightforward and numerically very stable.

At the transverse boundary of the spatial region of interest boundary conditions of Dirichlet or von Neumann type are specified for the macroscopic fields electric field and carrier density. In longitudinal direction the boundary condition is given by the reflections of the optical fields at the facets of the cavity.

As summarisation of the discretisation scheme and the numerical algorithm typical values and the sequence of iteration steps are indicated in the following table:

Hopscotch method, paraxial transverse wave equation model	
<i>typical values of numerical parameters:</i>	
spatial stepping Δx	250 nm
spatial stepping ² Δz	2.5 μm
time step Δt	0.5 fs
numerical diffusion D_x	0.01 $\cdot 1/(2k_0 n_{\text{eff}})$
numerical diffusion term ³ D_z	0.005
transverse index guiding ⁴ $\delta n_{\text{pas}}(x)$	0.003
<i>sequence of time integration steps:</i>	
1. explicit half step (white)	$p_k, n_k^\circ \rightarrow \text{spectral summation} \rightarrow E_{i,j} \rightarrow N_{i,j}, f_k^\circ$
2. implicit half step (black)	SBE \rightarrow (2.114)+(2.117) \rightarrow (A.8) \rightarrow diffusion eq.
3. exchange of colours	$t + \Delta t \rightarrow$ back to 1.

A.2 Discretisation Scheme of the Longitudinal Full Time-Domain Model

The numerical implementation of the one-dimensional Maxwell curl equations model (3.42)–(3.46) together with the dynamical nonlinear material response (realised by ordinary differential equations for the band-resolved polarisation and the distribution functions) within the finite-difference time-domain (FDTD) framework builds on an adequate choice of discretisation schemes and the correct centring of fields in time and space [58].

²This is a typical value in the case of a continuous wave operating laser, the numerical treatment of pulse propagation in semiconductor optical amplifiers requires a higher (by a factor of approximately 20) resolution.

³The chosen value is 100 times smaller than the elliptic (and strongly dissipative) stabilisation term suggested by Lax-Wendroff.

⁴This very small ridge waveguiding term is needful to avoid unphysical numerical solutions.

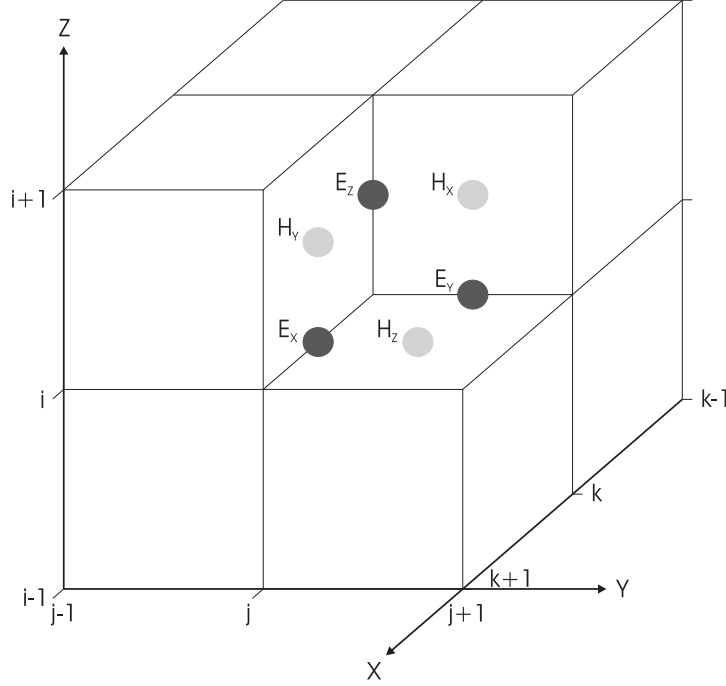


FIGURE A.2: Yee discretisation scheme (from [14]): Yee suggested a by half steps (in time and space) displaced arrangement of the various vector components of the electric and magnetic field quantities, what in a perfect way meets the natural rotational structure of the first order Maxwell curl equations.

A central finite-difference approximation of derivatives of the fields is applied

$$\partial_t F(z, t) = \partial_t F_i^n \rightarrow \frac{F_i^{n+1/2} - F_i^{n-1/2}}{\Delta t}, \quad \partial_z F_i^n \rightarrow \frac{F_{i+1/2}^n - F_{i-1/2}^n}{\Delta z}, \quad (\text{A.10})$$

and the fundamental idea of the Yee discretisation scheme to arrange the electric and magnetic field quantities on staggered grids, on temporal and spatial grids with relative offsets of half steps [158] (see FIGURE A.2), is taken on. This matches perfectly with the special type of first order Maxwell curl equations. This fully explicit leap-frog algorithm is non-dissipative and of second order accuracy in time and space, but only of around first order in discontinuous media. The scheme is adopted to discretise the two Maxwell curl equations ($E|D|P, H = E_y|D_y|P_y, H_x, \mathbb{R} \times \mathbb{R} \rightarrow \mathbb{R}$)

$$H_{i+1/2}^n = H_{i+1/2}^{n-1} + \frac{c\Delta t}{\Delta z} (E_{i+1}^{n-1/2} - E_i^{n-1/2}), \quad (\text{A.11})$$

$$D_i^{n+1/2} = D_i^{n-1/2} + \frac{c\Delta t}{\Delta z} (H_{i+1/2}^n - H_{i-1/2}^n) \quad (\text{A.12})$$

$$\rightarrow E_i^{n+1/2} = E_i^{n-1/2} + \frac{1}{\epsilon_i} \frac{c\Delta t}{\Delta z} (H_{i+1/2}^n - H_{i-1/2}^n) - \frac{1}{\epsilon_i} \Delta t \cdot (\Gamma_{x,y})_i \frac{(N_{QW})_i}{\Delta z} (\partial_t P_i^n).$$

The above field equations have been transformed to the Heaviside-Lorentz unit system to avoid the imbalance in the electric and magnetic field amplitudes (ϵ_0 has a very different

magnitude from μ_0). The material parameter $\epsilon(z)$ generally features step discontinuities (in refractive index structures like DBR mirrors or photonic crystals), thus, when mapping $\epsilon(z) \rightarrow \epsilon_i$, we do use weighted average values in some cells.

At the left and right boundary of our finite analysis window (for the core region, the spatial region of interest, we solve the above discretised curl equations) boundary conditions have to be specified. Metallic (or perfectly reflecting) boundary conditions are very simple to implement by setting the tangential electric field component $E_{\text{boundary}} = 0$ at every time step (Dirichlet type), but in most cases a more realistic model would be to simulate a system with the structure of interest embedded into infinite expanded space. Absorbing or open boundary conditions have to be defined in a way that an outgoing wave (across the interface) is completely absorbed without any reflection back. According to Mur [119] the simulation region can be closed (artificially) by demanding exclusively for the electric field the constraint, compatible to the wave operator equation with plane wave solutions travelling to the left or to the right respectively, $(\partial_z \mp \sqrt{\epsilon_{\text{boundary}}}/c\partial_t) E_{\text{boundary}} = 0$, written in a discretised formulation by (with the abbreviation $\mathcal{C} = c\Delta t/(\sqrt{\epsilon_{\text{boundary}}}\Delta z)$)

$$E_0^{n+1/2} = E_1^{n-1/2} + \frac{\mathcal{C} - 1}{\mathcal{C} + 1} \left(E_1^{n+1/2} - E_0^{n-1/2} \right), \quad (\text{A.13})$$

$$E_{i_{\text{max}}+1}^{n+1/2} = E_{i_{\text{max}}}^{n-1/2} + \frac{\mathcal{C} - 1}{\mathcal{C} + 1} \left(E_{i_{\text{max}}}^{n+1/2} - E_{i_{\text{max}}+1}^{n-1/2} \right). \quad (\text{A.14})$$

In order to optically pump, excite or probe the active laser or amplifier structure well defined external optical fields (plane waves) are injected into the system at the grid point i_{ext} (and travel e.g. to the right). With the total-field/scattered-field (TFSF) technique [58] we can insert external plane wave components. The name arises from the fact that the total electric field E_{total} (and the equivalent for the magnetic field) may be superposed by an incident part E_{ext} and the response, the scattered field E_{scat} . Having solved (A.11)+(A.12) for all grid points in the core region with the generic Yee scheme just at two positions the field values have to be corrected (or updated)

$$H_{i_{\text{ext}}-1/2}^n = \{H_{i_{\text{ext}}-1/2}^n\} - \frac{c\Delta t}{\Delta z} E_{\text{ext},i_{\text{ext}}}^{n-1/2}, \quad (\text{A.15})$$

$$D_{i_{\text{ext}}}^{n+1/2} = \{D_{i_{\text{ext}}}^{n+1/2}\} - \frac{c\Delta t}{\Delta z} H_{\text{ext},i_{\text{ext}}-1/2}^n. \quad (\text{A.16})$$

Targeting to simulate novel semiconductor laser structures with enclosed external mirror configurations (like VECSEL) an efficient method to model these external cavities, which is fast and has low memory requirements, is proposed by the longitudinal delayed optical feedback boundary conditions [12]. The concept behind it is outlined in the following: Light leaves the actual active laser structure, propagates to the mirrors some distance L_l, L_r away, is reflected there (with the intensity reflectivities R_l, R_r and with a phase shift of around π) and is finally feed backed (with a delay of the round trip times $\tau_l = 2L_l n_{\text{ext},l}/c$, $\tau_r = 2L_r n_{\text{ext},r}/c$) from the passive external cavity into the active laser or amplifier structure. We pick up the out-going part of the light fields (this can be done

by the correct choice of grid points) and put it into delay line buffers with $\tau_l/\Delta t + 1$, $\tau_r/\Delta t + 1$ elements

$$H_{\text{ext},l}^n = \frac{\sqrt{R_l}}{2} (H_{1+1/2}^n + H_{2+1/2}^n), \quad E_{\text{ext},l}^{n+1/2} = -\frac{\sqrt{R_l}}{2} (E_1^{n+1/2} + E_2^{n+1/2}), \quad (\text{A.17})$$

$$H_{\text{ext},r}^n = \frac{\sqrt{R_r}}{2} (H_{i_{\text{max}}-1+1/2}^n + H_{i_{\text{max}}-2+1/2}^n), \quad E_{\text{ext},r}^{n+1/2} = -\frac{\sqrt{R_r}}{2} (E_{i_{\text{max}}}^{n+1/2} + E_{i_{\text{max}}-1}^{n+1/2}). \quad (\text{A.18})$$

The fields stored in the buffers are inserted back into the active device with delay times of $N_l = \tau_l/\Delta t$, $N_r = \tau_r/\Delta t$ time steps taking use of the above explained total-field/scattered-field method

$$H_{3+1/2}^n = \{H_{3+1/2}^n\} - \frac{c\Delta t}{\Delta z} E_{\text{ext},l}^{n-1/2-N_l}, \quad D_4^{n+1/2} = \{D_4^{n+1/2}\} - \frac{c\Delta t}{\Delta z} H_{\text{ext},l}^{n-N_l}, \quad (\text{A.19})$$

$$H_{i_{\text{max}}-3+1/2}^n = \{H_{i_{\text{max}}-3+1/2}^n\} + \frac{c\Delta t}{\Delta z} E_{\text{ext},r}^{n-1/2-N_r}, \quad D_{i_{\text{max}}-3}^{n+1/2} = \{D_{i_{\text{max}}-3}^{n+1/2}\} + \frac{c\Delta t}{\Delta z} H_{\text{ext},r}^{n-N_r}. \quad (\text{A.20})$$

As next step we have to incorporate the dynamical equations for the active material part, which are formulated in real space, into the stable finite-difference time-domain solver in a self-consistent way. The induced macroscopic polarisation $P_i^{n+1/2}$ needs to be available to close the set of equations (A.11)+(A.12), this can be done by centring the (second order differential) equations of the set of damped harmonic oscillators around $n - 1/2$

$$\begin{aligned} \partial_t^2 \mathbf{p}_{\mathbf{k}} + 2\gamma_{\mathbf{k}}^p \partial_t \mathbf{p}_{\mathbf{k}} + \omega_{\mathbf{k}}^2 \mathbf{p}_{\mathbf{k}} \Big|_i^{n-1/2} &= -\Omega_{\mathbf{k}} \frac{M^{eh} E}{\hbar} (n_{\mathbf{k}}^e + n_{-\mathbf{k}}^h - 1) \Big|_i^{n-1/2} \\ \rightarrow \mathbf{p}_i^{n+1/2} \left(\frac{1}{(\Delta t)^2} + \frac{\gamma^p}{\Delta t} \right) &= \left(\frac{2}{(\Delta t)^2} - \omega^2 \right) \mathbf{p}_i^{n-1/2} + \left(-\frac{1}{(\Delta t)^2} + \frac{\gamma^p}{\Delta t} \right) \mathbf{p}_i^{n-3/2} \\ &\quad - \frac{\Omega M^{eh}}{\hbar} E_i^{n-1/2} (n_i^{e,n-1/2} + n_i^{h,n-1/2} - 1). \end{aligned} \quad (\text{A.21})$$

After calculating the spectral summation of the microscopic quantities $\mathbf{p}_{\mathbf{k}} \rightarrow P$, and then the electric field for the new time step $n + 1/2$ by

$$E_i^{n+1/2} = \frac{1}{\epsilon_i} \left(D_i^{n+1/2} - (\Gamma_{x,y})_i \frac{(N_{\text{QW}})_i}{\Delta z} P_i^{n+1/2} \right), \quad (\text{A.22})$$

we can evaluate the dynamical distribution functions at the new time step by centring the differential equations around n . At this, $n_{\mathbf{k}}^e, n_{-\mathbf{k}}^h, N$ are fixed to the same grid positions with the electric field quantities as suggested in [148]

$$\begin{aligned} n_i^{n+1/2} \left(\frac{1}{\Delta t} + \frac{\gamma^{\text{nr}} + \gamma + \bar{\Lambda}_i^{n-1/2}}{2} \right) &= \left(\frac{1}{\Delta t} - \frac{\gamma^{\text{nr}} + \gamma + \bar{\Lambda}_i^{n-1/2}}{2} \right) n_i^{n-1/2} + \gamma f_i^{n-1/2} \\ + \dots \Big|^{n-1/2} + \frac{M^{eh}}{\hbar \Omega} (E_i^{n+1/2} + E_i^{n-1/2}) &\left(\frac{p_i^{n+1/2} - p_i^{n-1/2}}{\Delta t} + \frac{\gamma^p}{2} (p_i^{n+1/2} + p_i^{n-1/2}) \right). \end{aligned} \quad (\text{A.23})$$

As some terms in the above equation (for instance $\bar{\Lambda}_i$ or the quasi-equilibrium distribution functions f_i) cannot be evaluated at the new time step we use the values at $n - 1/2$ without losing stability. The corresponding equation for the macroscopic carrier density $N_i^{n+1/2}$ is solved afterwards, since some physical effects (e.g. carrier diffusion) may only be qualified on the macroscopic level. The crucial property of our discretisation and integration scheme is the fact that the combined active material and passive refractive index structure model in full time-domain can be implemented in a fully explicit manner. The computational realisation turns out to be stable and pretty efficient [74] (because no iterative predictor-corrector step as required in another proposed numerical scheme [76] or costly Runge-Kutta integration scheme [77] has to be performed). Connecting the Maxwell curl equations written in the Heaviside-Lorentz unit system with the semiconductor gain dynamics formulated in the SI unit system some conversions are necessary.

As summarisation of the discretisation scheme and implementation typical numerical values and the sequence of integration steps (this sequence is determined by the chosen time centrings) are indicated in the following table:

Maxwell semiconductor Bloch equations in full time-domain	
<i>typical values of numerical parameters:</i>	
spatial stepping ⁵ Δz	$\lambda / (\max\{n\} \cdot 24)$
time step ⁶ Δt	$c\Delta t / \Delta z = 0.999$
aliasing of material parameters	linear weighted average values
<i>sequence of iteration steps:</i>	
1. $H_{i+1/2}^n$	Maxwell curl equation (A.11) \rightarrow fields injected by (A.15) + delayed feedback
2. $D_i^{n+1/2}$	Maxwell curl equation (A.12) \rightarrow fields corrected by (A.16) + delayed feedback
3. end of passive part	buffers updated \rightarrow at boundaries (A.13)+(A.14)
4. active gain material $\rightarrow E_i^{n+1/2}$	\mathbf{p}_k (A.21), $P_i^{n+1/2} \rightarrow E_i^{n+1/2}$ (A.22) \rightarrow n_k° (A.23), $N_i^{n+1/2}$, $(f_k^\circ)_i^{n+1/2}$

⁵In the medium with the highest refractive index in the investigated system the (shortest) optical wavelength is resolved with 24 grid points (Nyquist criterion), a typical value for a InGaAlAs-based structure operating at around 850 nm would be 10 nm. A much higher resolution (as sometimes discussed in literature) does not make sense: Smaller structures (than the above given Δz) are optically not active (are not seen by the electromagnetic fields) and, even more important, the macroscopic Maxwell equations with the material properties $\epsilon(z)$ are not the adapted concept for (sub-) nanometer structures, the vacuum Maxwell equations with all the bound charges and sources would be the correct choice.

⁶The algorithm is stable according to the Courant condition [58] for time steps $\Delta t \leq \Delta s / (c\sqrt{\text{Dim}})$ ($\Delta s / (c\sqrt{\text{Dim}})$ is called the magic time step), a typical value for the needed temporal resolution would be 0.03 fs.

A.3 Numerical Analysis of the Scattering Integrals

The numerical treatment of the carrier-phonon and in particular of the carrier-carrier scattering is exceedingly time-critical based on the fact that we have to sum or integrate over all possible interaction events. This implies in the case of Coulomb scattering to integrate over the momentum transfer vector \mathbf{q} and the momentum vector \mathbf{k}' of the scattering partner, plus a summation over all potential subband indices combinations. In the case of the Fröhlich interaction we integrate over the carrier momentum transfer, and add up the possible scattering incidents (that is to say, scattering under absorption and under emission of a longitudinal optical phonon, and various subband indices combinations). Consequently, the aim has to be to carry out analytically as many of the integrations as possible, in doing so we follow the numerical implementation scheme suggested in [64]⁷.

We start with the carrier-phonon scattering and indicate the integration algorithm considering as example the scattering matrix $\Gamma_{i_2 i_5, \mathbf{k}}^{ee, \text{out}}$ (which occurs for instance in the description of the relaxation dynamics $\partial_t n_{i_1 i_2, \mathbf{k}}^e|_{\text{relax}} = \sum_{i_5} [-\Gamma_{i_2 i_5, \mathbf{k}}^{ee, \text{out}} n_{i_1 i_5, \mathbf{k}}^e - \Gamma_{i_1 i_5, \mathbf{k}}^{ee, \text{out}*} n_{i_2 i_5, \mathbf{k}}^{e*}]$ of the electron expectation values)

$$\begin{aligned} & \sum_{\mathbf{q}, q_z} \sum_{i_4, i_6} \sum_{\pm} \frac{\pi}{\hbar} \delta(-E_{i_5, \mathbf{k}}^e + E_{i_6, \mathbf{k}-\mathbf{q}}^e \pm \hbar\omega_{1-o}) \\ & \times \gamma_{i_2 i_4}^*(\mathbf{q}, q_z) \gamma_{i_5 i_6}(\mathbf{q}, q_z) \left(n_{\text{ph}} + \frac{1}{2} \pm \frac{1}{2} \right) (\delta_{i_4, i_6} - f_{i_4 i_6, \mathbf{k}-\mathbf{q}}^{e*}). \end{aligned} \quad (\text{A.24})$$

We replace the summation by a continuous integral formulation and make the coordinate transformation $\mathbf{q} \rightarrow \mathbf{k}' = \mathbf{k} - \mathbf{q}$. Assuming isotropy in momentum space we obtain (for one subband indices combination)

$$\begin{aligned} & \int d^2 k' \frac{A}{(2\pi)^2} \frac{\pi}{\hbar} \delta \left(E_{i_5, k=0}^e - E_{i_6, k'=0}^e + \frac{\hbar^2}{2m_e} (k^2 - k'^2) \mp \hbar\omega_{1-o} \right) \\ & \times \left(n_{\text{ph}} + \frac{1}{2} \pm \frac{1}{2} \right) (\delta_{i_4, i_6} - f_{i_4 i_6, k'}^{e*}) \left(\int dq_z \frac{L}{2\pi} \gamma_{i_2 i_4}^*(\mathbf{q}, q_z) \gamma_{i_5 i_6}(\mathbf{q}, q_z) \right). \end{aligned} \quad (\text{A.25})$$

The integration over q_z can be carried out analytically. After introducing polar coordinates for the momentum vector by $\int d^2 k' \rightarrow \int dk' k' \int d\vartheta$, $\vartheta = \angle(\mathbf{k}, \mathbf{k}')$, the delta function (guaranteeing the energy conservation of each single scattering process) is used in the integration over the radius k'

$$\int d\vartheta k' \frac{A}{(2\pi)^2} \frac{\pi}{\hbar} \frac{m_e}{\hbar^2 k'} \left(n_{\text{ph}} + \frac{1}{2} \pm \frac{1}{2} \right) (\delta_{i_4, i_6} - f_{i_4 i_6, k'}^{e*}) \frac{(2\pi)^2}{A} \frac{e^2 \hbar}{\epsilon_0^2 (4\pi)^2 \omega_{1-o} \gamma} \frac{1}{q} F_{i_4 i_5 i_6 i_2}(q), \quad (\text{A.26})$$

⁷Another approach to compute the manifold integrals in the scattering matrices is to try to decouple the integrations with respect of the amplitude and the angle (they occur in the arguments of the distribution functions such as $\mathbf{k} - \mathbf{q}$) [36, 64].

thereby the solutions are given by

$$k' = k'(i_5, i_6, \mp) = \sqrt{k^2 \mp \frac{2m_e}{\hbar^2} (\hbar\omega_{1-o} \mp (E_{i_5,0} - E_{i_6,0}))}, \quad (\text{A.27})$$

$$q = |\mathbf{k} - \mathbf{k}'| = \sqrt{k^2 + k'^2 - 2kk' \cos \vartheta}. \quad (\text{A.28})$$

The threefold integral we started with is reduced to an integration over one coordinate⁸, but that remaining integration over the angle ϑ has to be evaluated numerically

$$\frac{e^2 m_e \omega_{1-o}}{16\pi \hbar^2 \epsilon_0} \left(\frac{1}{\epsilon_\infty} - \frac{1}{\epsilon_s} \right) \int_0^{2\pi} d\vartheta \frac{1}{q} F_{i_4 i_5 i_6 i_2}(q) \left(n_{\text{ph}} + \frac{1}{2} \pm \frac{1}{2} \right) (\delta_{i_4, i_6} - f_{i_4 i_6, k'}^{e*}). \quad (\text{A.29})$$

The upper sign is associated with the emission of a phonon, the lower sign is linked to an absorption event. A screening model may be added in the evaluation of the scattering contributions by the replacement $1/qF(q) \rightarrow 1/\epsilon(q, \omega) \cdot 1/qF(q)$.

For the carrier-carrier scattering we again look as example at the matrix $\Gamma_{i_2 i_5, \mathbf{k}}^{ee, \text{out}}$

$$\begin{aligned} & \sum_{\mathbf{k}', \mathbf{q}} \sum_{i_4, j_7, j_6, i_8, j_3, j_2} \frac{\pi}{\hbar} \delta(-E_{i_5, \mathbf{k}}^e - E_{j_7, -\mathbf{k}'}^h + E_{j_6, -\mathbf{k}' - \mathbf{q}}^h + E_{i_8, \mathbf{k} - \mathbf{q}}^e) V_{i_5 j_7 j_6 i_8}(\mathbf{q}) V_{i_1 j_3 j_2 i_4}(\mathbf{q}) \\ & \times f_{j_3 j_7, -\mathbf{k}'}^h (\delta_{j_2, j_6} - f_{j_6 j_2, -\mathbf{k}' - \mathbf{q}}^h) (\delta_{i_8, i_4} - f_{i_8 i_4, \mathbf{k} - \mathbf{q}}^e). \end{aligned} \quad (\text{A.30})$$

In the following abbreviations for an energy expression $E_s = E_{i_5,0}^e + E_{j_7,0}^h - E_{j_6,0}^h - E_{i_8,0}^e$ and for the reduced mass of the two-body system $\mu = m_e m_h / (m_e + m_h)$ are introduced. Undertaking a coordinate transformation for the momentum coordinates

$$\mathbf{g} = \frac{2\mu}{m_e} \mathbf{k} - \frac{2\mu}{m_h} \mathbf{k}' \rightarrow \mathbf{k}'(\mathbf{k}, \mathbf{g}) \quad (\text{A.31})$$

and a transition from sums to integrals over momentum vectors we obtain (a fourfold integral)

$$\begin{aligned} & \int d^2 g \frac{A}{(2\pi)^2} \left(\frac{m_h}{2\mu} \right)^2 \cdot 2 \int d^2 q \frac{A}{(2\pi)^2} \frac{\pi}{\hbar} \delta \left(E_s + \frac{\hbar^2}{2\mu} (\mathbf{g} \cdot \mathbf{q} - q^2) \right) V_{i_5 j_7 j_6 i_8}(q) V_{i_1 j_3 j_2 i_4}(q) \\ & \times f_{j_3 j_7, \mathbf{k}'}^h (\delta_{j_2, j_6} - f_{j_6 j_2, |\mathbf{k}' + \mathbf{q}|}^h) (\delta_{i_8, i_4} - f_{i_8 i_4, |\mathbf{k} - \mathbf{q}|}^e). \end{aligned} \quad (\text{A.32})$$

A factor of two as the number of scattering partners because of the degeneracy of electron and hole functions with regard to the spin degree of freedom has been added in the above equation (the Coulomb interaction of two charged particles is independent of the spin degree of freedom, and does not represent a spin-flip process). As next step in evaluating the integrals over momentum vectors polar coordinates $\int d^2 g \rightarrow \int dg g \int d\varphi$, $\varphi = \angle(\mathbf{k}, \mathbf{g}) = \angle(x\text{-axis}, \mathbf{g})$ and $\int d^2 q \rightarrow \int dq q \int d\vartheta$, $\vartheta = \angle(\mathbf{g}, \mathbf{q})$ are introduced. In the

⁸For bulk semiconductor structures (with the usual phenomenological screening models) the threefold integrals can be fully evaluated analytically.

integration over the angle ϑ the delta function, the total energy conservation of the many-body interaction, is used to filter out the two possible solutions

$$\vartheta_1 = \arccos\left(\frac{q^2 - 2\mu/\hbar^2 E_s}{gq}\right) \in [0, \pi], \quad \vartheta_2 = 2\pi - \vartheta_1 \quad (\text{A.33})$$

(and with it the momentum transfer \mathbf{q} is determined). The constraints for the existence of real-valued solutions (plus the fact that radii have to be positive numbers) give the limits of the integration areas, namely

$$q_{\min} = \max\left[\frac{g - \sqrt{g^2 + 8\mu/\hbar^2 E_s}}{2}, \frac{-g + \sqrt{g^2 + 8\mu/\hbar^2 E_s}}{2}\right], \quad (\text{A.34})$$

$$q_{\max} = \frac{g + \sqrt{g^2 + 8\mu/\hbar^2 E_s}}{2}, \quad (\text{A.35})$$

$$g_{\min} = \sqrt{\max\left[0, -\frac{8\mu}{\hbar^2} E_s\right]}. \quad (\text{A.36})$$

All these coordinate transformations and analyses result in the following expression of nested integrals

$$\begin{aligned} & \int_{g_{\min}}^{\infty} dg g \int_0^{2\pi} d\varphi \frac{A}{(2\pi)^2} \left(\frac{m_h}{2\mu}\right)^2 \cdot 2 \int_{q_{\min}}^{q_{\max}} dq q \frac{A}{(2\pi)^2} \frac{\pi}{\hbar} \frac{2\mu}{\hbar^2 \sqrt{g^2 q^2 - (q^2 - 2\mu/\hbar^2 E_s)^2}} \\ & \times \left(\frac{e^2}{2\epsilon_0 \epsilon A}\right)^2 \frac{1}{q^2} F_{i_5 j_7 j_6 i_8}(q) F_{i_1 j_3 j_2 i_4}(q) f_{j_3 j_7, k'}^h (\delta_{j_2, j_6} - f_{j_6, j_2, |\mathbf{k}' + \mathbf{q}|}^h) (\delta_{i_8, i_4} - f_{i_8 i_4, |\mathbf{k} - \mathbf{q}|}^e). \end{aligned} \quad (\text{A.37})$$

The fourfold integrals we started with are reduced to a threefold integrals formulation⁹. The sequence of the integrations is crucial ($g \rightarrow q \rightarrow \varphi$) by reason that the integral boundaries or the arguments of the integrands of the inner loops are dependent on the values of the variables defined in outer loops¹⁰. In the end we have derived the following term

$$\begin{aligned} & \frac{m_h^2 e^4}{64\pi^3 \hbar^3 \mu \epsilon_0^2 \epsilon^2} \int_{g_{\min}}^{\infty} dg g \int_{q_{\min}}^{q_{\max}} dq q \frac{1}{\sqrt{g^2 q^2 - (q^2 - 2\mu/\hbar^2 E_s)^2}} \frac{1}{q^2} F_{i_5 j_7 j_6 i_8}(q) F_{i_1 j_3 j_2 i_4}(q) \\ & \times \int_0^{2\pi} d\varphi f_{j_3 j_7, k'}^h (\delta_{j_2, j_6} - f_{j_6, j_2, |\mathbf{k}' + \mathbf{q}|}^h) (\delta_{i_8, i_4} - f_{i_8 i_4, |\mathbf{k} - \mathbf{q}|}^e). \end{aligned} \quad (\text{A.38})$$

⁹For bulk semiconductor structures the sixfold integrals can be simplified to twofold integrals which have to be treated numerically.

¹⁰Because of the complicated structure of the nested loops and the fact that still manifold integrals have to be carried out numerically, it is just impossible to perform dynamical simulations of the carrier-carrier scattering combined with a spatially resolved modelling of the laser fields. Therefore we replace in the scattering matrices the distribution functions by quasi-equilibrium (Fermi-Dirac) distribution functions. Scattering rates depending on the macroscopic active material state (that is to say, dependent on macroscopic field variables like carrier density or temperatures) as effective measures (of the importance of the interaction) enter our spatially resolved semiconductor laser descriptions.

The effects of screening of the interaction may be accounted for in the scattering integrals by $V(\mathbf{q}) \rightarrow V^{\text{sc}}(\mathbf{q}) = 1/\epsilon(\mathbf{q}, \omega) \cdot V(\mathbf{q})$.

As summary of the algorithms implemented to numerically evaluate the (many-body) scattering events necessary analyses and the sequence of integrations are specified in the following table:

numerical analysis of scattering integrals
<i>carrier-phonon scattering:</i>
1. $(k, \text{subband indices}, \pm) \rightarrow \text{calculate } k' \text{ (A.27)}$
2. integrate over angle $\vartheta \rightarrow \text{determine } q(k, k', \vartheta) \text{ (A.28)}$
3. evaluate (A.29) \rightarrow back to 2.
<i>carrier-carrier scattering:</i>
1. $(k, \text{subband indices}) \rightarrow \text{compute } g_{\min} \text{ (A.36)}$
2. integrate over g (outer loop) $\rightarrow \text{calculate } q_{\min}(g) \text{ (A.34)}, q_{\max}(g) \text{ (A.35)}$
3. integrate over $q \rightarrow \text{find solutions } \vartheta(g, q) \text{ (A.33)}$
4. integrate over angle $\varphi \rightarrow \mathbf{k}'(k, g, \varphi) = \mathbf{k}'(k, \mathbf{g}, \mathbf{q}(\mathbf{g}, \vartheta)) \rightarrow k', \mathbf{k}' + \mathbf{q} , \mathbf{k} - \mathbf{q} $
5. evaluate (A.38) \rightarrow back to 4. \rightarrow back to 3. \rightarrow back to 2.

A.4 Conclusion

In this chapter we have discussed fundamental properties of the numerical implementations of our theoretical time-domain models, that are the applied discretisations of the fields and differential operators on regular grids and the integration schemes. As we aim to numerically solve multi-dimensional partial differential equations in combination with a band-resolved description of the semiconductor material (a multi-physics and multi-scale problem) the numerical complexity of the algorithm, characterised by the number of iteration steps, the grid resolutions and memory requirements, represents besides the accuracy and the stability the very critical parameter. In more detail:

- For the paraxial transverse wave equation model, a frequency-/time-domain approach, we have proposed the Hopscotch method, which is very efficient and stable and reasonable accurate. This numerical scheme involves the partitioning of the two-dimensional grid into two groups of grid points (with stride two) plus an integration scheme with alternating explicit and implicit discretisations. That results in not having to solve a matrix-valued problem, the implicit character and for this reason necessary inversion arises only (spatially) locally. Adequate boundary conditions are introduced, and we have discussed the addition of terms of elliptic character to stabilise the equations.
- The finite-difference time-domain (FDTD) method solves the first order Maxwell curl equations by arranging the electric and magnetic field quantities on staggered grids in time and space according to the Yee scheme. This allows for the correct centring of time points and positions of the fields and differential operators in central finite-difference approximation. At the boundaries of our finite analysis window absorbing or open boundary conditions (Mur) are defined. External optical fields (plane

wave components) are injected using the total-field/scattered-field (TFSF) technique, and external homogeneous cavities are considered by the longitudinal delayed optical feedback boundary conditions. The additional field variables carrier density, induced polarisation and the microscopic distribution functions and interband polarisations share the same grid with the electric field quantities. The combined dynamical model in full time-domain of the (active) nonlinear material response and the passive refractive index structure can be numerically implemented in a fully explicit manner. Due to the time-domain character of the FDTD method a quite extensive effort of data extraction, basically Fourier transforms, is required to gain physical results.

- The computational realisations of our theoretical descriptions of carrier-carrier and carrier-phonon scattering processes and other loss mechanisms like Auger recombination involve the evaluation of nested manifold integrals (as the summation over all possible interaction events). The aim has to be to carry out analytically as many of the integrations as possible (and to utilise the conservation laws of the single interaction process for some physical quantities such as the energy or the total momentum). In the case of the Coulomb interaction we are left with the numerical calculation of threefold integrals, in the Fröhlich scattering with an integral over one coordinate.

B Dynamical Treatment of the Scattering Contributions

In SECTION 4.1 we have investigated the Boltzmann scattering integrals (4.2) assuming quasi-equilibrium Fermi-Dirac distributions. For these functions the collision terms become identically zero (the principle of detailed balance), but we can extract non-vanishing relaxation rates for the out-scattering and in-scattering processes [4]. In this chapter the relaxation of initially prepared non-equilibrium distributions and the way thermal equilibrium is approached are modelled (on sub-picosecond time scales). In the hydrodynamic approach [103], the non-equilibrium carrier state is characterised by the first moments of the distributions, a number of these physical quantities are conserved in the scattering processes¹ $\partial_t|_{\text{relax}} [1/V \sum_{\mathbf{k}} W^{(n)}(\mathbf{k})n_{\mathbf{k}}^{\circ}] = 0$. The carrier-carrier scattering interactions involve the conservation of the carrier density ($W^{(0)} = 1$), of the total momentum density (corresponding to $W^{(1)} = \mathbf{k}$), and of the kinetic energy density, that is to say the plasma temperature ($W^{(2)} \propto k^2$). Whereas the collision with other quasi-particles, namely with phonons (the most efficient process is given by the Fröhlich interaction with longitudinal optical phonons), leads to a relaxation of the carrier kinetic energy density, to plasma cooling [91, 106]. Because of the facts that the numerical analysis of the scattering integrals for bulk semiconductor structures can be executed much more efficient than for quantum well structures [64] (and also cf. APPENDIX B) and also the carrier density conservation is numerically better fulfilled [108], in order to understand in principle the characteristics of the relaxation of non-equilibrium distributions we do consider in this chapter bulk semiconductor structures. In doing so, the strengths of the scattering processes are specified by the interaction potentials

$$V(\mathbf{q}) = \frac{e^2}{\epsilon_0 \epsilon} \frac{1}{V} \frac{1}{q^2}, \quad \gamma^{e(\text{ph})}(\mathbf{q}) = -\frac{i}{\epsilon_0} \frac{1}{q} \sqrt{\frac{e^2 \hbar}{2\gamma\omega_{\text{LO}} V}}, \quad (\text{B.1})$$

and the dielectric function and screening constants

$$\kappa^2 = \frac{e^2}{\epsilon_0 \epsilon \pi^2 \hbar^2} \left[m_e \int_0^\infty dk f_k^e + m_h \int_0^\infty dk f_k^h \right], \quad \epsilon(\mathbf{q} \rightarrow \mathbf{0}, \omega \rightarrow 0) = 1 + \frac{\kappa^2}{q^2}, \quad (\text{B.2})$$

$$\omega_{\text{pl}}^2 = \frac{e^2 N}{\epsilon_0 \epsilon m_r}, \quad \omega_{\mathbf{q}}^2 = \omega_{\text{pl}}^2 \left(1 + \frac{q^2}{\kappa^2} \right) + \frac{C}{4} \left(\frac{\hbar q^2}{2m_r} \right)^2. \quad (\text{B.3})$$

¹These conservation rules can be derived from the quantum Boltzmann collision terms. However, the representation of scattering processes in the relaxation rate approximation (2.92) with \mathbf{k} -dependent scattering rates fails to preserve the moments of the distribution, such as the carrier density.

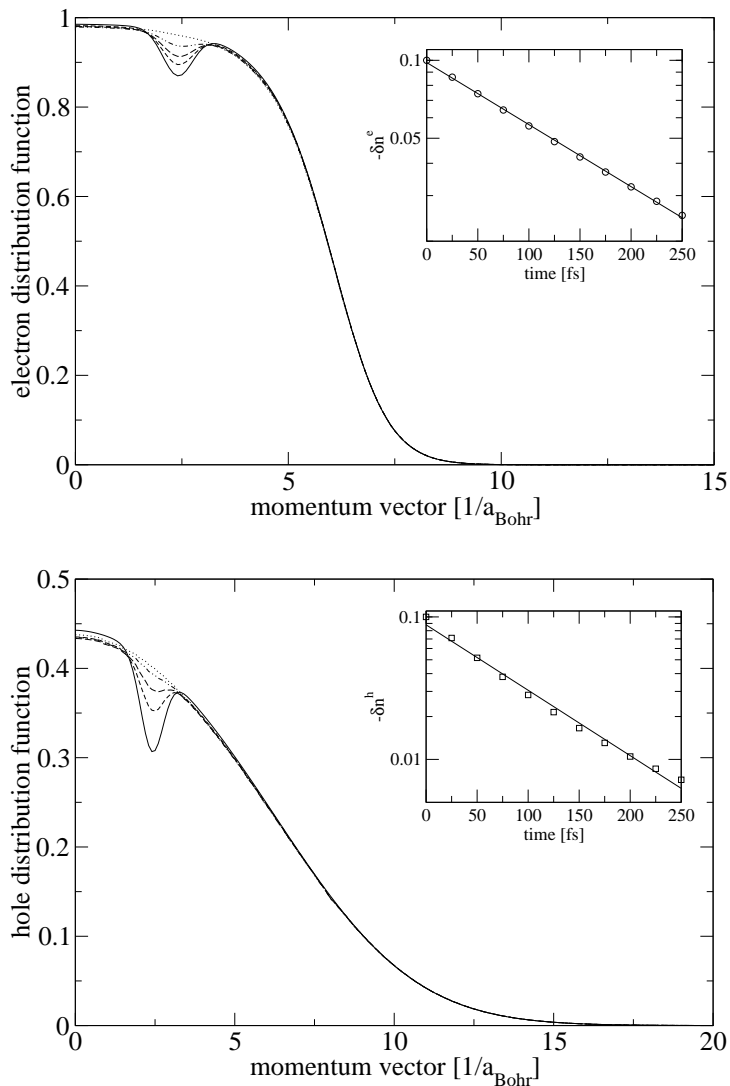


FIGURE B.1: Relaxation of a kinetic hole, due to screened carrier-carrier scattering and the interaction with longitudinal optical phonons, in the electron (top) and hole (bottom) distributions: The initially prepared non-equilibrium carrier distribution functions show strong spectral hole burning effects which may arise as the result of the interaction of the inhomogeneously broadened carrier system with the lasing modes in a resonator configuration (that is to say, from spectrally selective stimulated electron-hole recombination processes). Plotted are the distribution functions obtained from the direct numerical integration [36, 64] of the generalised Boltzmann equations [25, 159] at 0 fs (solid line), 50 fs, 100 fs, 200 fs and at 500 fs (dotted). The insets in the graphs give the decay of the (maximum) deviations from quasi-equilibrium (as symbols) over time plus an exponential fit of these data (we assume the relaxation of the system to be of a reservoir coupling type [4]). We find an electron relaxation time of 181 fs and an effective hole scattering time of 95 fs (in a GaAs bulk laser structure and a density of $N = N^e(t=0) = N^h(t=0) = 3 \cdot 10^{18} \text{ cm}^{-3}$).

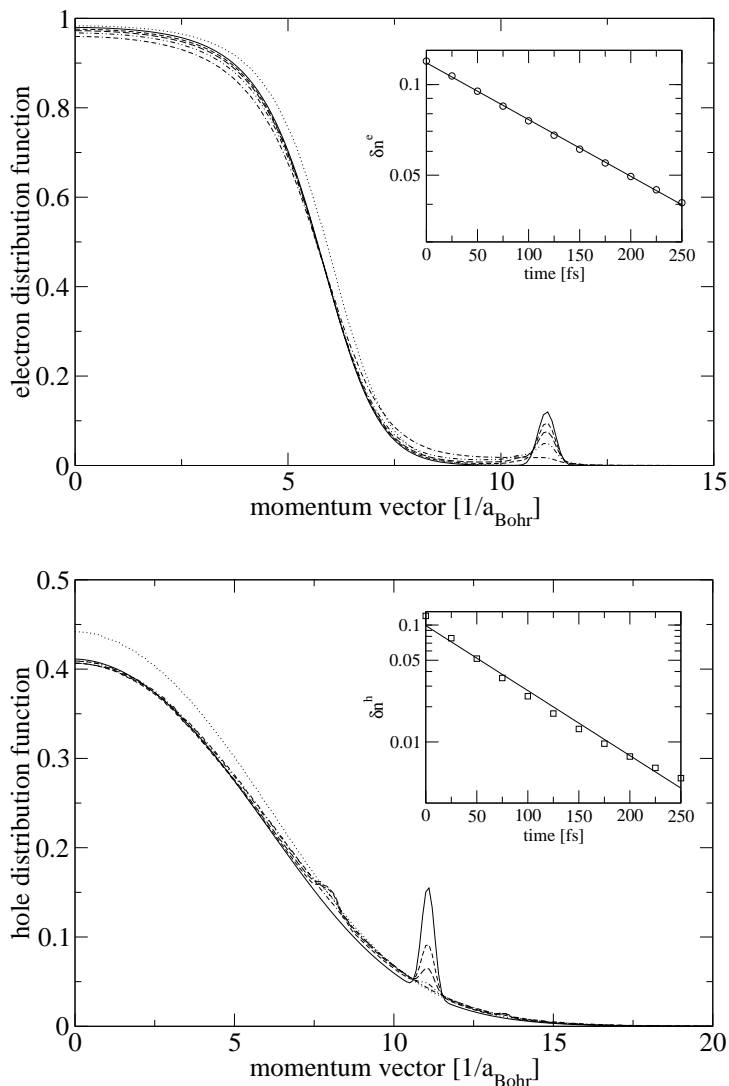


FIGURE B.2: Equivalent to FIGURE B.1, but this time the carrier and energy relaxation of optically excited distributions (as the result of the spectrally selective carrier generation by an optical pumping scheme [16,17,133,134] as applied in novel laser structures, e.g. VECSEL) is investigated. An exponential fit of the scattering enables the identification of effective relaxation rates [92]. The comparison of dynamical scattering calculations with simulations utilising the effective scattering times demonstrates a good qualitative agreement. In general, hole relaxation times are faster than electron scattering times $1/\gamma^h \approx 100 \text{ fs} \approx 0.5 \cdot 1/\gamma^e$. Lookup tables of scattering times and dephasing rates extracted from calculations for different carrier densities and temperatures, excitation parameters (and structural parameters in quantum confined structures) make it possible to microscopically model correlation contributions within spatially resolved time-domain simulations of semiconductor laser structures. These effective scattering times can be extracted from an exponential fit to the temporal decay of an excitation, at first suggested in [92], or with a quasi-equilibrium approach, for more details see SECTION 4.1.

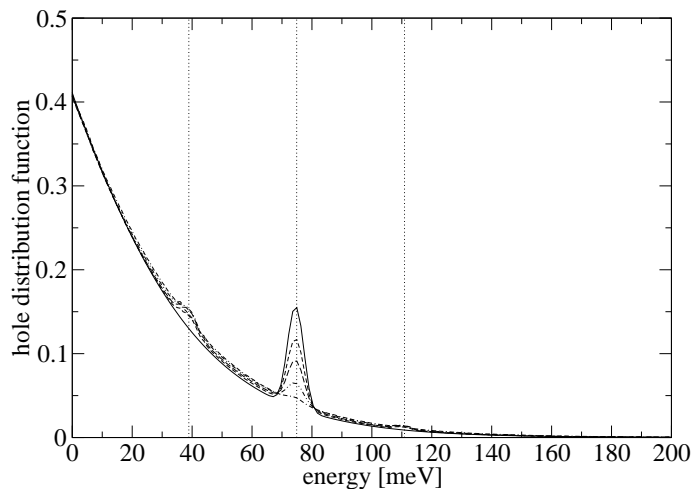


FIGURE B.3: Details of FIGURE B.2: The model of the correlation contributions of the many-body interactions separates the carrier momentum and energy relaxation into two processes. The carrier-carrier interaction by the screened Coulomb potential relaxes the system towards thermal quasi-equilibrium characterised by the plasma temperature T_{pl} . The carrier-phonon scattering, mediated by the Fröhlich interaction, establishes Fermi-Dirac distributions at the lattice (phonon) temperature T_{lat} . The carrier-phonon scattering proceeds (in a microscopic model) via the successive emission and absorption of longitudinal optical phonons, which leads to the occurrence of sidebands (of the excitations) in the carrier distribution at energy values $E_{\text{exc}} \pm n \cdot \hbar\omega_{\text{lo}}, n \in \mathbb{N}$. We have plotted the hole distribution function versus energy at time points 0 fs, 25 fs, 50 fs, 100 fs and 200 fs. As can be clearly seen, two sidebands with an energy distance (to the excitation energy) of $\hbar\omega_{\text{lo}} = 36$ meV occur, higher order sidebands are hindered by the strong screening effects and the dominant carrier-carrier scattering contributions.

Conclusion

In this part of the work we have analysed, by direct numerical integration of the (Markovian) quantum kinetic Boltzmann collision integrals, the relaxation of non-equilibrium distribution functions due to the screened carrier-carrier scattering and the interaction with longitudinal optical phonons in a bulk semiconductor structure. We have considered as the initially prepared non-equilibrium distribution functions two in laser systems relevant situations, namely the relaxation of a kinetic hole (spectral hole burning) and an optically excited distribution (spectrally selective carrier generation), and extracted effective scattering rates by exponential fits of the decay of these excitations. The results from dynamical scattering calculations agree well with microscopically calculated relaxation times assuming quasi-equilibrium. Consequently, an approach with lookup tables of scattering and dephasing rates allows for a microscopic treatment of correlation contributions along with spatially resolved time-domain simulations of semiconductor laser structures.

C Zusammenfassung

C.1 Kurzzusammenfassung

Diese Arbeit behandelt die Wechselwirkung von Licht und Materie und optische Nichtlinearitäten in Halbleiter-Nanostrukturen und präsentiert eine detaillierte numerische Analyse der raumzeitlichen Dynamik von neuartigen Hochleistungsdiodenlasern. Wir leiten ein mikroskopisches, räumlich aufgelöstes Modell ab, welches eine Dichtematrix-Beschreibung der optoelektronischen Eigenschaften von Quantenfilm-Gewinnmedien mit den makroskopischen Maxwell Gleichungen für die elektromagnetische Felddynamik kombiniert: die Maxwell Halbleiter-Bloch Gleichungen in Full Time-Domain. Diese beinhalten Vielteilchen-Wechselwirkungen, eine Vielzahl an Zeitskalen und an Gewinnsättigungsmechanismen und schließen die schnell oszillierende Trägerwelle und eine Subwellenlängen-Auflösung ein. Mikroskopisch berechnete Streuraten sind in den räumlich aufgelösten Simulationen eingebunden.

Unsere Arbeit konzentriert sich auf ultraschnelle Ladungsträgereffekte, das quantitative Verständnis von optischen Nichtlinearitäten, die gezielte Manipulation der Modenstruktur in Mikrokavitäten, und deren Einfluß auf die Kenngrößen der Laserstrahlung. Optische Dephasierung und die Ladungsträger- und Energieumverteilung aufgrund der abgeschirmten Coulomb-Wechselwirkung und der Streuung mit Phononen werden im Detail behandelt.

Wir untersuchen die technologisch wichtige Struktur eines kantenemittierenden Breitstreifenlasers im Rahmen der paraxialen Wellennäherung. Die Anregung von höheren transversalen Moden und das Auftreten von instabilen optischen Filamenten werden quantitativ analysiert. Wir zeigen, wie transversale Instabilitäten von räumlichem Lochbrennen, Gewinn- und Index-Führung und von Selbstfokussierung herrühren. Wir untersuchen die Abhängigkeit der Emissionsdynamik von Kenndaten des Gewinnmaterials (z. B. dem Amplituden-Phasen-Kopplungsfaktor), der Streifenbreite, Pumpe und Ladungsträgerdiffusion. Abhängig von der Breite der Laserstruktur können unterschiedliche dynamische Emissionsregimes festgestellt werden. Ferner projizieren wir die raumzeitliche Dynamik auf die Lasermoden.

Wir untersuchen VCSEL mit periodisch strukturiertem Defekt als Beispiel für einen photonischen Bandkanten-Laser. Insbesondere erforschen wir die Ausnutzung von photonischen Kristallstrukturen: die Gewinnüberhöhung für Bandkanten-Moden aufgrund der wirksameren Wechselwirkung von Photonen mit dem Gewinnmedium und der stärkeren Lokalisierung über den aktiven Schichten, und die Reduzierung von optischen Verlusten. Wir bestätigen numerisch, daß photonische Kristalleffekte für endliche Kristallstrukturen erzielt werden können, und zeigen, daß diese zu einer wesentlichen Optimierung der

Laserleistung, beispielsweise reduzierten Laserschwellen, führen.

Optisch gepumpte VECSEL sind ein Konzept entwickelt zur Steigerung der Ausgangsleistung von oberflächenemittierenden Lasern in Verbindung mit nahezu beugungsbegrenzter Strahlqualität. Wir untersuchen das komplexe Wechselspiel in VECSEL-Strukturen zwischen resonatorinternen optischen Feldern und dem Quantenfilm-Gewinnmaterial. Unsere Simulationen machen das dynamische Gleichgewicht zwischen Ladungsträgererzeugung in Zuständen hoch im Band (durch Pumpen), Relaxation von Ladungsträgern und stimulierter Rekombination an Zuständen nahe der Bandkante deutlich. Wir zeigen, daß das longitudinale Multimode-Verhalten zusammengesetzt ist aus mehreren externen Resonatormoden.

Außerdem betrachten wir die Wechselwirkung von Femtosekunden- und Pikosekunden-Pulsen hoher Intensität mit Halbleiterstrukturen. Wir bestimmen den mikroskopischen Ursprung der schnellen Nichtlinearitäten und untersuchen die physikalischen Effekte hinter den verschiedenen Sättigungsmechanismen. Außerdem gewinnen wir die nichtlinearen Gewinnkoeffizienten und Erholungsraten. Es wird gezeigt, daß die Dispersion der Gruppengeschwindigkeit, dynamische Gewinnsättigung und schnelle Selbstphasenmodulation die Hauptursachen für Änderungen und Asymmetrien in Form und Spektrum der verstärkten Pulse sind. Wir zeigen, daß die Zeitkonstanten der Intraband-Streuprozesse kritisch für die Gewinnerholung sind. Unsere Ergebnisse sind grundlegend für die Interpretation und das quantitative Verständnis von nichtlinearer Pulsformung in optischen Halbleiterverstärkern und -absorbern.

Die exakte und spektral breite Modellierung von Halbleiter-Gewinn und komplex strukturierten Laserkavitäten, die in dieser Arbeit dargestellt wird, erweitert die wissenschaftliche Diskussion von Halbleiterlasersystemen. Unser mikroskopischer Ansatz in der Zeitdomäne ist, aufbauend auf effizienten numerischen Algorithmen und der zunehmenden Verfügbarkeit kostengünstiger High Performance Computing-Ressourcen, gut geeignet für die Entwicklung und Designoptimierung von modernen nano-strukturierten Hochleistungsdiodelasern.

C.2 Einleitung und Motivation

Lichtverstärkung durch stimulierte Emission von Strahlung (d. h. LASER-Betrieb [1]) wurde in Halbleiter-Gewinnmaterialien zum ersten Mal im Jahr 1962 demonstriert. Einem theoretischen Vorschlag von Basov folgend haben drei Labors unabhängig voneinander Lasertätigkeit in Verbindungshalbleitern mit direkter Bandlücke und in gepulstem Betrieb bei tiefen Temperaturen berichtet [2–4]. Die stimulierte Emission von Strahlung wurde in diesen Halbleiterdiodelasern durch die strahlende Rekombination von Elektron-Loch-Paaren, injiziert in einen pn-Übergang, umgesetzt. Die Besetzungsinversion, die für den Laserbetrieb nötig ist, wurde in der Verarmungszone einer GaAs(P)-Homojunction erzeugt. Die Einführung von Heterostrukturen in 1970 war ein bahnbrechender Beitrag zur Entwicklung von effizienten optoelektronischen Bauteilen und ein Durchbruch in Richtung auf industrielle Anwendungen. Heterostrukturen sind aufgebaut aus mehreren Schichten von unterschiedlichen Verbindungshalbleitern. Insbesondere ha-

ben Doppelheterostrukturen bestehend aus einer intrinsischen, aktiven GaAs-Schicht, einem dünnen Film für die Lichterzeugung und -verstärkung, umgeben von dotierten AlGaAs-Mantelschichten einen Dauerstrichbetrieb bei Raumtemperatur ermöglicht [3]. Die verbesserten Leistungskennzahlen (z. B. hohe Effizienz, niedrige Umwandlung von Energie in Wärme) und die reduzierte Laserschwelle in solchen Strukturen wurde durch erhöhten Einschluß der Ladungsträger und optischen Feldmode erreicht [2–4].

Hochentwickelte Kristallwachstumsverfahren (z. B. Molekularstrahlepitaxie, metallorganisch chemische Gasphasenabscheidung, Flüssigphasenepitaxie, selbstorganisierte Wachstumsmethoden) [5] und Prozess- und Ätztechnologien ermöglichen die Herstellung von komplexen Halbleiter-Nanostrukturen (wie zum Beispiel GRIN-Strukturen, Übergitter, Quantenfilme und Quantenpunkte oder photonische Kristalle). Diese Technologien erlauben eine bessere Kontrolle über die elektronischen Eigenschaften des Gewinnmaterials durch die Anwendung der Konzepte der Size-Quantisierung und reduzierten Dimensionalität, und die gezielte Manipulation der optischen Modenstruktur und Zustandsdichte in funktionalen photonischen Materialien. Gleichzeitig haben sich die Theorie und Simulation der Laserdynamik zu einem Thema von mehr als nur akademischem Interesse entwickelt. Wegen der Vorhersagekraft stellt die Computermodellierung ein unschätzbbares Werkzeug zur Entwicklung neuartiger Laserstrukturen und zur Designoptimierung dar. Durch die Forderung nach höheren Ausgangsleistungen, anderen Betriebswellenlängen und Hochfrequenzmodulation wurde die Entwicklung neuartiger Laser- und Verstärkerstrukturen und die Einführung von neuen Gewinnmaterialien und Laserkonzepten vorangetrieben. Dies ist begleitet durch die fortlaufende Miniaturisierung von kohärenten Lichtquellen und Verstärkern (mit dem Ziel einer On-Chip Realisierung). Intensive Forschungsaktivitäten auf dem Gebiet der Halbleiterlaser haben den Übergang von einem Gegenstand im Labor zu einem Massenprodukt mit Anwendungen in unserem täglichen Leben angeregt. Halbleiterdiodenlaser weisen einige Vorteile gegenüber anderen kohärenten Lichtquellen auf: kompakte Größe, hohe Umwandlungseffizienz von Pumpenergie in kohärentes Licht, Abstimbarkeit und Manipulation der optoelektronischen Eigenschaften, direkte Signalmodulation bis zu einigen zehn GHz und kostengünstige Produktion. Dies hat einen riesigen Markt für Diodenlaser generiert, mit einem geschätzten weltweiten Marktvolumen für Halbleiterlaser von 3.2 Milliarden US-\$ in 2005. Die wichtigsten industriellen Anwendungen von Diodenlasern umfassen optische Datenspeicherung, Glasfaserkommunikation, Hochleistungs- (so wie zum Beispiel das Pumpen von Festkörperlasern) und medizinische Anwendungen. Neben der technologischen Bedeutung von Diodenlasern, machen die Komplexität der physikalischen Wechselwirkungen, die nichtlineare Kopplung der verschiedenen Teilsysteme und eine Vielzahl an Zeit- und Längenskalen Halbleiterlaser zu idealen Laboren zur Untersuchung von optisch nichtlinearen [6, 7] und quantenoptischen Phänomenen [8], sowie von ultraschnellen Prozessen in Halbleitern, und von Konzepten der nichtlinearen Dynamik und Synergetik [9, 10].

Neue und hochinteressante Entwicklungen zielen auf die Kontrolle und Manipulation der Wechselwirkung von Licht und Materie, Lichtemission und -propagation und auf die gezielte Beeinflussung der optoelektronischen Eigenschaften von Halbleiter-Gewinnme-

dien. Im Folgenden geben wir einen Überblick über neueste Forschungsbemühungen, die im Zusammenhang mit dieser Arbeit stehen.

Laser- und Verstärkerstrukturen: Vertikal emittierende Laserdioden (VCSEL) [11, 12] sind aufgebaut aus hochreflektiven Bragg-Spiegeln mit eingeschlossener Defektkavität und einem zusätzlichen transversalen Einschluß (durch Oxid-Apertur). Insbesondere zeigen VCSEL eine starke Kopplung zwischen Gewinnmaterial und dem Lichtfeld. Mikrokavitäten [13, 14] versprechen hohe Qualitätsfaktoren, kleine Modenvolumen und niedrige Laserschwellen. Sie sind Schlüsselwerkzeuge zur Untersuchung und Maßschneidung von Lichtquellen und erlauben die Modifizierung der Wechselwirkung von Licht und Materie, z. B. der spontanen Emission, da die lokale optische Zustandsdichte durch die dielektrische Struktur bestimmt ist. Optische Halbleiterverstärker (SOA) sind attraktiv als Zwischenverstärker und funktionelle Einheiten in optischen Netzwerken. Resonante periodische Gewinnstrukturen (PGS) [11, 15] bieten eine Überhöhung des effektiven modalen Gewinns. Oberflächenemitter mit vertikaler externer Kavität (VECSEL) [16, 17] sind ein Designschema zur Erhöhung der Laserleistung in Strahlen von hoher Qualität und geben leichten Zugang zu nichtlinear-optischen Effekten (aufgrund der hohen Innenintensitäten), wie zum Beispiel dynamische Gewinnsättigung und Pulsformung oder Frequenzumwandlung. Photonische Kristalle (PC) und Materialien mit photonischer Bandlücke ermöglichen die Lichtausbreitung mit sehr kleinen Gruppengeschwindigkeiten [18, 19]. Sie können als frequenzselektive Spiegel oder optische Mikrokavitäten fungieren und bieten einen Führungsmechanismus basierend auf Bragg-Vielfachinterferenz und nicht auf Totalreflexion [20]. Diese Führung im Niederindex-Kern (Luft) wird in photonischen Kristallfasern angewandt.

Halbleiter-Gewinnmaterialien: Neue binäre, ternäre und quaternäre Verbindungshalbleitermaterialien können entworfen werden für eine Vielfalt von optischen Emissionswellenlängen von Infrarot bis Ultraviolett. Neueste Forschung konzentriert sich auf II-VI Verbindungen, Gruppe III-Nitride mit großer Bandlücke [21–23] und verdünnte Nitride, z. B. GaInNAs [24], für hochentwickelte Anwendungen in der Telekommunikation. Aktive Nanostrukturen mit Quanten-Confinement [25] und reduzierter Dimensionalität, wie zum Beispiel Quantenfilme [26], Nanodrähte und Quanten-Dashes [27, 28], und Quantenpunkte [29], verändern grundlegend die elektronische Bandstruktur und optoelektronischen Eigenschaften durch Anwendung des Konzepts der Size-Quantisierung, was zu effizienterer Ladungsträgerinversion führt. Die Anwendung von Zug-/Druckspannung ermöglicht eine weitere Änderung von Bandstruktur und Gewinn. Außerdem stellen organische Halbleiter [30] mögliche neue Gewinnmaterialien für Festkörperlaser im grünen Spektralbereich für Bildschirm- und Beleuchtungstechnologien dar. Die einfache Herstellung und Formbarkeit dieser Filme aus konjugierten Polymeren sind attraktiv [31]. Die meisten Laser dieser Art verwenden Strukturen mit Korrugation, welche als Resonator basierend auf dem Prinzip der verteilten Rückkopplung wirken.

Laser- und Gewinn-Konzepte: Optische Pumpschemata stellen eine Alternative zu elektrischem Pumpen dar. Sie bieten die Möglichkeit, die räumliche Verteilung der Besetzungsinversion über große Bereiche festzulegen. Die Erzeugung ultrakurzer optischer Pulse durch passive Modenkopplung mit Hilfe von sättigbaren Absorbern [32, 33] baut auf eine gezielte Ausnutzung nichtlinearer Effekte und das komplexe dynamische Wechsel-

spiel zwischen Gewinn und Lichtfeld. Quantenkaskaden-Laser beruhen auf Intersubband-Übergängen (d. h. Intraband-Polarisationen). Diese Intersubband-Natur (nur eine einzelne Ladungsträgerart beteiligt) führt zu zahlreichen Vorteilen verglichen mit Diodenlasern basierend auf stimulierter Elektron-Loch-Rekombination [34]. Zum Beispiel Abstimmbarkeit aufgrund der Size-Quantisierung in diesen Vielfach-Quantenfilm Heterostrukturen (d. h. keine Beschränkung durch die Energiebandlücke gegeben) und höhere Effizienz. Das Erzielen von optischem Gewinn für Rekombinationsprozesse in Halbleitermaterialien mit indirekter Bandlücke ist schwierig, was eine Untersuchung nach anderen physikalischen Wechselwirkungen und Gewinnmechanismen motiviert. Kürzlich wurde Lichtverstärkung und Lasertätigkeit in Silizium demonstriert [35], wo die Verstärkung durch stimulierte Raman-Streuung erzielt wurde.

Die numerische Simulation von Halbleiterlasern spielt eine wichtige Rolle in der Entwicklung von neuartigen Strukturen und zur Designoptimierung. Des Weiteren sind sie wertvoll in der Untersuchung zugrunde liegender physikalischer Grenzen und der optischen und elektronischen Eigenschaften der verschiedenen Teilsysteme. Aufgrund der Komplexität des Problems und der nichtlinearen Kopplung der Teilsysteme (Optik, Ladungsträger, Phononen) ist eine analytische Behandlung schwierig. Mit nur wenigen Beschränkungen bezüglich Geometrie und physikalischen Wechselwirkungen bieten Methoden im Zeitbereich ein flexibles und ausbaufähiges Werkzeug, um die Lösung der gekoppelten Dynamik von optischem Feld innerhalb der Kavität und dem aktiven Gewinnmaterial anzugehen. Die einzige Einschränkung in der Umsetzung solcher Methoden ist durch die benötigten Computerressourcen gegeben. Der Ausgangspunkt für Halbleiterlaser-Modelle sind die Lasergleichungen, abgeleitet von Haken und Lamb, Jr. [36]: Der Basissatz dynamischer Variablen ist gegeben durch das optische Feld, die induzierte Polarisation im aktiven Material und die Ladungsträgerinversion. Einen Überblick häufig verwendeter Modelle in der Zeitdomäne zur Simulation von Halbleiterlasern im Rahmen der semiklassischen Näherung (d. h. eine Verknüpfung klassischer elektromagnetischer Felder mit den quantenelektronischen Eigenschaften des aktiven Materials) wird in [3, 37] präsentiert. Wir fassen die verschiedenen Zugänge zur Modellierung der Halbleiter-Gewinndynamik und der Dynamik der optischen Felder in ABBILDUNG 1.1 bzw. ABBILDUNG 1.2 zusammen. Dabei definieren wir auch die Anwendungsmöglichkeiten und Vorteile unserer neuentwickelten Modelle gegenüber anderen Ansätzen.

Im Unterschied zu anderen Laserstrukturen sind Halbleiterdiodenlaser durch einige besondere Eigenschaften gekennzeichnet, welche in realistischen Computermodellen berücksichtigt werden müssen [2, 4, 37]: Aufgrund der hohen Dichten sind Vielteilchen-Wechselwirkungen von großer Bedeutung, vor allem in Gewinnstrukturen mit Quanten-Confinement, und es tritt eine schnelle Dephasierung der induzierten Polarisation ein. Halbleiter-Gewinnmaterialien sind gekennzeichnet durch ein breites Gewinnspektrum und eine starke Kopplung von Amplituden- und Phasendynamik (quantitativ beschrieben durch den α Faktor). Diodenlaser schließen eine Vielzahl relevanter Zeitskalen, von wenigen Femtosekunden (für die Coulomb Intraband-Streuung) bis einigen Nanosekunden (für makroskopische Transportprozesse wie Ladungsträgerdiffusion), ein. Außerdem sind starkes räumliches und spektrales Lochbrennen, Nichtlinearitäten und Sättigungs-

effekte von Bedeutung. Moderne Diodenlaser sind aus komplex strukturierten Kavitäten aufgebaut. Die Lasermode kann stark von den Moden der kalten Kavität abweichen, da Laserbetrieb und Ladungsträgerdynamik (z. B. Lochbrennen und thermische Effekte) die Brechungsindexstruktur verändern. Die Ausgangsleistung und Kenndaten von Diodenlasern sind durch die nichtlinearen Eigenschaften des Gewinnmaterials limitiert. Wichtig dabei sind die Ladungsträgerdynamik in den Quantenfilmen (z. B. spektrales Lochbrennen und Streuprozesse), räumliche Effekte (z. B. räumliches Lochbrennen und Selbstfokussierung) und thermisch-induzierte Änderungen des Gewinnmediums. Zusammenfassend gesagt, die Theorie von Halbleiterlasern muß kontinuierlich überarbeitet und angepaßt werden an die in den vorherigen Abschnitten beschriebenen neuartigen Strukturen, Konzepte und Gewinnmaterialien.

Die Hauptzielsetzung dieser Arbeit ist die Entwicklung eines theoretischen Modells der raumzeitlichen Dynamik von neuartigen Hochleistungshalbleiterlasern. Wir streben außerdem ein quantitatives Verständnis des nichtlinearen Wechselspiels zwischen Halbleiter-Gewinndynamik und der resonatorinternen Lichtfelddynamik an. Hierzu verbessern und erweitern wir vorhandene theoretische Beschreibungsansätze der Halbleiterlaserdynamik, um den Anforderungen auferlegt durch die obig diskutierten Forschungsaktivitäten zu genügen. Besondere Berücksichtigung finden Gewinnstrukturen mit Quanten-Confinement, komplexe dielektrische Mikrokavitäten und photonische Strukturen (strukturiert auf einer Subwellenlängen-Skala). Zur realistischen Computermodellierung von Diodenlasern kombiniert unser Ansatz im Rahmen der semiklassischen Näherung die räumlich aufgelösten Maxwell Gleichungen, oder die paraxiale Wellengleichung, mit einer energieaufgelösten Beschreibung der Materialantwort, gegeben durch die Halbleiter-Bloch Gleichungen. Zwei Modelle wurden erarbeitet: 1) ein transversales Modell für die Untersuchung der transversalen Multimode-Dynamik in Breitstreifenlasern, und 2) ein longitudinales Modell zur Beschreibung der Propagation ultrakurzer Pulse in optischen Halbleiterverstärkern. Wir verwenden das letztere Modell auch zur Analyse komplex strukturierter aktiver Laser, z. B. Oberflächenemitter mit vertikaler Kavität und periodisch moduliertem Defekt, und optisch gepumpte oberflächenemittierende Laser mit einem externen Resonator. Zur gleichzeitigen Lösung der Modellgleichungen für die Lichtfelddynamik (partielle Differentialgleichungen) und der Polarisations- und Ladungsträgerdynamik in aktiven Halbleiterstrukturen wandeln wir die Gleichungen in finite Differenzgleichungen um, welche auf homogenen Gittern integriert werden.

C.3 Überblick

Diese Arbeit zielt auf ein verbessertes quantitatives Verständnis von Lasersystemen mit technologischer oder grundlegender Bedeutung. Wir streben einen Vergleich mit Experimenten an, d. h. wir müssen Material-, Struktur- und Kontrollparameter realistisch abbilden. Auf Basis eines mikroskopischen Gewinnmodells einschließlich von Vielteilchen-Wechselwirkungen konzentrieren wir uns auf die Untersuchung von Phänomenen auf der Femtosekunden- und Pikosekunden-Skala und analysieren die räumliche Musterbildung

im optischen Nahfeld. Wir untersuchen den mikroskopischen Ursprung von optischen Nichtlinearitäten und den Einfluß der Ladungsträgerdynamik auf die Ausgangskennzahlen von Diodenlasern. Wir konzentrieren uns auf Hochleistungsstrukturen wie Breitstreifenlaser und optische Halbleiterverstärker. Wir bestätigen numerisch neuartige Konzepte zur Erhöhung der Ausgangsleistung von oberflächenemittierenden Lasern, z. B. durch die gezielte Manipulation der optischen Modenstruktur. Genauer gesagt, wir untersuchen photonische Bandkanten-Bandlücken-Laser und optisch gepumpte VECSEL. Diese Arbeit ist folgendermaßen aufgebaut:

In KAPITEL 2 leiten wir die Multisubband-Halbleiter-Bloch Gleichungen ab, welche eine quantenmechanische Beschreibung der ultraschnellen Gewinndynamik in Quantenfilmen basierend auf dem Dichtematrix-Formalismus darstellen. Unser Ansatz, formuliert im Impulsraum, umfaßt die wichtigsten Wechselwirkungen in optisch aktiven Halbleiter-Gewinnmaterialien und eine Vielzahl an Zeitskalen. Die Wechselwirkung von Licht mit Halbleiter-Gewinnmedien ist im Rahmen der semiklassischen Näherung unter Anwendung der elektrischen Dipolnäherung modelliert. Vielteilchen-Wechselwirkungen, nämlich die abgeschirmte Coulomb-Wechselwirkung und die Streuung mit Phononen, haben die Renormierung von Übergangsenergien, das Coulomb-Enhancement der Rabi-Frequenzen und Relaxations- und Dephasierungsprozesse zur Folge. Wir geben voll mikroskopische Vielteilchen-Berechnungen an. Wir betrachten Gleichungen für die Dynamik der Wigner-Funktionen von diagonalen und nichtdiagonalen Elementen der Einteilchen-Dichtematrix:

$$\partial_t p_{ji,\mathbf{k}} = - (i\Omega_{ij,\mathbf{k}} + \gamma_{ij,\mathbf{k}}^p) p_{ji,\mathbf{k}} - \frac{i}{\hbar} U_{ij,\mathbf{k}} (n_{ii,\mathbf{k}}^e + n_{jj,-\mathbf{k}}^h - 1), \quad (\text{C.1})$$

$$\begin{aligned} \partial_t n_{ii,\mathbf{k}}^e &= \frac{i}{\hbar} \sum_j (U_{ij,\mathbf{k}} p_{ji,\mathbf{k}}^* - U_{ij,\mathbf{k}}^* p_{ji,\mathbf{k}}) - \gamma^{\text{nr}} n_{ii,\mathbf{k}}^e - \sum_j \gamma_{ij,\mathbf{k}}^{\text{sp}} n_{ii,\mathbf{k}}^e n_{jj,-\mathbf{k}}^h - \gamma_{ii,\mathbf{k}}^{e,\text{Auger}} \\ &+ \Lambda \frac{f_{ii,\mathbf{k}}^e(T_{\text{lat}}) (1 - n_{ii,\mathbf{k}}^e(T_{\text{pl}}))}{\sum_i 1/A \sum_{\mathbf{k}} f_{ii,\mathbf{k}}^e (1 - n_{ii,\mathbf{k}}^e)} - \gamma_{ii,\mathbf{k}}^{e(\text{ph})} (n_{ii,\mathbf{k}}^e(T_{\text{pl}}) - f_{ii,\mathbf{k}}^e(T_{\text{lat}})) \\ &- \gamma_{ii,\mathbf{k}}^{ee(\text{cc})} (n_{ii,\mathbf{k}}^e(T_{\text{pl}}) - f_{ii,\mathbf{k}}^e(T_{\text{pl}})) - \gamma_{ii,\mathbf{k}}^{eh(\text{cc})} (n_{ii,\mathbf{k}}^e(T_{\text{pl}}) - f_{ii,\mathbf{k}}^e(T_{\text{pl}}^h)). \end{aligned} \quad (\text{C.2})$$

Eine Formulierung vollständig in der Zeitdomäne wird ebenfalls abgeleitet (Halbleiter-Bloch Gleichungen in Full Time-Domain). Unser Ansatz setzt die übliche Rotating Wave Näherung (RWA) nicht voraus, und stellt somit eine genaue und spektral breite Modellierung des Gewinnmediums dar. Das Modell ermöglicht die Simulation ultraschneller, nichtlinearer Pulswechselwirkungen in Halbleiterlasern und -verstärkern. Die Antwort des Verstärkermediums auf optische Anregungen wird quantitativ beschrieben und bestimmt durch die induzierte makroskopische Polarisation $\mathbf{P}(\mathbf{r}, t)$ (ein nichtlineares Funktional), die Ladungsträgerdichte und die Materialdispersion $n_{\text{background}}(\mathbf{r}; \omega)$. Die relative Permittivität kennzeichnet den dielektrischen Resonator. Außerdem schlagen wir das Fitting und die Parametrisierung der komplexen dielektrischen Suszeptibilität durch wenige Oszillatoren als effektiven Weg einer Nachbildung der optoelektronischen Eigenschaften eines komplexen Halbleiter-Gewinnmediums vor.

KAPITEL 3 betrachtet die Beschreibung der Dynamik von Lichtfeldern in Laserkavitäten. Die Propagation, Beugung, Reflexion und Führung von elektromagnetischen

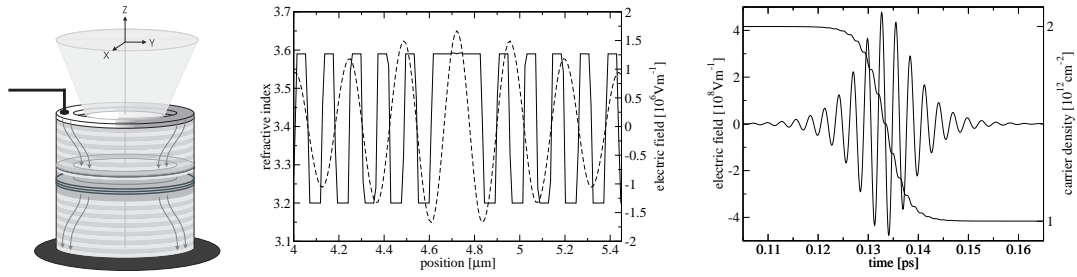


ABBILDUNG C.1: Beispielsysteme zu Modell (C.3)–(C.4): Oberflächenemittierende Laserstruktur; Lasermode in einem VCSEL; Propagation von Femtosekunden-Pulsen.

Feldern in Brechungsindex-Strukturen und optischen Kavitäten von Laserresonatoren wird modelliert über die makroskopischen Maxwell (Rotations-) Gleichungen oder eine davon abgeleitete (genäherte) Wellengleichung. Die spektral aufgelöste induzierte makroskopische Polarisation, welche wir in KAPITEL 2 berechnen, wirkt als Quellterm des optischen Laserfelds. Wir entwickeln zwei unterschiedliche Modelle zur Beschreibung des passiven Problems: 1) Die vollen Maxwell Gleichungen zielen auf Problemstellungen ab, welche ein breites Spektrum an relevanten Frequenzen oder räumlich stark lokalisierte Moden mit sich bringen (siehe ABBILDUNG C.1). Der Ansatz ist jedoch beschränkt auf wenige Mikrometer große aktive Strukturen. Wir untersuchen Mikrokavitäten-Laser und die nichtlineare Pulswechselwirkung in Halbleiterverstärkern. Wir verknüpfen die Maxwell Rotationsgleichungen mit einer band-aufgelösten Beschreibung der Dynamik des Halbleiter-Gewinnmaterials im Rahmen der Methode der Finiten Differenzen im Zeitbereich (FDTD):

$$\text{curl}\mathbf{E} + \partial_t\mathbf{B} = 0, \quad \text{curl}\mathbf{H} - \partial_t\mathbf{D} = 0, \quad (\text{C.3})$$

$$\partial_z E_x + \partial_t B_y = 0, \quad \frac{1}{\mu_0} \partial_z B_y + \partial_t D_x = 0, \quad \partial_z E_y - \partial_t B_x = 0, \quad \frac{1}{\mu_0} \partial_z B_x - \partial_t D_y = 0,$$

$$\mathbf{D}(z, t) = \epsilon_0 \epsilon(z) \mathbf{E}(z, t) + \Gamma_{x,y}(z) \frac{N_{\text{QW}}(z)}{L_{\text{ref}}} \mathbf{P}(z, t). \quad (\text{C.4})$$

Dieser numerisch herausfordernde, generische Zugang wurde in dieser Arbeit zum ersten Mal umgesetzt. 2) Abhängig von den Eigenschaften des Resonators werden zur Vereinfachung der Modellgleichungen die paraxiale, Slowly Varying Amplitude und RWA Näherungen angewandt:

$$\left(\frac{n^2}{cn_{\text{eff}}} \partial_t \pm \partial_z - i \frac{1}{2k_0 n_{\text{eff}}} \partial_x^2 - ik_0 \frac{n}{n_{\text{eff}}} \delta n_{\text{pas}}(x) \right) \tilde{E}^{\pm}(x, z, t) = i \frac{k_0 \Gamma_y}{\epsilon_0 2n_{\text{eff}}} \frac{N_{\text{QW}}}{L_{\text{ref}}} \tilde{P}^{\pm}(x, z, t). \quad (\text{C.5})$$

Das skalare, transversale Wellengleichungsmodell wurde entwickelt zur Untersuchung von großflächigen kantenemittierenden Halbleiterlasern und Verstärkerstrukturen hoher Leistung und zur Analyse transversaler Multimode-Dynamik (siehe ABBILDUNG C.2).

In KAPITEL 4 berechnen wir mit Hilfe räumlich nicht-aufgelöster Modelle charakteristische Größen von Laser-Gewinnmedien. Der Resonator wird dabei über effektive

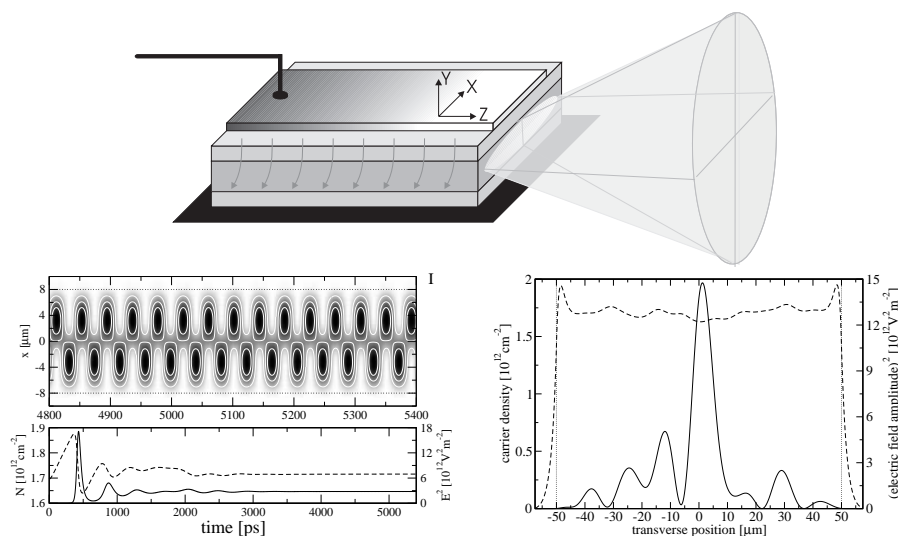


ABBILDUNG C.2: Beispielsysteme zu (C.5): Breitstreifenlaser; transversale Multimode-Dynamik in Kantenemittern.

Parameter berücksichtigt. Mikroskopische Streu- und Dephasierungsraten aufgrund der Coulomb- und Fröhlich-Wechselwirkung werden in GaAs-Quantenfilmen für verschiedene Ladungsträgerdichten und Temperaturen berechnet. Die Berechnungen erfolgen über die Quantum-Boltzmann Gleichung. Wichtig ist, daß individuelle Streuprozesse analysiert werden. Wir verwenden die mikroskopischen Relaxationsraten in unseren Simulationen der raumzeitlichen Laserdynamik (als Lookup Tabellen) und zeigen, daß dies das Modell quantitativ verbessert. Wir zeigen, daß die Relaxationsraten entscheidend sind für die Modellierung von Gewinn-Parametern, nichtlinearer Pulspropagation und das dynamische Sättigungsverhalten von Verstärker- und Absorberelementen. Eine dynamische Behandlung der Streuprozesse ist in ANHANG B dargestellt. Außerdem bestimmen wir Größen, die die Wechselwirkung von Licht und Materie charakterisieren. Die wichtigen optischen Gewinngrößen von Halbleiter-Verstärkermedien (Kleinsignalverstärkung, differentieller Gewinn), die Spektren der spontanen Emission und strahlende Rekombinationsraten werden mit einem mikroskopische Ansatz, in Screened Hartree-Fock Näherung, berechnet. Grundkonzepte von Halbleiterlasern, wie zum Beispiel Density Pinning und Gain Clamping, Gewinnsättigung und thermisches Überrollen werden im Rahmen unserer Modelle diskutiert. Die transiente dynamische Antwort, wenn ein Laser eingeschaltet oder während des Betriebs gestört wird, d. h. Relaxationsoszillationen, werden untersucht. Wir gewinnen realistische Eingangsparameter für die Analyse raumzeitlicher Laserdynamik, was den Ansatz quantitativ verbessert. Die gute Übereinstimmung der numerischen Ergebnisse mit experimentellen Resultaten, wie auch mit den Vorhersagen einfacherer theoretischer Modelle, bestätigt unseren Ansatz.

In KAPITEL 5 untersuchen wir Breitstreifenlaser mit Hilfe des paraxialen optischen Modells, wie in KAPITEL 3 vorgestellt. Dieser Kantenemitter ist charakterisiert durch einen einfachen Fabry-Pérot Resonator und einen dielektrischen Wellenleiter. Wir zeigen, daß mit zunehmender Breite der aktiven Zone oder Pumpleistung mehr transversale Mo-

den angeregt werden, räumliche wie zeitliche Fluktuationen im Nahfeld auftreten und instabile optische Filamente geformt werden. Wir weisen die Abhängigkeit des transversalen Multimode- und Fluktuationsverhalten von der Ladungsträger- und Gewinn-Dynamik und von der selektiven Verarmung der Ladungsträger aufgrund verschiedener transversaler Lasermoden nach. Wir zeigen, daß die Koexistenz mehrerer Moden unterstützt wird durch die Wechselwirkung der verschiedenen Moden mit getrennten Bereichen des Gewinnmaterials, räumlich aufgrund des transversalen Freiheitsgrades und spektral als Resultat der inhomogenen Verbreiterung. Für breitere Strukturen unterstützen Gewinn-, Dichte- und Indexprofile neben der Grundmode höhere transversale Moden. Der Einfluß von optischen Nichtlinearitäten hervorgerufen durch räumliches Lochbrennen und von den physikalischen Effekten Ladungsträgerdiffusion, Gewinn- und Index-Führung, Selbstfokussierung und Beugung werden quantitativ analysiert. Wir geben eine lineare Stabilitätsanalyse der transversalen Instabilität an. Dies ermöglicht es, die Hauptkontrollparameter zu identifizieren: die Streifenbreite, Pumpe und der Linienverbreiterungsfaktor. Wir zeigen numerisch, daß abhängig von der Breite der Struktur unterschiedliche Maße raumzeitlicher Komplexität und dynamische Emissionsregimes festgestellt werden können. Wir bestimmen zeitgemittelte Profile, verwenden eine Modenanalyse der komplexen Felder zur numerischen Berechnung optischer Feldamplituden und Laserfrequenzen, und projizieren das räumliche Nahfeld auf die Lasermoden. Im quasi-periodischen Regime läßt sich das nicht-transiente Verhalten als Überlagerung verschiedener Moden mit unterschiedlichem Profil, Symmetrie und Frequenz deuten.

In KAPITEL 6 wenden wir das Full Time-Domain Modell, d. h. die Maxwell Gleichungen gekoppelt mit den Halbleiter-Bloch Gleichungen, zur Untersuchung von longitudinaler Multimode-Dynamik in neuartigen Laserstrukturen und der Wechselwirkung von Femtosekunden- und Pikosekunden-Pulsen mit optisch aktiven Medien an. VCSEL mit eingeschlossener periodischer Gewinn- und Brechungsindex-Struktur werden betrachtet. Zur Erhöhung der Ausgangsleistung von Oberflächenemittern werden die Quantenfilme periodisch in Resonanz mit der Defektmode angeordnet (optimaler Überlapp). Die Bestimmung der Lasermoden, Laserfrequenzen und -schwelen beweist numerisch, daß PC-Effekte für endliche Kristalle erzielt werden können und zu einer merklichen Verbesserung der Laserleistung führen. Wir zeigen, wie in photonischen Bandkanten-Lasern spezielle Eigenschaften von Singularitäten im optischen Bandstruktur-Diagramm ausgenützt werden, z. B. die flache Dispersion an Bandkanten. Unsere Ergebnisse zeigen die Gewinnerhöhung über eine verstärkte Lokalisierung der Moden über den aktiven Quantenstrukturen und die effizientere Wechselwirkung von Photonen mit dem Gewinnmaterial (erhöhter Gewinn per Unit Length). Das letztere tritt aufgrund der reduzierten Gruppengeschwindigkeit auf. Wir untersuchen die Unterdrückung optischer Verluste der inneren endlichen photonischen Struktur durch die Verwendung einer umgebenden photonischen Struktur mit Bandlücke. Realistische optisch gepumpte oberflächenemittierende Laser mit externer Kavität werden untersucht. Das optische Pumpschema und die externe Kavität ermöglichen eine Skalierung der Leistung bei guter Strahlqualität in der TEM_{00} Grundmode. Wir zeigen, daß das longitudinale Multimode-Verhalten in VECSELn aus mehreren Moden der externen Kavität aufgebaut ist. Eine mikroskopische Analyse deckt das dynamische Gleichgewicht zwischen Ladungsträgererzeugung durch Pumpen ho-

her Energiezustände, Relaxation gegen die Fermi-Dirac Verteilung und Lasertätigkeit an Zuständen nahe der Bandkante auf. Außerdem betrachten wir die Propagation von Femtosekunden- und Pikosekunden-Pulsen in aktiven Halbleiterstrukturen und analysieren die puls-induzierten Änderungen des Halbleitermaterials. Wir führen umfangreiche numerische Pulspropagationsexperimente durch, in denen Probe-Pulse die Polarisationsantwort und den Nichtgleichgewichtszustand des Gewinnmaterials abtasten. Wir identifizieren den mikroskopischen Ursprung der schnellen Nichtlinearitäten und diskutieren die physikalischen Effekte hinter den verschiedenen Sättigungsmechanismen, z.B. die Verarmung an vorhandenen resonanten Ladungsträgern für stimulierte Emission. Wir berechnen auch die nichtlinearen Gewinnkoeffizienten und die verschiedenen Erholungsraten (über Pump-Probe-Experimente). Die Zeitkonstanten der Intraband-Streuprozesse sind kritische Parameter der dynamischen Gewinnsättigung und -erholung. Die Dispersion der Gruppengeschwindigkeit, dynamische Sättigung und schnelle Selbstphasenmodulation sind die Hauptursachen für die beobachteten Asymmetrien in Pulsform und -spektrum. Diese nichtlineare Pulsformung, z.B. Pulse Slowdown oder Advancement, Änderung von Pulsbreite und Pulsenvelope, Chirp, wird im Detail analysiert. Außerdem untersuchen wir nichtlineare kohärente Pulspropagationsphänomene in aktiven Gewinnmedien, insbesondere das Pulsflächentheorem (die Pulsfläche, definiert als das zeitliche Integral über die Rabi-Frequenz, strebt gegen bestimmte Attraktoren, Vielfache von π), Rabi-Oszillationen und selbstinduzierte Transparenz (zeitliches Soliton für eine Pulsfläche von 2π). Unsere Simulationen zeigen, daß bis auf kleine Abweichungen durch die Berücksichtigung der schnell oszillierenden Trägerwelle die numerischen Ergebnisse mit der Theorie übereinstimmen. In einem mikroskopischen Halbleitermodell mit realistischen Parametern für Dephasierungsprozesse und die homogene Verbreiterung dagegen treten unvollständige Rabi-Flops auf, der Puls wird gedämpft. Diese Ergebnisse zeigen, daß ultraschnelle kohärente nichtlineare Propagationseffekte in Halbleiter-Quantenfilm Gewinnmaterialien und bei Raumtemperatur wenig stark ausgeprägt sind.

ANHANG A gibt Einzelheiten zu den numerischen Umsetzungen der theoretischen Modelle in der Zeitdomäne, wie zum Beispiel die Diskretisierung der Felder und Differentialoperatoren auf regulären Gittern und die verwendeten Integrationsschemata. Außerdem diskutieren wir die numerische Komplexität, Genauigkeit und Stabilität unserer Algorithmen. Für das paraxiale transversale Wellengleichungsmodell schlagen wir die Hopscotch Methode als effizienten, stabilen und hinreichend genauen Ansatz vor. Wir wenden einen numerischen Algorithmus an, der die Partitionierung des Gitters in zwei Gruppen von Gitterpunkten und ein Integrationsschema mit abwechselnder expliziter und impliziter Diskretisierung einschließt. Der Vorzug dieser Methode ist, daß kein matrixwertiges Problem gelöst werden muß. Wir diskutieren die Finite Differenzen im Zeitbereich (FDTD) Methode, welche die Maxwell Rotationsgleichungen erster Ordnung durch Anordnen der elektrischen und magnetischen Feldkomponenten auf versetzten Gittern in Zeit und Raum gemäß dem Yee-Schema löst. Eine voll explizite numerische Implementierung unserer Full Time-Domain Modelle, von aktiver nichtlinearer Materialantwort und der passiven Brechungsindex-Struktur, wird entwickelt.

C.4 Ausblick

Zusammenfassend gesagt, in dieser Arbeit entwickeln und präsentieren wir Modelle in der Zeitdomäne, welche sich als wertvolle Werkzeuge für die Untersuchung der gekoppelten Dynamik von resonatorinternen optischen Feldern und der band-aufgelösten Antwort des Halbleitermaterials erweisen. Unsere neuartigen Ansätze werden erfolgreich angewandt zur Untersuchung von eindimensionalen photonischen Bandkanten-Bandlücken-Lasern und optisch gepumpten VECSELn. Außerdem betrachten wir Hochleistungsstrukturen, wie zum Beispiel Breitstreifenlaser und optische Halbleiterverstärker, in welchen optische Nichtlinearitäten und ultraschnelle Prozesse von großer Bedeutung sind. Das vorgestellte theoretische Gerüst kann auf komplexere Gewinnsysteme und Laserstrukturen erweitert werden. Ihre Umsetzung allerdings ist begrenzt durch die verfügbaren Kapazitäten auf Höchstleistungsrechnern.

Eine mögliche Erweiterung des Modells und Thema für zukünftige Forschung sind Mikrokavitäten- und PC-Laser, was die Betrachtung der dreidimensionalen vektoriiellen Maxwell Gleichungen erfordern würde [14,38]. Die Untersuchung von elektrischen Dipolübergängen σ -Typs, d. h. zirkulare Polarisierung, kann mit Hilfe komplexwertiger elektromagnetischer und Polarisationsfelder umgesetzt werden [39]. Die nichtlineare Wechselwirkung von Femtosekunden-Pulsen mit Halbleitermaterialien könnte analysiert werden. Hierzu sind eine mikroskopische Behandlung der Ladungsträgerstreuung und Energieumverteilung [40] und die Berücksichtigung von Gewinn- und Materialdispersion [41] von großer Bedeutung. Mit der Miniaturisierung von Laserstrukturen (z. B. Mikrokavitäten) wird die Untersuchung der spontanen Emission ein wichtiges Thema, da strahlende Lebensdauern über die dielektrische Struktur und das Design der Kavität kontrolliert werden können und Schwellenlose Laser möglich sind [20,42–44]. Wir schlagen somit vor, unser Full Time-Domain Modell zu erweitern durch die Berücksichtigung von Quantenrauschen, spontaner Emission und Cavity-Quantenelektrodynamik [45–47].

Bibliography

- [1] F. K. Kneubühl and M. W. Sigrist. *Laser*. Teubner, 5th edition, 1999.
- [2] G. P. Agrawal and N. K. Dutta. *Semiconductor Lasers*. Kluwer Academic Publishers, 2nd edition, 1993.
- [3] W. W. Chow, S. W. Koch, and M. Sargent III. *Semiconductor-Laser Physics*. Springer-Verlag, 1997.
- [4] W. W. Chow and S. W. Koch. *Semiconductor-Laser Fundamentals: Physics of the Gain Materials*. Springer-Verlag, 1999.
- [5] P. Y. Yu and M. Cardona. *Fundamentals of Semiconductors: Physics and Materials Properties*. Springer-Verlag, 3rd edition, 2005.
- [6] R. W. Boyd. *Nonlinear Optics*. Academic Press, 2nd edition, 2003.
- [7] Y. R. Shen. *The Principles of Nonlinear Optics*. John Wiley & Sons, 2003.
- [8] P. Meystre and M. Sargent III. *Elements of Quantum Optics*. Springer-Verlag, 3rd edition, 1999.
- [9] C. O. Weiss and R. Vilaseca. *Dynamics of Lasers*. Wiley-VCH, 1991.
- [10] H. Haken. *Synergetics: Introduction and Advanced Topics*. Springer-Verlag, 2004.
- [11] S. F. Yu. *Analysis and Design of Vertical Cavity Surface Emitting Lasers*. John Wiley & Sons, 2003.
- [12] J. Hamm. *Spatio-Temporal and Polarisation Dynamics of Semiconductor Microcavity Lasers*. PhD thesis, Universität Stuttgart, 2004.
- [13] K. J. Vahala. Optical microcavities. *Nature* 424:839–846, August 2003.
- [14] A. Klaedtke. *Spatio-Temporal Non-Linear Dynamics of Lasing in Micro-Cavities: Full Vectorial Maxwell-Bloch FDTD Simulations*. PhD thesis, Universität Stuttgart, 2004.
- [15] L. Fan, J. Hader, M. Schillgalies, M. Fallahi, A. R. Zakharian, J. V. Moloney, R. Bedford, J. T. Murray, S. W. Koch, and W. Stolz. High-power optically pumped VECSEL using a double-well resonant periodic gain structure. *IEEE Photon. Technol. Lett.* 17(9):1764–1766, September 2005.
- [16] M. Kuznetsov, F. Hakimi, R. Sprague, and A. Mooradian. Design and characteristics of high-power (>0.5 -W CW) diode-pumped vertical-external-cavity surface-emitting semiconductor lasers with circular TEM₀₀ beams. *IEEE J. Select. Topics Quantum Electron.* 5(3):561–573, May/June 1999.

- [17] A. C. Tropper, H. D. Foreman, A. Garnache, K. G. Wilcox, and S. H. Hoogland. Vertical-external-cavity semiconductor lasers. *J. Phys. D: Appl. Phys.* 37(9):R75–R85, April 2004.
- [18] S.-H. Kwon, S.-H. Kim, S.-K. Kim, Y.-H. Lee, and S.-B. Kim. Small, low-loss heterogeneous photonic bandedge laser. *Opt. Express* 12(22):5356–5361, November 2004.
- [19] E. Schwoob, H. Benisty, C. Weisbuch, C. Cuisin, E. Derouin, O. Drisse, G. H. Duan, L. Legouézigou, O. Legouézigou, and F. Pommereau. Enhanced gain measurement at mode singularities in InP-based photonic crystal waveguides. *Opt. Express* 12(8):1569–1574, April 2004.
- [20] C. Hermann. *Three Dimensional Finite-Difference Time-Domain-Simulations of Photonic Crystals*. PhD thesis, Universität Stuttgart, 2004.
- [21] S. Nakamura, T. Mukai, and M. Senoh. High-brightness InGaN/AlGaIn double-heterostructure blue-green-light-emitting diodes. *J. Appl. Phys.* 76(12):8189–8191, December 1994.
- [22] S. Nakamura. InGaIn-based violet laser diodes. *Semicond. Sci. Technol.* 14(6):R27–R40, June 1999.
- [23] B. Witzigmann, V. Laino, M. Luisier, U. T. Schwarz, G. Feicht, W. Wegscheider, K. Engl, M. Furlitsch, A. Leber, A. Lell, and V. Härle. Microscopic analysis of optical gain in InGaIn/GaIn quantum wells. *Appl. Phys. Lett.* 88(2):021104-1–3, January 2006.
- [24] M. R. Hofmann, N. Gerhardt, A. M. Wagner, C. Ellmers, F. Höhnsdorf, J. Koch, W. Stolz, S. W. Koch, W. W. Rühle, J. Hader, J. V. Moloney, E. P. O’Reilly, B. Borchert, A. Y. Egorov, H. Riechert, H. C. Schneider, and W. W. Chow. Emission dynamics and optical gain of 1.3- μm (GaIn)(NAs)/GaAs lasers. *IEEE J. Quantum Electron.* 38(2):213–221, February 2002.
- [25] H. Haug and S. W. Koch. *Quantum Theory of the Optical and Electronic Properties of Semiconductors*. World Scientific, 4th edition, 2004.
- [26] J. P. Loehr. *Physics of Strained Quantum Well Lasers*. Kluwer Academic Publishers, 1998.
- [27] Y. Xia, P. Yang, Y. Sun, Y. Wu, B. Mayers, B. Gates, Y. Yin, F. Kim, and H. Yan. One-dimensional nanostructures: synthesis, characterization, and applications. *Adv. Mater.* 15(5):353–389, March 2003.
- [28] A. V. Maslov and C. Z. Ning. Modal gain in a semiconductor nanowire laser with anisotropic bandstructure. *IEEE J. Quantum Electron.* 40(10):1389–1397, October 2004.
- [29] D. Bimberg and N. Ledentsov. Quantum dots: lasers and amplifiers. *J. Phys.: Condens. Matter* 15(24):R1063–R1076, June 2003.
- [30] G. Kranzelbinder and G. Leising. Organic solid-state lasers. *Rep. Prog. Phys.* 63(5):729–762, May 2000.

- [31] I. D. W. Samuel and G. A. Turnbull. Polymer lasers: recent advances. *Materials Today* 7(9):28–35, September 2004.
- [32] U. Keller. Recent developments in compact ultrafast lasers. *Nature* 424:831–838, August 2003.
- [33] U. Keller and A. C. Tropper. Passively modelocked surface-emitting semiconductor lasers. *Phys. Rep.* 429(2):67–120, June 2006.
- [34] C. Gmachl, F. Capasso, D. L. Sivco, and A. Y. Cho. Recent progress in quantum cascade lasers and applications. *Rep. Prog. Phys.* 64(11):1533–1601, November 2001.
- [35] H. Rong, R. Jones, A. Liu, O. Cohen, D. Hak, A. Fang, and M. Paniccia. A continuous-wave Raman silicon laser. *Nature* 433:725–728, February 2005.
- [36] D. Preißer. *Theorie der quantenoptischen und nichtlinear-dynamischen Eigenschaften von Halbleiterlasern*. PhD thesis, Universität Stuttgart, 2001.
- [37] O. Hess and T. Kuhn. Spatio-temporal dynamics of semiconductor lasers: theory, modelling and analysis. *Prog. Quant. Electr.* 20(2):85–179, 1996.
- [38] P. Bermel, E. Lidorikis, Y. Fink, and J. D. Joannopoulos. Active materials embedded in photonic crystals and coupled to electromagnetic radiation. *Phys. Rev. B* 73(16):165125-1–8, April 2006.
- [39] A. Klaedtke and O. Hess. Ultrafast nonlinear dynamics of whispering-gallery mode micro-cavity lasers. *Opt. Express* 14(7):2744–2752, April 2006.
- [40] S. Hughes, P. Borri, A. Knorr, F. Romstad, and J. M. Hvam. Ultrashort pulse-propagation effects in a semiconductor optical amplifier: microscopic theory and experiment. *IEEE J. Select. Topics Quantum Electron.* 7(4):694–702, July/August 2001.
- [41] C. O’Rourke, J. Allam, K. Boehringer, J. Hamm, A. Klaedtke, and O. Hess. Multiple Oscillator FDTD Simulation of Ultrashort Pulse Interaction in Semiconductor Lasers. (*submitted to IEEE J. Quantum Electron.*).
- [42] G. Björk, S. Machida, Y. Yamamoto, and K. Igeta. Modification of spontaneous emission rate in planar dielectric microcavity structures. *Phys. Rev. A* 44(1):669–681, July 1991.
- [43] Y. Xu, R. K. Lee, and A. Yariv. Quantum analysis and the classical analysis of spontaneous emission in a microcavity. *Phys. Rev. A* 61(3):033807-1–13, March 2000.
- [44] N. Vats, S. John, and K. Busch. Theory of fluorescence in photonic crystals. *Phys. Rev. A* 65(4):043808-1–13, April 2002.
- [45] G. Hackenbroich, C. Viviescas, and F. Haake. Field quantization for chaotic resonators with overlapping modes. *Phys. Rev. Lett.* 89(8):083902-1–4, August 2002.
- [46] C. Viviescas and G. Hackenbroich. Field quantization for open optical cavities. *Phys. Rev. A* 67(1):013805-1–16, January 2003.

- [47] S. M. Dutra. *Cavity Quantum Electrodynamics: The Strange Theory of Light in a Box*. John Wiley & Sons, 2005.
- [48] H. Haug and S. W. Koch. Semiconductor laser theory with many-body effects. *Phys. Rev. A* 39(4):1887–1898, February 1989.
- [49] A. Girndt, F. Jahnke, A. Knorr, S. W. Koch, and W. W. Chow. Multi-band Bloch equations and gain spectra of highly excited II-VI semiconductor quantum wells. *phys. stat. sol. (b)* 202(2):725–739, August 1997.
- [50] J. Hader, J. V. Moloney, and S. W. Koch. Microscopic theory of gain, absorption, and refractive index in semiconductor laser materials—influence of conduction-band nonparabolicity and Coulomb-induced intersubband coupling. *IEEE J. Quantum Electron.* 35(12):1878–1886, December 1999.
- [51] W. W. Chow, A. Girndt, and S. W. Koch. Calculation of quantum well laser gain spectra. *Opt. Express* 2(4):119–124, February 1998.
- [52] G. H. M. van Tartwijk and D. Lenstra. Semiconductor lasers with optical injection and feedback. *J. Opt. B: Quantum Semiclass. Opt.* 7(2):87–143, April 1995.
- [53] O. Hess and T. Kuhn. Maxwell-Bloch equations for spatially inhomogeneous semiconductor lasers. I. Theoretical formulation. *Phys. Rev. A* 54(4):3347–3359, October 1996.
- [54] S. Balle. Simple analytical approximations for the gain and refractive index spectra in quantum-well lasers. *Phys. Rev. A* 57(2):1304–1312, February 1998.
- [55] C. Z. Ning, R. A. Indik, and J. V. Moloney. Effective Bloch equations for semiconductor lasers and amplifiers. *IEEE J. Quantum Electron.* 33(9):1543–1550, September 1997.
- [56] S. Yamashita, Y. Inoue, S. Maruyama, Y. Murakami, H. Yaguchi, M. Jablonski, and S. Y. Set. Saturable absorbers incorporating carbon nanotubes directly synthesized onto substrates and fibers and their application to mode-locked fiber lasers. *Opt. Lett.* 29(14):1581–1583, July 2004.
- [57] S. S. Mao. Nanolasers: lasing from nanoscale quantum wires. *Int. J. of Nanotechnology* 1(1/2):42–85, 2004.
- [58] A. Taflov and S. C. Hagness. *Computational Electrodynamics: The Finite-Difference Time-Domain Method*. Artech House, 2nd edition, 2000.
- [59] J. L. Young and R. O. Nelson. A summary and systematic analysis of FDTD algorithms for linearly dispersive media. *IEEE Antennas Propagat. Mag.* 43(1):61–77, February 2001.
- [60] I. Vurgaftman, J. R. Meyer, and L. R. Ram-Mohan. Band parameters for III-V compound semiconductors and their alloys. *J. Appl. Phys.* 89(11):5815–5875, June 2001.
- [61] E. P. O’Reilly, A. Lindsay, S. Tomić, and M. Kamal-Saadi. Tight-binding and k-p models for the electronic structure of Ga(In)NAs and related alloys. *Semicond. Sci. Technol.* 17(8):870–879, August 2002.

- [62] U. Bandelow, H.-C. Kaiser, T. Koprucki, and J. Rehberg. Modeling and simulation of strained quantum wells in semiconductor lasers. WIAS Preprint No. 582, Berlin, 2000.
- [63] M. Grupen and K. Hess. Simulation of carrier transport and nonlinearities in quantum-well laser diodes. *IEEE J. Quantum Electron.* 34(1):120–140, January 1998.
- [64] E. Binder. *Kohärenzzerfall in optisch angeregten Halbleitern: Mikroskopische Modellierung des Zerfalls von Interband- und Intraband-Kohärenz in optisch angeregten Halbleitern*. PhD thesis, Universität Stuttgart, 1996.
- [65] J. J. Sakurai. *Modern Quantum Mechanics*. Addison-Wesley, 2nd edition, 1994.
- [66] T. Kuhn. Ladungsträgerdynamik in Halbleitersystemen fern vom Gleichgewicht: Elektronisches Rauschen und kohärente Prozesse. Habilitationsschrift, Universität Stuttgart, 1994.
- [67] P. Weetman and M. S. Wartak. Wigner function modeling of quantum well semiconductor lasers using classical electromagnetic field coupling. *J. Appl. Phys.* 93(12):9562–9575, June 2003.
- [68] C. Cohen-Tannoudji, J. Dupont-Roc, and G. Grynberg. *Photons & Atoms: Introduction to Quantum Electrodynamics*. John Wiley & Sons, 1997.
- [69] J. D. Jackson. *Classical Electrodynamics*. John Wiley & Sons, 3rd edition, 1999.
- [70] H. Römer. *Theoretical Optics: An Introduction*. Wiley-VCH, 2005.
- [71] F. T. Hioe and J. H. Eberly. Nonlinear constants of motion for three-level quantum systems. *Phys. Rev. A* 25(4):2168–2171, April 1982.
- [72] R. W. Ziolkowski. The design of Maxwellian absorbers for numerical boundary conditions and for practical applications using engineered artificial materials. *IEEE Trans. Antennas Propagat.* 45(4):656–671, April 1997.
- [73] P. P. Vasil’ev, I. H. White, and J. Gowar. Fast phenomena in semiconductor lasers. *Rep. Prog. Phys.* 63(12):1997–2042, December 2000.
- [74] A. Klaedtke, J. Hamm, and O. Hess. Simulation of Active and Nonlinear Photonic Nano-Materials in the Finite-Difference Time-Domain (FDTD) Framework, Lecture Notes in Physics 642, *Computational Materials Science: From Basic Principles to Material Properties*, 75–101. Springer-Verlag, 2004.
- [75] S.-H. Chang and A. Taflove. Finite-difference time-domain model of lasing action in a four-level two-electron atomic system. *Opt. Express* 12(16):3827–3833, August 2004.
- [76] R. W. Ziolkowski, J. M. Arnold, and D. M. Gogny. Ultrafast pulse interactions with two-level atoms. *Phys. Rev. A* 52(4):3082–3094, October 1995.
- [77] C. Dineen, J. Förstner, A. R. Zakharian, J. V. Moloney, and S. W. Koch. Electromagnetic field structure and normal mode coupling in photonic crystal nanocavities. *Opt. Express* 13(13):4980–4985, June 2005.

- [78] C. Weisbuch, M. Nishioka, A. Ishikawa, and Y. Arakawa. Observation of the coupled exciton-photon mode splitting in a semiconductor quantum microcavity. *Phys. Rev. Lett.* 69(23):3314–3317, December 1992.
- [79] G. Khitrova, H. M. Gibbs, F. Jahnke, M. Kira, and S. W. Koch. Nonlinear optics of normal-mode-coupling semiconductor microcavities. *Rev. Mod. Phys.* 71(5):1591–1639, October 1999.
- [80] S. Hughes. Breakdown of the area theorem: carrier-wave Rabi flopping of femtosecond optical pulses. *Phys. Rev. Lett.* 81(16):3363–3366, October 1998.
- [81] S. L. McCall and E. L. Hahn. Self-induced transparency by pulsed coherent light. *Phys. Rev. Lett.* 18(21):908–911, May 1967.
- [82] H. Giessen, S. Linden, J. Kuhl, A. Knorr, S. W. Koch, M. Hetterich, M. Grün, and C. Klingshirn. High-intensity pulse propagation in semiconductors: on-resonant self-induced transmission and effects in the continuum. *Opt. Express* 4(2):121–128, January 1999.
- [83] O. D. Mücke, T. Tritschler, M. Wegener, U. Morgner, and F. X. Kärtner. Signatures of carrier-wave Rabi flopping in GaAs. *Phys. Rev. Lett.* 87(5):057401-1–4, July 2001.
- [84] A. Knorr, R. Binder, M. Lindberg, and S. W. Koch. Theoretical study of resonant ultrashort-pulse propagation in semiconductors. *Phys. Rev. A* 46(11):7179–7186, December 1992.
- [85] Th. Östreich and A. Knorr. Various appearances of Rabi oscillations for 2π -pulse excitation in a semiconductor. *Phys. Rev. B* 48(24):17811–17817, December 1993.
- [86] A. R. Zakharian, J. Hader, J. V. Moloney, and S. W. Koch. VECSEL threshold and output power-shutoff dependence on the carrier recombination rates. *IEEE Photon. Technol. Lett.* 17(12):2511–2513, December 2005.
- [87] J. Hader, J. V. Moloney, and S. W. Koch. Microscopic evaluation of spontaneous emission- and Auger-processes in semiconductor lasers. *IEEE J. Quantum Electron.* 41(10):1217–1226, October 2005.
- [88] S. R. Jin, S. J. Sweeney, C. N. Ahmad, A. R. Adams, and B. N. Murdin. Radiative and Auger recombination in $1.3\ \mu\text{m}$ InGaAsP and $1.5\ \mu\text{m}$ InGaAs quantum-well lasers measured under high pressure at low and room temperatures. *Appl. Phys. Lett.* 85(3):357–359, July 2004.
- [89] H. Haken. *Quantenfeldtheorie des Festkörpers*. Teubner, 2nd edition, 1993.
- [90] E. Binder, T. Kuhn, and G. Mahler. Coherent intraband and interband dynamics in double quantum wells: exciton and free-carrier effects. *Phys. Rev. B* 50(24):18319–18329, December 1994.
- [91] C. Z. Ning, R. A. Indik, and J. V. Moloney. Self-consistent approach to thermal effects in vertical-cavity surface-emitting lasers. *J. Opt. Soc. Am. B* 12(10):1993–2004, October 1995.

- [92] A. Thränhardt, S. Becker, C. Schlichenmaier, I. Kuznetsova, T. Meier, S. W. Koch, J. Hader, J. V. Moloney, and W. W. Chow. Nonequilibrium gain in optically pumped GaInNAs laser structures. *Appl. Phys. Lett.* 85(23):5526–5528, December 2004.
- [93] D. O’Brien, S. P. Hegarty, G. Huyet, and A. V. Uskov. Sensitivity of quantum-dot semiconductor lasers to optical feedback. *Opt. Lett.* 29(10):1072–1074, May 2004.
- [94] P. Borri, W. Langbein, J. M. Hvam, F. Heinrichsdorff, M.-H. Mao, and D. Bimberg. Ultrafast gain dynamics in InAs-InGaAs quantum-dot amplifiers. *IEEE Photon. Technol. Lett.* 12(6):594–596, June 2000.
- [95] E. Gehrig and O. Hess. Mesoscopic spatiotemporal theory for quantum-dot lasers. *Phys. Rev. A* 65(3):033804-1–16, March 2002.
- [96] M. Bahl, H. Rao, N. C. Panoiu, and R. M. Osgood, Jr. Simulation of mode-locked surface-emitting lasers through a finite-difference time-domain algorithm. *Opt. Lett.* 29(14):1689–1691, July 2004.
- [97] F. Wang, G. Dukovic, E. Knoesel, L. E. Brus, and T. F. Heinz. Observation of rapid Auger recombination in optically excited semiconducting carbon nanotubes. *Phys. Rev. B* 70(24):241403(R)-1–4, December 2004.
- [98] N. S. Stoykov, T. A. Kuiken, M. M. Lowery, and A. Taflove. Finite-element time-domain algorithms for modeling linear Debye and Lorentz dielectric dispersions at low frequencies. *IEEE Trans. Biomed. Eng.* 50(9):1100–1107, September 2003.
- [99] R. Luebbers, F. P. Hunsberger, K. S. Kunz, R. B. Standler, and M. Schneider. A frequency-dependent finite-difference time-domain formulation for dispersive materials. *IEEE Trans. Electromagn. Compat.* 32(3):222–227, August 1990.
- [100] H. Amekura, Y. Takeda, and N. Kishimoto. Criteria for surface plasmon resonance energy of metal nanoparticles in silica glass. *Nucl. Inst. and Meth. B* 222(1-2):96–104, July 2004.
- [101] S. K. Gray and T. Kupka. Propagation of light in metallic nanowire arrays: finite-difference time-domain studies of silver cylinders. *Phys. Rev. B* 68(4):045415-1–11, July 2003.
- [102] M. Fujii, M. Tahara, I. Sakagami, W. Freude, and P. Russer. High-order FDTD and auxiliary differential equation formulation of optical pulse propagation in 2-D Kerr and Raman nonlinear dispersive media. *IEEE J. Quantum Electron.* 40(2):175–182, February 2004.
- [103] J. Li and C. Z. Ning. Hydrodynamic theory for spatially inhomogeneous semiconductor lasers. I. A microscopic approach. *Phys. Rev. A* 66(2):023802-1–18, August 2002.
- [104] B. Witzigmann, A. Witzig, and W. Fichtner. A multidimensional laser simulator for edge-emitters including quantum carrier capture. *IEEE Trans. Electron Devices* 47(10):1926–1934, October 2000.

- [105] J. Piprek, Y. A. Akulova, D. I. Babic, L. A. Coldren, and J. E. Bowers. Minimum temperature sensitivity of $1.55\ \mu\text{m}$ vertical-cavity lasers at $-30\ \text{nm}$ gain offset. *Appl. Phys. Lett.* 72(15):1814–1816, April 1998.
- [106] E. Gehrig. *Raumzeitliche Dynamik von Hochleistungshalbleiterlasern unter kohärenter Strahlungsinjektion*. PhD thesis, Universität Kaiserslautern, 1999.
- [107] J. Hamm, K. Böhringer, and O. Hess. Spatially resolved polarization and temperature dynamics in quantum-well vertical-cavity surface-emitters: a mesoscopic approach. In *Physics and Simulation of Optoelectronic Devices X, Proc. SPIE 4646*, 176–189, 2002.
- [108] D. Preißer, K. Boehringer, and O. Hess. Thermodynamics of V(E)CSELs: I. The influence of Auger recombination & II. Quantum mechanical and semiclassical approaches. (*submitted to IEEE J. Quantum Electron.*).
- [109] M. Streiff, A. Witzig, M. Pfeiffer, P. Royo, and W. Fichtner. A comprehensive VCSEL device simulator. *IEEE J. Select. Topics Quantum Electron.* 9(3):879–891, May/June 2003.
- [110] M. Born and E. Wolf. *Principles of Optics: Electromagnetic Theory of Propagation, Interference and Diffraction of Light*. Cambridge University Press, 7th edition, 1999.
- [111] K. Kawano and T. Kitoh. *Introduction to Optical Waveguide Analysis: Solving Maxwell's Equations and the Schrödinger Equation*. John Wiley & Sons, 2001.
- [112] M. Munkel. *Raum-zeitliche Strukturbildung in Halbleiterlasern mit zeitverzögerter Rückkopplung*. PhD thesis, Technische Universität Darmstadt, 1998.
- [113] K. A. Williams, M. G. Thompson, and I. H. White. Long-wavelength monolithic mode-locked diode lasers. *New J. Phys.* 6:179-1–30, November 2004.
- [114] M. Lax, W. H. Louisell, and W. B. McKnight. From Maxwell to paraxial wave optics. *Phys. Rev. A* 11(4):1365–1370, April 1975.
- [115] P. Ru, J. V. Moloney, and R. A. Indik. Mean-field approximation in semiconductor-laser modeling. *Phys. Rev. A* 50(1):831–838, July 1994.
- [116] J. Mulet and S. Balle. Mode-locking dynamics in electrically driven vertical-external-cavity surface-emitting lasers. *IEEE J. Quantum Electron.* 41(9):1148–1156, September 2005.
- [117] Xunya Jiang and C. M. Soukoulis. Time dependent theory for random lasers. *Phys. Rev. Lett.* 85(1):70–73, July 2000.
- [118] M. San Miguel, Q. Feng, and J. V. Moloney. Light-polarization dynamics in surface-emitting semiconductor lasers. *Phys. Rev. A* 52(2):1728–1739, August 1995.
- [119] G. Mur. Absorbing boundary conditions for the finite-difference approximation of the time-domain electromagnetic-field equations. *IEEE Trans. Electromagn. Compat.* 23(4):377–382, November 1981.

- [120] R. Binder, D. Scott, A. E. Paul, M. Lindberg, K. Henneberger, and S. W. Koch. Carrier-carrier scattering and optical dephasing in highly excited semiconductors. *Phys. Rev. B* 45(3):1107–1115, January 1992.
- [121] P. Harrison. The nature of the electron distribution functions in quantum cascade lasers. *Appl. Phys. Lett.* 75(18):2800–2802, November 1999.
- [122] R. C. Iotti and F. Rossi. Microscopic theory of hot-carrier relaxation in semiconductor-based quantum-cascade lasers. *Appl. Phys. Lett.* 76(16):2265–2267, April 2000.
- [123] S.-C. Lee and I. Galbraith. Multisubband nonequilibrium electron-electron scattering in semiconductor quantum wells. *Phys. Rev. B* 55(24):R16025–R16028, June 1997.
- [124] S.-C. Lee and I. Galbraith. Intersubband and intrasubband electronic scattering rates in semiconductor quantum wells. *Phys. Rev. B* 59(24):15796–15805, June 1999.
- [125] W. W. Chow, M. Kira, and S. W. Koch. Microscopic theory of optical nonlinearities and spontaneous emission lifetime in group-III nitride quantum wells. *Phys. Rev. B* 60(3):1947–1952, July 1999.
- [126] M. Bahl, N. C. Panoiu, and R. M. Osgood, Jr. Modeling ultrashort field dynamics in surface emitting lasers by using finite-difference time-domain method. *IEEE J. Quantum Electron.* 41(10):1244–1252, October 2005.
- [127] J. V. Moloney, R. A. Indik, J. Hader, and S. W. Koch. Modeling semiconductor amplifiers and lasers: from microscopic physics to device simulation. *J. Opt. Soc. Am. B* 16(11):2023–2029, November 1999.
- [128] Q. Feng, J. V. Moloney, and A. C. Newell. Transverse patterns in lasers. *Phys. Rev. A* 50(5):R3601–R3604, November 1994.
- [129] R. Gordon and J. Xu. Lateral mode dynamics of semiconductor lasers. *IEEE J. Quantum Electron.* 35(12):1904–1911, December 1999.
- [130] W. W. Chow, H. Amano, and I. Akasaki. Theoretical analysis of filamentation and fundamental-mode operation in InGaN quantum well lasers. *Appl. Phys. Lett.* 76(13):1647–1649, March 2000.
- [131] V. Voignier, J. Houlihan, J. R. O’Callaghan, C. Sailliot, and G. Huyet. Stabilization of self-focusing instability in wide-aperture semiconductor lasers. *Phys. Rev. A* 65(5):053807-1–5, May 2002.
- [132] S. K. Mandre, I. Fischer, and W. Elsässer. Spatiotemporal emission dynamics of a broad-area semiconductor laser in an external cavity: stabilization and feedback-induced instabilities. *Opt. Commun.* 244(1-6):355–365, January 2005.
- [133] A. R. Zakharian, J. Hader, J. V. Moloney, S. W. Koch, P. Brick, and S. Lutgen. Experimental and theoretical analysis of optically pumped semiconductor disk lasers. *Appl. Phys. Lett.* 83(7):1313–1315, August 2003.

- [134] J. E. Hastie, J.-M. Hopkins, C. W. Jeon, S. Calvez, D. Burns, M. D. Dawson, R. Abram, E. Riis, A. I. Ferguson, W. J. Alford, T. D. Raymond, and A. A. Allerman. Microchip vertical external cavity surface emitting lasers. *Electron. Lett.* 39(18):1324–1326, September 2003.
- [135] P. Vankwikelberge, G. Morthier, and R. Baets. CLADISS—a longitudinal multimode model for the analysis of the static, dynamic, and stochastic behavior of diode lasers with distributed feedback. *IEEE J. Quantum Electron.* 26(10):1728–1741, October 1990.
- [136] M. B. Flynn, L. O’Faolain, and T. F. Krauss. An experimental and numerical study of Q-switched mode-locking in monolithic semiconductor diode lasers. *IEEE J. Quantum Electron.* 40(8):1008–1013, August 2004.
- [137] M. Kauer, J. R. A. Cleaver, J. J. Baumberg, and A. P. Heberle. Femtosecond dynamics in semiconductor lasers: dark pulse formation. *Appl. Phys. Lett.* 72(13):1626–1628, March 1998.
- [138] H. F. Hofmann and O. Hess. Quantum Maxwell-Bloch equations for spatially inhomogeneous semiconductor lasers. *Phys. Rev. A* 59(3):2342–2358, March 1999.
- [139] T. Makino. Transfer-matrix theory of the modulation and noise of multielement semiconductor lasers. *IEEE J. Quantum Electron.* 29(11):2762–2770, November 1993.
- [140] M. O. Ziegler, M. Münkler, T. Burkhard, G. Jennemann, I. Fischer, and W. Elsässer. Spatiotemporal emission dynamics of ridge waveguide laser diodes: picosecond pulsing and switching. *J. Opt. Soc. Am. B* 16(11):2015–2022, November 1999.
- [141] P. Bienstman, R. Baets, J. Vukusic, A. Larsson, M. J. Noble, M. Brunner, K. Gulden, P. Debernardi, L. Fratta, G. P. Bava, H. Wenzel, B. Klein, O. Conradi, R. Pregla, S. A. Riyopoulos, J.-F. P. Seurin, and S. L. Chuang. Comparison of optical VCSEL models on the simulation of oxide-confined devices. *IEEE J. Quantum Electron.* 37(12):1618–1631, December 2001.
- [142] W. H. Press, S. A. Teukolsky, W. T. Vetterling, and B. P. Flannery. *Numerical Recipes in C: The Art of Scientific Computing*. Cambridge University Press, 2nd edition, 1992.
- [143] C. Hermann. Personal correspondence.
- [144] J. P. Dowling, M. Scalora, M. J. Bloemer, and C. M. Bowden. The photonic band edge laser: a new approach to gain enhancement. *J. Appl. Phys.* 75(4):1896–1899, February 1994.
- [145] J. Hamm. Personal correspondence.
- [146] S.-S. Beyertt, M. Zorn, T. Kübler, H. Wenzel, M. Weyers, A. Giesen, G. Tränkle, and U. Brauch. Optical in-well pumping of a semiconductor disk laser with high optical efficiency. *IEEE J. Quantum Electron.* 41(12):1439–1449, December 2005.

- [147] T. Leinonen, Y. A. Morozov, A. Härkönen, and M. Pessa. Vertical external-cavity surface-emitting laser for dual-wavelength generation. *IEEE Photon. Technol. Lett.* 17(12):2508–2510, December 2005.
- [148] A. S. Nagra and R. A. York. FDTD analysis of wave propagation in nonlinear absorbing and gain media. *IEEE Trans. Antennas Propagat.* 46(3):334–340, March 1998.
- [149] K. Boehringer and O. Hess. A full time-domain approach to spatio-temporal dynamics of active semiconductor devices. In *Numerical Simulation of Optoelectronic Devices (NUSOD)*, 79–80, 2005.
- [150] O. Okhotnikov, A. Grudinin, and M. Pessa. Ultra-fast fibre laser systems based on SESAM technology: new horizons and applications. *New J. Phys.* 6:177-1–22, November 2004.
- [151] H. A. Haus. Mode-locking of lasers. *IEEE J. Select. Topics Quantum Electron.* 6(6):1173–1185, November/December 2000.
- [152] M. van der Poel, J. Mørk, and J. M. Hvam. Controllable delay of ultrashort pulses in a quantum dot optical amplifier. *Opt. Express* 13(20):8032–8037, October 2005.
- [153] R. Trebino. *Frequency-Resolved Optical Gating: The Measurement of Ultrashort Laser Pulses*. Kluwer Academic Publishers, 2002.
- [154] S. L. McCall and E. L. Hahn. Self-induced transparency. *Phys. Rev.* 183(2):457–485, July 1969.
- [155] G. L. Lamb, Jr. Analytical descriptions of ultrashort optical pulse propagation in a resonant medium. *Rev. Mod. Phys.* 43(2):99–124, April 1971.
- [156] J. Xiao, Z. Wang, and Z. Xu. Area evolution of a few-cycle pulse laser in a two-level-atom medium. *Phys. Rev. A* 65(3):031402(R)-1–4, March 2002.
- [157] A. R. Gourlay and G. R. McGuire. General hopscotch algorithm for the numerical solution of partial differential equations. *J. Inst. Math. Appl.* 7(2):216–227, April 1971.
- [158] K. S. Yee. Numerical solution of initial boundary value problems involving Maxwell’s equations in isotropic media. *IEEE Trans. Antennas Propagat.* 14(3):302–307, May 1966.
- [159] F. Jahnke and S. W. Koch. Ultrafast intensity switching and nonthermal carrier effects in semiconductor microcavity lasers. *Appl. Phys. Lett.* 67(16):2278–2280, October 1995.

Acknowledgements

A number of people have contributed to this work in one way or another. I gratefully acknowledge the help and advice of all of them.

First of all, I would like to thank Prof. Dr. O. Hess for the opportunity to carry out this research project in his group, for the support and constant interest in the progress of the work, and for providing access to an excellent computing infrastructure.

I thank Prof. Dr. G. Mahler for writing the second report on my dissertation.

Many thanks go to Joachim Hamm and Eldad Yahel for proofreading the manuscript and correcting my English, and to Andreas Klaedtke and Dietmar Preißer for the assistance in the numerical implementation of the various semiconductor laser models.

I also want to thank all my friends and family, and my colleagues in the Theoretical Quantum Electronics group at the Institute of Technical Physics (German Aerospace Center, DLR Stuttgart) and in the Theory and Advanced Computation group at the Advanced Technology Institute (University of Surrey, Guildford, United Kingdom) for helping and supporting me over the past years.

Guildford (United Kingdom), May 2007

Klaus Böhringer